Study of nucleon structure through scattering of leptons

Mémoire d'Habilitation à Diriger des Recherches

Etienne Burtin

May 27, 2010

Contents

Introduction

The nucleons are composed of elementary particles, quarks and gluons. Evidence from the composite structure of the nucleons first came from the fact that their magnetic moment differs from the nuclear magneton which characterizes point-like particles. The existence of quarks within the nucleons was first postulated by Gell-Mann and Zweig (in1964) in order to explain the hadrons spectrum. Indeed, elastic scattering experiments (after 1955) revealed the extent of the charge distributions through the measurement of form factors. For protons the charge radius was found to be about 0.8 fm. At the end of the 60's, with the energy increase of the particle accelerator it became possible to break the nucleons into pieces in experiments known as «deep inelastic scattering» experiments. The scaling behavior of these experiments was received as the proof of scattering off point-like particles inside the nucleons. Increasing the kinematical domain later allowed to show that only half of the nucleon energy is actually carried by the quarks, the remaining half was then attributed to the gluons, mediator of the strong interaction.

In 1988, the European Muon Collaboration showed that the contribution of quarks to the nucleon spin is much smaller than expected and that the strange quark contribution is non-zero. These results, later referred to as the «spin crisis» have triggered an important experimental and theoretical work and new experiments were performed in order to confirm and precise them (SMC, SLAC, DESY). The outcome of this second campaign confirmed the EMC result. The community started a wide program of investigations. The contribution of strange quarks to other observables such as the elastic form factors was to be measured by studying the parity violation in elastic scattering experiment. The contribution of gluons to the nucleon spin was to be measured though the process of semi-inclusive deep inelastic scattering. And the contribution of angular momentum appeared to be accessible with hard exclusive photon or meson production reactions.

This habilitation work summarizes my contributions to the field. In the first chapter, I give the basic theoretical description of some of the various ways of probing the nucleon structure. In the second chapter I describe how the measurement of the parity violation in electrons scattering allows to access the strange form factor of the nucleon. I describe the HAPPEX experiment at Jefferson Lab and the Compton beam polarimeter that our group has built for this program and in which I was strongly involved. In the third chapter, I present the apparatus of the COMPASS experiment at CERN and I briefly show the result on the measurement of the contribution of gluons to the nucleon spin.

In the last two chapters, I focus on my recent work on the study of exclusive processes using COMPASS. The fourth chapter is devoted to the exclusive production of the ρ^0 meson. There, I present the first attempt to study this exclusive channel using the data accumulated in the previous years of running without a recoil detector which will be a must in the future program. I will discuss the selection of this channel and the results obtained on the transverse target spin asymmetries related to GPDs.

Finally, in the last chapter, I present the proposal for a measurement of the Deeply Virtual Compton Scattering process using the COMPASS spectrometer. I present the projections of errors for the different observables directly related to GPDs and obtained with a simulation program which I have developed. I will also show the preliminary results of beam tests performed to demonstrate the feasibility of the proposed experiment that conclude on the observation of the DVCS process at COMPASS.

Chapter 1

Probes of the nucleon structure

The scattering of accelerated particles has always been a way to learn about matter structure. We will examine three different ways to probe the nucleon structure. First, through elastic scattering one measures the form factors which are related to the overall size of the charge and magnetization distributions. This can be further decomposed on the quark flavors by using the weak interaction. Second, through deep inelastic scattering one measures the probability to find a parton with a given momentum. Then, with a polarized target, the contributions of quark flavors and gluons to the nucleon spin can be extracted. Finally, the two sets of observables are unified in the framework of the generalized parton distributions accessible through the hard exclusive production of a photon or a meson.

1.1   Elastic scattering

We consider the elastic scattering of an electron off a proton which is represented at Born approximation on figure 1.1. The electron has a quadri-momentum k and a spin s and the proton has quadri-momentum p and a spin S. In the final state, the momentum and spin of the particles are denoted with a prime ('). A virtual photon is exchanged and has the quadri-momentum q. For a given lepton energy, the kinematics of elastic
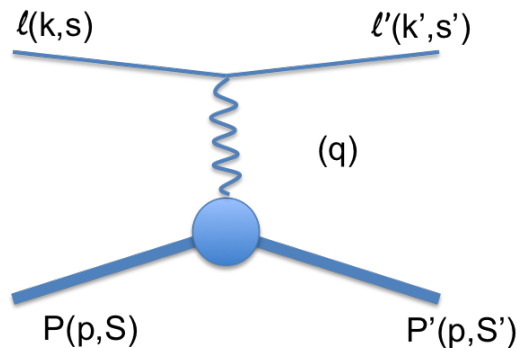

Figure 1.1: Elastic scattering of a lepton off a proton at Born approximation.

scattering is described with only one variable. It is often chosen to be the virtuality of the photon :

$$Q^2 = -q^2 = -(k - k')^2 \tag{1.1}$$

which in case of elastic scattering coincides with the momentum transfer to the proton, t :

$$t = (p' - p)^2 \tag{1.2}$$

The scattering amplitude for this process is :

$$M = j^\mu_{EM} \frac{g_{\mu\nu}}{Q^2} J^\mu_{EM} \tag{1.3}$$

where j^μ_{EM} is the electromagnetic current at the electron vertex, J^μ_{EM} is the electromagnetic current at the proton vertex and $g_{\mu\nu}$ is the metric tensor. As the electron is point-like and has spin $\frac{1}{2}$, its electromagnetic current is built on the Dirac matrix γ^μ and the spinors u and $\bar{u}$ and has the form :

$$j^\mu_{EM} = \bar{u}(k', s')\gamma^\mu u(k, s) \tag{1.4}$$

At the nucleon vertex, the expression of the coupling of the electromagnetic current is not straightforward since the nucleon is not a point-like particle. It can be built on the relevant Lorentz vectors and after applying current conservation, parity conservation and hermiticity it reduces to :

$$\langle P'(p', S')| J^\mu_{EM} |P(p, S)\rangle = \bar{u}(p', S') \left[\gamma^\mu F_1^{(\gamma, p)}(Q^2) + i\frac{\sigma^{\mu\nu} q_\nu}{2M} F_2^{(\gamma, p)}(Q^2) \right] u(p, S) \tag{1.5}$$

where M is the nucleon mass. Our lack of knowledge of the nucleon structure is then contained in the coefficients $F_1^{(\gamma, p)}(Q^2)$ and $F_2^{(\gamma, p)}(Q^2)$ known as the Dirac and Pauli form factors which depend on the scalar variable Q^2 used to describe the process. The interpretation of the form factors is better understood when considering the electric, $G_E(Q^2)$, and magnetic, $G_M(Q^2)$, Sachs form factors which are linear combinations of the Pauli and Dirac form factors [1]:

$$G_E(Q^2) = F_1(Q^2) - \tau F_2(Q^2) \quad \text{with } \tau = \frac{Q^2}{4M^2} \tag{1.6}$$

$$G_M(Q^2) = F_1(Q^2) + F_2(Q^2) \tag{1.7}$$

The Sachs form factor are related to some of the macroscopic properties of the nucleons. For example, at $Q^2 = 0$, they are normalized to the electric charge and magnetic moment :

$$G_E^P(0) = 1 \quad G_M^P(0) = \mu_P = 2.79 \tag{1.8}$$

$$G_E^N(0) = 0 \quad G_M^N(0) = \mu_N = -1.91 \tag{1.9}$$
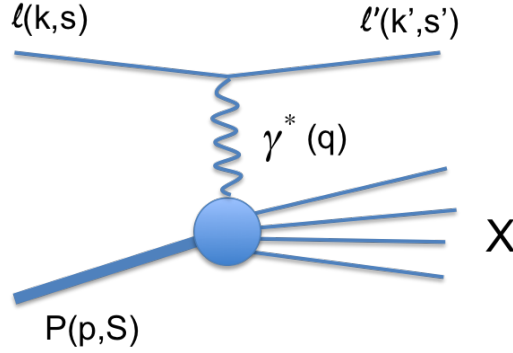
Figure 1.2: The deep inelastic scattering process

where we have separated the proton (P) and the neutron (N) quantities. Furthermore, at the limit of low recoil of the target nucleon ($|t| \ll M_N^2$), the form factors are the Fourier transform of the electric charge and magnetization spatial distributions. The Sachs form factors are, to a good precision (and up to $Q^2 \approx 1 \, (\text{GeV}/c)^2$) described by a dipole dependence :

$$G_M(Q^2) = \mu_P G_D(Q^2) = \frac{\mu_P}{(1 + \lambda_D \frac{Q^2}{4M^2})^2} \quad \text{with } \lambda_D = 4.97 \tag{1.10}$$

which is the Fourier transform of an exponential distribution $\rho(r) = e^{-\frac{r}{r_0}}$ with $r_0 \propto \sqrt{\lambda_D}/2M$. The first derivative of the form factors is related to the quadratic charge radius of the charge and magnetization distribution :

$$\left. \frac{dG_{E,M}(Q^2)}{dQ^2} \right|_{Q^2=0}^2 = -\frac{1}{6(\hbar c)^2} < r_{E,M}^2 > \tag{1.11}$$

Historically, the form factors were extracted from cross section measurements at different beam energies through the Rosenbluth separation [2]. In the last ten years, the knowledge of form factors [3] has progressed significantly with the onset of recoil particle polarization measurements [4, 5] at high quality electron accelerators such as MAMI and JLab.

1.2 Deep Inelastic Scattering

Description of the formalism

With the increased energy of available lepton beams the inner structure of nucleons could be revealed through the process of Deep Inelastic Scattering (represented in figure 1.2). In this process the energy available in the $\gamma^* - p$ system is much higher than the nucleon mass which breaks into fragments (denoted by X). At high momentum transfer ($Q^2 > 1 \, (\text{GeV}/c)^2$) the Compton wavelength of the photon becomes smaller than the nucleon size and the interaction occurs with the constituents of the nucleon. The cross

section of the deep inelastic scattering is obtained from the contraction of the leptonic and hadronic tensor :

$$\frac{d^2\sigma}{dxdQ^2} = \frac{\alpha^2}{4M^2E^2}\frac{1}{x^2Q^2}L^{\mu\nu}W_{\mu\nu} \tag{1.12}$$

The leptonic tensor, $L^{\mu\nu}$, is perfectly known and can be derived using the Feynman rules of Quantum Electro-Dynamics :

$$\begin{aligned}
L^{\mu\nu} &= \sum_{s'}\left[\bar{u}(k')\gamma^\mu u(k)\right]\left[\bar{u}(k')\gamma^\nu u(k)\right]^* \\
&= 2(k^\mu k'^\nu + k^\nu k'^\mu - g^{\mu\nu}k\cdot k' - i\epsilon^{\mu\nu\alpha\beta}q_\alpha s_\beta)
\end{aligned} \tag{1.13}$$

where the sum is done over the spin of the scattered lepton and terms involving the lepton mass were neglected. In this expression $g^{\mu\nu}$ is the metric tensor and $\epsilon^{\mu\nu\alpha\beta}$ is the Levi-Civita totally antisymmetric tensor. For the hadronic tensor, $W_{\mu\nu}$, the calculation is not straightforward since it would require to calculate the interaction between the hadronic current and all possible final state X:

$$W_{\mu\nu} = \sum_X \sum_{spins} \langle P| J_\mu |X\rangle \langle X| J_\nu |P\rangle \tag{1.14}$$

It is then preferred to parametrize the hadronic tensor from the independent tensors built on the problem variables : p_μ, q_μ, $g_{\mu\nu}$, s_μ and $\epsilon_{\mu\nu\alpha\beta}$. There are only 4 independent terms invariant under parity, charge conjugation, time reversal and which conserve the electromagnetic current at the vertex. The hadronic tensor is a linear combination of these tensors [9]:

$$\begin{aligned}
W_{\mu\nu} &= -F_1(x,Q^2)\,g_{\mu\nu} + \frac{F_2(x,Q^2)}{p\cdot q}\cdot p_\mu p_\nu \\
&\quad -iM\epsilon_{\mu\nu\alpha\beta}\left(\frac{g_1(x,Q^2)}{p\cdot q}\cdot q_\alpha S_\beta + \frac{g_2(x,Q^2)}{(p\cdot q)^2}\cdot q_\alpha(p\cdot qS^\beta - S\cdot qp^\beta)\right)
\end{aligned} \tag{1.15}$$

where our lack of knowledge of the nucleon structure is included in the multiplicative coefficients F_1 and F_2 which are the unpolarized structure function[1] of the nucleon and g_1 and g_2 which are the polarized structure functions. The structure functions depend on two scalar variables : x and Q^2 are traditionally used.

Quark Parton Model interpretation

The physics content of the deep inelastic scattering can be understood in the framework of the parton model. In this model the interaction is described in the proton infinite momentum frame where the quarks have only longitudinal momenta along the direction of the photon-proton collision and do not interact with each other. The interaction between the virtual photon and the nucleon is then seen as the incoherent sum of the

---

[1]these functions are different from the form factors although they are named with the same symbols

interactions between the virtual photon and each individual component of the nucleon (i.e. the partons). The structure functions are related to the parton distribution function $q_i(x)$ which are the probability to find a quark of a given flavor i carrying a fraction x of the proton momentum. In the parton model, the variable x is found to be equal to the Bjorken variable [6]:

$$x = x_{bj} \equiv \frac{Q^2}{2p \cdot q} \tag{1.16}$$

which can be measured experimentally using the quadri-vector of the incoming and scattered leptons. The parton distribution function receive contributions from quarks q and anti-quarks $\bar{q}$

$$q(x) = q_+(x) + q_-(x) + \bar{q}_+(x) + \bar{q}_-(x)) \tag{1.17}$$

where we have also separated the contribution of partons with their spin aligned $(+)$ or anti-aligned (-) with the nucleon spin. Then, the structure function have the following interpretation :

$$F_1(x) = \frac{1}{2} \sum_{q=u,d,s} e_q^2 q(x) \tag{1.18}$$

$$F_2(x) = \sum_{q=u,d,s} e_q^2 x q(x) \tag{1.19}$$

The integral of the structure function describe macroscopic properties of the nucleon. For instance, the integral of F_2 :

$$I = \int_0^1 F_2(x) dx = \sum_{q=u,d,s} \int_0^1 e_q^2 x q(x) dx \tag{1.20}$$

allows to measure the contribution of quarks to the nucleon momentum. The result obtained is of the order of 50% and deficit of momentum is attributed to gluons.

In the polarized case, the probability to find a quark with its spin aligned with the proton spin, $\Delta q(x)$, can be defined as :

$$\Delta q(x) = q_+(x) - q_-(x) + \bar{q}_+(x) - \bar{q}_-(x)) \tag{1.21}$$

and the structure function g_1 can be interpreted as :

$$g_1(x) = \frac{1}{2} \sum_{q=u,d,s} e_q^2 \Delta q(x) \tag{1.22}$$

and $g_2(x) = 0$. The polarized structure functions are measured through asymmetries with both the beam and the target polarized.

The Nucleon spin puzzle

The nucleon has a spin $1/2$ and it can be decomposed on its constituents. It receives contributions from the spin of the quarks, $\Delta\Sigma$, from the spin of the gluons ΔG and from the orbital angular momentum $L_{q,g}$ of the quarks and the gluons leading to what is known as the spin sum rule (in the Jaffe-Manohar decomposition [7]):

$$\frac{1}{2} = \frac{1}{2}\Delta\Sigma + \Delta G + L_q + L_g \tag{1.23}$$

In relativistic parton models [8] the contributions of the quarks can be estimated and typical values are :

$$\Delta\Sigma \sim 0.75 \qquad L_q \sim 0.125 \tag{1.24}$$

In the Operator Product Expansion formalism [9], one can relate the moments of the structure functions to matrix elements of local operators. For example, the first moment of the g_1 structure function can be expressed as :

$$\Gamma_1^p = \int_0^1 g_1^p(x)dx = \frac{1}{2} \sum_{q=u,d,s} e_q^2 a_q \tag{1.25}$$

where a_q are the matrix elements of the axial current of a given flavor and are defined as :

$$a_q = < P_i|\bar{\psi}_q\gamma^\mu\gamma^5\psi_q|P_j > \tag{1.26}$$

It follows that in the parton model : $a_q = \Delta q$. In SU(3) flavor symmetry, the axial currents can be rewritten with the SU(3) generators, λ_j :

$$A_j^\mu = \bar{\psi}\gamma^\mu\gamma^5\lambda_j\psi \quad with \quad \psi = \begin{pmatrix} \psi_u \\ \psi_d \\ \psi_s \end{pmatrix} \tag{1.27}$$

One can then rewrite the flavor matrix elements on the base of the SU(3) diagonal generators:

$$a_0 = a_u + a_d + a_s \tag{1.28}$$
$$a_3 = a_u - a_d \tag{1.29}$$
$$a_8 = \frac{1}{\sqrt{3}}(a_u + a_d - 2a_s) \tag{1.30}$$

where a_0 is the singlet flavor axial matrix element and a_3 and a_8 are non-singlet. If we now assume SU(3) symmetry to be valid, the weak decay of the hyperons provides measurements of a_3 and a_8. The third constrain comes from the integral of the polarized structure function, g_1 :

$$\Gamma_1^p = \int_0^1 g_1^p(x)dx = \frac{1}{36}(4a_0 + 3a_3 + a_8) \tag{1.31}$$
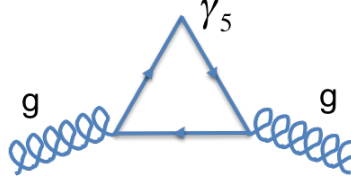
Figure 1.3: Diagram responsible of the "axial anomaly".

Going back to the parton model, we find that the matrix element a_0 is equal to the spin carried by the quarks :

$$a_0 = \Delta u + \Delta d + \Delta s = \Delta \Sigma \qquad (1.32)$$

In 1988 the EMC experiment at CERN published the striking result that the contribution of quarks to the nucleon spin is rather small and compatible with zero in complete contradiction with the relativistic quark model and that the strange quarks are polarized. This result triggered what is known as the "spin crisis". Since then, many experiments were performed at SLAC, CERN, DESY and JLab and recent results now state that only 30% of the nucleon spin arises from the quarks.

It was also shown that taking into account higher order diagrams in α_S which couple gluons of the nucleon wave function to the axial current (see figure 1.3) contribute to a_0 in the following manner :

$$a_0(Q^2) = \Delta \Sigma - 3 \frac{\alpha_S(Q^2)}{2\pi} \Delta G(Q^2) \qquad (1.33)$$

$$a_s(Q^2) = \Delta s - \frac{\alpha_S(Q^2)}{2\pi} \Delta G(Q^2) \qquad (1.34)$$

where we have explicitly written the Q^2 dependence arising from the fact that this axial contribution breaks the conservation of the axial current in what is known as the "axial anomaly". It appeared then that large values of $\Delta G \sim 2$ would reconcile the measurements and the predictions of relativistic quark models. Although, indirect determination of ΔG through the QCD evolution equations of polarized parton distributions seemed to point towards lower values. The measurement of ΔG is one of the main goals of the COMPASS experiment at CERN and at RHIC and is briefly presented in the third chapter of this document.

Having a large value of ΔG implies qualitatively to have a large and opposite value for the angular orbital momentum in order to fulfill the nucleon spin sum rule. From a theoretical point of view [10], there is no representation yet where all components of Eq. 1.23 correspond to physics observables defined by gauge invariant operators and no direct access to the parton orbital angular momentum has been identified. In contrast, in the next section, we present the Ji decomposition [14] and the possibility to access the angular momentum through the measurement of the Generalized Parton Distributions.
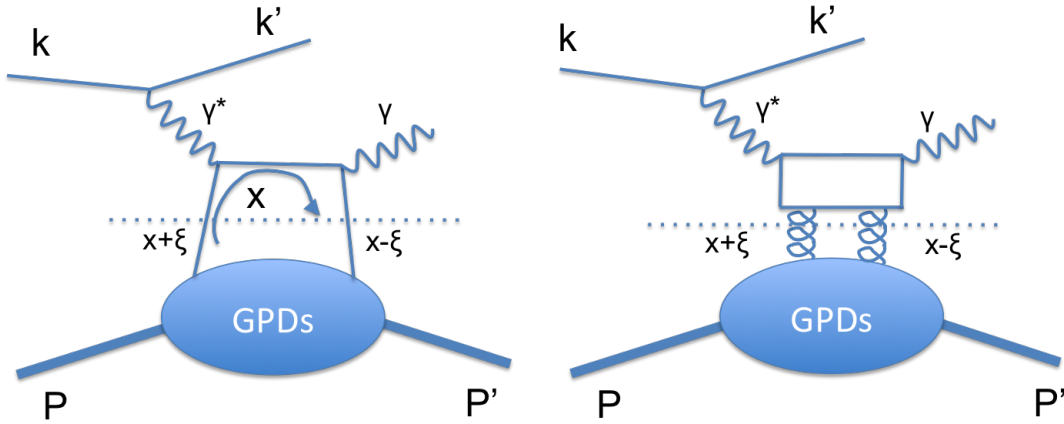
Figure 1.4: Leading twist Feynman diagrams for the DVCS process involving the exchange of quarks (left) or gluons (right). The dotted lines illustrate the factorization between the perturbative QCD calculable probe (top) and the non perturbative nucleon structure (bottom).

1.3   Generalized Partons Distributions

Generalized Partons Distributions (GPDs) are theoretical objects which were introduced only 15 years ago [11, 14, 15]. They provide a novel description of the nucleon and unify the already measured quantities such as form factors and unpolarized and polarized parton distributions functions. They can be accessed through the process of Deeply Virtual Compton Scattering (DVCS) or Hard Exclusive Meson Production (HEMP). In figure 1.4, we have represented the leading twist "handbag" diagrams contributing to the DVCS process which can proceed either through the exchange of 2 quarks or 2 gluons. At high Q^2 and for momentum transfer $|t| \ll Q^2$, the amplitude can be factorized into a term containing the hard probe calculable in QCD (top part of the graphs) and a term containing the non-perturbative nucleon structure [12]. In the case of HEMP, the real photon in the final state is replaced by a meson and the factorization is only valid for longitudinal virtual photons [13]. For DVCS, the gluons contribution is suppressed by a factor α_S with respect to the quarks contribution whereas for the HEMP they appear at the same order in α_S.

We now examine the definitions and properties of the GPDs. The lower part of the graph (below the dotted line) can be expressed as the matrix element of the bi-local quark field operator :

$$\Lambda^\mu = \int \frac{d\lambda}{2\pi} e^{ix\lambda} \left\langle P + \frac{\Delta}{2} \left| \bar{q}(-\frac{\lambda}{2}n) \gamma^\mu q(+\frac{\lambda}{2}n) \right| P - \frac{\Delta}{2} \right\rangle \qquad (1.35)$$

where $\Delta^2 = -(p - p')^2 = -t$ is the momentum transfer to the proton. Similarly to the DIS case, the nucleon structure is parametrized by two generalized parton distributions H and E which are the coefficients of the expansion in the possible vectors and axial-

vector components γ^μ and $\sigma^{\mu\nu}\Delta_\nu$

$$\Lambda^\mu = u(P+\frac{\Delta}{2})\left[H(x,\xi,t)\gamma^\mu + iE(x,\xi,t)\sigma^{\mu\nu}\frac{\Delta_\nu}{2M}\right]u(P+\frac{\Delta}{2}) \qquad (1.36)$$

The functions introduced depends on 3 variables. It is chosen to use x, the longitudinal proton momentum fraction carried by the quark circulating in the loop, ξ, the longitudinal momentum fraction imbalance between the quark lines which has the interesting property to be related to x_{bj} through : $\xi = x_{bj}/(2-x_{bj})$. Finally, the transfer t is used as the third variable to describe the GPDs. For the axial-vector part, we introduce two other generalized parton distributions $\tilde{H}$ and $\tilde{E}$ to describe the corresponding matrix element :

$$\int \frac{d\lambda}{2\pi}e^{ix\lambda}\left\langle P+\frac{\Delta}{2}\big| \bar{q}(-\frac{\lambda}{2}n)\,\gamma^\mu\gamma^5\,q(+\frac{\lambda}{2}n)\,\big|P-\frac{\Delta}{2}\right\rangle = \qquad (1.37)$$

$$\bar{u}(P+\frac{\Delta}{2})\left[\tilde{H}(x,\xi,t)\gamma^\mu\gamma^5 + i\tilde{E}(x,\xi,t)\frac{\Delta_\nu}{2M}\gamma^5\right]u(P+\frac{\Delta}{2}) \qquad (1.38)$$

In the case of forward deep inelastic scattering the application of the optical theorem [9] states that $\Delta = 0$. This implies that the functions E and $\tilde{E}$ which are multiplied by Δ were not accessible through DIS and that they can bring new information on the nucleon structure.

1.3.1 Sum rules

At the limit $\xi \to 0$ and $t \to 0$, the GPDs tend to the parton distribution functions:

$$H(x,0,0) = q(x) \qquad (1.39)$$
$$\tilde{H}(x,\xi=0,t=0) = \Delta q(x) \qquad (1.40)$$

There are no corresponding relations E and $\tilde{E}$ for the reason mentioned above that they are always multiplied by the transfer Δ and that their contribution vanishes at the DIS limit.

Then, the first moments of the GPDs are linked to the elastic form factors through their integral over x:

$$\int H(x,\xi,t)dx = F_1(t) \qquad \forall\xi \qquad (1.41)$$

$$\int E(x,\xi,t)dx = F_2(t) \qquad \forall\xi \qquad (1.42)$$

$$\int \tilde{H}(x,\xi,t)dx = G_A(t) \qquad \forall\xi \qquad (1.43)$$

$$\int \tilde{E}(x,\xi,t)dx = G_P(t) \qquad \forall\xi \qquad (1.44)$$

where F_1 and F_2 are the Dirac and Pauli form factors and G_A and G_P are the axial vector and pseudo-scalar form factors of the nucleons. They were absent of the description

of electromagnetic elastic scattering but will come into play when we will examine the measurement of the weak form factors.

Finally, the GPDs can be related to the total angular momentum carried by the quarks, J_q, through the Ji sum rule [14] , which states that :

$$J_q = \int x(H(x,\xi,t=0) + E(x,\xi,t=0))dx \qquad (1.45)$$

In Ji's representation J_q is the sum of the spin carried by the quarks and their orbital momentum:

$$J_q = \frac{1}{2}\Delta\Sigma + \mathcal{L}_q \qquad (1.46)$$

where the orbital angular momentum contribution $\mathcal{L}_q$ has a different definition than the one used in equation 1.23 although the definition of $\Delta\Sigma$ is the same. Accessing the Ji's sum rule will bring another constrain in the search of the origin of the nucleon spin complementary to intrinsic quarks and gluons contributions measurement and has allowed to envisage a possible solution of the "proton spin crisis".

1.3.2   Transverse distribution of partons in the nucleon

A particularly simple physical interpretation for GPDs as probability density exists in the limiting case $\xi = 0$ where the parton carries the same longitudinal momentum fraction x in initial and final state and hence the momentum transfer is purely transverse, $t = -\Delta_\perp^2$. In this case, in analogy to the case of form factors, the Fourier transform of the GPD $H_f(x, 0, -\Delta_\perp^2)$ for fixed x describes the spatial distribution $q(x, b_\perp)$ of partons of species f carrying the longitudinal momentum fraction x located at a transverse distance $b_\perp$ from the center of momentum of the nucleon [20, 16]:

$$q_f(x, b_\perp) = \int \frac{d^2\Delta_\perp}{(2\pi)^2} e^{-i\Delta_\perp \cdot b_\perp} H_f(x, 0, -\Delta_\perp) \qquad (1.47)$$

With this relation, it will become possible to observe whether the valence quarks are located in a small core at center of the nucleon or whether the gluons distribution extends to larger distances as described in figure 1.5. The average squared impact parameter is linked to the GPD H through the relation:

$$< b_\perp^2 > = \frac{\int d^2b_\perp b_\perp^2 q_f(x, b_\perp)}{\int d^2b_\perp q_f(x, b_\perp)} = 4\frac{\partial}{\partial t} \log H^f(x, 0, t)\Big|_{t=0} \qquad (1.48)$$

which is similar to the relation linking the Form Factors and the quadratic charge radius of the nucleon (equation 1.11). The quantity $< b_\perp^2 >$ can be predicted by lattice calculations [24] and the results are consistent with the image depicted above.
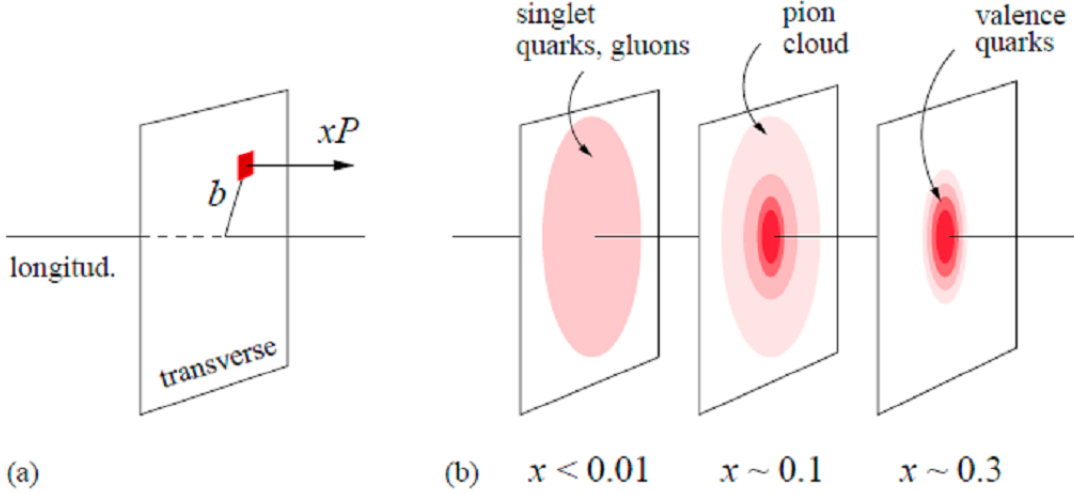
Figure 1.5: Scheme of the transverse size of the partonic structure for increasing x..

1.3.3 Compton Form Factors

The notion of form factor has been extended to the GPDs formalism under the denomination of Compton Form Factors [18]. In the measurement of GPDs through DVCS, the loop in the handbag diagram results in an integral over the variable x. The Compton Form Factors $\mathcal{H}$ are defined as (similar relation holds for each GPD) :

$$\mathcal{H}(\xi, t; Q^2) = \sum_f e_f^2 \int_{-1}^{1} dx H^f(x, \xi, t; Q^2) \left(\frac{1}{\xi - x - i\epsilon} - \frac{1}{\xi + x - i\epsilon} \right) \qquad (1.49)$$

where the function H_f are the GPDs for a given parton specie ($f = u, d, s, g$), the coefficient e_f is the electric charge for quarks and is equal to 1 for gluons. The Compton Form Factors now depend only on ξ and t although we have explicitly mentioned the Q^2 dependence because measurements are not performed at infinite Q^2 and QCD evolution has to be taken into account. Compton Form Factors are complex functions and their real and imaginary parts are fundamental quantities which can be measured by the experiments independently of models.

The real part is related to the integral of the GPDs through the following relation :

$$Re\mathcal{H}(\xi, t; Q^2) = \sum_f e_f^2 \int_{-1}^{1} dx H^f(x, \xi, t; Q^2) \left(\frac{1}{x + \xi} - \frac{1}{x - \xi} \right) \qquad (1.50)$$

The imaginary part is given by the residue theorem and only the contributions at the poles in $x = \xi$ and $x = -\xi$ remain :

$$Im\mathcal{H}(\xi, t; Q^2) = \sum_f e_f^2 (H(\xi, \xi, t; Q^2) + H(-\xi, \xi, t; Q^2)) \qquad (1.51)$$

This particular property gives the only way to access the GPDs at a given point in the $(x; \xi)$ plane. The Compton Form Factors will be a sort of "crossroad" for the understanding of the nucleon structure in terms of generalized parton distributions where experimental results and models will be compared.

1.3.4 Case of meson production

Similarly to Compton Form Factor one can define a Generalized Form Factor for the exclusive production of a given meson M. It is written as a function of the meson decay constant f_M, the meson distribution amplitude $\phi(z)$ and the universal GPD of a given specie H^f and different coefficients for each specie which depend on various parameters like the the electric charge of the quarks[2] or the wave function or the possibility to couple gluons. It reads [23]:

$$
\begin{aligned}
\mathcal{H}_M(\xi, t; Q^2) = \frac{4\pi\alpha_S}{9} \frac{f_M}{\sqrt{2}} \int_0^1 dz \frac{\phi_\rho(z)}{z(1-z)} \int dx \left(\frac{1}{\xi - x + i\xi} - \frac{1}{\xi - x - i\xi} \right) \\
\cdot \left(c_u^M H^u(x, \xi, t) + c_d^M H^d(x, \xi, t) + c_s^M H^s(x, \xi, t) + c_g^M H^g(x, \xi, t) \right)
\end{aligned} \quad (1.52)
$$

Considering different vector mesons allow to separate the quark flavors and gluons contributions. For example, for the ρ, ω and ϕ mesons, the Generalized form factors will be sensitive to:

$$
\begin{aligned}
H_\rho &= \frac{1}{\sqrt{2}} \left(\frac{2}{3} H^u + \frac{1}{3} H^d + \frac{3}{8} H^g \right) & (1.53) \\
H_\omega &= \frac{1}{\sqrt{2}} \left(\frac{2}{3} H^u - \frac{1}{3} H^d + \frac{1}{8} H^g \right) & (1.54) \\
H_\phi &= -\frac{1}{3} H^s - \frac{1}{8} H^g & (1.55)
\end{aligned}
$$

The measurement of the Compton and Generalized Form Factors is one of the main goals of the future COMPASS experimental program.

---

[2]it is not squared since there is only 1 electromagnetic vertex in this case

Chapter 2

The HAPPEX Experiment

One of the results of the EMC experiment was to show that there was a sizable contribution of strange quarks to the nucleon spin. It was then proposed by various groups at MAMI, MIT-Bates and JLab to determine the contribution of strangeness to the elastic form factors of the nucleon and hence to see if strangeness contributes also to the electric charge and magnetic moment. At Jefferson Lab, the HAPPEX experiment was approved in 1994 and started in 1998. Three data taking periods were conducted, first data were taken at Q^2=0.48 $(\text{GeV}/c)^2$ in 1999 where a large signal could be expected in view of the existing models. Then with the progress made in the systematic errors reduction data was taken at Q^2=0.10 $(\text{GeV}/c)^2$ for Hydrogen and Helium targets allowing for a separation of the electric and magnetic contributions.

In this chapter, we will first present the measurement of the weak form factors and how they allow to access the strange form factors. Then, we will present the experimental setup used by the HAPPEX experiment and present the results obtained. The last section of this chapter is dedicated to the description of the Compton polarimeter which was built by our group for the purpose of monitoring the electron beam polarization in the Hall A of Jefferson Lab.

2.1   Measurement of strange form factors

2.1.1   Weak form factors

In the introduction we have presented the measurement of nucleon form factors using the electromagnetic interaction. We now consider the elastic scattering of an electron off a proton to proceed also through the exchange of a Z^0 as shown in the right graph of figure 2.1.

At the electron vertex, the neutral weak current can be written:

$$\langle e'(k', s')| \, j_W^\mu \, |e(k, s)\rangle = \bar{u}(k', s')\gamma^\mu(g_V^e - g_A^e\gamma_5)u(k, s) \qquad (2.1)$$

The interaction of the neutral weak current with the proton is described in term of form factors similarly to the electromagnetic interaction. Due to the structure of the
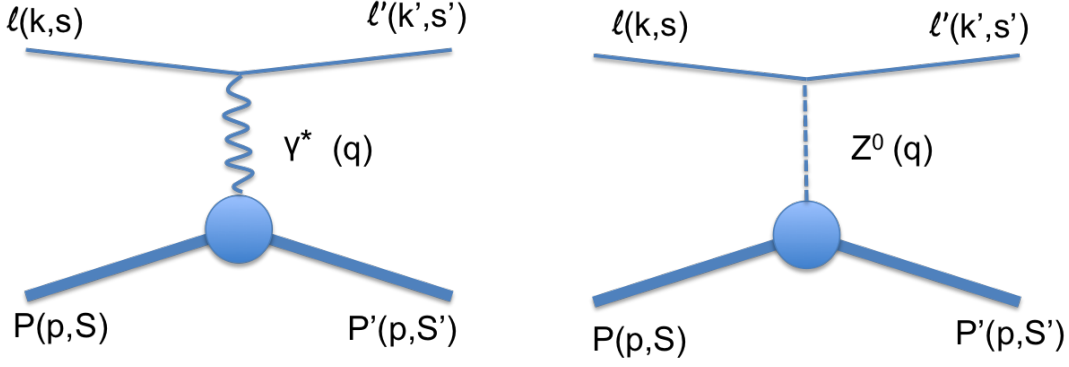
Figure 2.1: Graphs contributing to elastic scattering: electromagnetic interaction (left) and weak interaction (right)

	Q	g_V	g_A
e	-1	$-1 + 4\sin^2\theta_W$	+1
u, c, t	$\frac{2}{3}$	$1 - \frac{8}{3}\sin^2\theta_W$	-1
d, s, b	$-\frac{1}{3}$	$-1 + \frac{4}{3}\sin^2\theta_W$	+1

Table 2.1: Electromagnetic and weak vector and axial charges for electron and quarks

weak interaction, the current is written:

$$\langle P'(p',s')|\, J_W^\mu\, |P(p,s)\rangle =$$
$$\bar{u}(p',s')\left[\gamma^\mu F_1^{(Z,p)}(Q^2) + i\frac{\sigma^{\mu\nu}q_\nu}{2M}F_2^{(Z,p)}(Q^2) + \gamma^\mu\gamma_5 G_A^e(Q^2) + \frac{q^\mu\gamma^5}{M}G_P(Q^2)\right]u(p,s)\ (2.2)$$

where F_1 and F_2 are analogous to the Dirac and Pauli form factors and G_A and G_P are the axial vector and pseudo-scalar form factors of the nucleons.

2.1.2   Extraction of strange form factors

The form factors can be decomposed on "quark flavors" form factors $G_{E,M}^f$ which quantify the contribution of each flavor to the nucleon form factors. Going back to the electromagnetic interaction we can derive the following relations:

$$G_{E,M}^{\gamma,p} = \frac{2}{3}G_{E,M}^{u(p)}(Q^2) - \frac{1}{3}G_{E,M}^{d(p)}(Q^2) - \frac{1}{3}G_{E,M}^{s(p)}(Q^2) \tag{2.3}$$

$$G_{E,M}^{\gamma,n} = \frac{2}{3}G_{E,M}^{u(n)}(Q^2) - \frac{1}{3}G_{E,M}^{d(n)}(Q^2) - \frac{1}{3}G_{E,M}^{s(n)}(Q^2) \tag{2.4}$$

where the coefficients are the electric charges and only light flavors have been taken into account. The number of flavor form factors is further reduced to 6 by applying the isospin symmetry:

$$G_{E,M}^{u(p)} = G_{E,M}^{u(p)} \equiv G_{E,M}^u \tag{2.5}$$

$$G_{E,M}^{d(p)} = G_{E,M}^{u(n)} \equiv G_{E,M}^d \qquad (2.6)$$

$$G_{E,M}^{s(p)} = G_{E,M}^{s(n)} \equiv G_{E,M}^s \qquad (2.7)$$

And then the electromagnetic form factors are rewritten:

$$G_{E,M}^{\gamma,p}(Q^2) = \frac{2}{3}G_{E,M}^u(Q^2) - \frac{1}{3}G_{E,M}^d(Q^2) - \frac{1}{3}G_{E,M}^s(Q^2) \qquad (2.8)$$

$$G_{E,M}^{\gamma,n}(Q^2) = \frac{2}{3}G_{E,M}^d(Q^2) - \frac{1}{3}G_{E,M}^u(Q^2) - \frac{1}{3}G_{E,M}^s(Q^2) \qquad (2.9)$$

which provide four measurements for six unknown quantities. The weak interaction is used to provide an additional constrain. The electroweak unification guarantees that the flavor form factors are universal and do not depend on whether the probe is a photon or a Z^0. Then, for the weak interaction the coupling to a given flavor is given by the weak vector charge leading to:

$$G_{E,M}^{(Z,p)} = (1 - \frac{8}{3}\sin^2\theta_W)G_{E,M}^u + (-1 + \frac{4}{3}\sin^2\theta_W)(G_{E,M}^d + G_{E,M}^s) \qquad (2.10)$$

Using this additional measurement, the strange contribution to the form factors are extracted as:

$$G_{E,M}^s = (1 - 4\sin^2\theta_W)G_{E,M}^{(\gamma,p)} - G_{E,M}^{(\gamma,n)} - G_{E,M}^{(Z,p)} \qquad (2.11)$$

This demonstrates the interest in the measurement of the weak form factors. In the next section, we show how they can be determined from the parity violation asymmetry in elastic scattering.

2.1.3 Parity violating asymmetry

The weak interaction does not conserve parity meaning that the amplitude, $\mathcal{M}_Z$, for the exchange of the Z^0 depends on the helicity (right or left) of the incoming electron, contrary to the amplitude, $\mathcal{M}_\gamma$, for the exchange of a photon. The cross section dependent helicity is written:

$$\sigma_R \propto |\mathcal{M}_\gamma + \mathcal{M}_Z^R|^2 = |\mathcal{M}_\gamma|^2 + 2\Re\left(\mathcal{M}_\gamma \cdot \mathcal{M}_Z^R\right) + |\mathcal{M}_Z^R|^2 \qquad (2.12)$$

$$\sigma_L \propto |\mathcal{M}_\gamma + \mathcal{M}_Z^L|^2 = |\mathcal{M}_\gamma|^2 + 2\Re\left(\mathcal{M}_\gamma \cdot \mathcal{M}_Z^L\right) + |\mathcal{M}_Z^L|^2 \qquad (2.13)$$

It shows that the weak amplitude appears in the interference and in the pure weak terms. The magnitude of each term is given by:

$$|M_\gamma|^2 \propto \left(\frac{\alpha}{Q^2}\right)^2 \qquad (1)$$

$$2\Re(M_\gamma \cdot M_{Z^0}) \propto \frac{\alpha}{Q^2}G_F \qquad (3\,10^{-5})$$

$$|M_{Z^0}|^2 \propto G_F^2 \qquad (10^{-9})$$

where $\alpha \simeq 1/137$ is the fine structure constant and $G_F = 1.17 \cdot 10^{-5}\,\text{GeV}^{-2}$ is the Fermi constant. The relative size of each term is written in brackets for $Q^2 = 0.48\,(\text{GeV}/c)^2$. The pure weak term is out of reach but it appears in the interference which acts as an "amplifier" and can be accessed through asymmetry measurements at high quality polarized electron accelerators. From the cross section for right- and left-handed electrons off an unpolarized target the parity violating cross section asymmetry, A_{PV}, reads:

$$A_{PV} = \frac{\sigma_R - \sigma_L}{\sigma_R + \sigma_L} = \frac{\left|\mathcal{M}_\gamma + \mathcal{M}_Z^R\right|^2 - (\mathcal{M}_\gamma + \mathcal{M}_Z^L)^2}{(\mathcal{M}_\gamma + \mathcal{M}_Z^R)^2 + (\mathcal{M}_\gamma + \mathcal{M}_Z^L)^2} \tag{2.14}$$

$$\simeq \frac{\mathcal{M}_\gamma \left(\mathcal{M}_Z^R - \mathcal{M}_Z^L\right)}{\mathcal{M}_\gamma^2} \tag{2.15}$$

where sub-leading terms have been dropped out. With the exact amplitudes depending on the proton's electric and magnetic form factors the tree-level parity-violating asymmetry is calculated to be [26]:

$$A_{PV} = -\frac{G_F Q^2}{4\pi\alpha\sqrt{2}}\, \frac{\varepsilon G_E^{(\gamma,p)} G_E^{(Z,p)} + \tau G_M^{(\gamma,p)} G_M^{(Z,p)} - (1 - 4\sin^2\theta_W \epsilon' G_M^{(\gamma,p)} G_A^{(Z,p)})}{\varepsilon \left(G_{E,M}^{(\gamma,p)}\right)^2 + \tau \left(G_{E,M}^{(\gamma,p)}\right)^2} \tag{2.16}$$

where $\tau = Q^2/4M_P^2$, $\epsilon = [1 + 2(1+\tau)\tan^2\theta/2]^{-1}$, $\epsilon' = \sqrt{\tau(1+\tau)(1-\epsilon^2)}$ are kinematical factors. The measurement of the parity violating asymmetry provides a measurement of the weak form factors of the nucleon and hence of the strange form factors which appear as a linear combination of the electric and magnetic terms:

$$A_{PV} \to G_E^s + \eta G_M^s \tag{2.17}$$

At backward scattering angles the electric term is kinematically suppressed and the experiments are sensitive to G_M^s and G_A^Z. For a spinless isoscalar target such as Helium, the magnetic term drops and the parity violating asymmetry is only sensitive to the electric term, G_E^s:

$$A_{PV}^{He} = -\frac{G_F Q^2}{4\pi\alpha\sqrt{2}}\left[4\sin^2\theta_W + \frac{2G_E^s)}{G_E^{(\gamma,p)} + G_E^{(\gamma,n)}}\right] \tag{2.18}$$

An extensive parity-violation program was undertaken to measure the strange quark vector form factors and will be commented in the results section of this chapter.

2.2 The HAPPEX experiment

In this section we describe the HAPPEX experiment performed in the Hall A at Jefferson Lab in which our group has been involved. We give a brief description of the experimental setup and present the results obtained. The last section is dedicated to the Compton polarimeter.

2.2.1 Polarized electron source

We have used an optically pumped a GaAs crystal as a polarized electron source. In this device, a 780 nm Laser is used to shine circularly polarized light onto the crystal. The laser is pulsed to the accelerator frequency (500 MHz) and the bunch-length is 50 ps. Left and right circular polarization of the light are obtained with a Pockels Cell by applying the voltage corresponding to the quarter wave retardation. Electrons are extracted using an electric field and then injected in the accelerator. In the first campaign of HAPPEX measurements, a bulk GaAs crystal was used and polarization of the order of 40 % were obtained. In the second campaign, the use of "strained crystals" for which the band structure is modified allowed to reach more than 80 % polarization

The helicity is flipped at a 30 Hz frequency and is phase locked to the 60 Hz AC cycle. Helicity pulses are associated in pairs of which the second pulse has an helicity opposite to the first one. The helicity of the first one is chosen by a 24-bit pseudo-random number generator. The helicity signal is transferred delayed by 8 pairs and true helicity is determined afterwards in software. Asymmetries and differences are then calculated for pairs.

A half-wave plate can be inserted in the laser beam line. As it swaps left and right helicities it reverses the sign of the experimental asymmetry and provides a useful systematic check. The half wave plate was put in or taken out after every 24 hours of full data taking.

2.2.2 Detection of the elastically scattered electrons

After being accelerated to 3.355 GeV, the polarized electrons are extracted and deflected to the proton target. The target is a 15 cm long cell of liquid hydrogen cooled at 19 K. The cryogenic installation is able to evacuate the 500 Watts deposited in the target by a 100 μA electron beam. Tests performed prior to the experiment have shown that no significant boiling was induced in the target by the beam.

The two identical High Resolution Spectrometers (HRS) in Jefferson Lab's Hall A [28] are used to detect the elastically scattered electrons. The spectrometers (see figure 2.2 (top)) were placed at the most forward scattering angle ($\theta = 12.5°$) and the field in the magnets (the configuration is QQDQ) was set to detect electrons at a quadri-momentum transfer $Q^2 = 0.48\,(\text{GeV}/c)^2$. These settings were chosen to maximize the figure of merit ($A\,(d\sigma)^{\frac{1}{2}}$) in a kinematical region where some models on strangeness predicted a sizable effect. In the running period at $Q^2 = 0.10\,(\text{GeV}/c)^2$, a septum magnet was installed and the target was moved upstream in order to access scattering angles of 6° (figure 2.2 (bottom)).

One property of the HRS is to spatially separate elastic from inelastic scattering. Thus, elastic scattering can be identified without reconstruction of the trajectories (figure 2.3). To detect the scattered electrons total absorption electron calorimeters were placed in the focal plane of both spectrometers. These detectors are made of 5 layers of lead and Lucite interleaved. The Cerenkov light produced by the electron
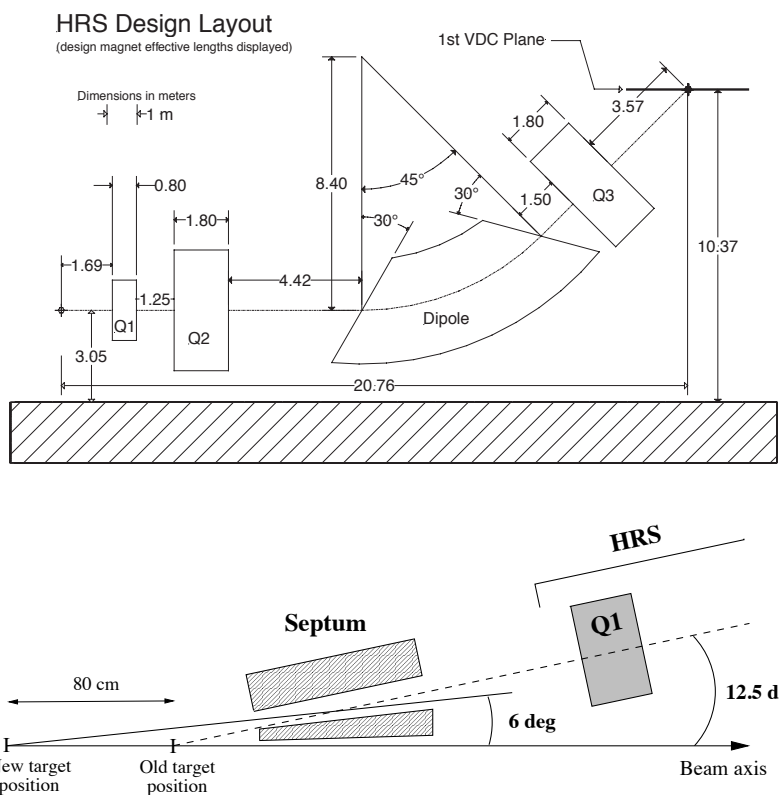
Figure 2.2: Top: side view of one of the Hall A High resolution spectrometers. Bottom: top view of the target region describing the use of a septum magnet in order to access scattering angles down to 6 degrees.
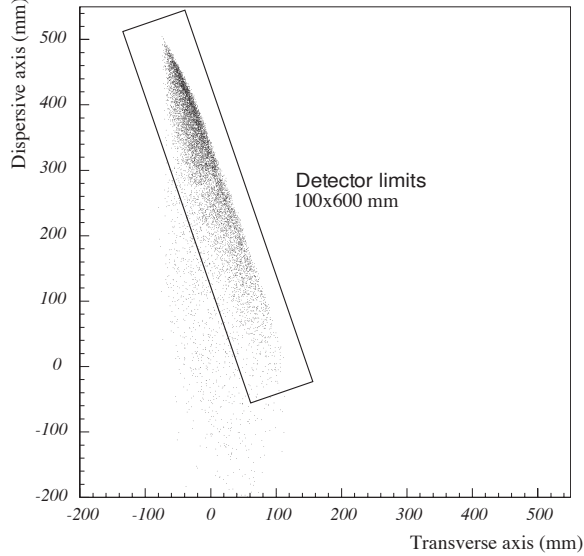
Figure 2.3: Impact point of the elastically scattered electron in the focal plane of the spectrometer. The rectangular area shows the surface of the electron detector.

shower is detected by a 5 inch photomultiplier tube. The resolution of such a device is 14 % at the energy of the scattered electrons. Rates of 2 MHz were obtained and since the output current of the PMTs is integrated over the helicity pulse, the effect of the resolution is only to increase the time needed to achieve a given accuracy by less than a percent.

Data was also taken using the standard detector package of the HRSs and DAQ system in order to determine the averaged Q^2 of each experiment. Even if the spectrometers have a 10^{-4} momentum resolution, for the purpose of our experiment we only need precision of the order of a percent. An eventual contamination of background was also studied by detuning the magnets.

2.2.3 Control of beam parameters

The control of the beam parameters is a key point of the parity violation experiments. For example, a helicity correlated difference in beam position is transformed into a difference in counting rates in the spectrometer as a consequence of accepted solid angle variations. To correct for these effects, one need to know the value of the helicity correlated differences and to know the sensitivity of the counting rates with respect to these variations [27]. This is done by steering the beam using small magnetic coils and monitoring the effect in the Beam Position Monitors for spatial coordinates and for energy since one of the monitor is located at the highest dispersion point in the magnetic arc (see figure 2.4).

The experimental asymmetry, A_{exp}, is calculated from the integrated signal $S_{+/-}$ and the normalized to the beam current $c_{+/-}$ and is related to the physics asymmetry,
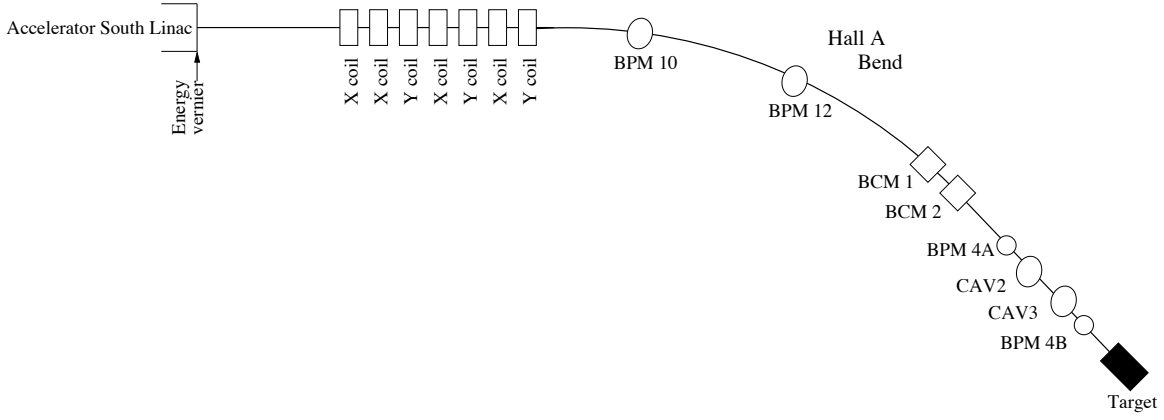
Figure 2.4: Schematic view of the Hall A beam-line. 7 coils are used to modulate the beam position. Beam position monitors (BPM) and Beam current monitors (CAV) are used to control the induced beam parameter modifications.

A_{PV}, through:

$$A_{exp} = \frac{S_+/c_+ - S_-/c_-}{S_+/c_+ + S_-/c_-} = P_e A_{PV} \tag{2.19}$$

The beam current is determined using cavity monitors and the beam polarization, P_e, was measured using Compton and Moller polarimeters. The Compton polarimeter gave the best precision of the two devices and allowed for a continuous monitoring of the beam polarization.

2.2.4   Results

The first measurement of the HAPPEX experiment was at $Q^2 = 0.48\,(\text{GeV}/c)^2$. The result obtained is [29]:

$$G_E^s + 0.39 G_M^s = 0.025 \pm 0.020_{exp} \pm 0.014_{ff} \tag{2.20}$$

where the first systematic errors arises from experimental aspects (statistics and systematics) and the second term originates from the knowledge of the form factors and could be improved in the future. The result is compatible with zero and ruled out models predicting large strange contribution to the nucleon form factor. The first experiment also served as a benchmark for future measurements.

In view of a possible cancellation between the magnetic and electric contribution at high Q^2 it was decided that the second HAPPEX measurement campaign would be performed at $Q^2 \simeq 0.10\,(\text{GeV}/c)^2$. Data was taken on both Hydrogen and Helium targets to separate the electric and magnetic term [30]. It is worth noting that the measured asymmetries and precision achieved are very small ($1\,\text{ppm} = 10^{-6}$):

$$A_{phys}^{He} = +6.40 \pm 0.23(\text{stat}) \pm 0.12(\text{syst})\,\text{ppm} \tag{2.21}$$
$$A_{phys}^{H} = -1.58 \pm 0.12(\text{stat}) \pm 0.04(\text{syst})\,\text{ppm} \tag{2.22}$$
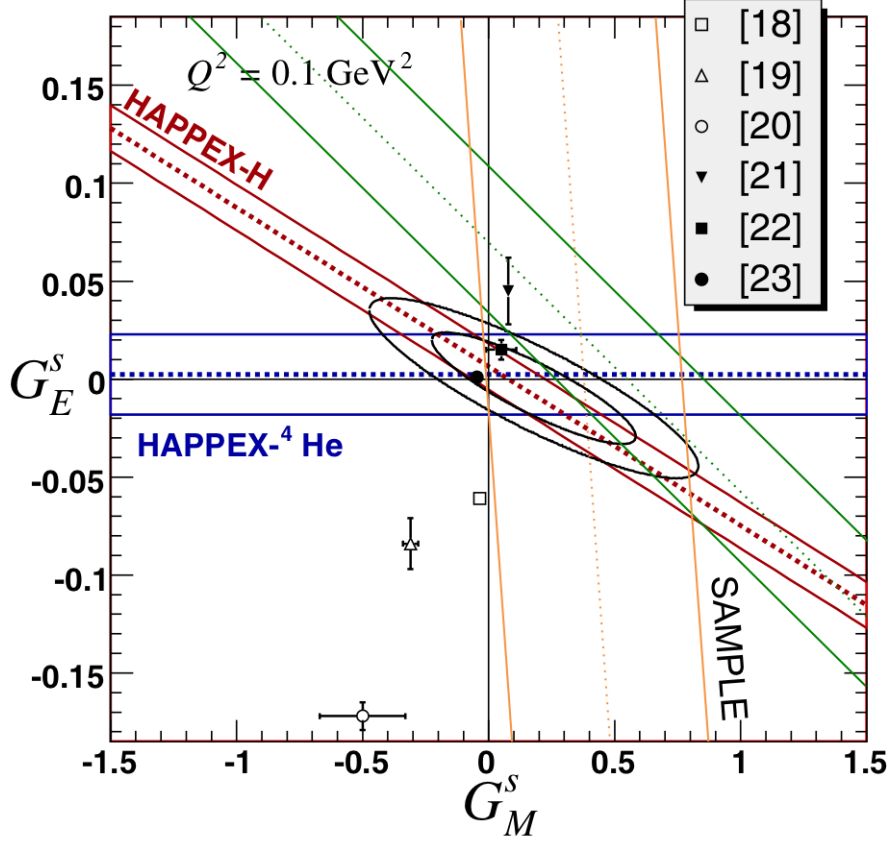
Figure 2.5: Results of HAPPEX at $Q^2 = 0.1 GeV^2$. Also represented are the results of SAMPLE (orange band) and PVA4 (green band) at the same Q^2.

which have to be compared to the prediction in the absence of strange quarks contributions:

$$A_{phys}^{He} = +6.37 \pm 0.12 (syst) \, ppm \qquad (2.23)$$
$$A_{phys}^{H} = -1.66 \pm 0.05 \, ppm \qquad (2.24)$$

Using expressions 2.16 and 2.18 one can extract the strange form factor information:

$$G_E^s + 0.09 G_M^s = 0.007 \pm 0.011 \pm 0.006 \qquad (2.25)$$
$$G_E^s = 0.002 \pm 0.014 \pm 0.007 \qquad (2.26)$$

These two results are represented in figure 2.5 in the (G_M^s, G_E^s) plane showing their complementarity to separate electric and magnetic contributions along with predictions for which the references are found in Appendix 2. The electric and magnetic strange contributions to the proton are found to be very small. This implies that the strange and anti-strange spatial distribution are quasi-identical and that the contribution of strangeness to the magnetic moment of the nucleon is less than $3 \pm 4\%$ and that the
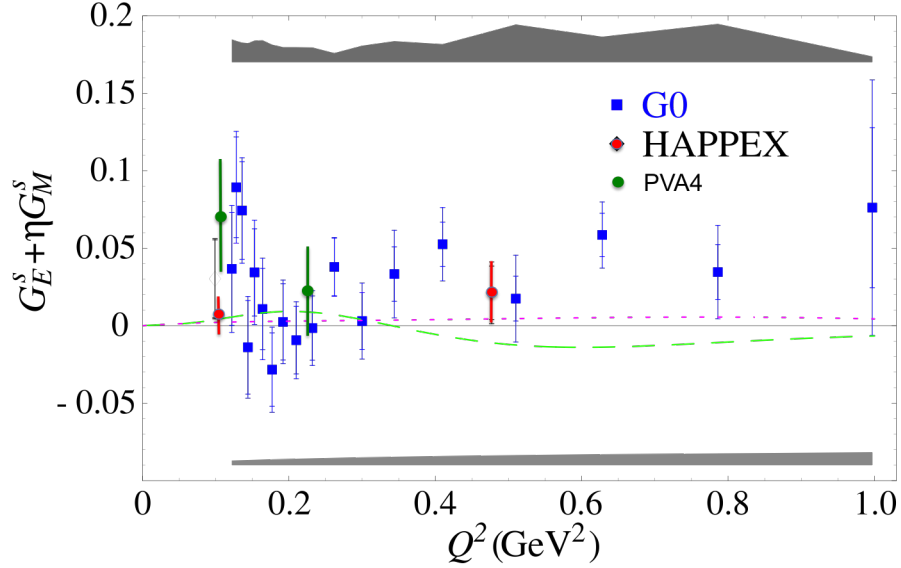
Figure 2.6: World data on $G^s_E + \eta G^s_M$.

contribution to the electric charge is $0.2 \pm 0.8\%$ [31]. At $Q^2 = 0.1 GeV^2$, there are also measurements performed by the A4 experiment [32] at the Mainz Microtron. Their actual result is $2\,\sigma$ off zero but is not in contradiction with HAPPEX results within errors. Also represented is the measurement performed by the SAMPLE experiment at MIT-Bates [33] which is mostly sensitive to G^s_M.

The HAPPEX data are compared to the results of the G0 experiment at Jefferson Lab which has measured $G^s_E + \eta G^s_M$ for Q^2 values from 0.12 to 0.8 GeV^2 [35] in figure 2.6. Also plotted is the A4 result at $Q^2 = 0.23\,\text{GeV}^2$ [34][1]. These data confirm the small contribution of strange quarks at low Q^2 and suggest that there might be a non-zero contribution at higher Q^2. To solve this issue the A4 and HAPPEX collaboration shall provide a measurement at $Q^2 = 0.6\,\text{GeV}^2$ in the near future.

In conclusion, the measurement of strange the form factors has been performed using parity violation in electron scattering. It has benefit from the advance in highly polarized electron source and extensive control of the systematic errors down to a few 10^{-8}. The results point towards small strangeness contributions to the form factors of the nucleon.

2.3   The Compton Polarimeter

The polarization of the electron beam had to be measured with an accuracy better than 2% with a strong need for a continuous monitoring of the variation of the polarization. To fulfill these goals it was proposed to build a polarimeter using the polarized Compton scattering of the electrons off a photon beam.

[1]This paper also provides a strong constrain on G^s_M
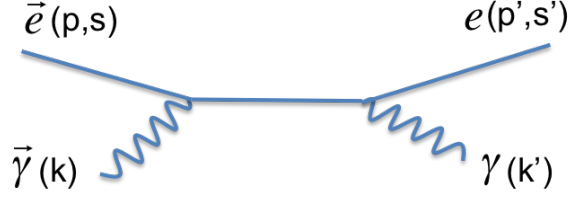
Figure 2.7: Compton scattering

2.3.1 Kinematics

The Compton process is the scattering of photons off electrons and is represented in figure 2.7. In this process the energy of the back-scattered photon k reaches a maximum depending on the beam energy, E_{beam}:

$$k_{max} = 4ak\frac{E^2}{m^2} \qquad \text{with } a = \frac{1}{1 + \frac{4kE}{m^2}} \qquad (2.27)$$

The cross section is described as a function of the variable $\rho = k/k_{max}$ by:

$$\frac{d\sigma}{d\rho} = 2\pi r_0^2 a \left(1 + \frac{\rho^2(1-a)^2}{1 - \rho(1-a)} + \left(\frac{1 - \rho(1+a)}{1 - \rho(1-a)} \right)^2 \right) \qquad (2.28)$$

where $r_0 = \alpha\hbar c/mc^2$ is the classical radius of the electron. It is shown as a function of the photon energy in figure 2.8 with the characteristic Compton edge. The asymmetry of the Compton scattering of longitudinally polarized electrons off circularly polarized photon can be determined to first order in QED and is expressed as:

$$A_{\gamma e}(\rho) = \frac{\sigma_R - \sigma_L}{\sigma_R + \sigma_L} = \frac{2\pi r_0^2 a}{d\sigma/d\rho} (1 - \rho(1+a)) \left(1 - \frac{1}{(1 - \rho(1-a))^2} \right) \qquad (2.29)$$

An JLab energies (2 to 6 GeV) asymmetries of the order of 4 to 8 % can be expected.

2.3.2 Experimental set-up

To enhance the statistics, it was decided to use a low power infrared Nd-YAG Laser (300mW) coupled with an optical cavity of high finesse ($F = 30000$) as a photon source. The cavity is located at the center of a magnetic chicane as shown in figure 2.9. The back-scattered photons are detected in a electromagnetic calorimeter made of a matrix of 5×5 blocks of $PbWO_4$ (block size is $2 \times 2\,cm^2$). This material was chosen for its small Molière radius allowing to contain the shower in the limited space available. The scattered electrons are deviated by the magnetic field of the third dipole of the chicane and are detected in 4 planes of Silicon multi-strip detectors of 48 strips each (650 μm pitch) approaching the primary beam up to 4 mm.

The optical cavity system is described in figure 2.10 and in reference [36]. It was
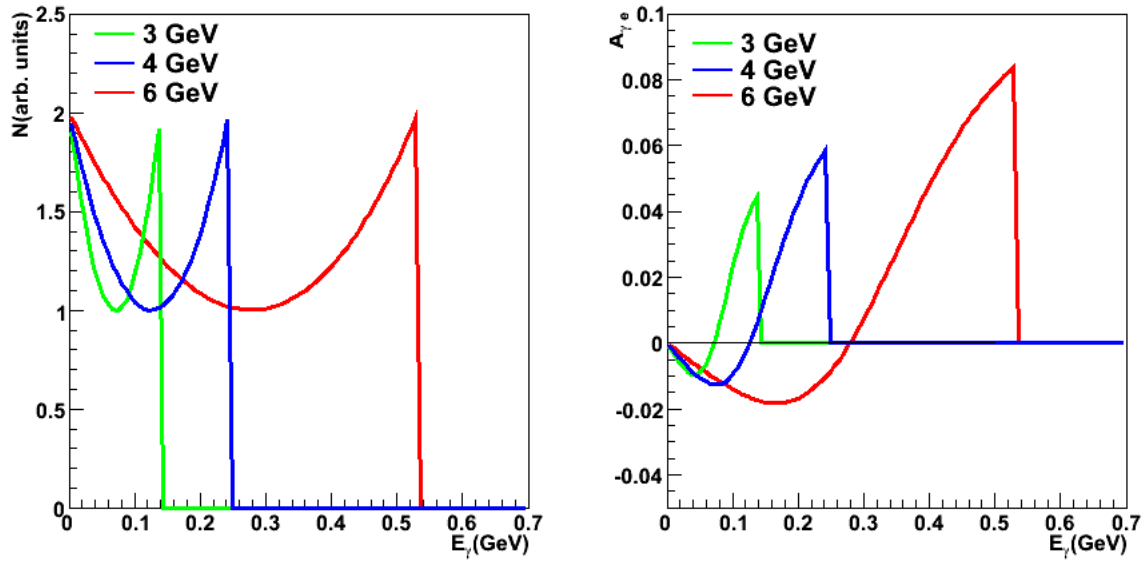
Figure 2.8: Energy spectrum of the back-scattered photon (left) and theoretical asymmetry (right) for three beam energies.
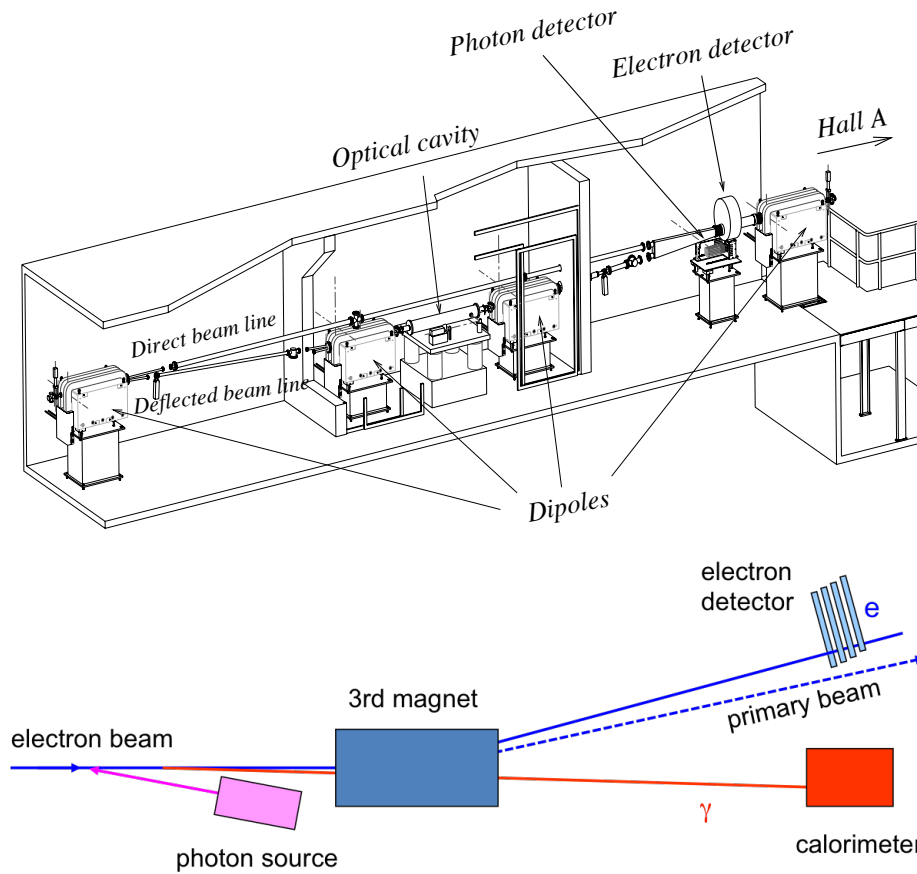

Figure 2.9: View of the Compton magnetic chicane layout (top) and principle of the detection of the scattered particles (bottom).
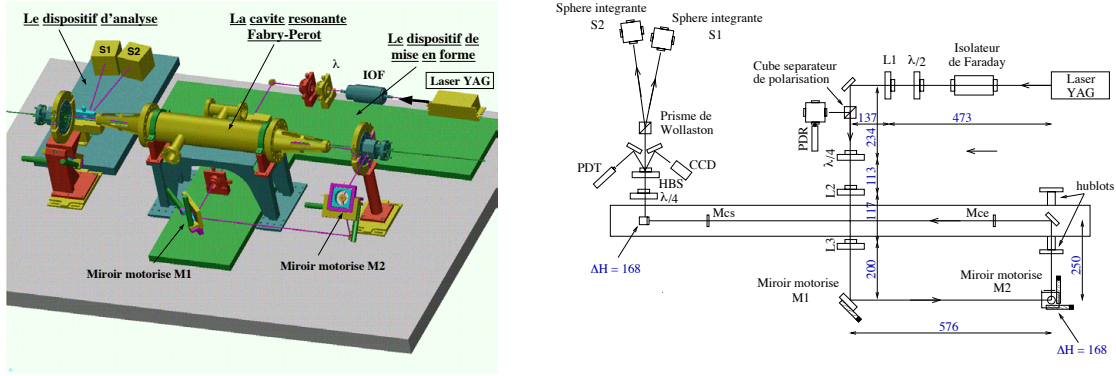
Figure 2.10: Experimental optical set-up of the monolithic cavity system.

chosen to use a "monolithic" design for the cavity. This implies that the cavity mirrors are attached to a single support frame and that the optical axis is fixed mechanically. Motorized mirrors are then used to bring the circularly polarized light along this axis. The cavity is locked by a feed-back on the laser frequency using the signal reflected by the cavity. The power in the cavity reaches 1700 W and is stable over many hours. A system of polarizers, quarter wave plates and lenses allows to provide up to 99.8% circularly polarized light at the entrance of the cavity. Another subsystem using a Wollaston prism and integrating spheres is used to measure the polarization at the exit of the cavity. Special measurement where the cavity was removed were performed in order to estimate the transfer function of the exit line and allowed to reach 0.36% precision on the polarization in the cavity.

2.3.3 Analysis of the data

2.3.3.1 The «electron» method

The electron detector data was used to determine the beam polarization without the use of the photon detector. It was also used to determine the calibration and the response function of the photon detector. The counting rates viewed by the strips of the electron detector are represented in figure 2.11(left) when the cavity is ON (blue points) and OFF (red points). It follows the distribution shown in figure 2.8 and the Compton edge is clearly seen. Knowing the field integral in the dipole magnet allows to determine the momentum calibration of each detector strip. Then, the asymmetry when the beam polarization is reversed can be measured for each strip of the electron detector is shown in figure 2.11(right). It is fitted with the relation:

$$A_{exp} = P_e P_\gamma A_{\gamma e} \tag{2.30}$$

where P_e and P_γ are the electron and photon polarization and $A_{\gamma e}$ is the Compton process asymmetry given in equation 2.29. This provides the polarization measurement as well as redundancy in the calibration.
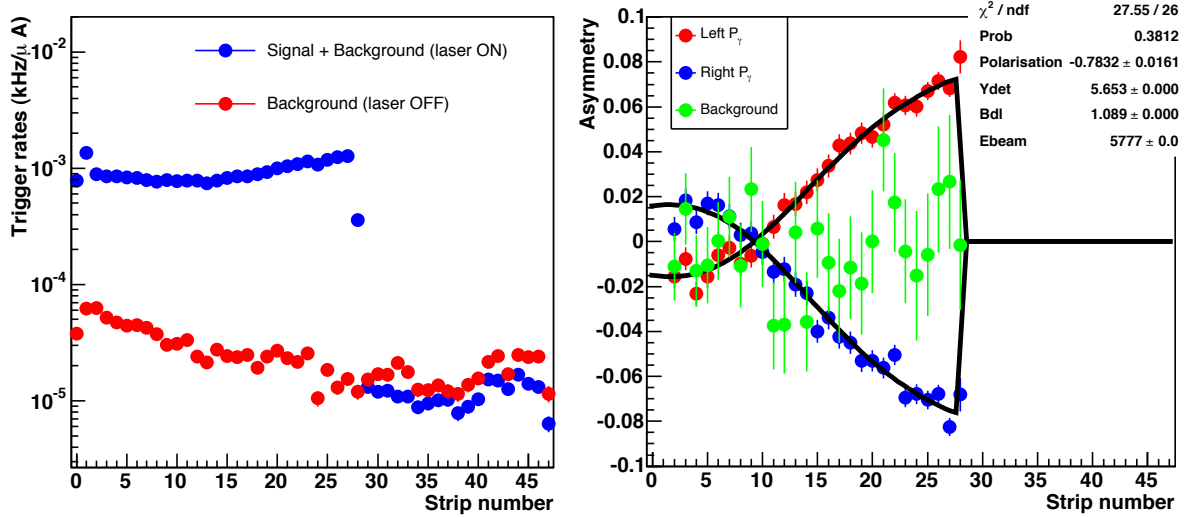
Figure 2.11: Counting rates in the strips of the electron detector (E=5.777 GeV)

2.3.3.2   The «photon» method

In the calorimeter, a photon with incident energy k produces a shower which is converted to an ADC value at the end of the detection chain. Due to the high counting rate it was decided to store the energy information in a 20-bin array and to transfer this array at the end of each beam polarization orientation window. In principle one could estimate the asymmetry and analyzing power for each bin but this "differential" method suffers large systematic errors. It was preferred to use an "integrated" method [37] for which the counting rates above a given threshold are integrated. The analyzing power is then expressed as:

$$\mathcal{A}(\mathrm{ADC_t}) = \frac{\int_0^{k_{max}} p(k, \mathrm{ADC_t})\frac{d\sigma}{dk}A_{\gamma e}(k)dk}{\int_0^{k_{max}} p(k, \mathrm{ADC_t})\frac{d\sigma}{dk}dk} \tag{2.31}$$

where we have introduced the function $p(k, \mathrm{ADC}_t)$ which is the probability to detect a photon with incident energy and to register it at an ADC value greater than ADC_t. This function can be estimated using specific data where the scattered electron and photon of the Compton process are detected in coincidence. It depends on the response function of the calorimeter, $\mathcal{R}(\mathrm{ADC}, k)$, *i.e.* the distribution of ADC values for a given incident energy, and has the following expression :

$$p(k, \mathrm{ADC_t}) = \frac{\int_{ADC_t}^{\infty} \mathcal{R}(\mathrm{ADC}, k)d\mathrm{ADC}}{\int_0^{\infty} \mathcal{R}(\mathrm{ADC}, k)d\mathrm{ADC}} \tag{2.32}$$

The response of the calorimeter when a given strip of the electron detector was hit is shown in figure 2.12 and relies on the calibration of the electron detector. It shows an asymmetric tail extending to lower ADC values corresponding to shower leakage. The response function is parametrized using an ad-hoc function and allows to well reproduce the unintegrated ADC spectrum (right panel). The analyzing power is then calculated
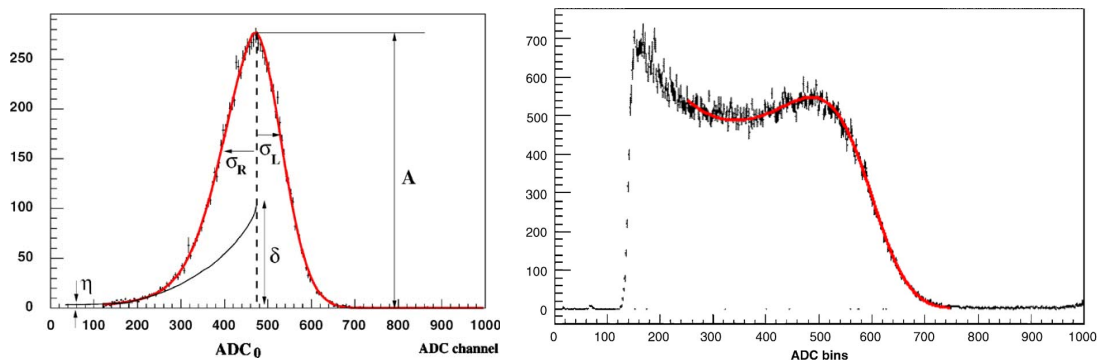
Figure 2.12: Response function of the calorimeter when the strip number 14 of the electron detector was hit.

and the polarization is given by:

$$A_{exp} = P_e P_\gamma \mathcal{A}(\mathrm{ADC_t})$$

2.3.4 Results

The systematic errors entering the beam polarization measurement for the "photon" and "electron" methods are presented in table 2.2. For the "photon" method the main error comes from the modeling of the response function and the effect of pile-up in the photon detector. For the "electron" method the main source of error arises from the calibration. The error on the photon polarization is not a limiting factor thanks to the effort put in this direction. We have achieved a total precision using the electron method of 1% and the systematic error in the parity violation asymmetry measurements is kept well below the statistical error.

The Compton polarimeter has also monitored continuously the electron beam used by Jefferson Lab Hal A experiments. The graph in figure 2.13 shows the variation of the beam polarization during a two-month period. It shows that substantial polarization variation are observed and are correlated in time with intervention at the polarized electron source. Between these interventions the polarization is stable to better than 1% and is a confirmation that the polarimeter systematic errors are under control.

”photon method”	Error
response function	1.25
pile-up	1.00
dead-time	0.50
photon polarization	0.36
radiative corrections	0.25
Total	**1.73**

”electron method”	Error
calibration	0.79
data quality checks	0.50
photon polarization	0.36
radiative corrections	0.25
beam energy	0.10
efficiency	0.10
background	0.04
Total	**1.04**

Table 2.2: Systematic errors entering the beam polarization measurement for the photon and electron analysis methods.
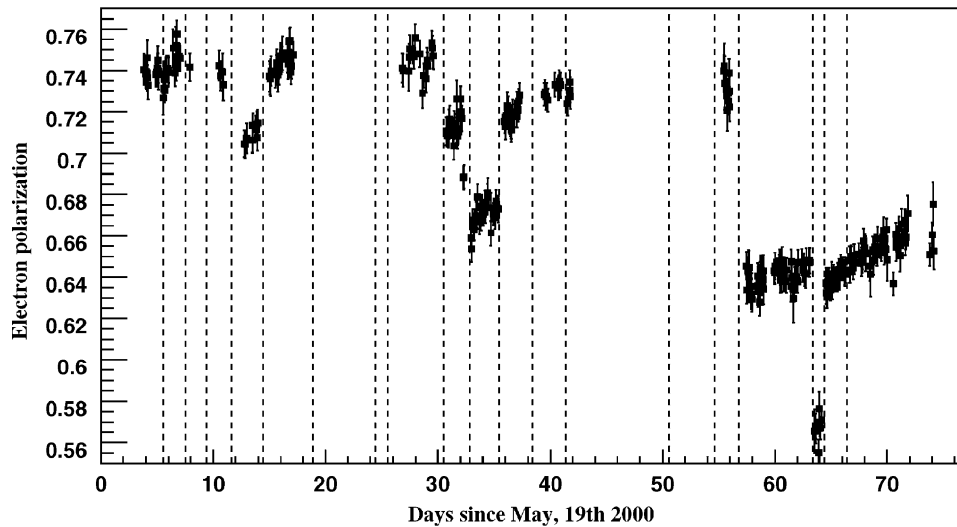

Figure 2.13: Monitoring of the electron beam polarization over a 80-day period. Vertical dashed lines corresponds to intervention at the polarized electron source.

Chapter 3

The COMPASS Experiment

The COMPASS experiment is located in the north area of the CERN complex at the end of the M2 muon beam line. The experimental set-up (see figure 3.1) is composed of a two stage spectrometer placed after a 1.2 m long polarized target. In can be decomposed in a beam telescope, a large angle spectrometer around the first dipole magnet (SM1) and a short angle spectrometer around the second dipole magnet (SM2). The apparatus was extensively described in reference [38] which we only summarize here.

3.1 The M2 muon beam line

The beam available at the COMPASS experimental hall is originating from the CERN Super Proton Synchrotron. It accelerates protons up to 400 GeV/c in a 2 km diameter circular accelerator. The protons are extracted from the SPS and are sent to a 500 mm Beryllium target. Following the interaction, secondary particles (mainly pions and kaons) are produced and are selected according to their momenta (172 GeV/c). The pions enter a section of 600 m where they can decay into muons through the weak interaction : $\pi \to \mu\nu$. Due to the parity violation of the weak interaction there is a strong correlation between the momentum and the polarization of the muons. Therefore, selecting a band in momentum results in a natural polarization of the beam as shown in the left panel of figure 3.2. The COMPASS muon beam energy is 160 GeV with a dispersion of 5 GeV. The resulting average polarization of the beam is around $P_\mu = 80\%$. The muon beam intensity, I_μ, also depends on the energy of the muons and is represented in the right panel of figure 3.2. It shows that the experiment does not run at the maximal available intensity which is due to the fact that the figure of merit for asymmetry measurements is proportional to $P_\mu^2 I_\mu$ (for a fixed parent pion energy). The beam is focused at the location of the target and has a size of $0.8 \times 0.8 \, \mathrm{cm}^2$.

3.2 The polarized target

The polarized target is made of cylindrical cells along the beam line filled with a solid state material. The choice of material done by maximizing statistical figure of merit,
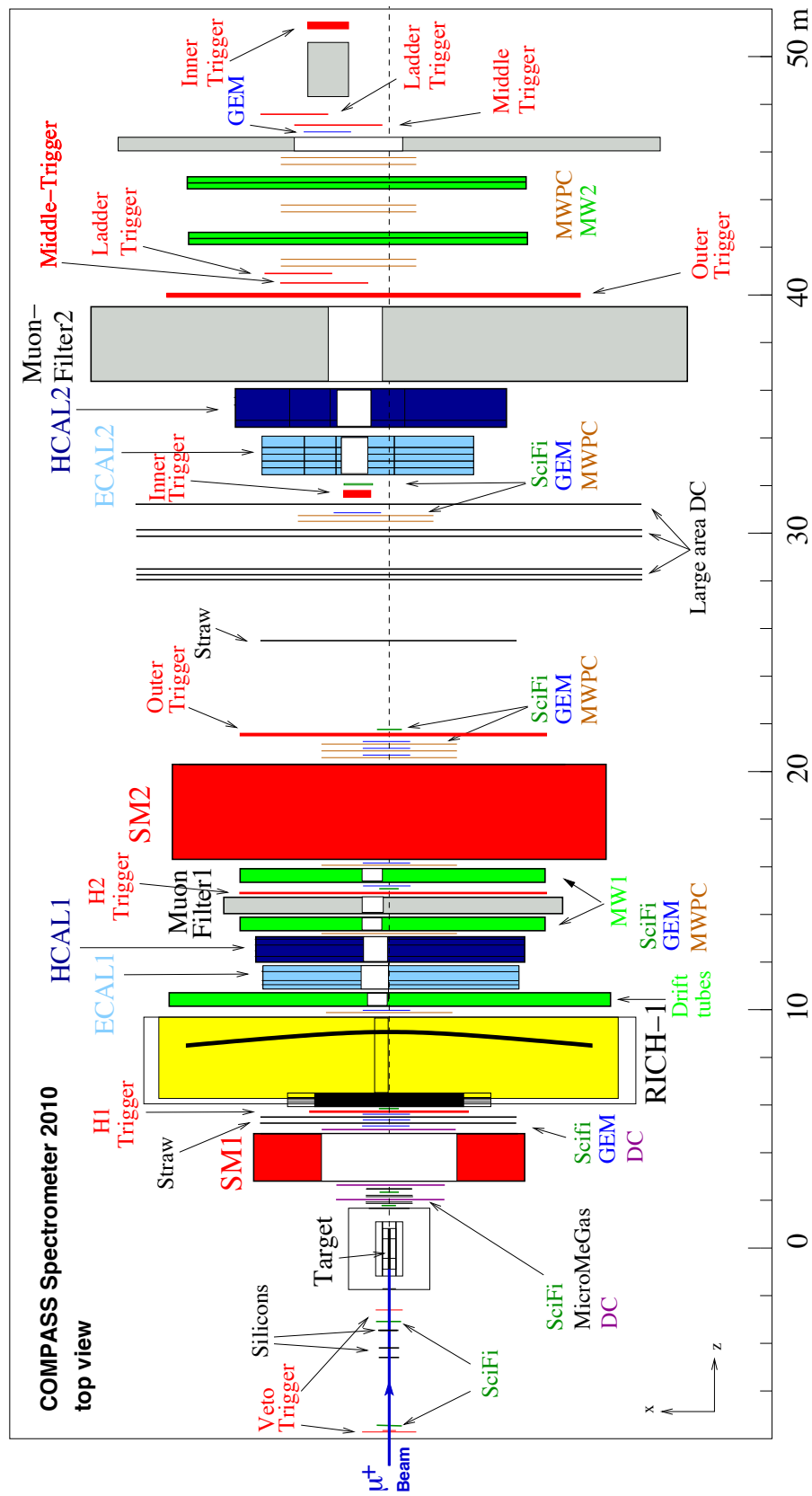
Figure 3.1: The COMPASS experimental setup as used in 2010.
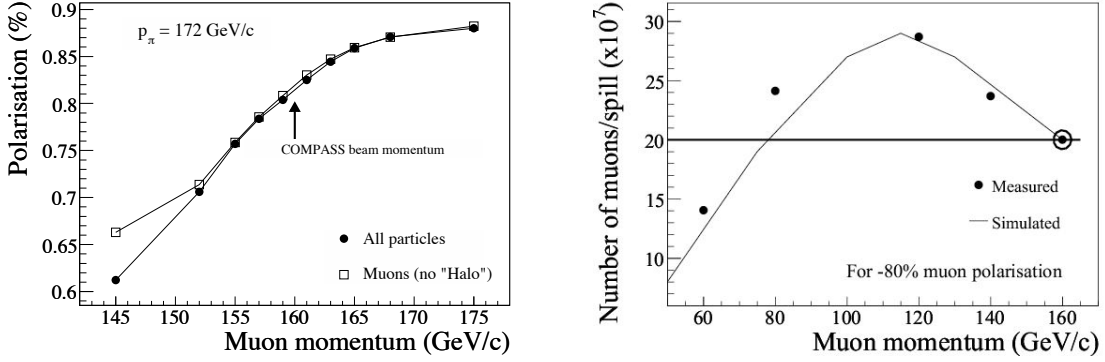
Figure 3.2: Muon beam polarization and intensity as a function of the muon momentum (the parent pion has 172GeV/c).

fP_t^2, where f is the dilution factor (i.e. the fraction of polarizable nucleons) and P_t is the achievable target polarization. The deuterated Lithium, ^{6}LiD, has been chosen as target material from 2002 to 2006. In this molecule, the^{6}Li nucleus can be considered as spin 0 ^{4}He nucleus plus a deuteron. With the additional D in ^{6}LiD it leads to a theoretical dilution factor of 0.5 but the material has a bead structure and the spaces are filled by the liquid helium of the cooling system leading to a realistic dilution factor of 0.36. Typical polarizations up to 50% are obtained. With rising interest for measurements of the transversity distribution function on the proton, it was chosen in 2007 to use ammonia, NH_3. For this material, the dilution factor is quite lower ($f = 0.15$) but it is compensated by higher polarizations of the order of 80%.

The polarization process arises from the Dynamic Nuclear Polarization. In this technique, the material has first to be irradiated in order to create paramagnetic centers (electrons). Then, under the presence of a magnetic field and at low temperature (50mK), there is a splitting between the levels of the electron-nucleon system which can be exploited. Indeed, by applying an adequate microwave frequency the system can be brought to a state where both the electron and the nucleon are polarized. Then the electron polarization is relaxed in milliseconds and the electron is again available for polarizing another nucleon which relaxation time is of the order of 1000 hours. The nucleon exchanges its spin by interacting with its neighbors and the polarization spreads over the volume of the material. This technique allows for a buildup of the polarization which takes a few days.

The field is provided by a super-conducting magnet. Up to 2004, the magnet used was the one build for the SMC experiment but resulted in a reduced acceptance. A new magnet originally planed for the beginning of COMPASS has been available since 2006 and matches the 180 mrad polar angle of the acceptance of the spectrometer. These two magnets have a solenoid and a dipole field. The solenoid field is 2.5 T along the beam axis. The dipole field is 0.8 T and is transverse to the beam. It allows to hold the polarization during the rotation and also to hold a polarization transverse to the beam.
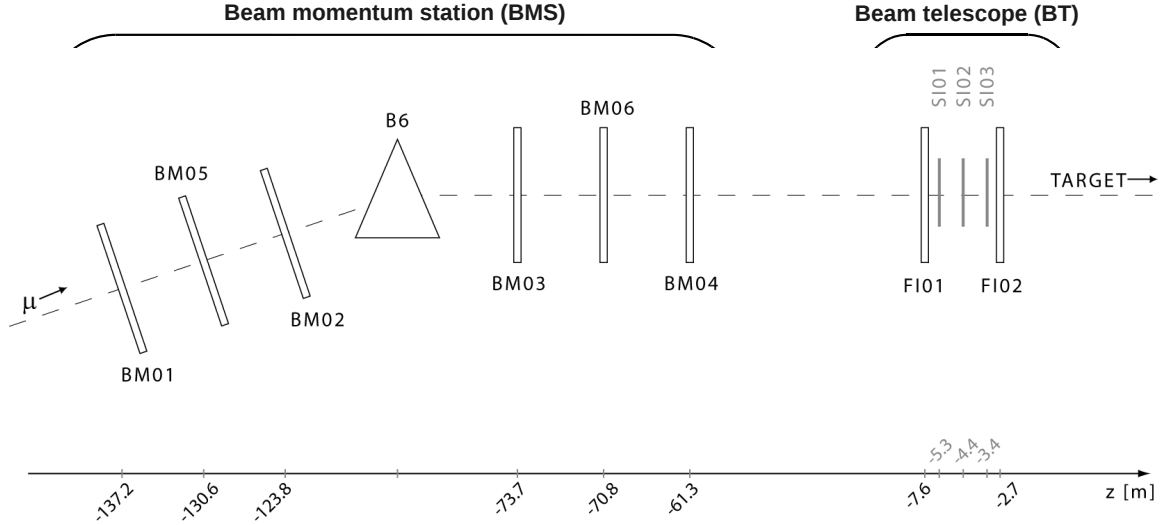
Figure 3.3: Set-up used for the measurement of the beam momentum and beam track definition.

The target is decomposed in 2 or 3 cells which can be polarized in opposite directions by tuning the microwave frequencies. This allows to take data for the two polarizations at the same time and minimizes systematic effects. The spin of the nucleons can also be rotated by reversing the solenoid field. This operation can be done in 20 minutes and is performed every 8 hours. Furthermore, exchanging the microwave frequencies between the cells can also be done but it requires to fully re-polarize the target and is performed a few times per data taking year.

3.3   The COMPASS Spectrometer

Beam telescope

The momentum of the beam particle is measured using the beam momentum station. The system was first composed of 4 planes of hodoscopes placed upstream and downstream of a bending magnet. To cope for the increase in instantaneous rate and to disentangle ambiguities 2 planes of scintillating fibers were added. The achieved momentum resolution is 0.5% and the efficiency is 93%. The beam track is measured upstream of the target in a telescope made of 3 stations of silicon micro-strip detectors each composed of 4 planes and 2 planes of scintillating fibers. The silicon stations provide a position resolution of 10 microns and the fiber has a poorer position resolution (200μm) but it has good timing resolution (400ps) and can be used to correlate the incoming track to the beam momentum station.

Large angle spectrometer

Just after the polarized target is the region of the large angle spectrometer. It is built around a large aperture magnet SM1 ($1.8 \times 1.3\,\mathrm{m}^2$) of 1.1 T.m field integral and covers polar angles up to 180 mrad. Upstream of the magnet, three types of detector are used: at short radial distance from the beam and on both sides of the magnet, scintillating fibers are used for their ability to stand high rates; at larger radial distance, i.e. up to 30 cm, modern micro-pattern gaseous detector of the Micromegas type are used. They can withstand a rate of $300\,\mathrm{kHz/mm}^2$ and have a spatial resolution of 100 microns; at large radial distance and up to 60 cm from the beam, drift chambers designed to operate at high rates[1] are used.

Downstream of the SM1 magnet, Drift Chambers and Straw Chambers are used for their ability to cover large areas. In the beam region scintillating fibers are used along with another type of micro-pattern gaseous detector, namely the Gas Electron Multiplier (GEM).

After leaving the trackers, the particles enter the identification section. They first encounter a Ring Imaging CHerenkov detector (RICH). It is a fairly large vessel ($3 \times 4 \times 5\,\mathrm{m}^3$) filled with C_4F_{10} gas. The Cerenkov light produced along the particle path is focused on photo-detectors placed at the rear of the vessel out of the acceptance. The photo-detectors are multi-anode PMTs in the central region where the counting rates are the highest and CsI coated cathode read out by fast electronics in the outer region. To complete the particle identification, electromagnetic and hadronic calorimeters are also used. The electromagnetic calorimeter ECAL 1 covers an area of $4.0 \times 2.9\,\mathrm{m}^2$ with a central hole of $1.0 \times 0.6\,\mathrm{m}^2$. It is composed of three types of Lead Glass blocks of sizes $3.8 \times 3.8\,\mathrm{cm}^2$ in the region closest to the beam, of $7.5 \times 7.5\,\mathrm{cm}^2$ in the intermediate region and $14.3 \times 14.3\,\mathrm{cm}^2$ in the outer region. Muon identification (in both spectrometers) is performed using up to 30 radiation length of concrete and iron blocks.

Small angle spectrometer

The small angle spectrometer is resembling the first one and has tracking planes placed on both sides of a spectrometer magnet, SM2, which has a field integral of 4.4 T.m in order to curve high momentum tracks. Similarly to the large angle spectrometer, different types of detectors are used depending on local rates and resolution needs. In the beam vicinity it is covered by scintillating fibers and GEMS. At larger distance, straws and large area drift chambers are used. After the second absorber, multi-wire proportional chambers can be used since the rates are lower. Particle identification is completed in this region by the use of an electromagnetic calorimeter (ECAL2) and a hadronic calorimeter (HCAL2). The electromagnetic calorimeter ECAL 2 covers an area of $2.4 \times 1.8\,\mathrm{m}^2$ and the central hole can be as large as $0.4 \times 0.4\,\mathrm{m}^2$. It is composed of one types of Lead Glass blocks of size $3.8 \times 3.8\,\mathrm{cm}^2$.

---

[1]rates are as high as 800 kHz/wire
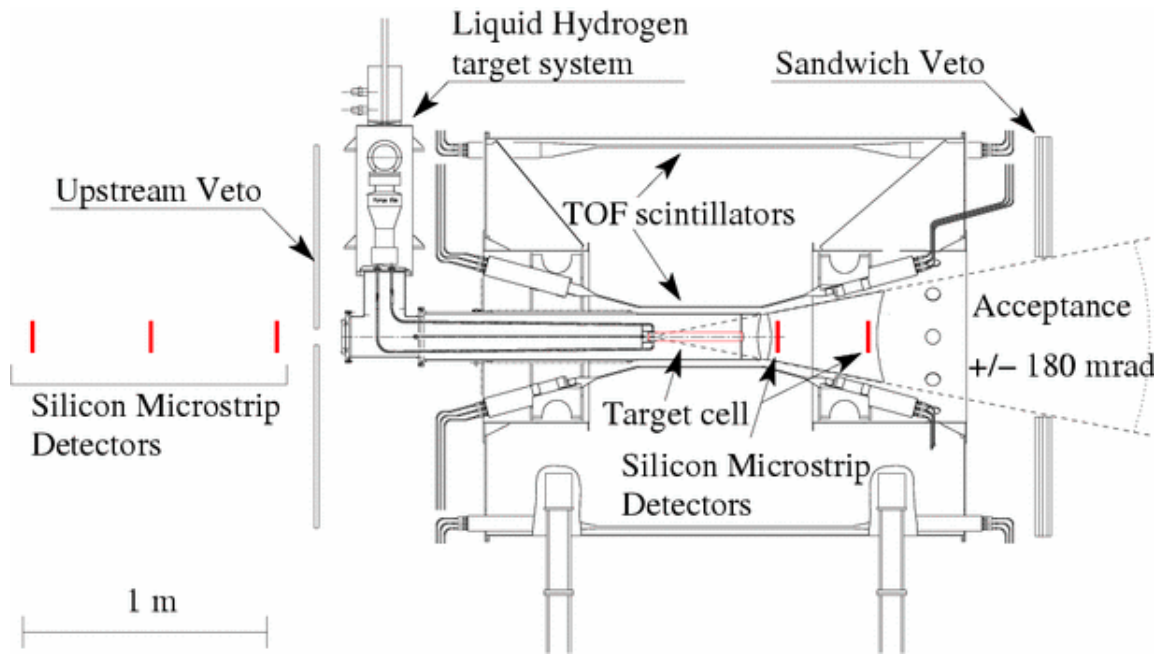
Figure 3.4: The Recoil Proton Detector and liquid hydrogen target used for the COM-PASS hadron program and for the DVCS beam tests.

Trigger and Veto system

The trigger and veto system uses hodoscopes of scintillating counters and calorimeters. The hodoscopes are placed behind the absorbers and detect the passage of a particle (a muon) at 2 points along the track. They are associated in pairs so that the track points back to the target region and produces a inclusive trigger. Further conditions using the energy deposition in the calorimeters can be used to improve the purity of the trigger system. The muon beam is accompanied by a halo which extends to large distance (up to 2 m) and are vetoed using a set of hodoscopes placed upstream of the target.

Recoil Proton Detector

Our group has built a Recoil Proton Detector (RPD) for the COMPASS hadron program. It is made of two concentric barrels of plastic scintillators read at both sides by photomultiplier tubes and surrounds the liquid hydrogen. The first ring of scintillator is composed of 12 counters of 50 cm length and 5 mm thick. The outer ring is composed of 24 counters of 106 cm length and 1cm thickness. We have designed a fast logic trigger performing the coincidences between the facing counters and it constituted an important piece of the trigger system for hadron running. This detector is not used muon running with a polarized target but it provided the opportunity to observe DVCS in some dedicated beam tests in 2008 and 2009. The performances of the RPD are summarized in chapter 5 when we present the results of these tests.
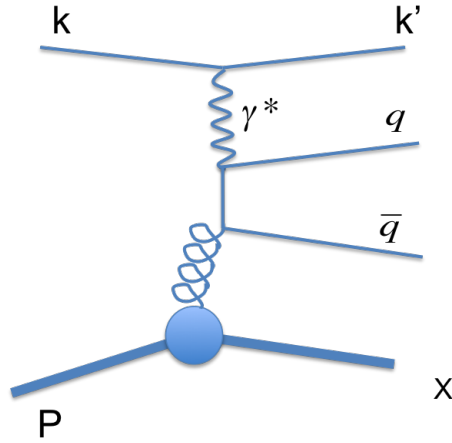
Figure 3.5: Graph of the photon-gluon fusion process.

3.4   Gluon contribution to the nucleon spin

The contribution of the gluons to the nucleon spin can be measured from the process of photon-gluon fusion (PGF) where the virtual photon interacts with a gluon through a quark line (see figure 3.5). In the final state, it produces a quark anti-quark pair and the nucleon is broken into fragments as in inclusive deep inelastic scattering. Following this process, the quarks will hadronize into mesons which can be detected. This "semi-inclusive" process can then be measured experimentally. We consider two types of signature for the PGF process : the production of charmed mesons and the production of high transverse momentum hadron pairs.

The measurement of the gluon polarization is performed by scattering the muon beam off the polarized target and measuring the asymmetry in the number of PGF events for opposite polarization of the target nucleons. The counting rate asymmetry, A, can be written:

$$A = \frac{N^+ - N^-}{N^+ + N^-} = f \cdot D \cdot P_\mu \cdot P_t \cdot a_{LL}^{PGF} \cdot \frac{\Delta G}{G}$$

where f is the dilution factor, D is the depolarization factor, P_μ is the target polarization, P_t is the target polarization, a_{LL}^{PGF} is the asymmetry of the QCD calculable part of the photon-gluon process and $\frac{\Delta G}{G}$ is the gluon polarization normalized to the gluon density.

Production of charmed mesons

The gluon polarization is determined assuming that open charm production is dominated by the PGF mechanism yielding a $c\bar{c}$ pair which fragments mainly into D mesons. This method has the advantage that in lowest order there are no other contributions to the cross section, however, it is statistically limited. In our analysis only one charmed meson is required in every event. This meson is selected through its decay in one of the
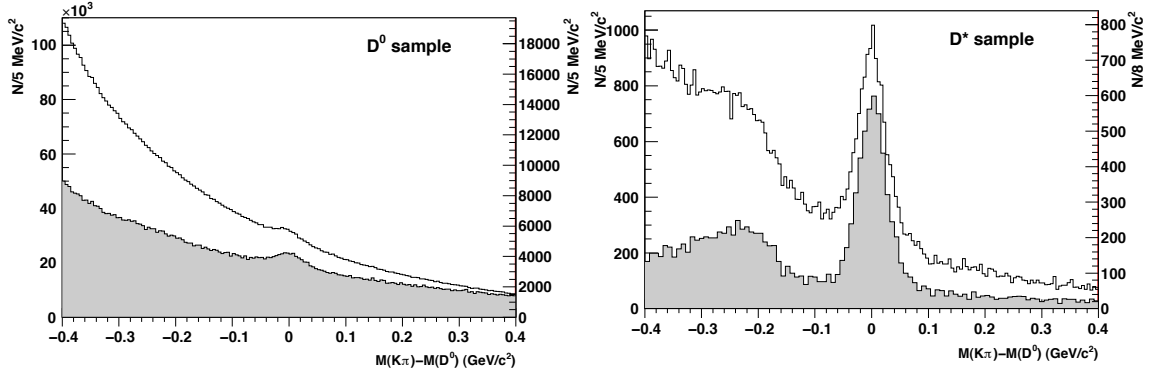
Figure 3.6: Invariant mass of the K-π system for the D^0 sample (left) and for the D^* sample (right) where the presence of an additional soft pion is required.

two channels : $D^0 \to K^+\pi^-$ and $D^*(2010)^+ \to D^0\pi^+_{\text{slow}} \to K^+\pi^-\pi^+_{\text{slow}}$. The hadrons are identified in the RICH and events with one scattered muon and at least a kaon and a pion are selected. The invariant mass of the K-π system is shown in figure 3.6 for the D^0 (left graph) showing a high combinatorial background under the peak which limits the statistical precision achievable. In the case of the D^* (right graph) it is required that an additional slow pion is detected acting as a D^* -tagger. The background for this channel is highly reduced. Refined analysis of the signal including clever re-weighting of the events was performed yielding to the distributions shown in the shaded areas and helped in improving the statistical precision of the method. The result for the gluon polarization obtained with this method is [40]:

$$\left\langle \frac{\Delta G}{G} \right\rangle = -0.08 \pm (0.21)_{stat} \pm (0.11)_{syst}$$

for the range of $0.06 < x < 0.22$ with $\langle x \rangle \approx 0.11$, and a hard scale $\langle \mu^2 \rangle \approx 13 (GeV/c)^2$. It provides a direct and model independent determination of the gluon polarization and the precision is dominated by the statistical error. Large values of $\triangle G$, postulated to solve the spin crisis, are ruled out by this measurement which is also found to be in agreement with previous results (see figure 3.7). On this figure, the results of a QCD analysis of the polarized structure function data is also presented corresponding to $\Delta G = \pm 0.3$.

Production of high-pt hadron pairs

The selection of the event sample in the case of high transverse momentum hadron is rather simple. The transverse momentum, p_t, with respect to the direction of the virtual photon is measured and events for which two hadrons have:

$$p_t(h_1) > 0.7 \, GeV/c \qquad p_t(h_2) > 0.7 \, GeV/c \qquad p_t^2(h_1) + p_t^2(h_2) > 2.5 \, (GeV/c)^2$$
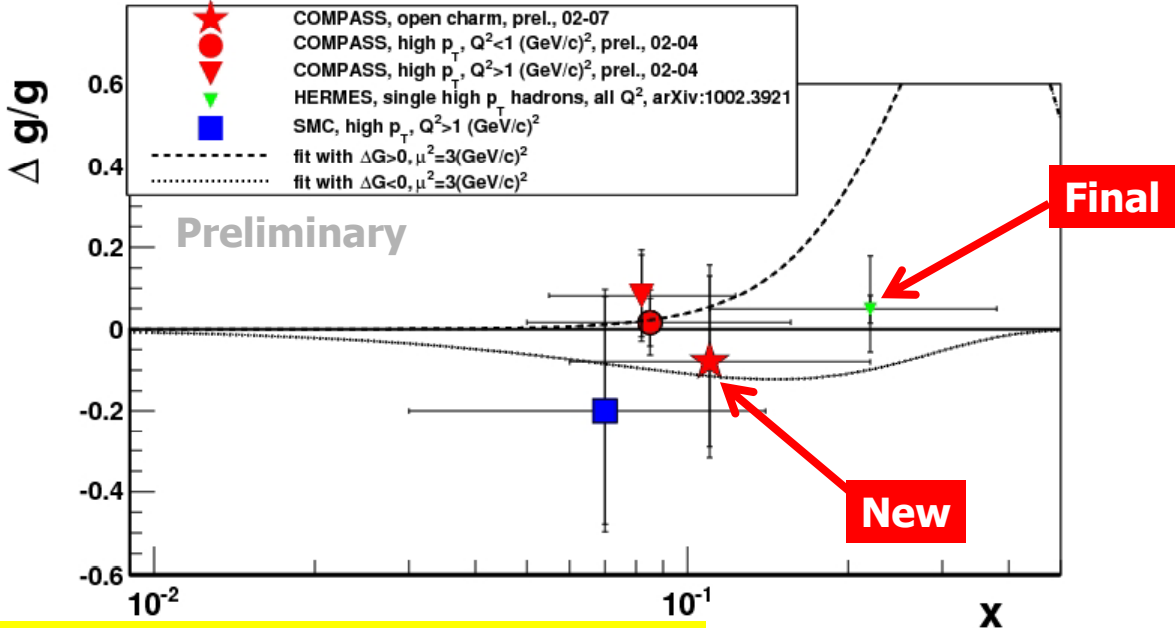
Figure 3.7: Comparison of the measurements of the polarized gluon structure function. The lines is a result of a QCD analysis of the polarized structure function data for $\Delta G > 0$ and $\Delta G < 0$ yielding $|\Delta G| = 0.3$

are selected. The third requirement acts a hard scale for the process in the sample since all Q^2 are accepted and since the nature of the mesons is not constrained. There are various QCD processes which can contribute to this sample of events and they are represented in figure 3.8. Their relative contributions were estimated using the PYTHIA physics simulation program [39] and a extensive Monte-Carlo simulation of the experiment. They are classified in 3 classes (apart from PGF): the QCD Compton describes the radiation of a quarks, the "Leading order" is the standard deep inelastic process and the graphs on the right of the figure correspond to "resolved photons" where the photon content in terms of quarks and gluons interact with the nucleon. The graph in the center of the figure shows the relative abundance of the various processes. The experimental asymmetry depends now on the analyzing power (a_{LL}^i) and abundance (R^i) of the different contributions:

$$A = \frac{N^+ - N^-}{N^+ + N^-} = f \cdot D \cdot P_\mu \cdot P_t \cdot \left(A_1 a_{LL}^{LO} R^{LO} + A_1 a_{LL}^{QCDC} R^{QCDC} + \frac{\Delta G}{G} a_{LL}^{PGF} R^{PGF} \right)$$

where A_1 is the asymmetry originating from the quark polarization. The contribution of the resolved photons is treated as a systematic error. The value obtained for the gluon polarization with this method is [41]:

$$\frac{\Delta G}{G} = 0.016 \pm (0.058)_{stat} \pm (0.014)_{syst.exp} \pm (0.052)_{syst.MC} \pm (0.013)_{res.\gamma}$$
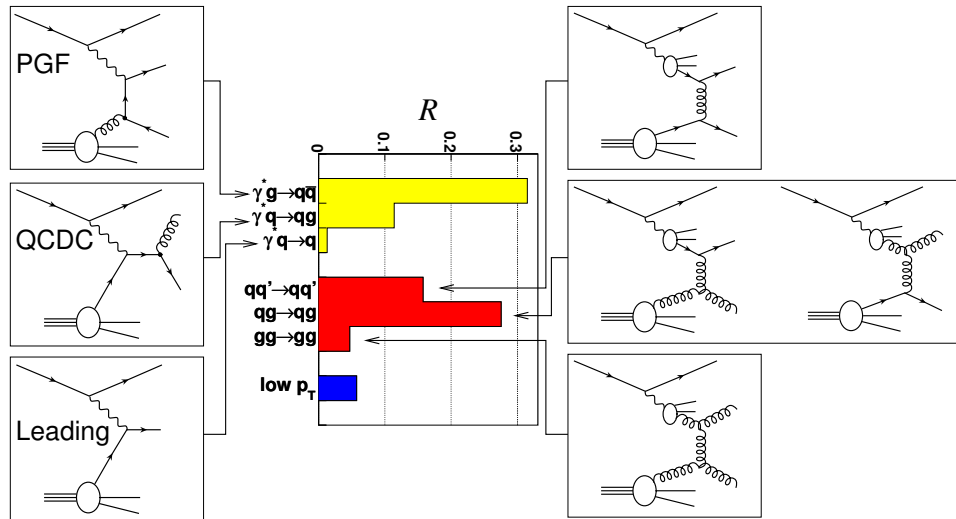
Figure 3.8: Diagram contributing to the production of high transverse momentum hadron pairs estimated using the PYTHIA simulation program. The graph in the center shows the relative abundance of each process.

for $< x_g >= 0.095$ and at a scale $< \mu^2 >= 3(GeV/c)^2$. The systematic error is dominated by the Monte-Carlo and does not include the model dependence. This results is compatible with 0 and points towards a small polarization of the gluons.

Chapter 4

Exclusive production of rho mesons

The exclusive lepto-production of the ρ^0 vector meson :

$$l + p \rightarrow l + p + \rho^0$$

has been the subject of extensive studies at the HERA collider and at fixed target experiment facilities such as Fermilab, CERN and JLab [44, 45].

The exclusive ρ^0 production where the ρ decays into a pion pair can be detected using the COMPASS experiment and constitute a good case for the investigation of observables sensitive to generalized parton distributions and we have chosen to focus on the analysis of this channel. The graphs contributing to the process are shown in figure 4.1. In the experimental set-up which was used there was no recoil proton detector and the exclusivity can only be partially insured. At the time this analysis was started (2003), the calorimeters were either not existing or not usable for exclusive photon searches.

In a first analysis, we have evaluated the quality of the selection of exclusive incoherent meson production from which we have investigated three sets of observables depending on target or beam polarizations. We have measured spin density matrix elements (SDME) leading to the measurement of the ratio of longitudinal to transverse cross section. SDME allows to test the validity of the s-Channel Helicity Conservation and to estimate the parity of the object exchanged in the interaction. Then, with increased statistics we have measured the asymmetry when the muon beam is polarized and the target polarization is longitudinal. This also allows to test the parity of the exchanged object and it is sensitive to the GPD $\tilde{H}_g$. Finally, we have measured the asymmetry with transversely polarized deuteron and proton targets which has some sensitivity to the GPD E which is linked to the orbital angular momentum of constituents of the nucleon.

In this chapter, we describe the selection of the incoherent exclusive events and then examine the results obtained from the data on the three topics of interest that we have mentioned. At a later stage, improvements in the estimation of acceptance and background subtraction were carried out during the thesis of G. Jegou [42]. These improvements in the analysis are described and the results are presented.
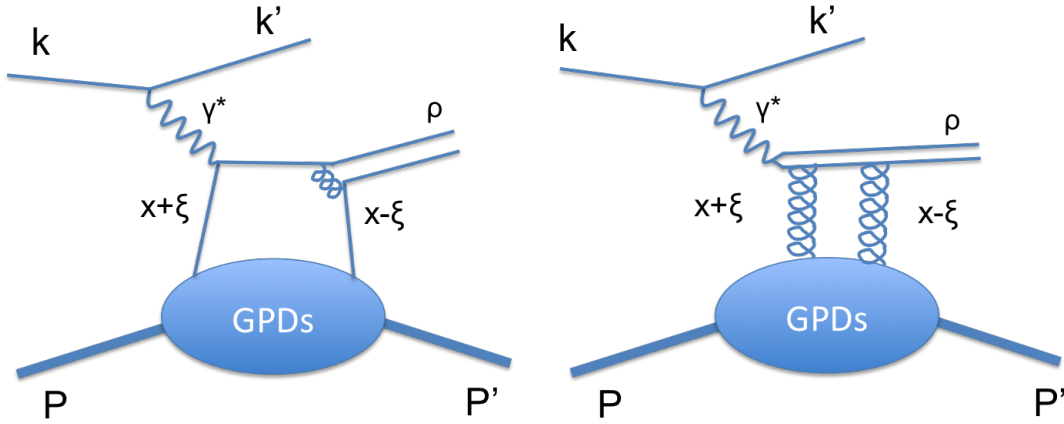
Figure 4.1: Quarks and gluons exchange mechanisms describing the exclusive production of ρ^0.

4.1   Selection of the events

In this section we describe the selection of exclusive ρ^0 production events from the COMPASS data and illustrate with the distributions obtained for the relevant kinematical variables.

Topological selection

- One vertex with one incoming muon, one scattered muon and two hadron charged tracks of opposite charges associated.

- Hadron charged tracks are required to end before the absorber. This insures that they are not misidentified scattered muons.

- The vertex has to lie in the target active volume (figure 4.2)

- The flux of the beam particles crossing the target cell is forced to be the same by keeping only beam tracks where the extrapolated beam track is passing through both the entrance and the exit windows of the target.

Identification of the ρ^0

From the two charged hadrons detected in the events one can calculate the invariant mass of the system after having assumed that the particles are pions. In principle, the RICH detector could be used to identify the pions but at the time of this analysis, the RICH detector performances were not fully established and the efficiency was low. The mass spectrum of the two-hadron system constructed under this assumption is shown on figure 4.3. We see a clear peak of the ρ^0 resonance centered at 770 MeV on top of the non resonant $\pi^+\pi^-$ pairs and the distribution is slightly asymmetric due to an interference with this non-resonant contribution. A small peak is present for invariant masses around 400 MeV and is due to production of the ϕ mesons where the decay kaons
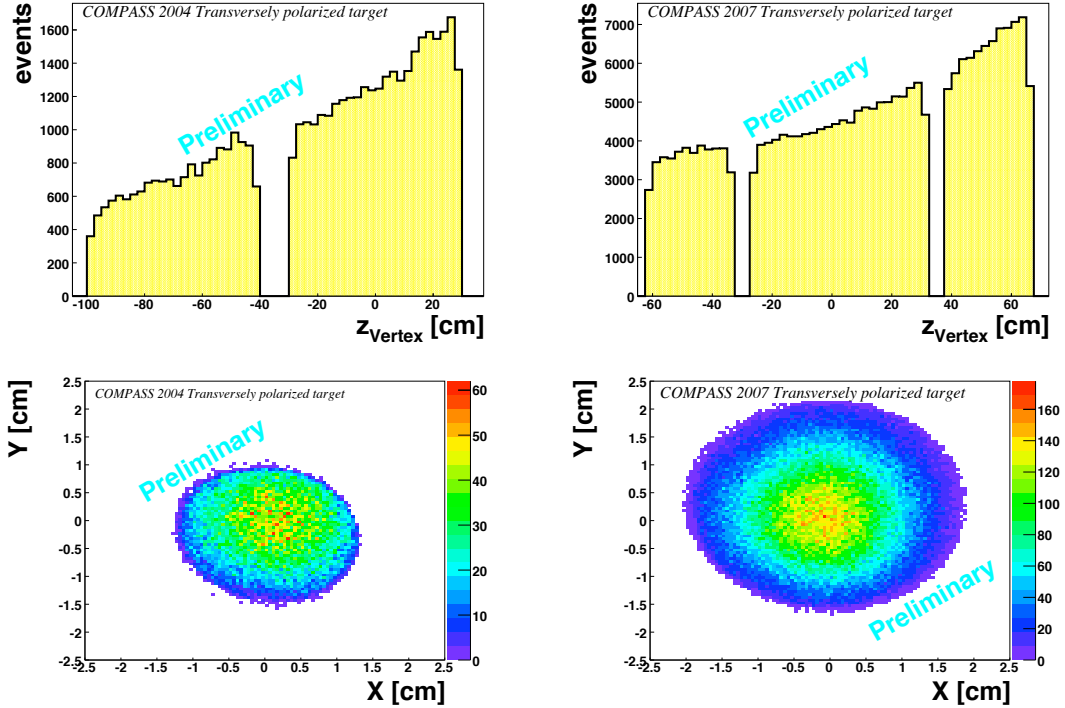
Figure 4.2: Vertex distribution along the beam axis (top plots) and in the transverse plane (bottom plots). Left column is for 2004 data with a 2-cell polarized target. Right column is for 2007 with a 3-cell polarized target.

were assigned a pion mass. The presence of a ρ^0 is insured by applying the following cut :

$$m_\rho - 300\,\text{MeV} < m_{\pi\pi} < m_\rho + 300\,\text{MeV}$$

Exclusivity of the reaction

In the absence of recoil particle detection the exclusivity of the reaction has to rely on the missing mass technique. In the topological selection, it was already required that there are no other charged tracks associated to the vertex. But it does not prevent events with neutral particles or high angle charged tracks to enter the selection. To discard this events we have evaluate a quantity, E_{miss}, defined as :

$$E_{\text{miss}} = \frac{M_X^2 - M_P^2}{2M_P}$$

where M_X^2 is the mass of the undetected recoil system constructed from the muons and the pions and M_P is the proton mass. The distribution of E_{miss} for the events fulfilling the previous criteria is shown on figure 4.4. It shows an exclusive peak at $E_{miss} = 0$ with a resolution of 1 GeV which is mostly due to the momentum resolution on the incoming and scattered muons. It also shows a tail of non-exclusive background extending to larger values of E_{miss}. This background is composed of different sources. It arises from
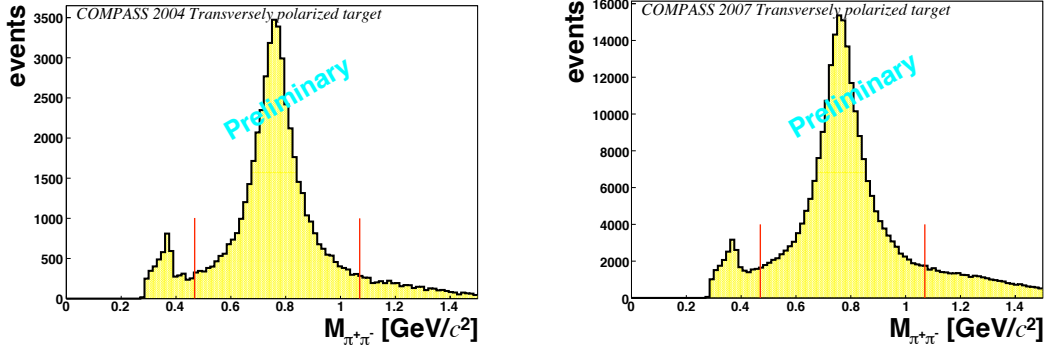
Figure 4.3: Invariant mass of the two-pion system (left : 2004; right : 2007)
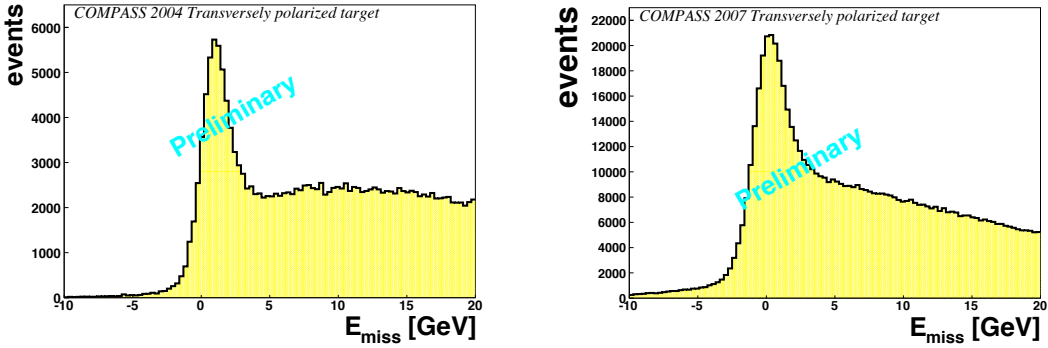
Figure 4.4: Missing energy (left : 2004 data; right : 2007 data)

semi-inclusive deep inelastic scattering events where a few particles are produced and only one ρ^0 is detected. Also, a lower component starting at $E_{miss} = 1$ GeV, is due to diffractive dissociation where the ρ^0 interacts with a nucleon exited state which then decays into hadrons ($\sim$13% of the exclusive signal). These events are partially cut by applying the following requirement :

$$-2.5 < E_{miss} < 2.5 \text{ GeV}$$

The non-exclusive background remaining under the exclusive peaks to be estimated using the PYTHIA physics generator [39] and diffractive dissociation is treated as a systematic error.

Incoherent scattering off the nucleon

The slope of the p_t^2 distribution for exclusive production is a characteristic feature of the size of the object off which the scattering occurred. We have used solid polarized nuclear targets of ^{6}LiD for deuteron measurement and NH$_3$ for proton measurement. The reaction is therefore the sum of incoherent scattering off quasi-free nucleons and of coherent scattering off nucleons bounded in nucleus. The p_t^2 distributions for the two types of targets are presented in figure 4.5. They are fitted with the sum of three
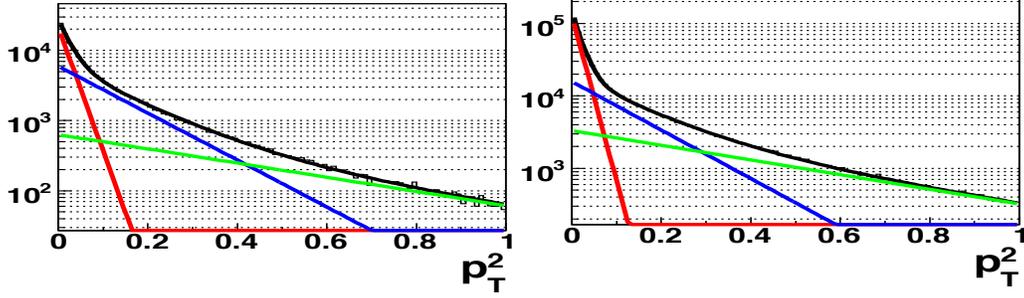
Figure 4.5: The p_T^2 distribution for exclusive production for a ^{6}LiD target (left) and for NH$_3$ (right).

FIG. 4.5 – Distribution en , toutes coupures appliquées sauf la coupure en , pour 2004 (à gauche) et 2007 (à droite). Les lignes rouges correspondent aux coupures appliquées.

FIG. 4.6 – Distribution de la variable pour 2004 (à gauche) et 2007 (à droite). Toutes les coupures sont appliquées sauf la coupure sur . Pour la figure de 2004, la coupure est appliquée pour 2007.
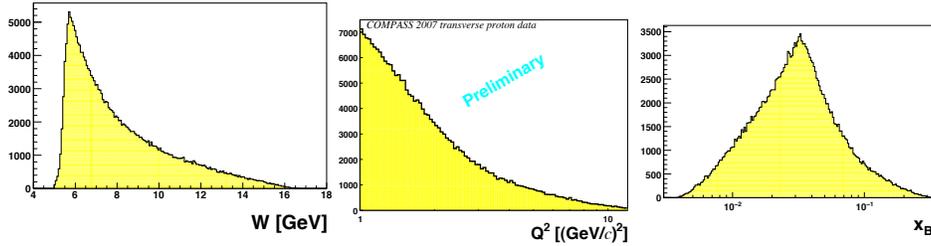
Figure 4.6: Distributions in the kinematical variables W, Q^2 and x_{bj} for the exclusive ρ^0 sample for 2007 proton data.

Cette coupure affecte seulement le bruit de fond et rendra plus cohérente la soustraction de celui-ci. En effet sans cette coupure, nous serions dépendant de la qualité de nos simulations de bruit de fond dans toute la gamme en énergie du . En appliquant cette coupure, nous nous affranchissons des problèmes liés au bruit de fond pour .

4.1.2 Selection de production d'autres mésons

Nous avons également étudié la production exclusive d'autres mésons. Quelques modifications dans la sélection d'événements permettant de sélectionner les événements de production de , et du contiennent des photons, nous utiliserons donc les calorimètres. Les produits de désintégration et nous avons mis au point une méthode de sélection des bons clusters[2] car les calorimètres

[2]un cluster est un agrégat de cellules du calorimètre qui sont corrélés spatialement.

exponential functions : coherent scattering which dies quite rapidly with p_t^2 (in red), incoherent which needs to be added in order to reproduce the high p_t^2 part of the distribution and which arises from non-exclusive scattering (green). The incoherent sample is selected by requiring that $p_t^2 > 0.1\,\mathrm{GeV}^2$ for the ^{6}LiD target and $p_t^2 > 0.05\,\mathrm{GeV}^2$ for the NH$_3$. This value is different due to the size of the nucleus involved : mainly deuterium for the ^{6}LiD and N for NH$_3$. The contamination of coherent scattering has been estimated [50] and amounts to 8% for ^{6}LiD and 5 % for NH$_3$.

Non exclusive scattering events are rejected in the sample by requiring that $p_t^2 < 0.5\,\mathrm{GeV}^2$. Anyway, over the whole accepted range, the background level can be extracted from the data and then subtracted. This method is presented at the end of this chapter.

FIG. 4.4 – Nombre d'événements en fonction de . En rouge le cohérent, bleu l'incohérent, vert le bruit de fond. Haut à gauche le fit par 3 exponentielles, haut à droite (bas à gauche) la fraction de bruit de fond en fonction de la valeur minimale de . En bas à droite la fraction de bruit de fond en fonction de la valeur maximale de . Les 4 graphes du haut (resp. bas) sont pour les données de 2004 (resp. 2007).

Kinematical domain of the final sample

The distributions in the kinematical variables W, Q^2 and x_{bj} for the exclusive ρ^0 sample are shown in figure 4.6. The W starts around 5 GeV, well above the resonance region and extends to 16 GeV with an average value of 8 GeV. According to models, the contributions of the mechanism involving quarks or gluons exchange have similar magnitude at this value of W [23, 46, 60]. The Q^2 domain accessed is between 1 and 10 $(\mathrm{GeV}/c)^2$. Many exclusive events fall below $1(\mathrm{GeV}/c)^2$ and can be used for systematic studies (not shown here). The x_{bj} range is between $3 \cdot 10^{-3}$ and $2 \cdot 10^{-1}$.

4.2   Spin density matrix elements

4.2.1   Formalism

The decay distribution can be related to the spin density matrix $\rho^\alpha_{\lambda,\lambda'}$ of the vector meson, where $\lambda, \lambda' = -1, 0, 1$ label the meson spin states and α represents the production by different virtual polarization states ($\alpha = 0$: unpolarized transverse photons, $\alpha = 1, 2$: the two directions of linear polarization, $\alpha = 3$: circular polarization, $\alpha = 4$: longitudinal polarized photon, $\alpha = 5...8$: interference of the longitudinal and transverse amplitudes) [47]. Only $\alpha = 0, 1, 2, 4, 5, 6$ contribute for an unpolarized lepton beam while polarized lepton gives the additional $\alpha = 3, 7, 8$. In practice, the angular distributions can be described in terms of the following linear combinations of the $\rho^\alpha_{\lambda,\lambda'}$:

$$r^{04}_{\lambda,\lambda'} = \frac{\rho^0_{\lambda,\lambda'} + (\varepsilon + \delta)R\rho^4_{\lambda,\lambda'}}{1 + (\varepsilon + \delta)R} \tag{4.1}$$

$$r^\alpha_{\lambda,\lambda'} = \frac{\rho^\alpha_{\lambda,\lambda'}}{1 + (\varepsilon + \delta)R} \qquad \alpha = 1, 2, 3 \tag{4.2}$$

$$r^\alpha_{\lambda,\lambda'} = \frac{\sqrt{R}\rho^\alpha_{\lambda,\lambda'}}{1 + (\varepsilon + \delta)R} \qquad \alpha = 5, 6, 7, 8 \tag{4.3}$$

where $R = \sigma_L/\sigma_T$ is the ratio of longitudinal to transverse virtual-photon cross section for exclusive ρ^0 production, ε is the virtual photon polarization parameter and δ is the lepton mass correction parameter. In principle, 23 spin density matrix elements can be determined using a polarized beam.

The spin density matrix element are bi-linear combinations of the nine helicity amplitudes $T_{\lambda\gamma}$ for a photon of helicity $\gamma (= \pm 1, 0)$ to produce a meson of helicity $\lambda (= \pm 1, 0)$ and summed over the nucleon spin. In case of natural parity exchange (i.e. the exchanged particle satisfies $P = (-1)^J$) the following relation holds $T_{-\lambda-\gamma} = (-1)^{\lambda-\gamma}T_{\lambda\gamma}$ and the number of independent helicity amplitudes is reduced to 5. If in addition one assumes that the helicity of the photon is fully transferred to the meson (s-channel helicity conservation, SCHC) holds, $\lambda = \gamma$ and only two non-zero helicity amplitudes remain : T_{00} and T_{11}. One can define a total longitudinal (N_L) and a total transverse (N_L) squared amplitude :

$$N_L = \sum_{\lambda=-1,0,1} |T_{\lambda 0}|^2 \tag{4.4}$$

$$N_T = \frac{1}{2} \sum_{\lambda=-1,0,1} |T_{\lambda 1}|^2 + |T_{\lambda-1}|^2 \tag{4.5}$$

Using these relations one can then express the spin density matrix elements using helicity amplitudes. For example, some of these matrix elements read :

$$r^{04}_{00} = \frac{1}{1 + (\varepsilon + \delta)R}\left[\frac{|T_{01}|^2 + |T_{0-1}|^2}{2N_T} + \frac{(\varepsilon + \delta)R\,|T_{00}|^2}{N_L}\right] \tag{4.6}$$
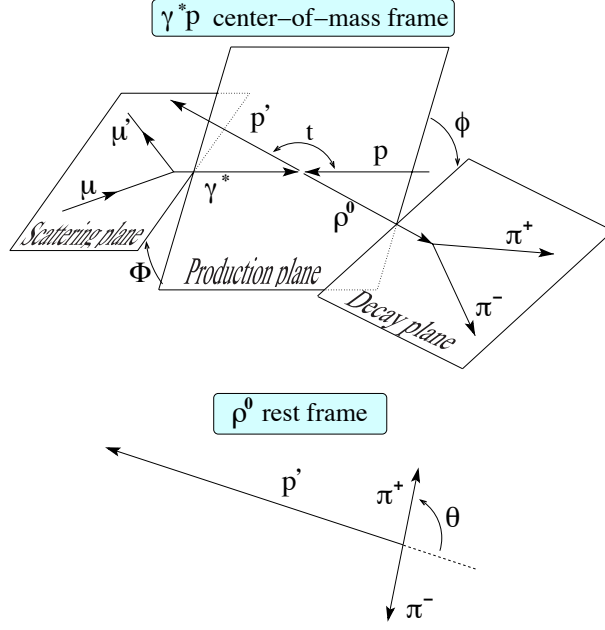
Figure 4.7: Definition of the angles used in the Spin-density matrix element formalism

$$r^1_{1-1} = \frac{1}{1+(\varepsilon+\delta)R}\frac{T_{11}T^*_{-1-1}+T_{1-1}T^*_{-11}}{2N_T} \tag{4.7}$$

$$r^{04}_{1-1} = \frac{1}{1+(\varepsilon+\delta)R}\Re\mathfrak{e}\left[\frac{T_{11}T^*_{-11}+T_{1-1}T^*_{-1-1}}{2N_T}+\frac{(\varepsilon+\delta)RT_{10}T^*_{-10}}{N_L}\right] \tag{4.8}$$

If one assumes further that SCHC is valid and NPE, we obtain the following relation :

$$r^{04}_{00} \longrightarrow \frac{(\varepsilon+\delta)R}{1+(\varepsilon+\delta)R} \tag{4.9}$$

$$r^1_{1-1} \longrightarrow \frac{1}{2}(1-r^{04}_{00}) \tag{4.10}$$

$$r^{04}_{1-1} \longrightarrow 0 \tag{4.11}$$

We see that r^{04}_{00} is then related directly to the ratio R of longitudinal to transverse cross section and that a non-zero value for r^{04}_{1-1} (along with other spin density matrix elements not described here) will quantify the violation of SCHC.

4.2.2 Extraction of the matrix elements

The angular distribution $W(\cos\theta,\phi,\Phi)$ for the process is studied in the s-channel helicity frame where it depends on 3 angles (see figure 4.7) : ϑ is the polar angle of the π^+production in the ρ^0 rest frame, ϕ is the angle between the production plane and the decay plane and Φ is the angle between the lepton scattering plane and the production plane. At the stage of the analysis, we considered only one-dimensional projections of the angular distribution leading to the determination of a few spin density matrix

elements. For $\cos\theta$ and ϕ the angular distributions are:

$$W(\cos\vartheta) \;=\; \frac{3}{4}(1-r_{00}^{04}) + (3r_{00}^{04}-1)\cos 2\vartheta \tag{4.12}$$

$$W(\phi) \;=\; \frac{1}{2\pi}\left[1-2r_{1-1}^{04}\cos 2\varphi + 2P_\mu\sqrt{1-\varepsilon^2}\,\mathfrak{Im}\,r_{1-1}^{3}\sin 2\varphi\right] \tag{4.13}$$

where $P_\mu = -0.76$ is the average muon beam polarization and ε is the virtual photon polarization parameter. The s-channel helicity conservation hypothesis is valid then both r_{1-1}^{04} and $\mathfrak{Im}\,r_{1-1}^{3}$ must be equal to 0. Moreover, the angular distribution reduces to W($\cos\vartheta$, Ψ) where $\Psi = \varphi - \Phi$ is the angle between the leptonic and the ρ^0 decay plane, and one has :

$$W(\Psi) = \frac{1}{2\pi}\left[1 + 2\varepsilon r_{1-1}^{1}\cos 2\Psi\right] \tag{4.14}$$

The measured distributions have to be corrected for experimental effect by a "generalized acceptance" which takes care of the combined effects of acceptance, efficiency and smearing and have to be determined using Monte-Carlo simulations. Events generated using the DIPSI [49] event generator are processed by the Geant-based simulation of the COMPASS spectrometer and analyzed by the usual COMPASS data analysis programs. Only 1-dimensional acceptance functions were used at this early stage of the analysis and no re-weighting of the events was performed to better match the observed distributions. This has been studied in a refined analysis presented at the end of this chapter.

4.2.3 Results

The variation of r_{00}^{04} as a function of Q^2 extracted from the $\cos\theta$ distribution is displayed in the left panel of Fig. 4.8 where statistical errors only have been indicated. Our data cover a wide range of Q^2 from quasi-real photo-production to the hard scattering regime ($0.01 < Q^2 < 10$ GeV^2) and have a very good statistical precision. The data are found to be in agreement with other experiments (see references in [48]). Assuming SCHC,

$$R = \frac{\sigma_L}{\sigma_T} = \frac{1}{\varepsilon+\delta}\frac{r_{00}^{04}}{1-r_{00}^{04}} \tag{4.15}$$

is determined and displayed on Fig.4.8 (right panel). Our results confirm the tendency observed that R increases with Q^2. Therefore, the production of longitudinal ρ^0 is found to be dominant at high Q^2. This is an important point for further investigations of the Generalized Parton Distributions because the factorization has only been proved valid for the longitudinal case. From the φ distribution, two other matrix elements, r_{1-1}^{04} and $\mathfrak{Im}r_{1-1}^{3}$, are extracted and displayed in figure 4.9. The matrix element r_{1-1}^{04} is found to be non-zero over the whole Q^2 domain indicating a mild violation of SCHC. Although, $\mathfrak{Im}r_{1-1}^{3}$, which can only be accessed using a polarized beam, is found to be compatible with 0. Finally, the matrix element r_{1-1}^{1} is extracted from the Ψ distribution and is found to be different to the expectation $r_{1-1}^{1} = \frac{1}{2}(1 - r_{00}^{04})$ assuming SCHC and
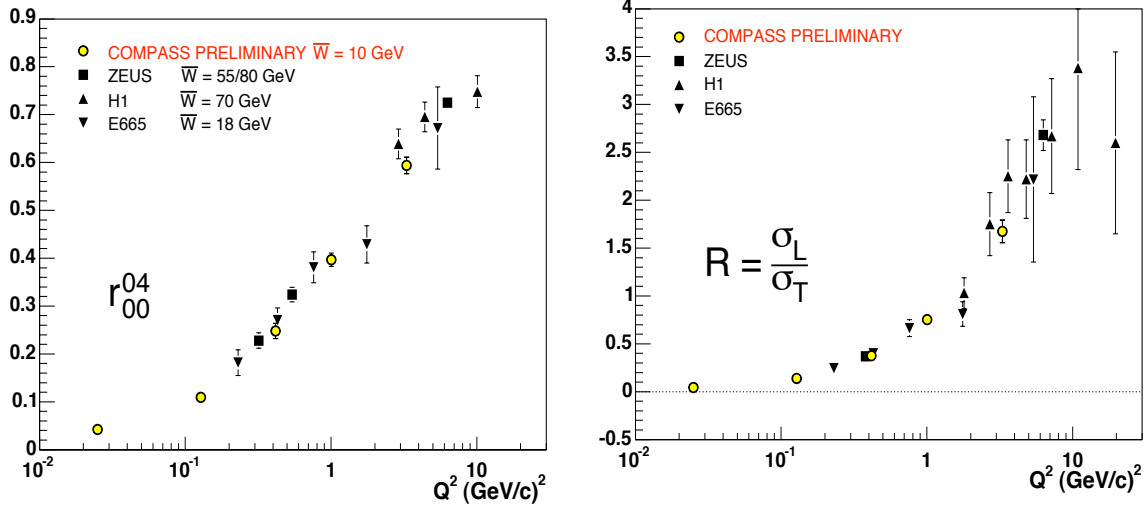
Figure 4.8: The r_{00}^{04} spin density matrix element as a function of Q^2 (left plot) and the ratio of longitudinal to transverse cross section assuming that the SCHC hypothesis is correct (right plot). Results from previous experiment are indicated.

natural parity exchange. Since only 1-dimension acceptance corrections were applied it is possible that the difference observed may be due to experimental effect not properly taken into account.

4.3 Asymmetries

Asymmetries are usually a good way to extract physics without having to estimate the acceptance. At the time this preliminary analysis was performed it was not clear what could be the achievable precision on the acceptance and we started investigating spin asymmetries. This analysis used the COMPASS data which was taken with a longitudinally or transversely polarized targets which leads us to address two types of asymmetries.

4.3.1 Longitudinal double spin asymmetries

Here we present the formalism used to extract the longitudinal asymmetry for exclusive ρ^0 production which is similar to the one used for COMPASS inclusive polarized deep inelastic asymmetries measurement. The quantity of interest is the longitudinal asymmetry, A_1^ρ, for the reaction $\gamma^* N \to \rho^0 N$ and is defined as :

$$A_1^\rho = \frac{\sigma_{1/2} - \sigma_{3/2}}{\sigma_{1/2} + \sigma_{3/2}}$$

where $\sigma_{1/2}$ and $\sigma_{3/2}$ refers to cross sections when the sum of the virtual photon and nucleon spin projections are $1/2$ and $3/2$. It is related to the experimental asymmetry, A_{LL}^{exp}, obtained with polarized muons for the reaction, $\mu N \to \rho^0 N$, through the following
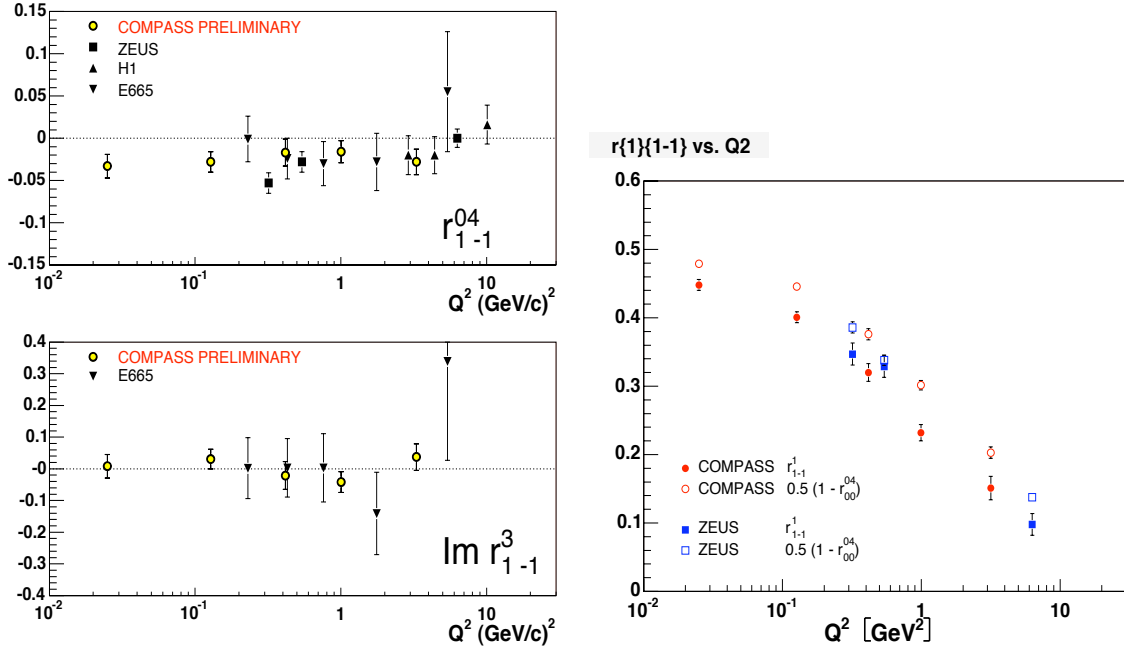
Figure 4.9: The r^{04}_{1-1} spin density matrix element as a function of Q^2 (top,left) showing a slightly non-zero value indicating a mild violation of SCHC. The $Im\,r^3_{1-1}$ spin density matrix element as a function of Q^2 (bottom,left) is found consistent with zero. The r^1_{1-1} spin density matrix element as a function of Q^2 (right) along with the prediction from r^{04}_{1-1} showing a Unnatural Parity Exchange contribution

relation :

$$A^{exp}_{LL} = \frac{N_{\uparrow\Downarrow} - N_{\uparrow\Uparrow}}{N_{\uparrow\Downarrow} + N_{\uparrow\Uparrow}} = f \cdot P_b \cdot P_t \cdot D \cdot A^{\rho}_1$$

where the arrow-indices $\uparrow\Uparrow$ ($\uparrow\Downarrow$) relate to the situation in which the spin of the muon and the proton are parallel (anti-parallel). In this expression, f is the dilution factor and represents the fraction of polarizable nucleons, P_b is the beam polarization, P_t is the target polarization and D is a kinematical factor expressing the fraction of longitudinal polarization transferred from the muon to the virtual photon. Transverse polarization effects are kinematically suppressed and are treated as a systematic errors. The values for f and D are derived using the cross section of exclusive ρ^0 production obtained in previous experiments. Experimentally, data is taken with the two target cells polarized in opposite directions and the two cells do not have the same acceptance. To cancel this effect the polarization is reversed (once per day) and the asymmetry is averaged over the two configurations :

$$A^{\exp}_{LL} = \frac{1}{2} \left(\frac{N^u_{+-} - N^d_{++}}{N^u_{+-} + N^d_{++}} + \frac{N'^d_{+-} - N'^u_{++}}{N'^d_{+-} + N'^u_{++}} \right)$$

where N (N') denotes the number of events produced in a given target cell before (after) target polarization reversal. The superscript u (d) relates to the upstream (downstream) target cell and the subscripts ++ (+−) indicate the situation when beam and target

cells polarization orientation are the same (opposite).

Results and physics impact

The results for the asymmetry obtained for a polarized deuteron target [51] (data taken in 2003) are presented as a function of Q^2 and x_{Bj} in figure 4.10 (top panels). The statistical errors are represented by vertical bars and the total systematic errors by shaded bands. The wide range in Q^2 covers four orders of magnitude from $3 \cdot 10^{-3}$ to 7 $(\text{GeV}/c)^2$. The domain in x_{Bj} which is strongly correlated with Q^2, varies from $5 \cdot 10^{-5}$ to about 0.05. For the whole kinematical range the A_1^ρ asymmetry measured by COMPASS is consistent with zero. The large systematic errors at high Q^2 and x_{Bj} arises from the non-exclusive background estimation.

Our result is also compared to the result obtained by the HERMES collaboration using a deuteron target [53] (lower panels). Note that the lowest Q^2 and x_{Bj} HERMES points, referred to as 'quasi-photo-production', come from measurements where the kinematics of the small-angle scattered electron was not measured but estimated from a MC simulation. This is in contrast to COMPASS, where scattered muon kinematics is measured even at the smallest Q^2. The results from both experiments are consistent within errors. The kinematical range covered by the present analysis extends further towards small values of Q^2 and x_{Bj} by almost two orders of magnitude. In each of the two experiments A_1^ρ is measured at different average W, which is equal to about 10 GeV for COMPASS and 5 GeV for HERMES. Thus, no significant W dependence is observed for A_1^ρ on an isoscalar nucleon target.

In the Regge approach [54] a longitudinal double spin asymmetry A_1^ρ originates from the interference of amplitudes for exchange in the t-channel of Reggeons with natural parity (Pomeron, ρ, ω, f, A_2) with amplitudes for Reggeons with unnatural parity (π, A_1). No significant asymmetry is expected when only a non-perturbative Pomeron is exchanged because it has small spin-dependent couplings as found from hadron-nucleon data for cross sections and polarizations. Our data disfavor the exchange of unnatural parity object since no significant asymmetry is observed.

The x_{Bj} dependence of the measured A_1^ρ is also compared to a theoretical prediction, which was based on the description of forward exclusive ρ^0 lepto-production and inclusive inelastic lepton-nucleon scattering by the off-diagonal Vector Meson Dominance model [52], applied to the case of polarized lepton and nucleon. At $x_{Bj} < 0.2$, with additional assumptions [53], A_1^ρ can be related through the optical theorem to the A_1 asymmetry for inclusive inelastic lepton scattering at the same x_{bj}:

$$A_1^\rho \simeq \frac{2A_1}{1 + (A_1)^2}$$

The prediction is obtained using a fit of $A_1(x)$ to the world data from polarized deuteron targets including COMPASS (see [55] and references therein). Within the present accuracy the results on A_1^ρ are consistent with this prediction.

More recently another pQCD-inspired model involving GPDs has been proposed by
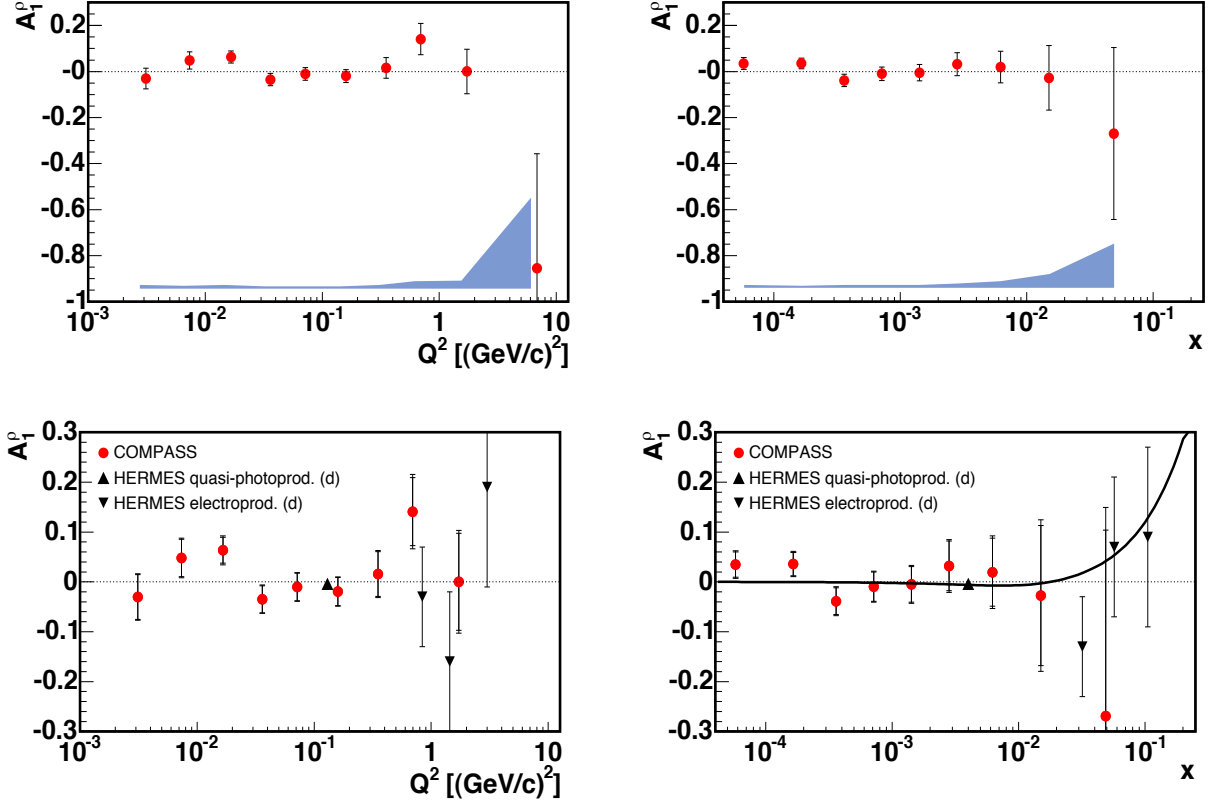
Figure 4.10: Longitudinal double spin asymmetry A_1^ρ as a function of Q^2 and as a function of x_{Bj}. The top graphs show the result obtained by COMPASS ; the shaded band shows the systematic error. The bottom graphs show the comparison with the results of the HERMES experiment along with the prediction obtained from VMD mentioned in the text[53].

Goloskokov and Kroll [56]. In this model a non-leading twist asymmetry arises from the interference between the dominant GPD H_g and the helicity-dependent GPD $\tilde{H}_g$ and is estimated to be of the order $k_T^2 \tilde{H}_g/(Q^2 H_g)$, where k_T is the transverse momentum of the quark and the anti-quark. In the domain of validity of this model ($Q^2 > 2\,(\mathrm{GeV}/c)^2$ and $x_{bj} < 0.2$) our result implies that $\tilde{H}_g$ is small with respect to H_g .

4.3.2   Transverse target spin asymmetry

The cross section of the exclusive ρ^0 production off a transversely polarized nucleon is a function of the usual kinematical variable (x_{Bj}, Q^2, t) and of two angles: ϕ_h is the azimuthal angle between the leptonic and the hadronic planes and ϕ_S is the azimuthal angle of the target spin vector around the virtual photon direction as shown in figure 4.11. Data were taken using transversely polarized deuteron and proton targets in 2004 and 2007 respectively. From this data, one can measure an azimuthal asymmetry around the direction of polarization. This observable called Transverse Target Spin Asymmetry is sensitive to the GPD E provided that the factorization domain is reached.
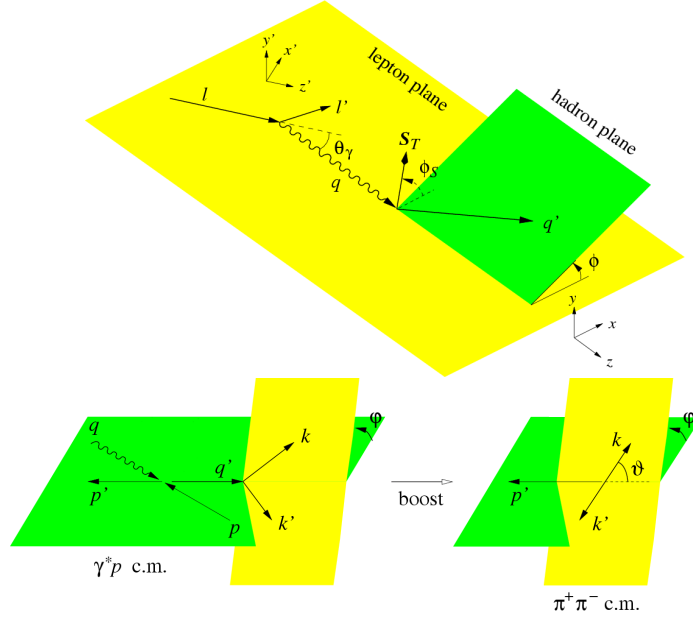
Figure 4.11: Definition of the angles relevant to the description of the exclusive ρ^0 production off a transversely polarized target (taken from ref. [58]).

Formalism

We moved from the Schilling-Wolf formalism to the recently developed formalism proposed by M. Diehl and S. Sapeta[58]. Note that unfortunately the variable names describing the angles have changed and one should now refer to the definitions given in figure 4.11($\Phi \to -\phi$, $\phi \to \varphi$, $\theta \to \vartheta$). In this[11] formalism, the spin-dependent photo-absorption cross section and interference terms, σ_{mn}^{ij}, can be expressed in terms of the amplitudes $\mathcal{A}_m^i$ and $\mathcal{A}_n^j$ for the interaction of a photon of helicity m (n) and a nucleon of helicity i (j):

$$\sigma_{mn}^{ij}(x_{Bj}, Q^2, t) \propto \sum_{\text{spins}} (\mathcal{A}_m^i)^* \mathcal{A}_n^j$$

The only leading-twist observables are the longitudinal cross section σ_{00}^{++} and the interference term σ_{00}^{+-} which can be related to the Compton Form Factors [59]. For the longitudinal cross section, we have :

$$\frac{d\sigma_{00}^{++}}{dt} = (1 - \xi^2)\, |\mathcal{H}_M|^2 - (\xi^2 + \frac{t}{4M_p^2})\, |\mathcal{E}_M|^2 - 2\xi^2 Re(\mathcal{E}_M^* \mathcal{H}_M)$$

In the COMPASS domain, $\xi = x_{Bj}/(2 - x_{Bj})$ is of the order of a few 10^{-2} and t is smaller than M_p therefore only the first term has a sizable value and $\frac{d\sigma_{00}^{++}}{dt}$ is mainly sensitive to $|\mathcal{H}_M|^2$. And for the interference term, we have :

$$\frac{d\sigma_{00}^{+-}}{dt} = -\sqrt{1 - \xi^2}\, \frac{\sqrt{t_0 - t}}{M_p} Im(\mathcal{E}_M^* \mathcal{H}_M)$$

which shows explicit sensitivity to $\mathcal{E}_M$.

The lepton photon 5-fold differential cross section for a transversely polarized target has a complex harmonic structure depending upon linear combinations of the angles ϕ (the angle between the leptonic and hadronic planes) and ϕ_S (the angle between the leptonic plane and the polarization vector) and θ_γ (the angle between the virtual photon and the incoming lepton):

$$
\left[\frac{\cos\theta_\gamma}{1-\sin^2\theta_\gamma\,\sin^2\phi_S}\right]^{-1}\left[\frac{\alpha_{\text{em}}}{8\pi^3}\frac{y^2}{1-\epsilon}\frac{1-x_B}{x_B}\frac{1}{Q^2}\right]^{-1}\frac{d\sigma}{dx_B\,dQ^2\,d\phi\,d\phi_S}= \tag{4.16}
$$

$$
\frac{1}{2}(\sigma^{++}_{++}+\sigma^{--}_{++})+\epsilon\,\sigma^{++}_{00}-\epsilon\cos(2\phi)\,\mathrm{Re}\sigma^{++}_{+-}-\sqrt{\epsilon(1+\epsilon)}\,\cos\phi\,\mathrm{Re}(\sigma^{++}_{+0}+\sigma^{--}_{+0})
$$

$$
-\frac{P_T}{\sqrt{1-\sin^2\theta_\gamma\,\sin^2\phi_S}}\left[\sin\phi_S\,\cos\theta_\gamma\,\sqrt{\epsilon(1+\epsilon)}\,\mathrm{Im}\sigma^{+-}_{+0}\right.
$$

$$
+\sin(\phi-\phi_s)\,(\cos\theta_\gamma\,\mathrm{Im}(\sigma^{+-}_{++}+\epsilon\,\sigma^{+-}_{00})+\frac{1}{2}\sin\theta_\gamma\,\sqrt{\epsilon(1+\epsilon)}\,\mathrm{Im}(\sigma^{++}_{+0}-\sigma^{--}_{+0}))
$$

$$
+\sin(\phi+\phi_s)\,(\cos\theta_\gamma\,\frac{\epsilon}{2}\,\mathrm{Im}\sigma^{+-}_{+-}+\frac{1}{2}\sin\theta_\gamma\,\sqrt{\epsilon(1+\epsilon)}\,\mathrm{Im}(\sigma^{++}_{+0}-\sigma^{--}_{+0}))
$$

$$
+\sin(2\phi-\phi_s)\,(\cos\theta_\gamma\,\sqrt{\epsilon(1+\epsilon)}\,\mathrm{Im}\sigma^{-+}_{+0}+\frac{1}{2}\sin\theta_\gamma\,\epsilon\,\mathrm{Im}\sigma^{++}_{+-})
$$

$$
+\sin(2\phi+\phi_s)\,\frac{1}{2}\sin\theta_\gamma\,\epsilon\,\mathrm{Im}\sigma^{++}_{+-}
$$

$$
\left.+\sin(3\phi-\phi_s)\,\cos\theta_\gamma\,\frac{\epsilon}{2}\,\mathrm{Im}\sigma^{-+}_{+-}\right]
$$

$$
+\text{ terms dependent on the lepton polarization }P_\ell.
$$

Therefore, measuring the angular distribution for exclusive ρ^0 production in a complete set of angles allows to fully describe the process. The magnitude of the $\sin(\phi-\phi_S)$ modulation of the angular distribution is :

$$
A^{\sin(\phi-\phi_S)}_{UT}(\phi,\phi_S)\sim\frac{Im(\sigma^{+-}_{++}+\varepsilon\sigma^{+-}_{00})}{\frac{1}{2}(\sigma^{++}_{++}+\sigma^{--}_{++})+\varepsilon\sigma^{++}_{00}}
$$

It has some sensitivity to σ^{++}_{00} and σ^{+-}_{00} and is a good case for exploratory measurements using the COMPASS data taken with a transversely polarized target.

Experimental procedure

The data were taken with target cells polarized in opposite directions simultaneously. The number of registered events in the upstream (N_u) and downstream (N_d) cells can be written :

$$
\begin{aligned}
N^{\uparrow}_u(\phi-\phi_S) &= Fn_u a^{\uparrow}_u(1+f\cdot P_t\cdot A_{UT}\sin(\phi-\phi_S))\\
N^{\downarrow}_d(\phi-\phi_S) &= Fn_d a^{\downarrow}_d(1-f\cdot P_t\cdot A_{UT}\sin(\phi-\phi_S))
\end{aligned}
$$

where the arrow refers to the polarization of the target cell, F is the beam flux, $n_{u,d}$ is the number of scattering centers in the upstream and downstream cells, $a_{u,d}$ is the acceptance for the exclusive ρ production from the upstream and downstream cells, f is the dilution factor and P_t is the target polarization. The number of scattering centers in a given cell is assumed to be constant and the flux in the two target cells can be equalized by applying selection criteria on the incoming beam tracks. Target polarization is also assumed to be constant for the sake of legibility. Therefore only the effects of acceptance remains. After a polarization reversal the number of events can be expressed as :

$$
\begin{aligned}
N_u^\downarrow(\phi - \phi_S) &= F' n_u a_u^\downarrow (1 - f \cdot P_t \cdot A_{UT} \sin(\phi - \phi_S)) \\
N_d^\uparrow(\phi - \phi_S) &= F' n_d a_d^\uparrow (1 + f \cdot P_t \cdot A_{UT} \sin(\phi - \phi_S))
\end{aligned}
$$

where we have allowed the flux to be different. If one further makes the reasonable assumption that the ratio of acceptance between the upstream and downstream cell remains constant after the polarization is reversed :

$$
\frac{a_u^\uparrow}{a_d^\downarrow} = \frac{a_u^\downarrow}{a_d^\uparrow}
$$

Then the "double ratio" of counting rates allows to directly access the transverse target spin asymmetry, A_{UT}, without having to estimate the acceptance :

$$
\frac{N_u^\uparrow N_d^\uparrow}{N_u^\downarrow N_d^\downarrow} = \left[\frac{1 - f \cdot P_t \cdot A_{UT} \sin(\phi - \phi_S)}{1 + f \cdot P_t \cdot A_{UT} \sin(\phi - \phi_S)} \right]^2
$$

The results obtained on A_{UT} for deuterons and protons [57] are shown in figure 4.12 as a function of Q^2 and x_{bj} and are found to be compatible with 0. The interpretation and comparison with the HERMES data will be discussed at the end of this chapter.

4.4 Improvements in the analysis

The ultimate goal of the analysis of the exclusive production of ρ^0 is to separate the longitudinal and transverse contributions and hence to single out the longitudinal cross section σ_{00}^{++} and the interference σ_{00}^{+-}. It was demonstrated by Diehl and Sapeta that the $\cos\theta$ angular distribution (after integration over φ, the azimuthal angle of the pions with respect to the hadronic plane) of each σ_{mn}^{ij} can be decomposed into a longitudinal and a transverse ρ polarization components :

$$
\frac{d\sigma_{mn}^{ij}(\gamma^* p \to \rho p)}{d(\cos\theta)} = \frac{3\cos^2\theta}{2} \sigma_{mn}^{ij}(\gamma^* p \to \rho_L p) + \frac{3\sin^2\theta}{4} \sigma_{mn}^{ij}(\gamma^* p \to \rho_T p) \qquad (4.17)
$$
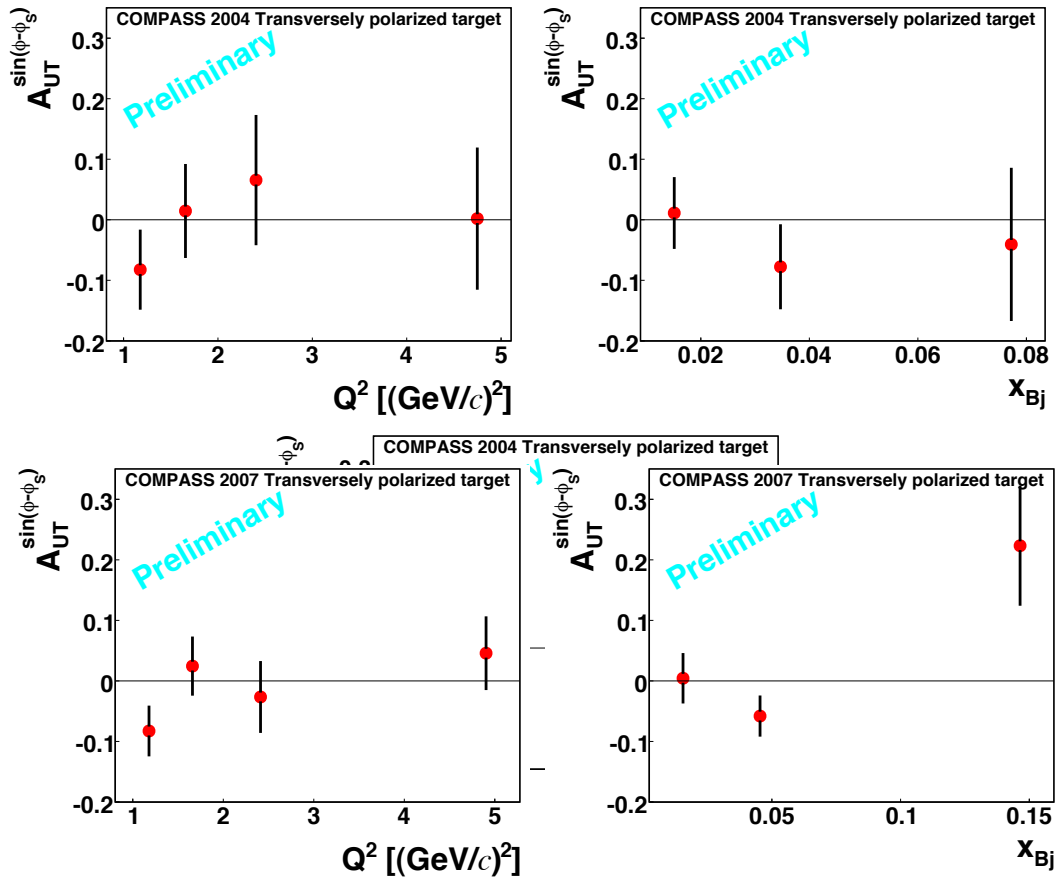
Figure 4.12: Transverse target spin asymmetry in exclusive ρ^0 production off the deuteron (top) and off the proton (bottom) as a function of Q^2 and x_{Bj}.
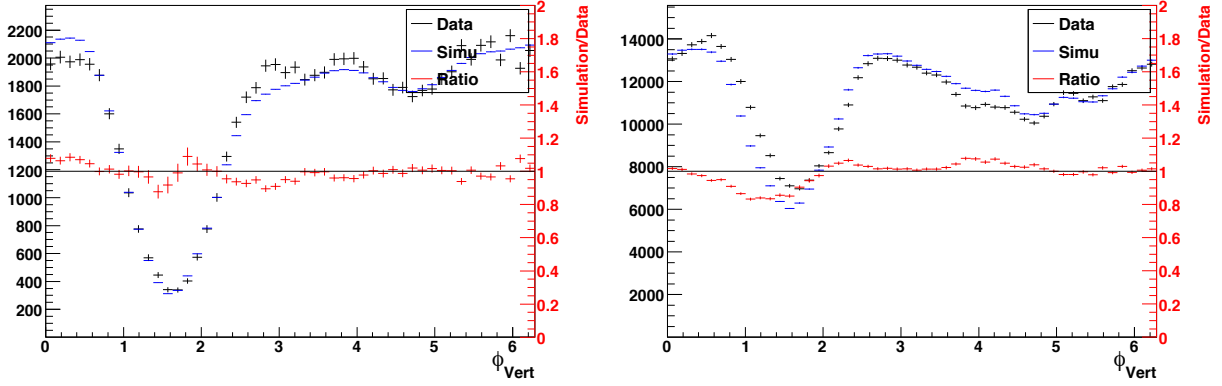
FIG. 5.8 – Comparaison des données mesurées (Noir) et des données simulées reconstruites
Figure 4.13: Comparison of data and Monte-Carlo distributions in the angle ϕ_{vert} for
après pondération (Bleu). Le rapport "données simulées" sur "données mesurées" figure en
2004 (left) and 2007 (right).
rouge. À gauche 2004, à droite 2007.

If in addition s-channel helicity conservation is valid then we have :
des effets de *smearing*. En effet, la distribution physique est très piquée à , à
cause de la résolution du spectromètre, la distribution reconstruite en masse invariante est
moins piquée. C'est pourquoi la fonction de correction diminue en (fig.5.11).
Les distributions physiques influent donc sur l'*acceptance* généralisée.

$$\sigma_{00}^{ij}(\gamma^* p \to \rho_L p) = \sigma_{00}^{ij}$$

and the terms σ_{TL}^{++} and σ_{TL}^{+-} can be extracted from the data. To perform this measure-
Les figures 5.16, 5.17 et 5.18 montrent la fonction d'*acceptance* généralisée à une dimen-
ment, an estimation of the multi dimension acceptance function in the angular variables
sion.
$(\cos\theta, \phi, \phi_S)$ is mandatory.

This work along with the estimation of the non-exclusive background, has been the
core subject of the thesis of G. Jegou [42] and is described here.

4.4.1 Study of acceptance

The multi dimension acceptance was estimated using the DIPSI event generator and the
Geant simulation program of the COMPASS experiment. The acceptance is determined
as a function of 8 variables :

$$\cos\theta, \phi, \phi_S, \varphi, x_{bj}, Q^2, p_t^2, z_{\text{vertex}}$$

with between 2 and 8 bins in each variable resulting in up to 400 000 bins. The ac-
ceptance function includes geometric effects, detector efficiency and smearing due to
detectors resolution. The generated sample is re-weighted such that the MC distri-
bution reproduces best the data. This re-weighting is performed using the x_{bj}, Q^2, p_t^2
distributions and guarantees that smearing effects are treated correctly. The quality
of the reproduction is shown in figure 4.13 as a function of the azimuthal angle of the
outgoing meson with respect to the beam axis, ϕ_{vert}.

After the re-weighting has been performed, the acceptance functions are extracted
from the Monte-Carlo. In figure 4.14, we have represented the variations of the ac-
ceptance for the pair of variables (φ, ϕ). For instance, it shows that the acceptance
is minimum for $\phi = -\varphi \,(\text{mod}\,\pi)$ corresponding to configurations were the muon and
the pions are in the same plane and that variations of the order of 20% are observed.
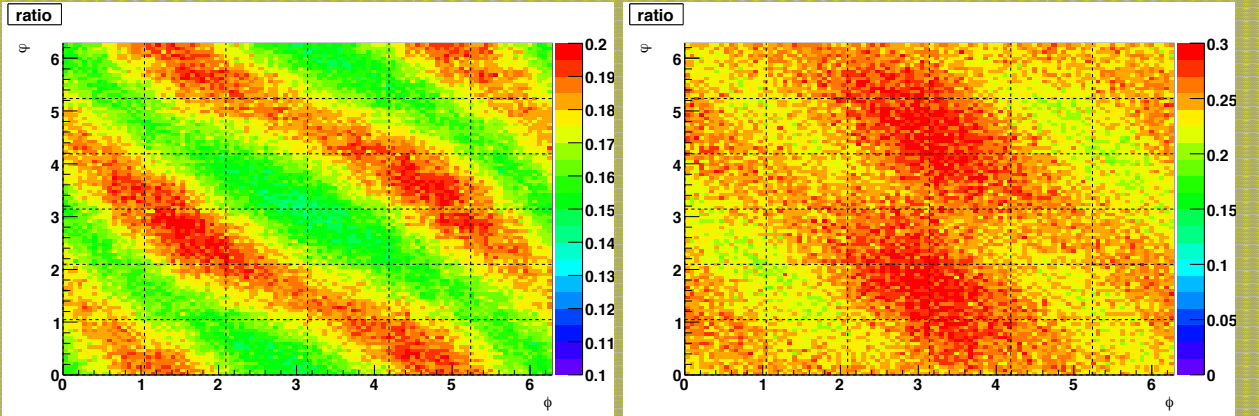
Figure 4.14: Acceptance function versus ϕ_{vert} for 2004 (left) and 2007 (right) and a 2-D variations of the acceptance for the pair of variables (φ, ϕ).

It demonstrates that the multi-variable acceptance determination is important even if variables are integrated out in the extraction of physics observables as it is the case for φ. One should also note that this correlation tends to disappear in 2007 after the large acceptance magnet was installed.

The quality of the acceptance determination can also be estimated by comparing the result content close the kinematic $d\nu_T$ obtained with the fit of the angular production exclusive de ρ.

4.4.2 Study of the non-exclusive background

The non-exclusive background contribution varies noticeably over the kinematical domain of the experiment and on the experimental set-up. In figure 4.17, we have represented the E_{miss} distributions in bins of Q^2 and p_t^2 for 2007 data. The exclusive signal is parametrized with a Gaussian distribution centered at 0 :

$$D_{excl} = \alpha_{excl} \, 87 \, e^{\frac{E_{\mathrm{miss}}^2}{2\sigma_{excl}^2}} \tag{4.18}$$

and the resolution, σ_{excl}, is fitted on the Monte-Carlo. The aim of these studies is to determine the amount of background under the exclusive peak in the region : $-2.5 < E_{\mathrm{miss}} < 2.5\,\mathrm{GeV}$, where they obviously cannot be disentangled on an event-by-event basis. In the first analysis, a crude method using a polynomial fit on the sideband was performed but was abandoned since it had no physics grounds.

The background was then studied using Monte-Carlo simulations. A set of unbiased deep inelastic scattering events was generated using the PYTHIA event generator [39] and the process involved was recorded. In PYTHIA, exclusive production of mesons and diffractive dissociation are also parametrized but the yields are different than the data and were not considered in this study. The events are then propagated in the COM-

dans la figure 6.17 en fonction des variables   et   .
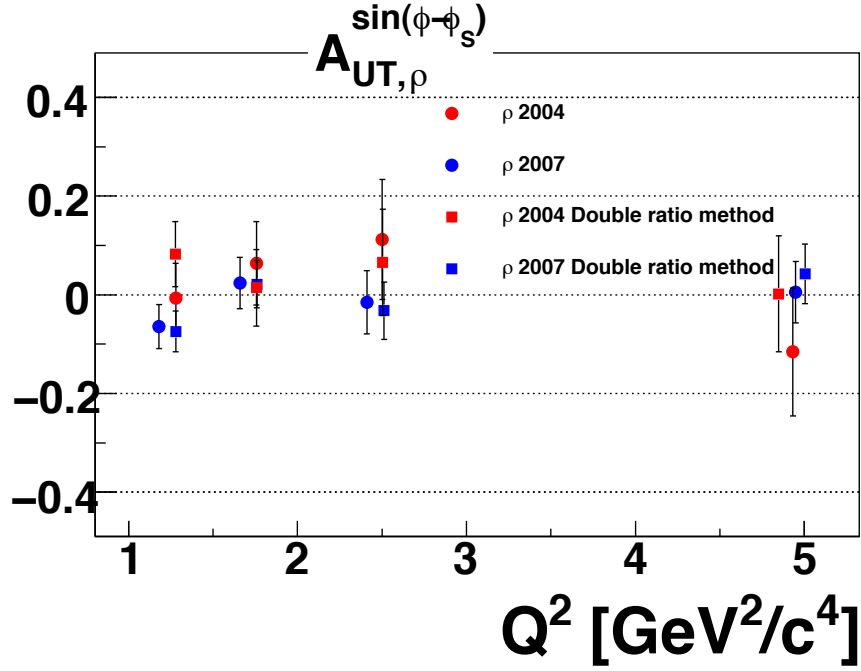
Figure 4.15: Comparison of method of extraction of the transverse target spin asymmetry A_{UT} (background subtraction not done)

FIG. 6.17   extrait par 2 méthodes : 1) méthode
des distributions angulaires   avec correction d'acc
bruit de fond, (les données 2004 ne sont pas corrigées en
avec la méthode des *Double Ratio*.)

PYSS Geant simulation program and reconstructed using the standard reconstruction program. Then, they undergo the same selection criteria as the real data.

The shape of the E_{miss} distribution of DIS tagged background events is fitted on the Monte-Carlo using an ad-hoc parametrization composed of two Fermi functions, one describing the rising part of the distribution and one for the falling part :

6.3.2
$$D_{\mathrm{non-excl}}(E_{\mathrm{miss}}) = \alpha_{non-excl}\left[1 - \frac{\text{mesurée}}{\sqrt{1 + e^{\frac{E_{\mathrm{miss}}-\mu_1}{\sigma_1}}}}\right] \cdot \left[\frac{\text{par la méthode des}}{\sqrt{1 + e^{\frac{E_{\mathrm{miss}}-\mu_2}{\sigma_2}}}}\right] \quad (4.19)$$

where the parameters μ_1, σ_1, μ_2, σ_2 are determined for each bin separately. Example

Comme dans la section 6.2 nous considérons les distribu
que l'on sait corriger de l'acceptance
Soit les distributions angulaires sont analysées en

of these fits are shown for three bins in Q^2 (and for a given p_t interval). In the analysis performed it is needed to estimate the background shape in 3-dimension bins and there is a limitation due to MC statistics. Furthermore, the systematic error from the background subtraction could be large and cannot be estimated. So, an estimation of a systematic uncertainty of 5% for the 2-dimension background estimation is assumed.

The E_{miss} distribution presents a tail for negative values which could not be reproduced by resolution effects. It was demonstrated that these events, which represent 10% of the data, are due to a wrong assignment of the beam momentum to the beam track. Under these assumptions the beam momentum is randomly drawn in the normal

afin d'extraire les 3 contributions   ,

beam momentum distribution. It is then modeled as the convolution of the exclusive

respectivement les   longitudinaux, d'interférence et t
variables angulaires   et   réalisée par la correction de

FIG. 5.23 – Détermination de la forme   sur les distributions en   des événements simulés de première catégorie. Les quatre figures correspondent aux quatre bins en   pour
GeV   .
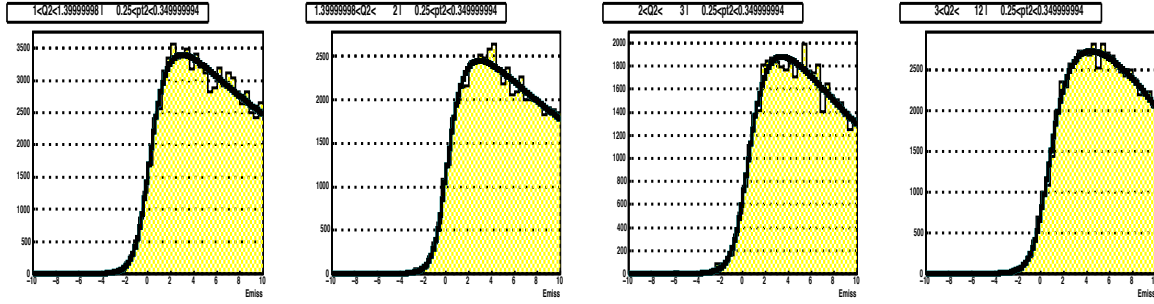
Figure 4.16: E_{miss} distribution of Monte-Carlo DIS tagged background events as a function of Q^2 and fitted using the ad-hoc parametrization described in the text.

FIG. 5.24 – Détermination de la forme   Monte-Carlo   sur les distributions en   des événements simulés de troisième catégorie. Les quatre figures correspondent aux quatre bins en   pour
GeV   .

and background distributions convoluted by the beam profile of width $\sigma_E \simeq 5$ GeV:

$$D_{mom}(E_{\text{miss}}) = \alpha_{mom} \left[\alpha_{\text{non-excl}} D_{\text{non-excl}}(E_{\text{miss}}) + \alpha_{\text{excl}} D_{\text{excl}}(E_{\text{miss}}) \right] \otimes e^{\frac{E_{\text{miss}}^2}{2\sigma_E^2}} \qquad (4.20)$$

It receives contribution from both signal and background and although the fraction of signal could have been derived it was preferred not to retain it in the exclusive sample.

The total function which is fitted on the data is then:

$$D(E_{\text{miss}}) = \alpha_{\text{non-excl}} D_{\text{non-excl}}(E_{\text{miss}}) + \alpha_{\text{excl}} D_{\text{excl}}(E_{\text{miss}}) + \alpha_{mom} D_{\text{mom}}(E_{\text{miss}}) \qquad (4.21)$$

The contribution of diffractive dissociation could not be included in the fit function due to convergence problems. Studies have shown that it contributes mostly to the exclusive peak and more work is required to take it properly into account.

The quality of the background subtraction procedure can be evaluated using the extraction of the spin density matrix elements. In figure 4.18, we have represented the value of the combination $u_{++}^{00} + \epsilon \, u_{00}^{00} \equiv r_{00}^{04}$ as a function of Q^2 for various sets of data with and without background subtraction. It shows that, before background subtraction, the results for this observable for 2004 and 2007 are incompatible because data were taken with different set-ups (blue and red squares). After background subtraction (blue and red circles), the two data sets are compatible within statistical errors over the full range Q^2.

4.4.3   Results

In figure 4.19 (top row), we have represented the result obtained for the transverse target spin asymmetry A_{UT} as a function of Q^2 and p_t^2. Our result points towards small values of the asymmetry for both deuteron (2004 data set) and proton (2007 data set) targets. At transfer $t = 0$, the GPD E is related to the anomalous magnetic moment of the proton or the neutron as a consequence of equation 1.42:

$$\int E^p(x, \xi = 0, t = 0) = \kappa^p = 1.79 \qquad (4.22)$$
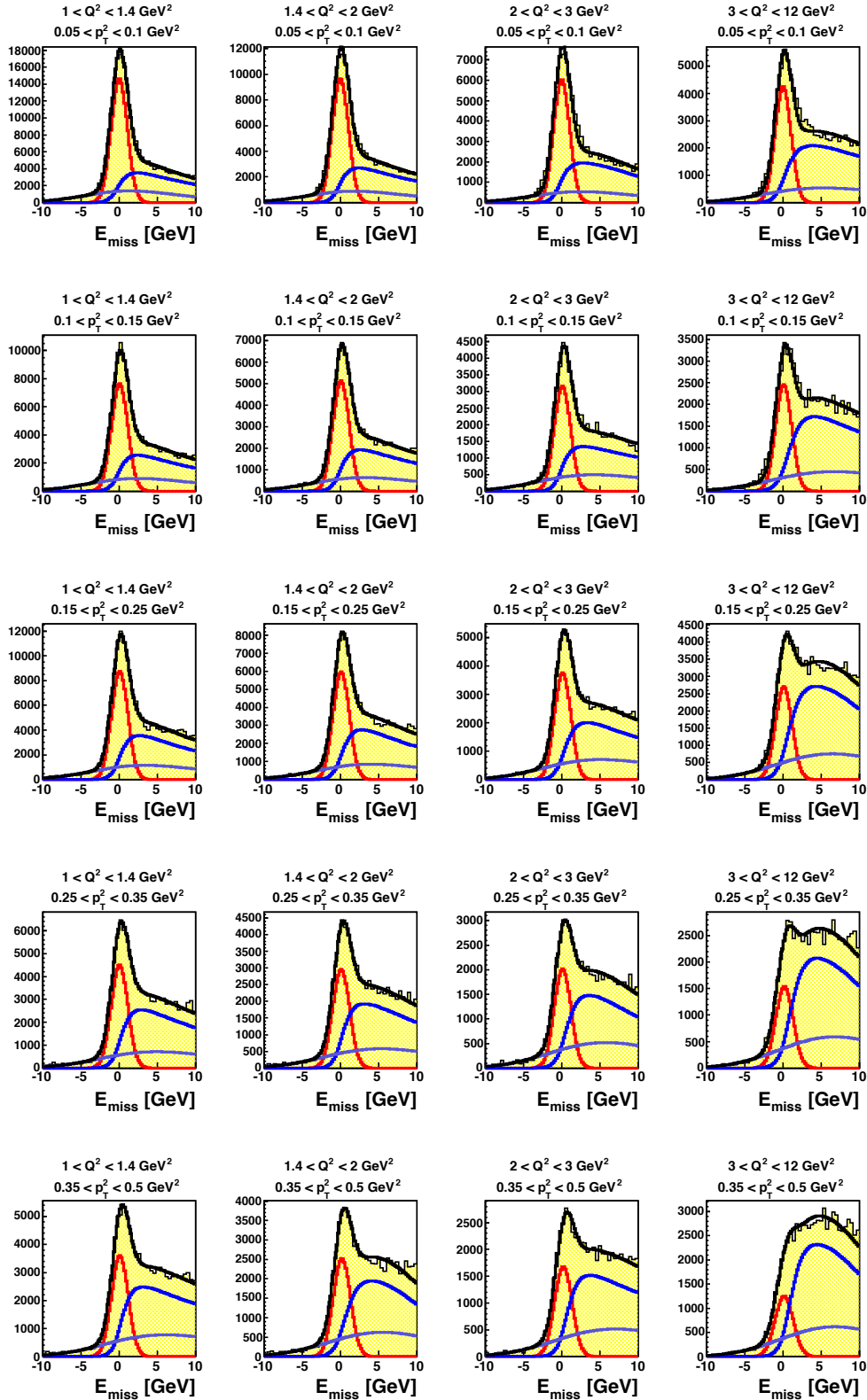
Figure 4.17: E_{miss} distributions in bins of Q^2 and p_T^2. The filled histogram is the data and the black curve is the fit to the data. The red curve is the exclusive signal, the blue curve is the non-exclusive background and the green curve is the misidentifiaction of the muon momentum.

FIG. 5.24 – Ajustement de la fonction totale de bruit au fond sur les données en fonction de et en 2004.

90
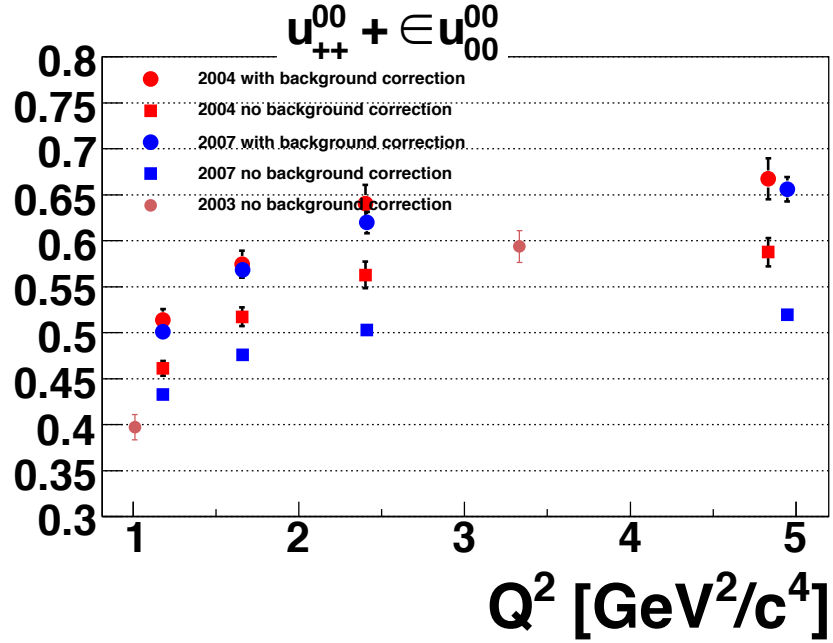
Figure 4.18: Measurement of the combination of spin density matrix elements : $u_{++}^{00} + \epsilon\, u_{00}^{00}\, (\equiv r_{00}^{04})$ as a function of Q^2 for various sets of data with and without background subtraction.

$$\int E^n(x, \xi = 0, t = 0) = \kappa^n = -1.91 \tag{4.23}$$

Then the integral of the GPD E for the deuteron is of the order of $\kappa^p + \kappa^n$ and is expected to be small as observed in the data.

To understand the proton results one can make the assumption that only u and d quarks contribute. In this case, the equations 4.22 and 4.23 imply that $E^u \sim -E^d$. Due to the ρ meson wave function (see equation 1.53), the asymmetry for the proton is sensitive to:

$$\tfrac{2}{3}E^u + \tfrac{1}{3}E^d \sim \tfrac{1}{3}E^u$$

and is also expected to be small.

The second and third rows of figure 4.19 show our results on the separation of longitudinal and transverse polarization components. For these, one has to use 3-dimension estimations of the non-exclusive background for which the systematic error is higher and shows the present limitation of our method. To overcome this issue, it would be needed to simulate an order of magnitude more events than is presently done. The method would also benefit from a parametrization of this 3-D background which would allow to smooth out the statistical fluctuations. Ultimately, data taking with a recoil detector allowing to tag the proton in the final state will allow to apply further selection criteria to ensure better exclusivity. This program is part of the proposal of future COMPASS measurements.

The results are compared to a prediction using the model of exclusive mesons production of Goloskokov and Kroll [60]. This model is based on the double distribution

ansatz for the GPDs and transverse momentum effects as well as gluons contributions are taken into account. The asymmetry predicted in this model is close to 0 in agreement with our measurement. This model predicts also a much bigger asymmetries for the production of ω and ρ^+ (ω : $\frac{2}{3}E^u$-$\frac{1}{3}E^d$ and ρ^+ : E^u-E^d) but these channels could not be accessed either due to a high non-exclusive background or due to statistics.

The result on the same observable as obtained by the HERMES collaboration is represented in figure 4.20. It is in agreement with our measurement and the statistical precision on A_{UT} is similar. Nevertheless, HERMES extraction of the longitudinal and transverse contribution suffers less uncertainty and a value consistent with 0 is obtained for both contributions.
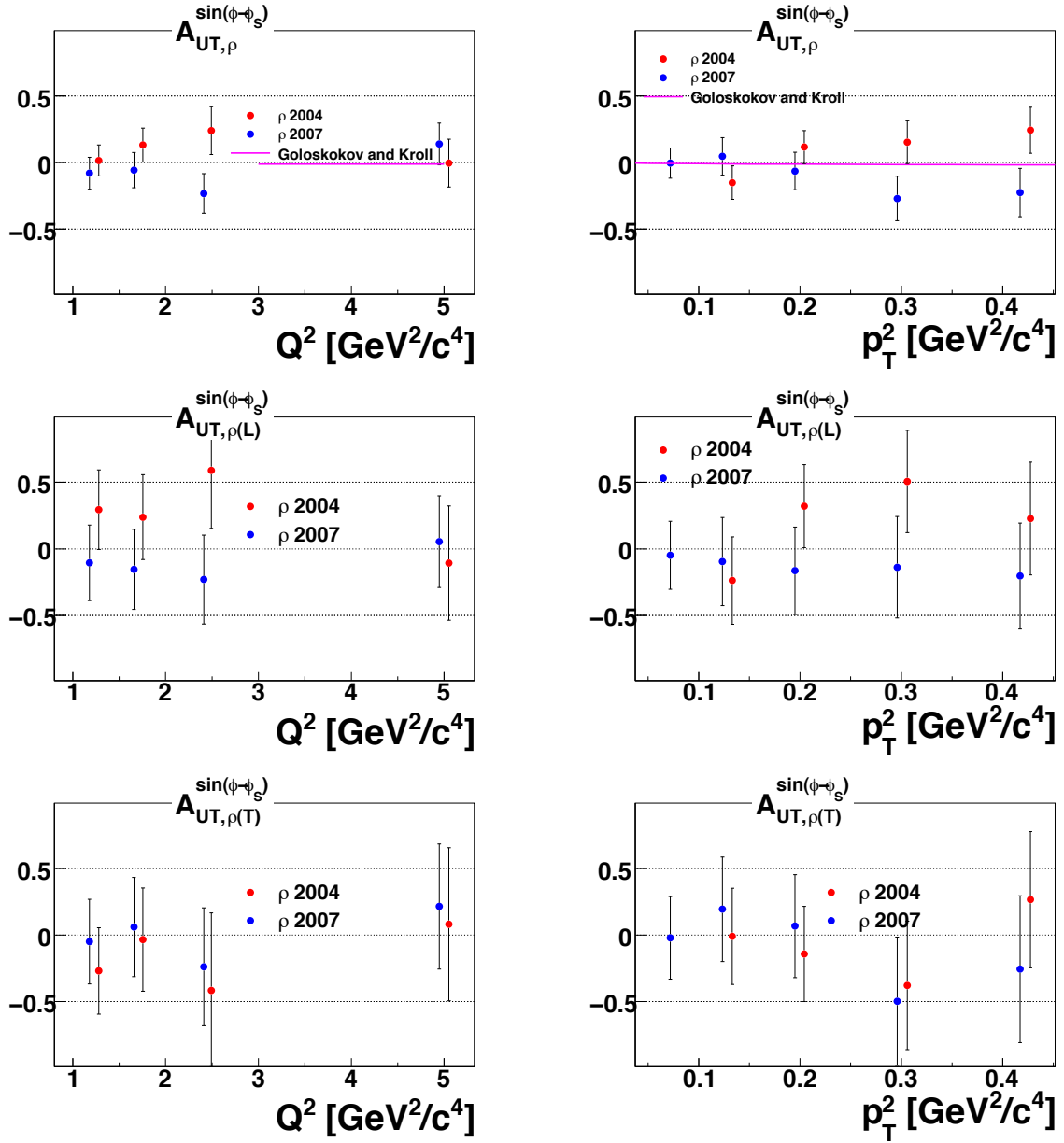
FIG. 6.18 – Figure 4.19: Results of A_{UT} from COMPASS on a deuteron target (2004 data set) and de longitudinaux au milieu, de transverses en bas. Cette détermination est basée sur on a proton target (2007 data set) and separation of the longitudinal and transverse l'analyse des distributions angulaires et avec correction d'accep- components. tance et bruit de fond. Les données 2004 sont corrigées d'un décalage de 1 GeV sur le muon incident.

La figure 6.17 montre le résultat en fonction de et par cette méthode avec l'analyse des distributions angulaires (intégrées en), corrigée de l'acceptance mais non du bruit de fond. A priori ce résultat doit être similaire à celui obtenu par la méthode des *Double Ratio* où la correction d'acceptance est faite naturellement par construction de ce

Figure 4.20: Results of the HERMES experiment for A_{UT} on a proton target and separation of the longitudinal and transverse components.

Chapter 5

Future DVCS measurement at COMPASS

In this chapter, we describe the future experiment which could be performed using the COMPASS spectrometer at the CERN SPS [61] in order to measure the generalized parton distributions through the Deeply Virtual Compton Scattering process[1]. We will first review the decomposition of the cross section of the exclusive photon muo-production and show how data taken with positive and negative incoming lepton charge can be combined to measure Compton form factors. We present all the observables and the projection of errors using GPD models and a simulation of the experimental set-up equipped with a recoil detector. Then, we will present the experimental studies which were conducted in order to demonstrate the feasibility of the DVCS measurement program at COMPASS.

5.1   Experimental considerations

The experimental set-up of the COMPASS experiment provides solid grounds for the measurement of the DVCS process as well as hard exclusive meson production. Given the energy of 160 GeV of the muon beam it opens a wide range in the x_{bj}-Q^2 domain as shown in figure 5.1. COMPASS can then explore a region from $x_{bj} \sim 0.005$ where the gluons and sea quarks are dominating up to $x_{bj} \sim 0.1$ where contributions from valence quarks take over. This domain is presently uncharted and COMPASS will allow to bridge the gap between high energy collider experiments such as ZEUS and H1 [64] and lower energy fixed target published experiments (HERMES [66], JLab-CLAS [67], JLab-Hall A [68]) and future projects (JLab 12 GeV upgrade [62]). The range in Q^2 which can be accessed is limited by the luminosity and reaches from 8 to 10 $(\text{GeV}/c)^2$ with the current beam intensity in order to collect enough statistics for DVCS study. The experiment will use the maximum available beam intensity of 4.10^8 muons per SPS spill with a cycle length of 48 seconds. The COMPASS set-up needs to be complemented in order to perform the DVCS measurement. The scattering will take

---

[1]of course at the same time, Hard Exclusive Meson Production will be also investigated
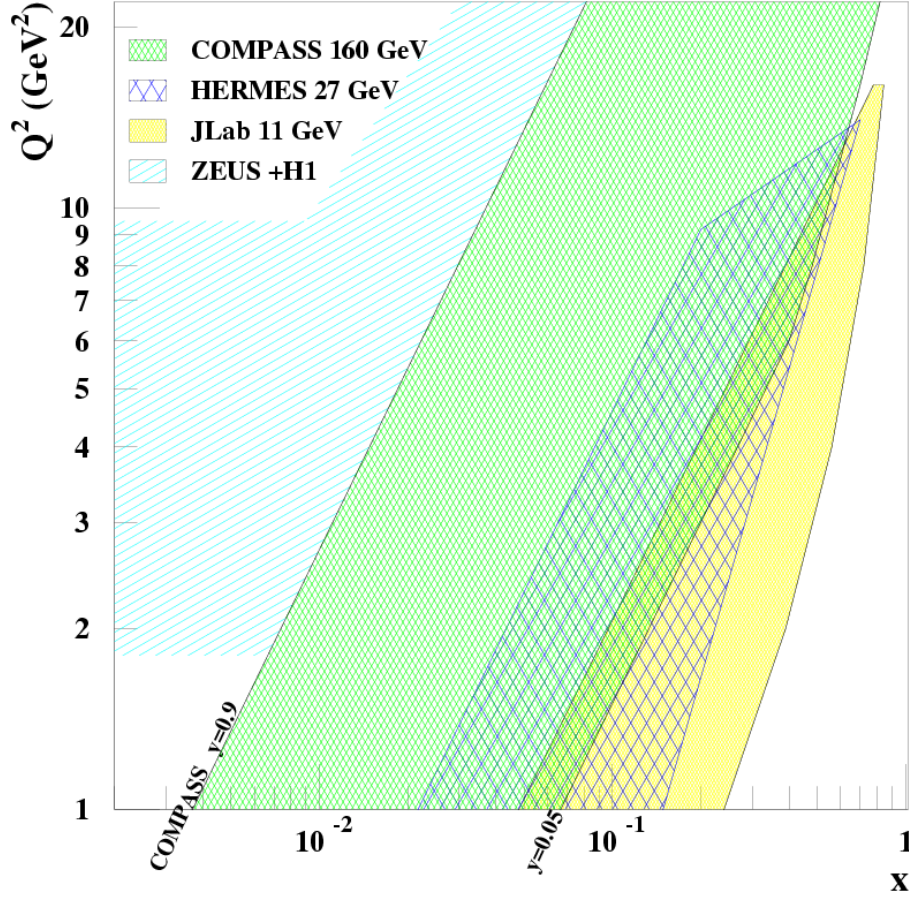
Figure 5.1: Kinematical domain in x_{bj} and Q^2 accessible by the COMPASS experiment.

place in a 2.5 meter long liquid hydrogen target surrounded by a recoil proton detector composed of two concentric barrels of plastic scintillators. The scattered muons will be detected in the spectrometer trackers and the outgoing photon in the electromagnetic calorimeters. The calorimeter coverage will have to be extended at large polar angle by an additional calorimeter in order to enlarge the x_{bj}-Q^2 domain accessible, to flatten the acceptance and to better detect photons from a possible exclusive π^0 contamination. In the projections of errors of future measurements, we consider a standard two-year running period with a global efficiency of 10%. This standard running period includes 1/4 of positive muon running and 3/4 of negative muon running which can be done with only 1/3 of the positive muon intensity. The efficiency includes detectors and tracking efficiencies, SPS and COMPASS availabilities and DAQ and veto dead-times.

5.2   Exclusive photon cross section

The process of exclusive muo-production of one photon off a proton, $\mu P \rightarrow \mu P \gamma$, receives contributions from the Deeply Virtual Compton Scattering (DVCS) and from the Bethe-Heitler (BH) processes as shown in figure 5.2. The cross section for this
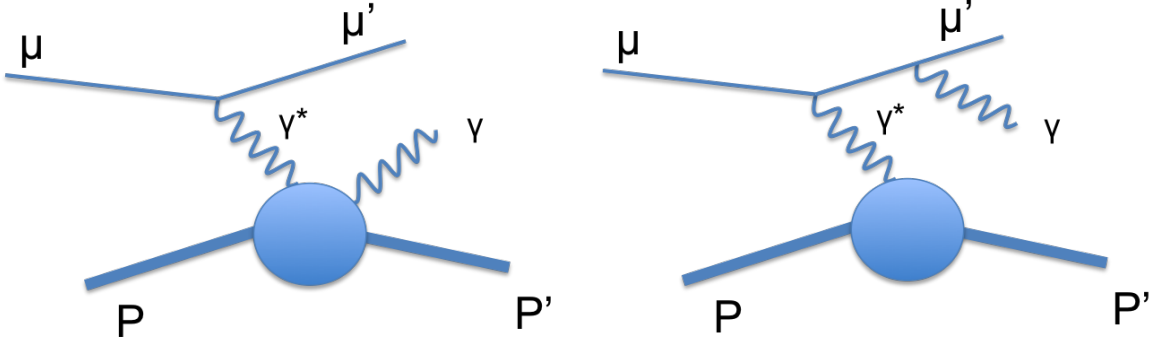
Figure 5.2: Processes contributing to exclusive photon production : Deeply Virtual Compton Scattering (left) and Bethe-Heitler (right). In the case of Bethe-Heitler, the photon can also be radiated by the incoming lepton line.
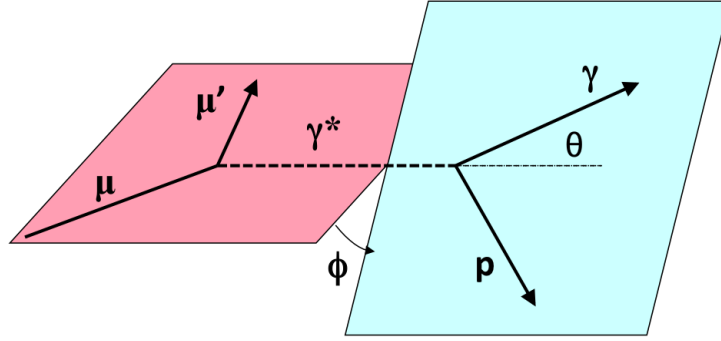

Figure 5.3: Definition of the angle ϕ between the leptonic and hadronic planes.

process is then the sum of the pure BH and DVCS contributions and of their interference since both processes have the same final state :

$$d\sigma(\quad \mu P \to \mu P \gamma \quad) \propto |T_{BH}|^2 + |T_{DVCS}|^2 + T_{DVCS}^* T_{BH} + T_{DVCS} T_{BH}^* \qquad (5.1)$$

In the case of COMPASS, as envisaged in this study, the muon beam is polarized and the target is unpolarized (at a later stage we are also considering using a transversely polarized target). The cross section can be expressed in terms where the sensitivity to the beam charge, e_μ, and beam polarization, P_μ, are mentioned explicitly:

$$\frac{d^4\sigma(\mu p \to \mu p \gamma)}{dx_{Bj} dQ^2 d|t| d\varphi} = d\sigma_{BH} + [d\sigma_{DVCS}^{unpol} + P_\mu d\sigma_{DVCS}^{pol}] + e_\mu[\Re\mathfrak{e}I + P_\mu \Im\mathfrak{m}I] \qquad (5.2)$$

It is important to note that the contribution of the interference term changes sign when the charge of the beam is changed. This property will permit to isolate the interference term unambiguously. Further decomposition can be performed [18] using the dependence of the different contributions with respect to the azimuthal angle between the leptonic and the hadronic planes, ϕ, as described in figure 5.3. The pure

Bethe-Heitler term reads :

$$d\sigma_{BH} = \frac{\Gamma(x_{bj}, Q^2, t)}{P_1(\phi)P_2(\phi)} \left(c_0^{BH} + c_1^{BH}\cos\phi + c_2^{BH}\cos 2\phi\right) \tag{5.3}$$

where the function $\Gamma(x_{bj}, Q^2, t)$ depends on the nucleon form factors and $P_1(\phi)$ and $P_2(\phi)$ are kinematical terms representing the well known BH propagators involving $\cos n\phi$ terms. The coefficients c_i^{BH} are related to helicity amplitudes which can also be calculated in QED. Then, the unpolarized and polarized DVCS terms read

$$d\sigma_{DVCS}^{unpol} = \frac{e^6}{y^2 Q^2}\left(c_0^{DVCS} + \{c_1^{DVCS}\cos\phi + c_2^{DVCS}\cos 2\phi\}\right) \tag{5.4}$$

$$d\sigma_{DVCS}^{pol} = \frac{e^6}{y^2 Q^2}\left(\{s_1^{DVCS}\sin\phi\}\right) \tag{5.5}$$

where the terms enclosed in brackets are either higher-twist or higher-order effects. Finally, the interference terms involving the real and imaginary part of the DVCS amplitude are :

$$\mathfrak{Re}I = \frac{e^6}{x_{Bj}y^3 t P_1(\phi)P_2(\phi)}\left(c_0^I + c_1^I\cos\phi + \{c_2^I\cos 2\phi + c_3^I\cos 3\phi\}\right) \tag{5.6}$$

$$ImI = \frac{e^6}{x_{Bj}y^3 t P_1(\phi)P_2(\phi)}\left(s_1^I\sin\phi + \{s_2^I\sin 2\phi\}\right). \tag{5.7}$$

Using this harmonic decomposition and equation 5.2, it is possible to construct observables which will permit to isolate the different contributions. With the M2 muon beam available at COMPASS the most favorable configuration is to reverse both the charge and the polarization of the beam. This allows to reach high intensities keeping the same beam-line settings (apart from changing the sign of the field in the dipoles). Data will be taken in these two configurations and from the data sets one can construct two quantities. First, the «Beam Charge and Spin Difference», :

$$D_{CS,U} = \sigma(+,\leftarrow) - \sigma(-,\rightarrow) = 2\mathfrak{Re}I - 2P_\mu d\sigma_{DVCS}^{pol}$$

where only the real part of the interference term (which has a $\cos n\phi$ dependence (Eq 5.6)) and the polarized DVCS term (which has a $\sin\phi$ dependence (Eq 5.5)) remain. This properties allows to extract the real part of the DVCS amplitude and hence to obtain information concerning mainly the GPD H. The second observable of interest is the «Beam Charge and Spin Sum»:

$$\mathcal{S}_{CS,U} = \sigma(+,\leftarrow) + \sigma(-,\rightarrow) = 2d\sigma_{BH} + 2d\sigma_{DVCS}^{unpol} - 2P_\mu\mathfrak{Im}I$$

For this quantity, the various contributions have also different harmonic structure and can be isolated. This allows to extract the imaginary part of the DVCS amplitude and to measure the unpolarized DVCS cross section which can be related to nucleon

transverse size through its t-distribution. We will now examine these cases in more details.

5.3   Beam charge and spin sum

We have shown that the «beam charge and spin sum» is sensitive to :

$$\mathcal{S}_{CS,U} = \sigma(+,\leftarrow) + \sigma(-,\rightarrow) = 2d\sigma_{BH} + 2d\sigma_{DVCS}^{unpol} - 2P_\mu \mathfrak{Im} I$$

Using the harmonic decomposition and neglecting higher twist terms it can be expressed as :

$$
\begin{aligned}
\mathcal{S}_{CS,U} \quad = \quad & 2\frac{\Gamma(x_{Bj}, Q^2, t)}{P1(\phi)P2(\phi)} \left(c_0^{BH} + c_1^{BH}\cos\phi + c_2^{BH}\cos 2\phi \right) \\
+ \quad & 2\frac{e^6}{y^2 Q^2} \left(c_0^{DVCS} \right) \\
+ \quad & 2e_\mu P_\mu \frac{e^6}{x_{Bj} y^3 t P_1(\phi) P_2(\phi)} \left(s_1^I \sin\phi \right)
\end{aligned}
$$

Pure DVCS cross section

The Bethe-Heitler term in this expansion is calculable and can be therefore subtracted. The interference term has a $\sin\phi$ dependence but is divided by $P_1(\phi)$ and $P_2(\phi)$ which are even functions of ϕ. Hence, after integrating over ϕ the contribution of the interference cancels and only the pure DVCS contribution c_0^{DVCS} remains (this is also true if higher twists are not neglected). The variation of the DVCS cross section has an exponential t-dependence which can be determined experimentally through a fit of the functional form :

$$\frac{d\sigma^{DVCS}(x_{bj}, t)}{dt} \propto e^{-B(x_{bj})t}$$

The slope of the distribution, $B(x_{bj})$, can be extracted independently of models. In the dipole model, it is related to the transverse size $r_\perp$ of the nucleon at a given x_{bj} :

$$B(x_{bj}) \sim \frac{1}{2} < r_\perp^2(x_{bj}) >$$

Interference term

From the unintegrated ϕ-distribution, the amplitude of the $\sin\phi$ modulation can be extracted. It is related to the Compton form factors through :

$$s_1^I \propto \mathfrak{Im}(F_1 \mathcal{H} + \xi(F_1 + F_2)\tilde{\mathcal{H}} - \frac{t}{4M^2} F_2 \mathcal{E})$$

At COMPASS kinematics, the second term can be neglected because $\xi \approx x_{bj}/2 \ll 1$. Furthermore, the proposed experiment will be performed at low transfer t and hence
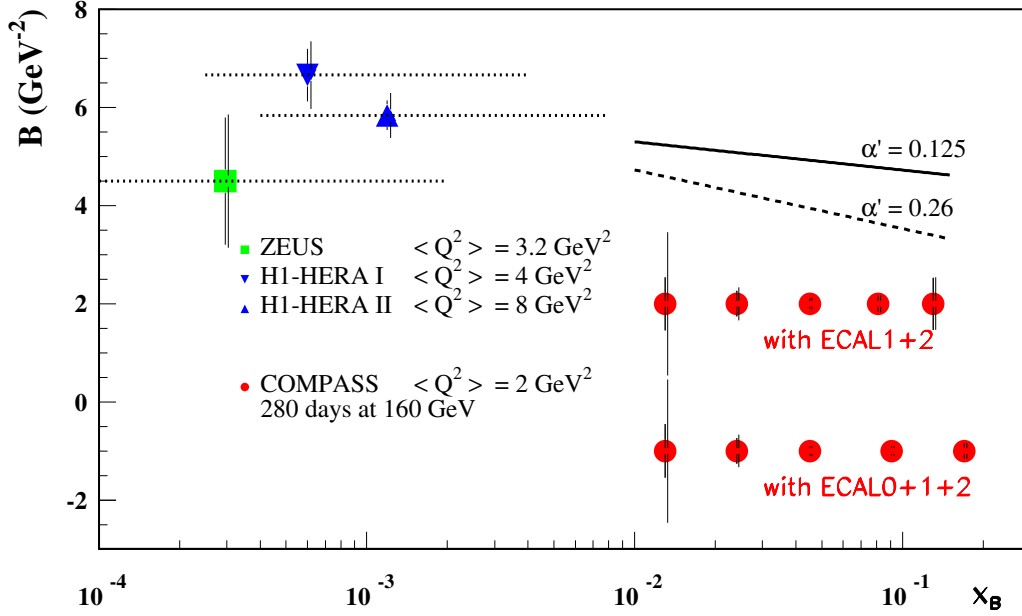
Figure 5.4: Projection of errors for the slope of the t-distribution for a 2-year running period and comparison with Zeus and H1 measurements. The first error bar (on the left of each point) includes only statistical uncertainty while the second error bar (on the right) includes a systematic uncertainty of 3% in the estimation of the Bethe-Heitler contribution which is subtracted. It is done for a setup without (top) and with (bottom) the adjunction of a large angle calorimeter (ECAL0).

the third term involving the CFF $\mathcal{E}$ is small. Therefore, we have :

$$s_1^I \propto \mathfrak{Im}(F_1\mathcal{H})$$

and then the $\sin\phi$ modulation in the cross section after subtraction of the Bethe-Heitler will allow to single out the contribution of the imaginary part of the Compton form factor $\mathcal{H}$ which itself is related to the GPD H for $x = \pm\xi$ (see Eq. 1.51).

Sensitivity to models and comparison with previous experiments

The projected errors of the measurement of the slope of the t-distribution is shown as a function of x_{bj} in figure 5.4. This study was done using the FFS model [63] including a simple ansatz where the slope of the t-distribution follows the relation : $B(x_{bj}) = B_0 + 2\alpha' \log(\frac{x_0}{x_{bj}})$. The errors presented include statistical and systematic errors (right bar of each point). The comparison between the top and bottom projection of errors shows the importance of the adjunction of a calorimeter at large angle (ECAL0). With such a calorimeter the lever arm will be sufficient to observe a shrinkage of the nucleon size for increasing x_{bj} values. Moreover, it will complement the measurements performed by the H1 and Zeus experiments which have already constrained the size of the nucleon in the gluon sector to be $\sqrt{<r_\perp^2>} = 0.64 \pm 0.02\,\text{fm}$ [64].

5.4 Beam charge and spin difference and asymmetry

The difference of cross section when both the beam charge and spin are reversed is sensitive to the real part of the interference and to the polarized DVCS contributions :

$$\mathcal{D}_{CS,U} = \sigma(+,\leftarrow) - \sigma(-,\rightarrow) = 2\mathfrak{Re}I - 2P_\mu d\sigma_{DVCS}^{pol}$$

Using the harmonic decomposition and neglecting higher twist terms it reduces to :

$$\mathcal{D}_{CS,U} = \frac{e^6}{x_{bj}y^3 t P_1(\varphi)P_2(\varphi)}\left(c_0^I + c_1^I \cos\phi\right)$$

It allows to evaluate the coefficient c_1^I which is related to the Compton form factors through the following expression :

$$c_1^I \propto \mathfrak{Re}(F_1\mathcal{H} + \xi(F_1 + F_2)\tilde{\mathcal{H}} - \frac{t}{4M^2}F_2\mathcal{E}).$$

Again, under COMPASS kinematics and experimental conditions, it provides a measurement of the real part of the Compton form factor $\mathcal{H}$:

$$c_1^I \propto \mathfrak{Re}(F_1\mathcal{H}). \tag{5.8}$$

The measurement of both the real and imaginary part will also allow to test the validity of the dispersion relations that link one with the other. Furthermore, from the difference and the sum, one can also construct a *beam charge and spin asymmetry* defined as :

$$\mathcal{A}_{CS,U} = \frac{\mathcal{D}_{CS,U}}{\mathcal{S}_{CS,U}}$$

Sensitivity to models and comparison with previous experiments

The projected error for a measurement of the beam charge and spin difference is shown on figure 5.5 (for one of the $\sim$ 12 bins available). For this task we have developed a fast MC program based on an event generator [22] using the VGG parametrization [23] of the GPDs and assuming a Reggeized (x,t) correlation [?] (black line). The geometry of the experimental setup was modeled and realistic detector resolutions as well as multiple scattering were taken into account. The error on each point is statistical and the grey band along the points represents the systematic error arising from beam charge dependent effects as described in the following section. The expectation for a factorized (x,t)-dependence as determined in the VGG parametrization displays a small value (blue line). The green curves represent the results of the fit on the world data [65] including JLAB Hall A data (dashed line) or not (dotted line).

The sensitivity of the measurement is better estimated using the coefficients of the harmonic decomposition of the beam charge and spin difference. Albeit, for the sake of comparison with HERMES data, one can examine the amplitude of the $\cos\phi$
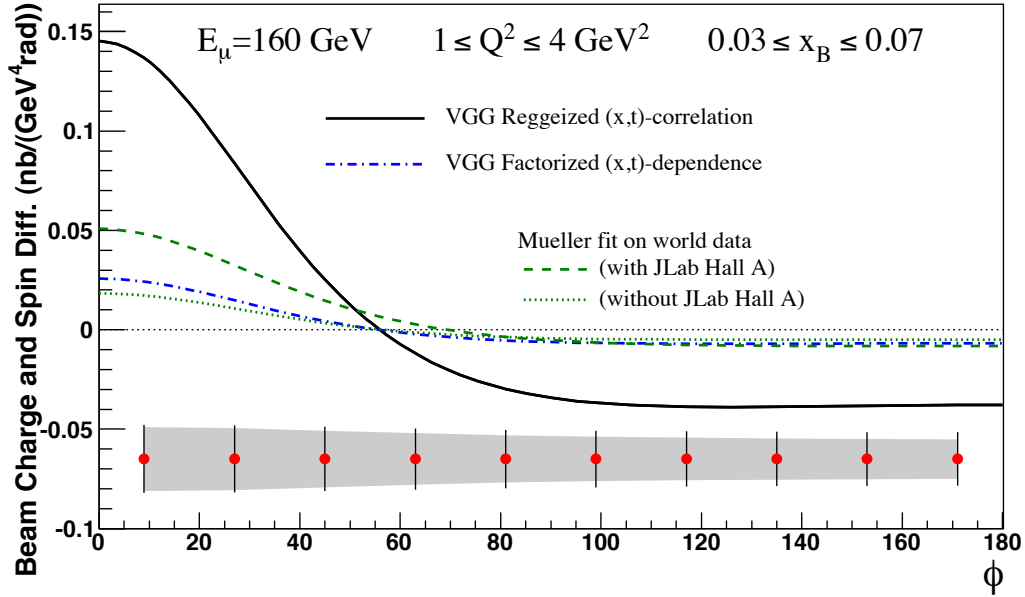
Figure 5.5: Precision achievable on the Beam Charge and Spin Difference showing the sensitivity to models. The statistical error is represented by the vertical bars and the systematic error assuming 3% error on the estimation of the Beam Charge and Spin Sum is represented by the shaded band. Results from D. Muller fits on world data are shown in green (all data: dashed line, all data except JLab Hall A: dotted line). The prediction are calculated using the VGG model.

modulation term in the beam charge and spin asymmetry. The precision expected on this quantity is shown on figure 5.6 as a function of the transfer t and for six possible x_{bj} bins. It shows that in the region of overlap with HERMES, COMPASS can provide a competitive measurement.

The asymmetry amplitude $A_{CS,U}$ is related via the coefficient c_1^I to the real part of the CFF $\mathcal{H}$ (Eq. 5.8). This real part was found positive at Hera and negative at Hermes and JLab. The kinematic domain of Compass, in particular the region $0.005 < x_{bj} < 0.03$, is expected to allow the determination of the x_{bj} position of the node of this function, which is important input for the fitting procedure since no data exist in this region and since it is out of reach of planned future experiments proposed for the JLab upgrade to 12 GeV.

5.5   Systematic errors

The two observables S and D require to combine data taken with μ^+ and μ^-. The normalization of these two sets of data constitute a major challenge from a systematic point of view. For example, changing the beam charge implies to change the polarity of the spectrometer magnets and the low energy charged particle background will be displaced introducing local effects. Also, data in the two configurations will be taken at different beam intensities and at different times where environmental factor such as
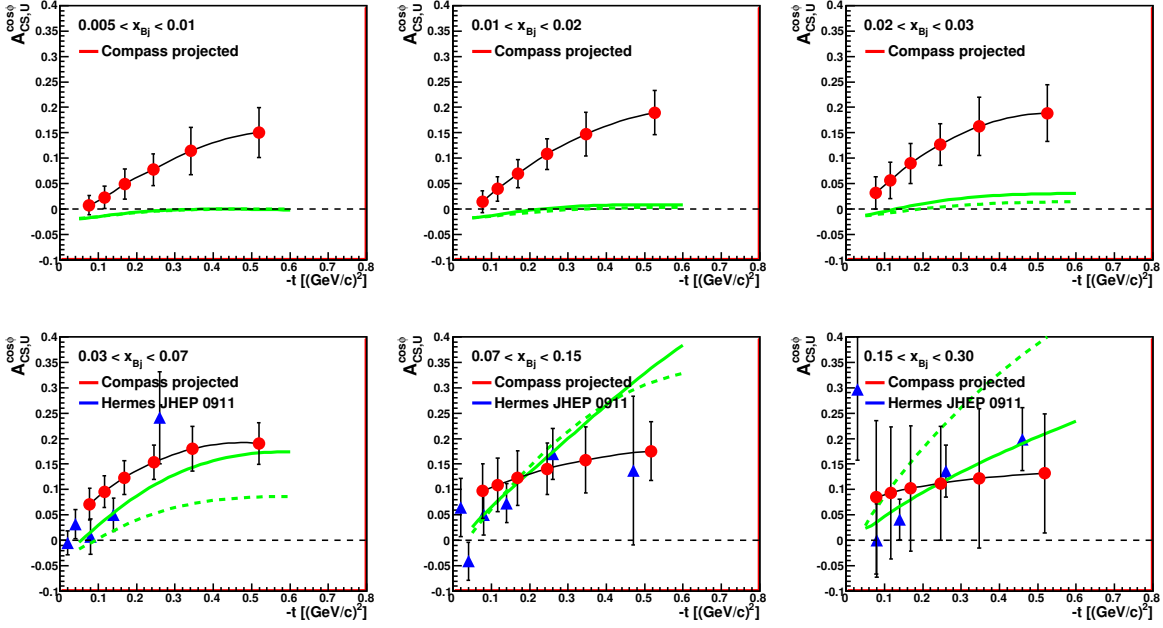
Figure 5.6: Projection of errors of the amplitude of the $\cos\phi$ modulation term in the beam charge and spin asymmetry.

temperature and pressure will be different and where detector performances may also differ due to malfunctioning of some equipments. To evaluate the effect, one can write the number of Single Exclusive Photon events detected for each beam charge setting as:

$$N^+ = \sigma(\mu^+)F^+\varepsilon^+(\mu)\varepsilon^+(\mu')\varepsilon^+(\gamma)\varepsilon^+(p)$$
$$N^- = \sigma(\mu^-)F^-\varepsilon^-(\mu)\varepsilon^-(\mu')\varepsilon^-(\gamma)\varepsilon^-(p)$$

where F is the flux of beam particles, the $\epsilon()$ are the efficiencies to detect the particles of the reaction (incoming muon(μ), scattered muon(μ'), photon (γ) and proton (p)) and the $(+/-)$ subscripts denote the beam-line and spectrometer configurations (i.e. μ^+ or μ^-). We have considered *a priori* that all these normalization factors are different for the two charge configurations. Considering the fact that they appear as a product and supposing that they are uncorrelated it appears that they will have a similar impact on the observables and will have to be monitored at the same level of precision. For completeness, the DAQ live-time needs also to be taken into account and is folded into the flux factor.

Case of the Beam Charge and Spin difference

In the case of the Beam Charge and spin cross section difference the observable is calculated from the number of events of the two configurations and knowing the normalization factors :

$$D = \sigma(\mu^+) - \sigma(\mu^-) = \frac{N^+}{F^+\varepsilon^+(\mu)\varepsilon^+(\mu')\varepsilon^+(\gamma)\varepsilon^+(p)} - \frac{N^-}{F\varepsilon^-(\mu)\varepsilon^-(\mu')\varepsilon^-(\gamma)\varepsilon^-(p)}$$

Any of the parameter will have to be estimated for the two charge states of the muon beam and has uncertainties arising from the statistics precision to which it is measured and from systematic effects which can themselves be decomposed into charge independent and charge dependent contributions. For simplicity we group all efficiencies in a single factor a which is similar to an acceptance. Then, the estimated value for a has the following form for each of the configuration :

$$a_{est}^+ = a^+ + \Delta a_{stat}^+ + \Delta a_{syst} + \Delta a_{syst}^+$$
$$a_{est}^- = a^- + \Delta a_{stat}^- + \Delta a_{syst} + \Delta a_{syst}^-$$

The statistical precision can in principle be made much smaller than the systematic errors and will be neglected although we have to ensure experimentally that it is the case. If it is not the case it will then contribute on the same footing as a charge dependent systematic error. Going back to the measurement of the observable D, we can write :

$$
\begin{aligned}
D_{meas} &= \frac{N^+}{a^+ + \Delta a_{syst} + \Delta a_{syst}^+} - \frac{N^-}{a^- + \Delta a_{syst} + \Delta a_{syst}^-} \\
&= \left(\frac{N^+}{a^+} - \frac{N^-}{a^-}\right)(1 - \Delta a_{syst}/a) - \frac{N^+}{a^+}\frac{\Delta a_{syst}^+}{a^+} + \frac{N^-}{a^-}\frac{\Delta a_{syst}^-}{a^-}
\end{aligned}
$$

The overall impact of charge dependent effects is maximum when the individual effects are opposite, i.e. $\Delta a_{syst}^+/a^+ = -\Delta a_{syst}^-/a^- = \Delta a_{syst}^q/a$. Then, we have :

$$
\begin{aligned}
D_{meas} &= D(1 - \Delta a_{syst}/a) - \Delta a_{syst}^q/a\left(\frac{N^+}{a^+} + \frac{N^-}{a^-}\right) \\
&= D \times (1 - \Delta a_{syst}/a) - S \times \Delta a_{syst}^q/a
\end{aligned}
$$

From this expression one can draw two conclusions. First, the charge independent systematic error Δa_{syst} acts as a scaling factor on the observable D. Given the statistical precision that one wants to reach (see figure 5.5) a 10% overall effect on efficiencies can be accepted. In other words, it implies that the absolute normalization needs to be known at a precision of 10% in the scope of the Beam Charge and Spin Difference. Nevertheless, the 5 factors described previously enter this error and each of them will have to be controlled to $10\%/\sqrt{5} = 4\%$. Second and more important, the charge dependent systematic effect is multiplied by the sum (S). To keep it at an acceptable level we consider that it has to be less than the statistical precision. With the present binning the best statistical precision in a given bin is of the order of 3% of the sum S. Therefore charge dependent effects have to be controlled to this level of precision.

Some of the difficulties have already been identified. At 160 GeV, the beam intensity

for the negative muon beam is 1/3 of the intensity of the positive beam and the impact on the reconstruction efficiency has to be known. The steering of the beam will be important for the detection of photons close to the acceptance edges of the ECAL2 calorimeter. Then, time variation of the detector performances have to be monitored for the two configurations.

The charge dependent effect can be studied with different reactions than the low-rate DVCS. For instance, inclusive deep inelastic scattering, $\mu p \to \mu X$, has a cross section 3 orders of magnitude higher than DVCS. Given the topology of such events, they will allow to study the behavior of the product of the terms $F\varepsilon(\mu)\varepsilon(\mu')$. The semi-inclusive production of π^0 (decay into 2 photons) can be used to evaluate calorimeter edge effects and elastic scattering off the protons can allow to determine proton detection efficiency variations. Data was taken in 2009 to quantify the level of precision which can be reached.

Case of the beam charge and spin sum

Using the description for the charge dependent and independent errors used in the previous paragraph, we obtain for the Beam Charge and Spin sum the following effect :

$$
\begin{aligned}
S_{meas} & = \frac{N^+}{a^+ + \Delta a_{syst} + \Delta a_{syst}^q} + \frac{N^-}{a^- + \Delta a_{syst} - \Delta a_{syst}^q} \\
& = S \times (1 - \Delta a_{syst}/a) - D \times \Delta a_{syst}^q/a
\end{aligned}
$$

The charge dependent error appears to be multiplied by the beam charge and spin difference and hence can be neglected. An then, for counting rates measurement it will only remain a scaling error arising from the charge independent errors. In the extraction of cross section or of the slope of the t-distribution the contribution of the Bethe-Heitler process has to be subtracted. It has been assumed that it can be measured with 3% precision over the whole acceptance. In kinematical regions where it is dominant the impact on the DVCS cross section is amplified (low x_{Bj} points in figure 5.4) and this effect is dominating the systematic error. Experimentally it requires that the measured event rates are corrected for acceptance. This task has to be done using extensive Monte-Carlo simulation of the apparatus. The quality of the simulation can be evaluated at the low x_{bj} and low Q^2 region of the accessible kinematical domain where the Bethe-Heitler is 10 to 40 times more abundant than DVCS. At high x_{bj} it can be also checked through the use of GPD models for DVCS although less precisely.

5.6   The recoil proton detector

5.6.1   Description

The recoil detector foreseen is shown in figure 5.7. It comprises two rings of scintillating counters of 24 elements each read at both sides by photomultiplier tubes. The inner
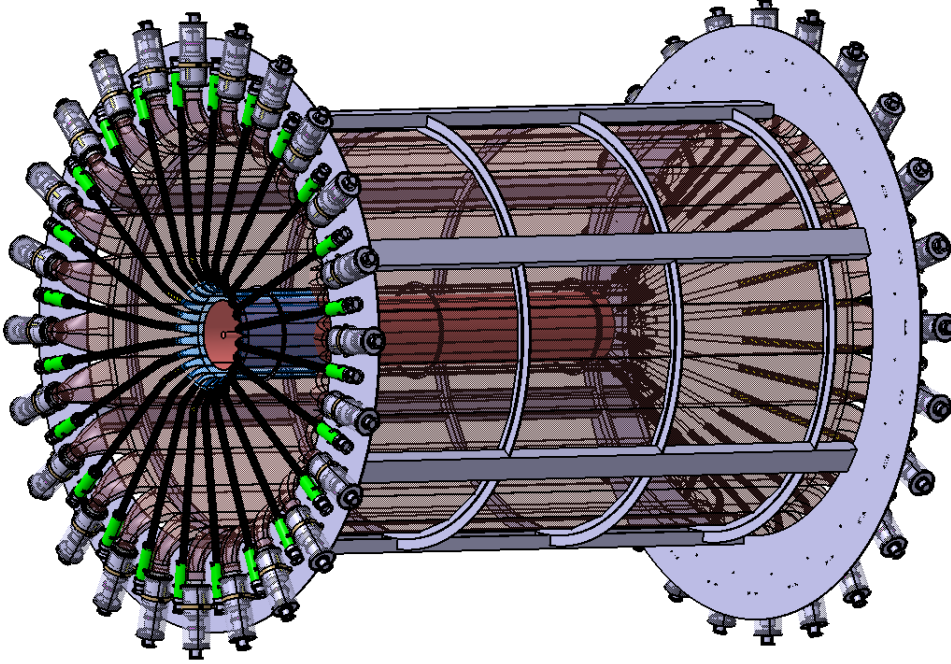
Figure 5.7: View of the recoil proton detector foreseen for the future DVCS experiment. The overall diameter is about 3 m and the length is 4.2 m.

ring (i.e. ring A) is at a radius of 25 cm from the target axis and the outer ring (i.e. ring B) is at a radius of 110 cm. The momentum of recoiling particles will be determined from the time-of-flight measurement and from the impact points measured on each scintillator element. With a 300 ps time resolution, the distance of flight ($\sim$ 85 cm) guarantees that the proton momentum be measured with a precision from 4% (at 260 MeV/c up to 10% (at 700 MeV/c). The ring A elements have a length of 280 cm and a width of 6 cm. The thickness is chosen to be 4 mm with the constrain of low momentum protons detection (down to 260 MeV/c) and of a sufficient number of photons produced for good timing resolution. The ring B elements have a length of 360 cm and a width of 30 cm. For this outer layer, the thickness is chosen to ensure proton-pion separation up to momenta of 600 MeV/c.

5.6.2   Monte Carlo Simulations

A Geant based program was developed to estimate the reconstruction efficiency using the recoil detector as designed for future measurements. The goal of this studies was to evaluate the feasibility of the detection in the presence of a high pile-up environment. The realistic geometry for the future set-up was used. The DVCS event kinematics are generated and the vertex is placed within the target and particles are propagated in the target volume and in the RPD. When reaching an active volume (i.e. scintillating material) the energy loss by the particle is converted into photo-electrons using atten-

uation and quantum efficiency of the photomultiplier tube (PMT) and the time of the hit is modified by the propagation time from the interaction to the PMT. Then, the photo-electron information are transformed into a waveform reflecting the signal seen at the output of the PMT. A software analysis of the waveform is performed : the time is taken from a constant fraction discrimination and the energy loss from the integration over 50 ns.

The proton momentum range of interest of DVCS is 250MeV-1GeV and it produces variations of the time of flight from 3 to 80 nanoseconds. Light propagation over the length of the scintillator can add up to 30 ns (13 cm/ns over 4 m) and finally waveform signals from the same events are spread over 120 ns. The muon beam intensity at which the experiment is planned is 4.10^8 muons in a 10 s spill and an average of 5 muons is passing through the target for each time window. There is 1.5 δ-ray electron with enough energy to reach ring A scintillator produced by each muon in the target. Therefore almost half of the PMTs of the RPD will have sizable signals in the 120ns time window. The occupancy in the RPD elements for a typical DVCS event including pile-up is represented in figure 5.8. This has three implications :

1. Fast triggering using NIM logic modules appears non feasible. This can be overcome with a trigger on the scattered muon only for which DIS kinematics are favored provided that the rate is acceptable. This implies a modification of the existing trigger system for which the coverage can be optimized.

2. Sampling and recording of all PMT waveforms is mandatory. The system should be able to sample the signal with a frequency of 1GHz with 10-12 bits resolution.

3. External information from the muons tracks and timing are required to disentangle the DVCS proton from background electrons.

4. A cross check of the rates in ring A and B with real data is required.

The feasibility of the detection of the DVCS proton was then estimated in these conditions. For each event, each scintillator is examined and from each pair of upstream-downstream PMT a «hit» is defined by a position and a time deduced. Hits are discarded when the reconstructed position is out of the physical volume of the scintillator. Each pair of «hit» of a ring A and a facing ring B element is used to determine a «pseudo-track». The velocity β is determined for each track using the position and the time-of-flight and tracks with unphysical β are discarded. Finally, a cut is applied on the time difference between the RPD track and the muon vertex (figure 5.9 left) at $|\Delta t| < 6$ ns. The time resolution arises from the relatively modest resolution of the beam detectors (Sci-Fi). In practice a cut could also be applied on the position difference (figure 5.9 right) but we have chosen to use this as a mean to evaluate the fraction of signal in the selection of events.

This exercise was done under different instantaneous beam intensities and the results obtained are summarized in the table 5.1. The efficiency is defined as the probability that the DVCS proton is identified provided that at least one Ring A-Ring B coincidence
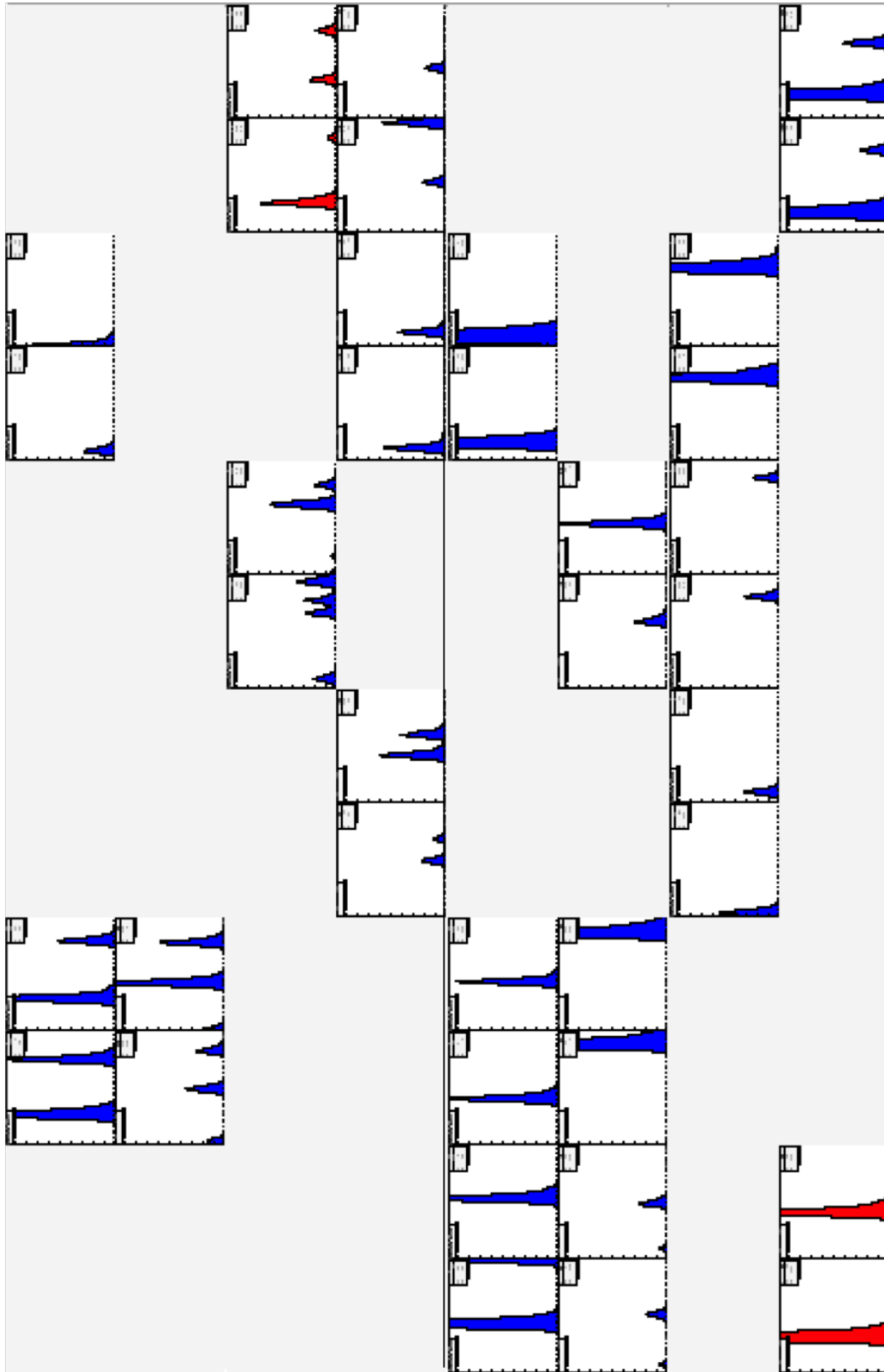
Figure 5.8: Occupancy in the RPD elements for a DVCS event including pile-up. Each plot represents the output of a PMT over a 120 ns time window. Each pair corresponds to the upstream and downstream PMT signals of a given counter. Red plots indicate in which elements the DVCS proton was generated. The left half of the plots (or the top plots if your rotate the page) correspond to ring A elements. The right (bottom) plots correspond to ring B elements.
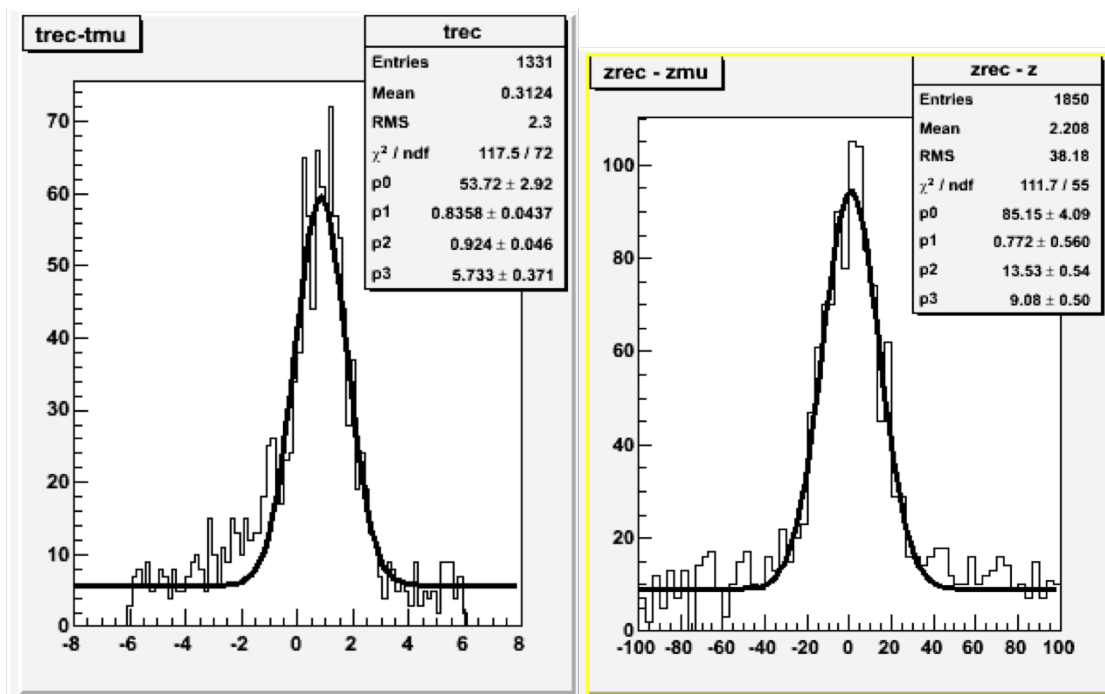
Figure 5.9: Position and time difference between the RPD track and the vertex defined by the incoming and the scattered muons. A cut at $|\Delta t| < 6\,\mathrm{ns}$ was applied.

	$I = 0\,\mu.s^{-1}$	$I = 2.10^7\,\mu.s^{-1}$	$I = 4.10^7\,\mu.s^{-1}$	$I = 8.10^7\,\mu.s^{-1}$
efficiency	0.97	0.91	0.90	0.87
S/(S+B)	0.83	0.80	0.74	0.64

Table 5.1: Efficiency and purity of the RPD reconstruction algorithm for different instantaneous beam intensity ($I = 4.10^7\,\mu.s^{-1}$ is the nominal intensity).

was found. It shows a slowly decreasing behavior and at the nominal intensity ($I = 4.10^7\,\mu.s^{-1}$) the efficiency is 90%. Also presented is the fraction of signal which shows that the purity of the sample is degrading with increasing intensity and that at nominal intensity it is still better than 74%.

These GEANT Monte-Carlo studies have shown that the background produced by additional beam muons has an important impact on the detection scheme. It has triggered the development of a high standards electronics board to realize the 1 GHz sampling of the PMT signals along with the integration in the COMPASS DAQ system (GANDALF project - Freiburg University).

5.6.3 Murex Prototype (2006)

Experimental studies of the Recoil Proton Detector were conducted in order to validate the detection concept. The characteristics and performances of the ring A and ring B tested elements are summarized in table 5.2 and are compared to the RPD built for the COMPASS hadron program. The performances were measured using a cosmic

	L (cm)	l (cm)	t (cm)	λ_{att}	σ_t(ps)	σ_{pos}(cm)	PMT	Scintillator
muRex : A	284	6	0.4	2.0	270	3.5	XP20H0	BC 408
muRex : B	400	29	5	4.0	200	2.5	XP4512	BC 408
RPD : A	50	6	0.5	0.7	180	2.3	EMI9813B	BC 404
RPD : B	106	20	1	4.0	200	3.8	EMI9813B	IHEP

Table 5.2: Characteristics of the ring A and ring B of the muRex prototype and of the RPD built for the COMPASS hadron program.
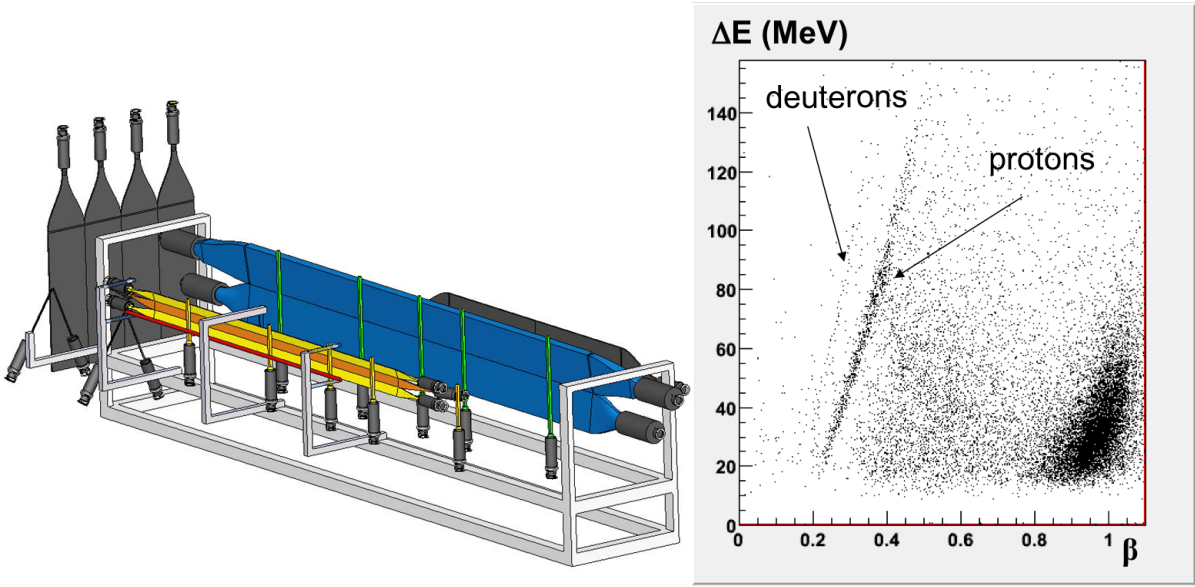
Figure 5.10: Left panel : view of muRex, a prototype of recoil proton detector tested at CERN on the muon beam line. Right panel : measurement of energy loss in the ring B elements as a function of the measured velocity of the particle.

ray muons test bench and they fulfill the requirements in terms of position and time resolution as well as attenuation length. The photo-detection was further optimized by studying the geometry of the light guides, the optical coupling between light guides and scintillator and the wrapping of the scintillators [69].

In a second stage, a mechanical support was built and the detector was assembled in a configuration similar to the future detector covering a 30 degree azimuthal angle (see left panel of figure 5.10). The detector was placed on the COMPASS beam line downstream of the experiment and a set of polyethylene (CH2) targets were used as a mock-up of the future hydrogen target. A sharp proton signal was observed as seen in the right panel of figure 5.10. It shows the energy loss by the particle in the ring B scintillator as a function of the velocity measured using the timing information. The protons observed are the one which are stopped in the B scintillator ($\beta < 0.4$). At higher velocities, the protons cross the scintillator and the energy deposition depends on the velocity and the angle of the trajectory which blurs the signal. A faint deuteron signal is also observed as well as a signal corresponding to δ-ray electrons. These tests have validated most of the points in the detection concept except pile-up effects.
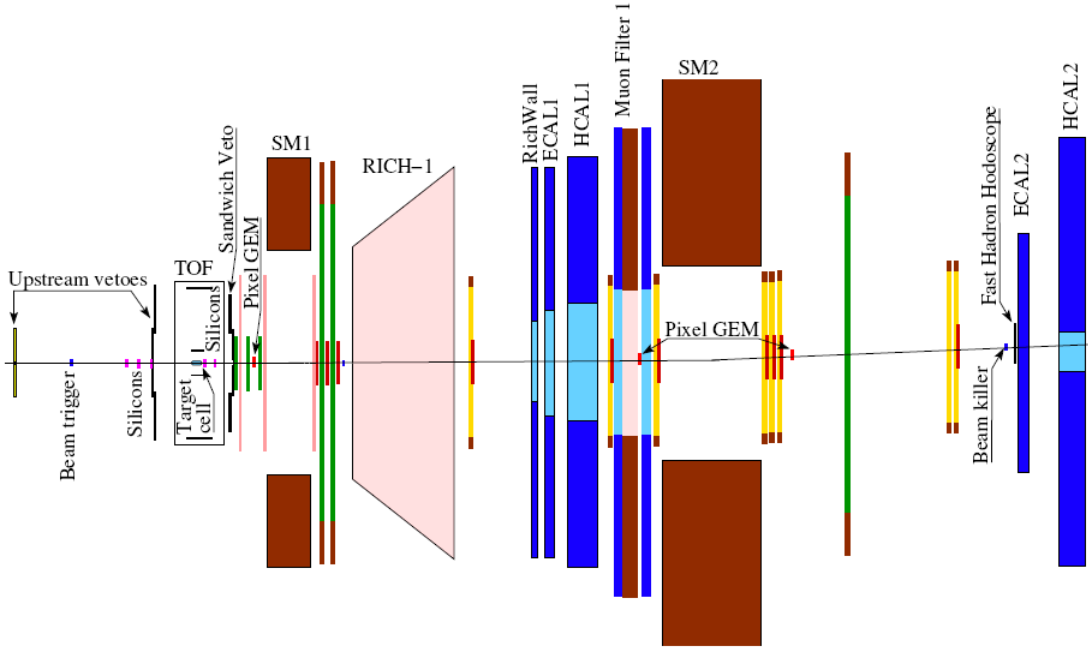
Figure 5.11: Experimental setup used for the DVCS beam tests (a closer view of the target and RPD can be seen on figure 3.4).

5.7 Analysis of the 2008 and 2009 DVCS test runs

5.7.1 Experimental conditions

At the end of the 2008, we took data with the 160 GeV muon beam impinging on the liquid hydrogen target. The goal was to demonstrate the detectability of the exclusive photon production in the COMPASS condition. The test period was planned to last 8 days including 3 days of installation. Unfortunately, due to the accident on LHC it was shorten to 2 days and important components such as the «Beam Momentum Station» and the trigger based on the scattered muon kinematics could not be installed. The experimental set-up used is shown on figure 5.11. The Recoil Proton Detector developed for the Hadron program of COMPASS was fully operational and the calibration could be taken from previous hadron beam data. The calorimeters ECAL1 and ECAL2 were also operational and could be used in this analysis.

5.7.2 Detectability of exclusive photon production

The events are first filtered according to the topology of the reaction to be detected :

$$\mu P \rightarrow \mu P \gamma$$

The selection of event is performed on the reconstructed tracks in the spectrometer, the energy clusters in the calorimeters and the particles seen in the RPD through the following «topological» conditions :
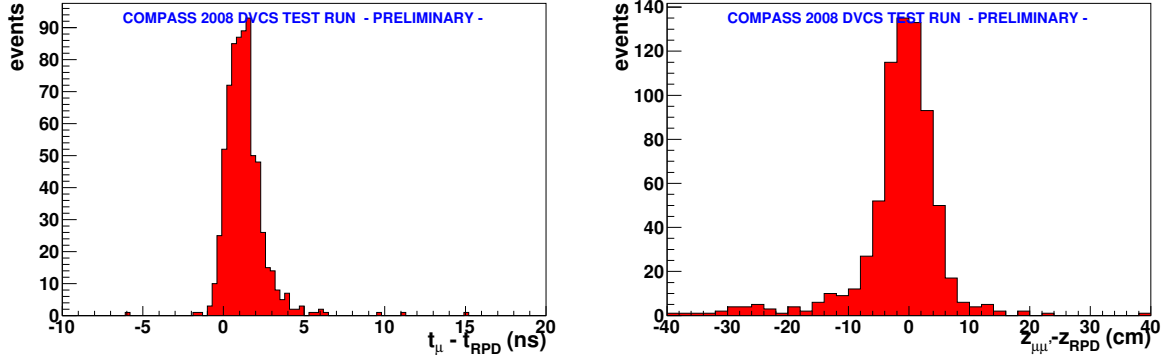
Figure 5.12: Difference of timing between the incident muon and the RPD track (left). Difference of position between the primary vertex and the RPD track extrapolated to x=y=0 (right).

- scattered muon : there is only one charged particle originating from the reconstructed primary vertex

- photon : there is only one high energy cluster with $E > 5$ GeV if photon in ECAL1 or $E > 10$ GeV if in ECAL2. These limits arise from kinematical constraints on the photon energy for the DVCS and BH process.

- proton : there is only one RPD track reconstructed with $p < 1$ GeV/c.

5.7.3   Vertex resolution

The correlation between the muon vertex and the RPD information is shown in figure (5.12). The left plot shows the difference of the incoming muon time and the RPD time extrapolated at the vertex using the reconstructed momentum of the particle. The level of random noise in the 30 ns window is found to be less than 2% and a Gaussian fit gives a time resolution of 1 ns. The right plot shows the difference between the longitudinal position of the vertex reconstructed using the incoming and the scattered muons and the position reconstructed using the RPD. It shows a peak of 3 cm resolution and a tail in the left part of the distribution. This tail is given by non exclusive events and cuts performed later in the analysis will discard these events. Since the random noise is very low, no cuts are applied on these differences.

5.7.4   Event selection

Exclusivity can be insured by comparing kinematical quantities. In the data taken in 2008, the beam momentum station could not be re-installed and only the beam direction could be measured. The beam energy spread is 5 GeV and forbids any tight exclusivity condition on missing mass or missing energy. Putting aside beam momentum, quantities in the plane transverse to the beam particle direction can be used. From the scattered muon and emitted photon one can construct a fictive «missing» particle which we can
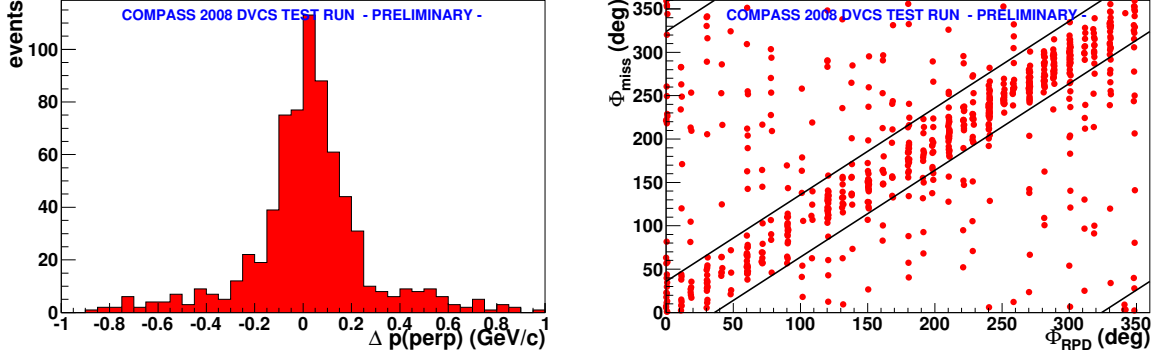
Figure 5.13: Difference of momentum in the transverse plane, a cut at $\pm$ 0.2 GeV is applied (left). Correlation of azimuthal angle, a cut at $\pm$ 36 degrees shown by the black line is applied (right).

correlate to the measured proton in the RPD. The comparison of the momentum and the azimuthal angle of these two particles are shown in figure 5.13. The transverse momentum distribution has a width of the order of 100 MeV/c and a cut at ± 200 MeV/c is applied (left panel). Concerning the azimuthal angle (right panel), a clean correlation is observed and a cut at ± 36 degrees is applied by keeping event in the band shown in black.

The correlation between the energy loss by the recoiling particle in the outer scintillator and the β of the particle is used to perform identification (Figure 5.14). The identification can only be performed for particle with $\beta < 0.4$. This limit is due to the small thickness of the outer scintillator (1 cm). Increasing this value to 5 cm will allow for identification up to $\beta = 0.6$. Furthermore, the angle between the virtual photon and the real photon, $\theta_{\gamma^*\gamma}$, can be used to check whether the identification of the reaction is correct. Indeed, this variable can be either determined using the muons tracks and the photon or using the muon tracks and the recoiling proton and kinematical relations of the reactions, $\mu p \to \mu p \gamma$:

$$\cos\theta_{\gamma^*\gamma}^{\mu\mu'p} = \frac{1}{\sqrt{1 + 4M_P^2 x_{Bj}^2/Q^2}} \left(1 + \frac{2M_P^2 x_{Bj}}{Q^2} \frac{t + Q^2}{t + Q^2/x_{Bj}} \right)$$

The difference of the two estimations is shown in figure 5.14 where the solid line shows the distribution for all events. The red-filled (grey) distribution shows events that are rejected by exclusivity cuts on transverse momentum and azimuthal angle. It cuts events mostly on the tail of the distribution leaving the exclusive photon production peak intact. This result implies that the non-exclusive background is much smaller than the exclusive signal.
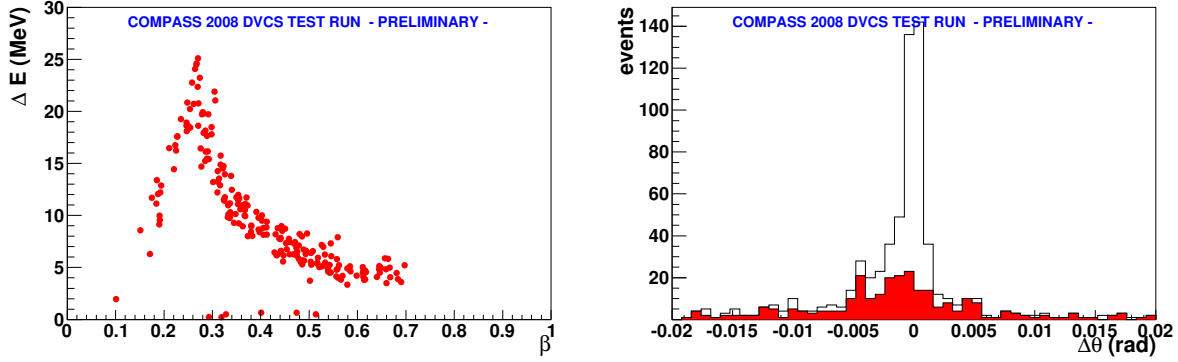
Figure 5.14: Energy loss in ring B as a function of β for particle fulfilling the exclusivity criteria (left). Difference of real photon polar angle measured either with the photon or with the proton (right). The solid line represents the distribution for all events and the red (grey) area represents the events that were discarded by the exclusivity conditions.
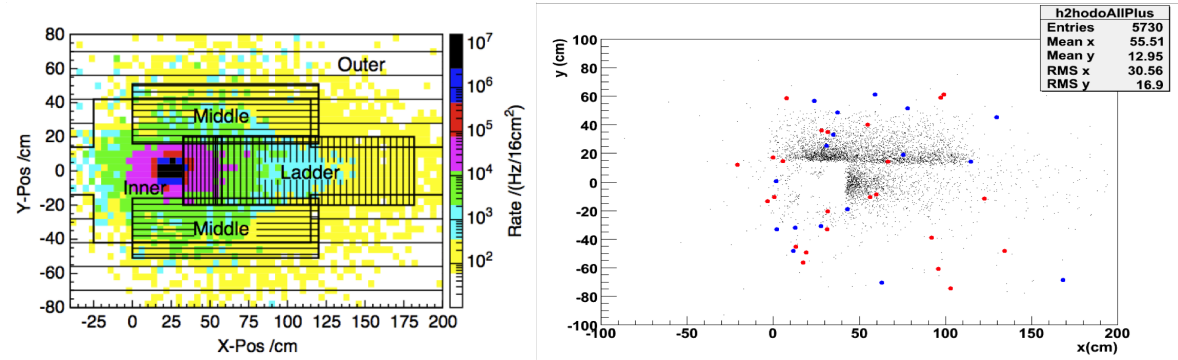

Figure 5.15: Impact point of the scattered muons at z=40 m. Left panel : geometry of the various trigger hodoscopes elements. Right panel : 2008 data, all events showing that only the top part of the Middle Trigger was activated (black dots). The red (resp. blue) dots are events for μ^- (resp. μ^+) beam for which the RPD trigger have fired.

5.7.5   Trigger issues

The trigger scheme of the future DVCS experiment relies on the inclusive triggers which were developed for the COMPASS muon program. Because of the lack of time in the preparation of the beam test only the upper part of the "Middle Trigger" was operational (figure 5.15). Although, the RPD trigger system developed for the COMPASS hadron program was also used with the veto condition and a prescaling factor applied. For μ^+ running, a prescaling factor of 6 was applied to RPD trigger to cope for the higher intensity and trigger rate. The reconstructed position of the scattered muon in the transverse plane at the position of the H4 hodoscopes (z=40 m) is shown on figure 5.15. It shows that for this data taking period only the top part of the Middle Trigger was activated (black dots). The red (resp. blue) dots are events for μ^- (resp. μ^+) beam for which the RPD trigger have fired. They are homogeneously spread and show the optimal coverage required for future trigger systems.

trigger	μ^-	μ^+	μ^+corr	total
RPD only	21	16 (prescaled by 6)	96	117
MT only	0	0	0	0
MT & RPD	3	11	11	14
Total	24	27	107	131+/-25
Flux ($10^{11}\mu$)	0.73	2.55	2.55	3.3
evts / $10^{11}\mu$	33		42	40

Table 5.3: Number of single exclusive photon events for different triggers conditions.

The sharing between the different triggers is shown in the table below for μ^+ and μ^-. It shows a relative enhancement of the MT&RPD trigger for μ^+ which is a consequence of the prescaling of the RPD trigger mentioned above. The third column of numbers contains the number of events corrected for this factor. The overall statistical error has to incorporate this correction and the total number of events estimated is 131 ± 25 for an integrated flux of $3.3\,10^{11}\mu$.

5.7.6 Expected rates and FOM

We have measured a number of events for a given muon flux. This figure can be used to evaluate the efficiency of detection of the exclusive photon production using the present COMPASS set-up. For this task, two "fast" Monte-Carlo simulation programs were used and the expected number of events has been cross-checked to 3% making the reasonable assumption that events come mostly from the Bethe-Heitler process. A way to tag this process is to look at the distribution of the angle between the leptonic and the hadronic plane. The Bethe-Heitler process which should dominate our sample presents a peak when this angle is close to 0. The observed distribution is shown on figure 5.16 along with the prediction from the Monte-Carlo simulation. The shape of the observed distribution is compatible with the Bethe-Heitler process [70].

The detection efficiency is deduced from the normalization of the two distributions. The result is : $\epsilon = 0.38 \pm 0.15$. It is the product of the efficiency of detection of the muons, the scattered photon and the recoiling protons. The muon vertex reconstruction efficiency is estimated to be 80% and has been measured by Monte-Carlo simulations [38]. Inefficiency for photon detection arise from the absorption in the material crossed before entering the calorimeters and is of the order of 40%. Efficiency for scintillator based recoil detectors [71] are of the order of 80% and accounts for nuclear interaction in the target and in the scintillators as well as space between the strips. From these considerations, the estimated efficiency is in agreement with the measured value.

The global efficiency has to incorporate other effect such as availability of the SPS and of the spectrometer and also realistic trigger efficiencies and veto live-time. All this items can be evaluated from either previous running or dedicated studies and they amount to an additional $\epsilon = 0.40$ factor. Finally, we obtain a global efficiency for exclusive photon detection of $\epsilon = 0.16 \pm 0.06$. The value used in the predictions for
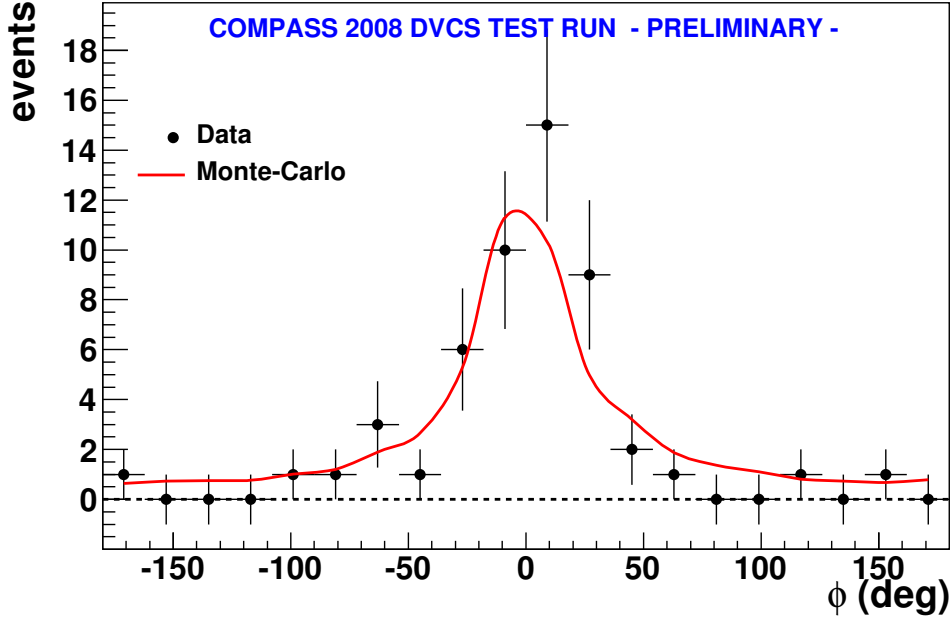
Figure 5.16: ϕ distribution of the exclusive photon production events with $Q^2 > 1\,\mathrm{GeV}/c^2$. Superimposed on this graph is the contribution of pure BH obtained from the Monte-Carlo simulation presented before where the BH is dominant.

future experiments, $\varepsilon_{global} = 10\%$ is confirmed by this first observation of exclusive photon production. Improvements in the accelerator complex are underway and could result in a higher availability of the SPS. Nevertheless, the increased target length of future experiments may impair the RPD efficiency and future simulations will help clarify this issue.

5.7.7   Observation of exclusive π^0 production

The selection of events can be modified to keep events with 2 photons in the calorimeter. Assuming that they originate from the primary vertex one can construct the invariant mass of the 2-γ system. A clean way to disentangle π^0 from background is to correlate the invariant mass with respect to the polar angle of one of the photon, θ_γ, in the rest frame of the π^0. Since the π^0 has spin 0 the decay should be isotropic in the rest frame and the distribution should be flat in $\cos\theta_\gamma$. This correlation is shown in figure 5.17 for events passing the exclusivity selection (open circle). We observe an accumulation of events at the mass of the π^0 (135MeV) which also populates the whole $\cos\theta_\gamma$ domain. A background component is also seen for small values of the mass and for $|\cos\theta_\gamma| < 0.2$ or $|\cos\theta_\gamma| > 0.8$. Out of this region, a clear π^0 signal is observed. The solid points in figure 5.17 represent the events with $Q^2 > 1\,(\mathrm{GeV}/c)^2$. For these events, only the contribution in the background region remains and no π^0 can be observed although the statistics is very limited.
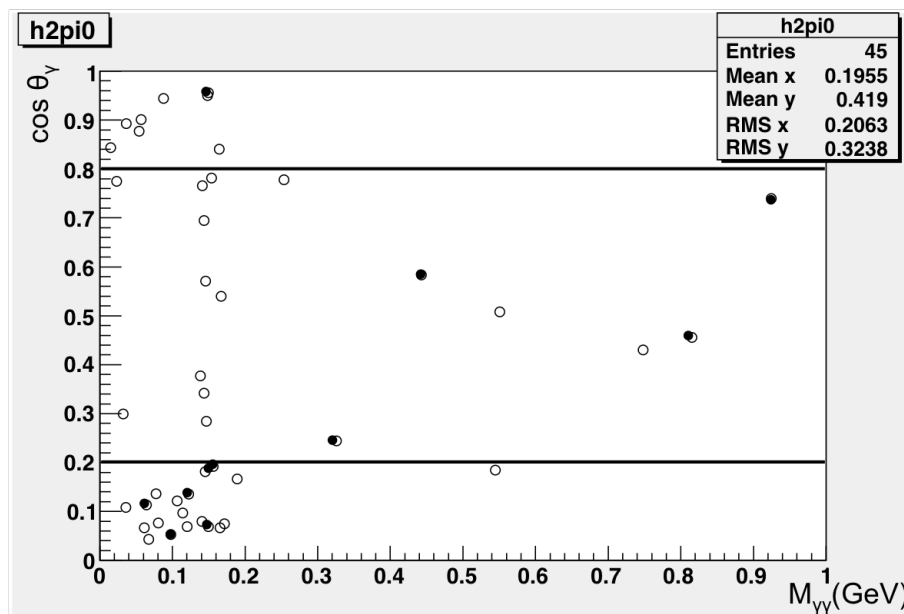
Figure 5.17: Polar angle of the photon emission in the π^0 rest frame as a function of the invariant mass of the 2 gammas. The open circle represents all events fulfilling the exclusivity criteria. The full circle is the sub-sample of these events with $Q^2 > 1\,(\text{GeV}/c)^2$.

5.7.8   2009 DVCS signal

The tests were continued in 2009 for a 1-week data taking period. One of the main goals of the DVCS test run performed in 2009 was to provide a first evaluation of the relative contributions of the $|\text{DVCS}|^2$ and $|\text{BH}|^2$ terms, and of the DVCS-BH interference term at Compass kinematics. In comparison to the shorter 2008 test run, the 2009 test run was improved in several aspects: longer run (8 days) and beam nominal intensity (increased by a factor of three), use of the full set of inclusive triggers, beam momentum station reinstalled to measure the momentum of the incoming muon. The selection of exclusive single-photon production events and the use of the precise photon timing were performed as for the 2008 data analysis. The ϕ distribution of the exclusive photon production events with $Q^2 > 1\,\text{GeV}/c^2$ are represented in figure 5.18 for three bins in x_{bj}. Superimposed on these graphs are the pure BH contribution ($|\text{BH}|^2$, dashed line) and the coherent sum of BH and DVCS ($|\text{BH} + \text{DVCS}|^2$, solid line) obtained from the Monte-Carlo simulation presented before and normalized on the low-x_{bj} bin where the BH is highly dominant. In the high-x_{bj} bin, this study suggests a significant contribution of DVCS events (about 44 events out of 54 events observed in this bin) [72].
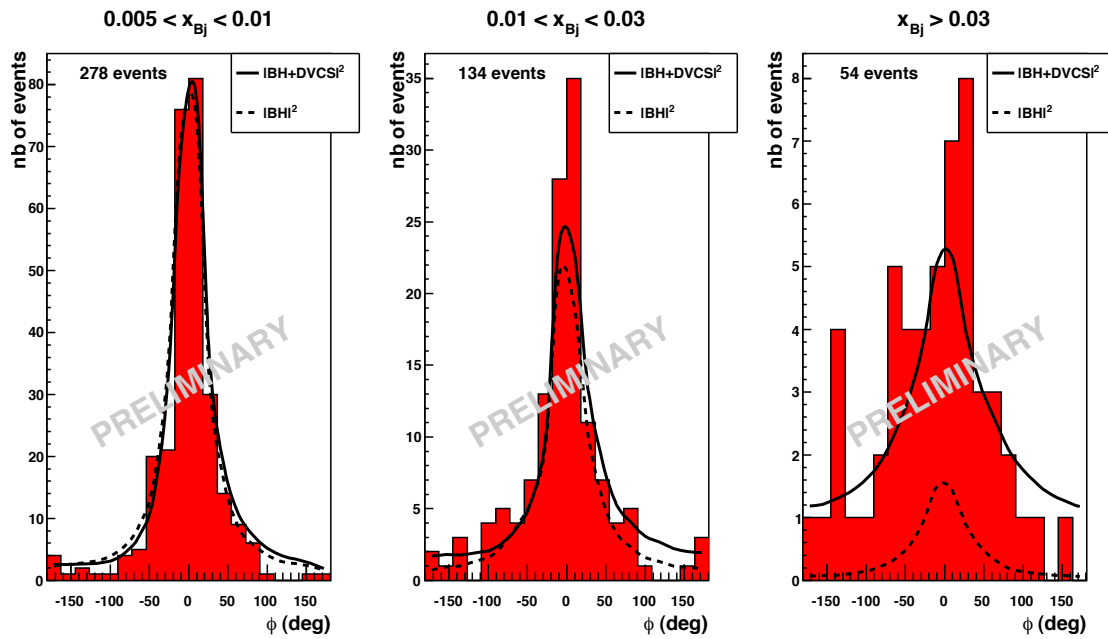
Figure 5.18: ϕ distributions of the exclusive photon production events with $Q^2 > 1\,\text{GeV}/c^2$ for three bins in x_{bj}. Superimposed on these graphs are the pure BH contribution ($|\text{BH}|^2$, dashed line) and the coherent sum of BH and DVCS ($|\text{BH} + \text{DVCS}|^2$, solid line) obtained from the Monte-Carlo simulation presented before and normalized on the low-x_{bj} bin where the BH is highly dominant. In the high-x_{bj} bin, this study suggests a significant contribution of DVCS events.

Conclusions and prospects

More than 20 years after the EMC experiment, we have a better understanding of the nucleon structure. The strange quarks do not contribute to the charge and magnetization distributions in the nucleon. The nucleon spin puzzle is progressing and the contribution of gluons to the nucleon spin has been measured through the measurement of charmed mesons and high transverse momentum hadrons. This contribution seems small and it rules out the "axial anomaly" as a possibility to explain why the quark contribution to the nucleon spin is much lower than the expectation based on relativistic quarks parton models.

The formalism of Generalized Parton Distribution has emerged as a framework for understanding form factors measured in elastic scattering and structure functions measured in deep inelastic scattering as the daughters of the same parent distributions. The GPDs are related to the angular momentum of the partons in the nucleon through the Ji Sum Rule and they can be accessed through the measurement of simple exclusive processes such as Deeply Virtual Compton Scattering ($l + p \rightarrow l + p + \gamma$) and hard exclusive meson production ($l + p \rightarrow l + p + V$). These processes have been studied at the HERA collider by the ZEUS, H1 and HERMES experiments and at Jefferson Lab. We joined the effort and have started the study of hard exclusive ρ^0 production using COMPASS data taken with a polarized target and only partial exclusivity. Experimental techniques for determining the acceptance and the background contributions were developed. Results off deuteron and proton targets were presented.

Our main goal was to study the feasibility and the impact of a possible DVCS experiment using the COMPASS apparatus. The results of these studies are positive in all aspects. The sensitivity of the physics observables should allow to make a significant step forward in the determination of the Compton Form Factors and should be an important constrain for GPD models. Taking advantage of the recoil detector built for the COMPASS hadron program, beam tests have demonstrated the detectability of the DVCS process.

The COMPASS II proposal [61] has just been submitted (May 17, 2010) to the SPS Committee and presents this GPD program to complement the description of the nucleon structure in term of the transverse position distributions of partons. It is also proposed to study the transverse momentum distribution through the study of the Drell-Yan process.

Appendix

HAPPEX Collaboration, K.A. Aniol, et al., Phys. Rev. C 69, 065501 (2004).

ELSEVIER

New measurement of parity violation in elastic electron–proton scattering and implications for strange form factors

HAPPEX Collaboration

K.A. Aniol [a], D.S. Armstrong [ah], T. Averett [ah], M. Baylac [aa], E. Burtin [aa], J. Calarco [t],
G.D. Cates [x], C. Cavata [aa], Z. Chai [s], C.C. Chang [q], J.-P. Chen [l], E. Chudakov [l],
E. Cisbani [k], M. Coman [d], D. Dale [n], A. Deur [l], P. Djawotho [ah], M.B. Epstein [a],
S. Escoffier [aa], L. Ewell [q], N. Falletto [aa], J.M. Finn [ah], A. Fleck [y], B. Frois [aa], S. Frullani [k],
J. Gao [s], F. Garibaldi [k], A. Gasparian [g], G.M. Gerstner [ah], R. Gilman [l,z], A. Glamazdin [o],
J. Gomez [l], V. Gorbenko [o], O. Hansen [l], F. Hersman [t], D.W. Higinbotham [ag],
R. Holmes [ac], M. Holtrop [t], B. Humensky [x], S. Incerti [ad], M. Iodice [j], C.W. de Jager [l],
J. Jardillier [aa], X. Jiang [z], M.K. Jones [ah], J. Jorda [aa], C. Jutier [w], W. Kahl [ac], J.J. Kelly [q],
D.H. Kim [p], M.-J. Kim [p], M.S. Kim [p], I. Kominis [x], E. Kooijman [m], K. Kramer [ah],
K.S. Kumar [r,x], M. Kuss [l], J. LeRose [l], R. De Leo [i], M. Leuschner [t], D. Lhuillier [aa],
M. Liang [l], N. Liyanage [s], R. Lourie [ab], R. Madey [m], S. Malov [z], D.J. Margaziotis [a],
F. Marie [aa], P. Markowitz [l], J. Martino [aa], P. Mastromarino [x], K. McCormick [w],
J. McIntyre [z], Z.-E. Meziani [ad], R. Michaels [l], B. Milbrath [c], G.W. Miller [x], J. Mitchell [l],
L. Morand [e,aa], D. Neyret [aa], G.G. Petratos [m], R. Pomatsalyuk [o], J.S. Price [l], D. Prout [m],
T. Pussieux [aa], G. Quéméner [ah], R.D. Ransome [z], D. Relyea [x], Y. Roblin [b], J. Roche [ah],
G.A. Rutledge [ah], P.M. Rutt [l], M. Rvachev [s], F. Sabatie [w], A. Saha [l], P.A. Souder [ac],
M. Spradlin [h,x], S. Strauch [z], R. Suleiman [m], J. Templon [f], T. Teresawa [ae], J. Thompson [ah],
R. Tieulent [q], L. Todor [w], B.T. Tonguc [ac], P.E. Ulmer [w], G.M. Urciuoli [k], B. Vlahovic [l,v],
K. Wijesooriya [ah], R. Wilson [h], B. Wojtsekhowski [l], R. Woo [af], W. Xu [s], I. Younus [ac],
C. Zhang [q]

[a] California State University–Los Angeles, Los Angeles, CA 90032, USA
[b] Université Blaise Pascal/IN2P3, F-63177 Aubière, France
[c] Eastern Kentucky University, Richmond, KY 40475, USA
[d] Florida International University, Miami, FL 33199, USA
[e] Université Joseph Fourier, F-38041 Grenoble, France
[f] University of Georgia, Athens, GA 30602, USA
[g] Hampton University, Hampton, VA 23668, USA
[h] Harvard University, Cambridge, MA 02138, USA
[i] INFN, Sezione di Bari and University of Bari, I-70126 Bari, Italy
[j] INFN, Sezione di Roma III, 00146 Roma, Italy
[k] INFN, Sezione Sanità, 00161 Roma, Italy
[l] Thomas Jefferson National Accelerator Facility, Newport News, VA 23606, USA
[m] Kent State University, Kent, OH 44242, USA

[n] University of Kentucky, Lexington, KY 40506, USA
[o] Kharkov Institute of Physics and Technology, Kharkov 310108, Ukraine
[p] Kyungpook National University, Taegu 702-701, South Korea
[q] University of Maryland, College Park, MD 20742, USA
[r] University of Massachusetts Amherst, Amherst, MA 01003, USA
[s] Massachusetts Institute of Technology, Cambridge, MA 02139, USA
[t] University of New Hampshire, Durham, NH 03824, USA
[u] Norfolk State University, Norfolk, VA 23504, USA
[v] North Carolina Central University, Durham, NC 27707, USA
[w] Old Dominion University, Norfolk, VA 23508, USA
[x] Princeton University, Princeton, NJ 08544, USA
[y] University of Regina, Regina, SK S4S 0A2, Canada
[z] Rutgers, The State University of New Jersey, Piscataway, NJ 08855, USA
[aa] CEA Saclay, DAPNIA/SPhN, F-91191 Gif-sur-Yvette, France
[ab] State University of New York at Stony Brook, Stony Brook, NY 11794, USA
[ac] Syracuse University, Syracuse, NY 13244, USA
[ad] Temple University, Philadelphia, PA 19122, USA
[ae] Tohoku University, Sendai 9890, Japan
[af] TRIUMF, Vancouver, BC V6T 2A3, Canada
[ag] University of Virginia, Charlottesville, VA 22901, USA
[ah] College of William and Mary, Williamsburg, VA 23187, USA

Abstract

We have measured the parity-violating electroweak asymmetry in the elastic scattering of polarized electrons from the proton. The result is $A = -15.05 \pm 0.98\text{(stat)} \pm 0.56\text{(syst)}$ ppm at the kinematic point $\langle\theta_{\text{lab}}\rangle = 12.3°$ and $\langle Q^2 \rangle = 0.477$ (GeV/c)^2. Both errors are a factor of two smaller than those of the result reported previously. The value for the strange form factor extracted from the data is $(G_E^s + 0.392 G_M^s) = 0.025 \pm 0.020 \pm 0.014$, where the first error is experimental and the second arises from the uncertainties in electromagnetic form factors. This measurement is the first fixed-target parity violation experiment that used either a "strained" GaAs photocathode to produce highly polarized electrons or a Compton polarimeter to continuously monitor the electron beam polarization. © 2001 Published by Elsevier Science B.V.

PACS: 13.60.Fz; 11.30.Er; 13.40.Gp; 14.20.Dh

E-mail addresses: finn@physics.wm.edu (J.M. Finn),
souder@phy.syr.edu (P.A. Souder).

It is well known that strange quarks and antiquarks are present in the nucleon. An important open question is the role that sea (non-valence) quarks in general and strange quarks in particular [1] play in the fundamental properties of the nucleon. For example, do strange quarks contribute to the charge radius or magnetic moment of the proton? If so, the strange form factors G_E^s and G_M^s are relevant. A number of papers have suggested that indeed these form factors may be

large [1–10]. Others models suggest small contributions [11–14].

Strange form factors can be isolated from up and down quark form factors by measuring the parity-violating asymmetry $A = (\sigma_R - \sigma_L)/(\sigma_R + \sigma_L)$ in the elastic scattering of polarized electrons from protons [15,16]. The experiments are challenging since $A \approx A_0\tau \approx 10$ parts per million (ppm). Here $A_0 = (G_F M_p^2)/(\sqrt{2}\pi\alpha) = 316.7$ ppm, where G_F is the Fermi constant for muon decay and M_p is the proton mass. Also $\tau = Q^2/4M_p^2$ where Q^2 is the square of the four-momentum transfer. Nevertheless, several experiments have recently published results for

A [17–19]. In this Letter, we present the most precise measurement to date for *A* of the proton and determine new limits for the possible contribution of strange form factors.

Measurements of elastic electromagnetic and electroweak nucleon scattering provide three sets of vector form factors. From this information, the form factors for each flavor may be determined [20]: $G_{E,M}^u$, $G_{E,M}^d$, and $G_{E,M}^s$. A convenient alternate set, which is directly accessible in experimental measurements, is the electromagnetic form factors $G_{E,M}^{p\gamma}$, $G_{E,M}^{n\gamma}$, plus $G_{E,M}^0$. Here

$$G^0 = \frac{1}{3}(G^u + G^d + G^s),$$

$$G^{p\gamma} = \frac{2}{3}G^u - \frac{1}{3}G^d - \frac{1}{3}G^s,$$

$$G^{n\gamma} = \frac{2}{3}G^d - \frac{1}{3}G^u - \frac{1}{3}G^s,$$

where the last expression assumes charge symmetry. G^0 cannot be accessed in electromagnetic scattering and thus represents new information on nucleon dynamics that can be accessed only via measurements of the weak neutral current amplitude.

The theoretical asymmetry in the Standard Model has a convenient form in terms of G^0:

$$A_{th} = -A_0 \tau \rho'_{eq} \left(2 - 4\hat{\kappa}'_{eq}\sin^2\theta_W \right.$$
$$\left. - \frac{\varepsilon\eta_p}{\varepsilon\eta_p^2 + \tau\mu_p^2} \frac{G_E^0 + \beta G_M^0}{(G_M^{\gamma p}/\mu_p)} \right) - A_A,$$
(1)

where $\mu_p(\mu_n) \approx 2.79(-1.91)$ is the proton (neutron) magnetic moment in nuclear magnetons, $\eta_p(Q^2) = G_E^{p\gamma}(Q^2)/(G_M^{p\gamma}(Q^2)/\mu_p)$, $\varepsilon = (1 + 2(1 + \tau)\tan^2\theta/2)^{-1}$ is the longitudinal photon polarization, and $\beta = \tau\mu_p/(\varepsilon\eta_p)$. The scattering angle of the electron in the laboratory is θ. The contribution from the proton axial form factor, $A_A = (0.56 \pm 0.23)$ ppm, is calculated to be small for our kinematics [21,22]. The recent datum from the SAMPLE Collaboration [23] is 1.5 standard deviations larger than the prediction [21, 22]. The parameters $\rho'_{eq} = 0.9879$ and $\hat{\kappa}'_{eq} = 1.0029$ include the effect of electroweak radiative corrections [24], and $\sin^2\theta_W = 0.2314$. If, in addition to $G_{E,M}^0$, the proton and neutron electromagnetic form factors $G_{E,M}^{p\gamma}$ and $G_{E,M}^{n\gamma}$ are known, the strange form

factors may be determined from

$$G_{E,M}^s = G_{E,M}^0 - G_{E,M}^{p\gamma} - G_{E,M}^{n\gamma}.$$
(2)

This experiment took place in Hall A at the Thomas Jefferson National Accelerator Facility. An approximately 35 μA beam of 67–76% polarized electrons with an energy of 3.3 GeV scattered from a 15 cm liquid hydrogen target. Elastic events were detected by integrating the signal in total-absorption counters located at the focal plane of a pair of high-resolution magnetic spectrometers [18,25].

It is important that the signal be purely elastic, since background processes may have large asymmetries. For example, the production of the prominent Δ-resonance is calculated to have 3 times the asymmetry of elastic scattering [20]. To measure the rejection of unwanted events by our system, we measured the response of the detector, both in counting and integrating mode, as a function of the mismatch between the spectrometer setting and the momentum of elastic events. The result, shown in Fig. 1, is that the integrated response drops many orders of magnitude as the momentum mismatch increases. Based on these data, we determined that only 0.2% of our signal arises from inelastic background processes. Quasi-elastic scattering from the Al target windows contributed 1.5% to the measured signal. The net effect of all the backgrounds is listed in Table 1.

A new feature of the experiment is that the beam polarization $P_e \approx 70\%$. This was achieved by using
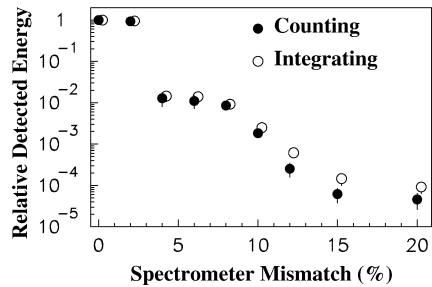

Fig. 1. Fraction of energy deposited in the detector as a function of spectrometer mismatch. The inelastic threshold corresponds to a mismatch of about 4.5%, where the response of the detector is already reduced by a factor of 100.

Table 1
Summary of corrections and contributions to the errors in % for the measured asymmetry

| Source	Correction (%)	$\delta A/A(\%)$:1998	$\delta A/A(\%)$:1999
Statistics	–	13.3	7.2
P_e	–	7.0	3.2
Q^2	–	1.8	1.8
Backgrounds	1.2	0.6	0.6
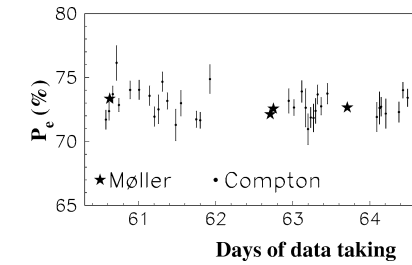
Fig. 2. Electron beam polarization for part of the run. The statistical errors on the Møller data are smaller than the points.

photoemission by circularly polarized laser light impinging on a "strained" GaAs crystal. A plot of the polarization versus time for part of the run is given in Fig. 2. The starred points are from Møller scattering and the dots are preliminary data from the recently commissioned Compton polarimeter. The errors in the Møller data have been reduced by a factor of two from those of Ref. [18] by improving our knowledge of the polarization of the electrons in the magnetized foil target and our understanding of rate effects in the Møller spectrometer. The Compton device continuously monitored the polarization of the beam on target and ruled out possible significant variations in polarizations between the daily Møller measurements. Both devices have an overall systematic error $\Delta P_e/P_e \sim 3.2\%$.

To study possible systematic errors in our small asymmetry, we sometimes inserted a second half-wave $(\lambda/2)$ plate in the laser beam at the source to reverse the sign of the helicity. Data were obtained in sets of 24–48 hour duration, and the state of the $\lambda/2$ plate was reversed for each set. The resulting asymmetries
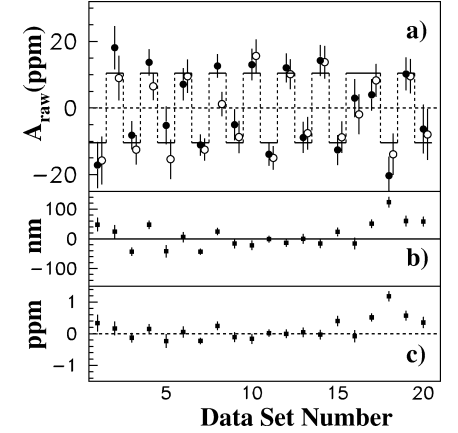

Fig. 3. (a) Raw asymmetry versus data set. Solid (open) circles are from the left (right) spectrometer. The step pattern is due to the insertion of the half-wave plate. The $\chi^2 = 33.7$ for 39 degrees of freedom. (b) Helicity-correlated horizontal position difference measured near the target. (c) Correction to left spectrometer data due to all of the beam parameter differences. The corrections for the right spectrometer are smaller.

are shown in Fig. 3(a). The asymmetry reverses as expected but otherwise behaves statistically.

The strained GaAs crystal, in contrast to the bulk GaAs used for our previous work [18], has a large analyzing power for linearly polarized light [26]. The consequence was a tendency for much larger helicity-correlated differences in the beam position. We found that an additional half-wave plate in the laser beam reduced this problem to a manageable level. In addition, the intensity asymmetry of the beam in another experimental hall was nulled to prevent beam loading in the accelerator from inducing position correlations in our beam. The remaining position and energy differences were measured with precision microwave monitors. One example of monitor data is shown in Fig. 3(b). The effect of these beam differences on the asymmetry was measured by calibrating the apparatus with beam correction coils and an energy vernier. The resultant correction, shown in Fig. 3(c), proved to have an average of 0.02 ± 0.02 ppm.

The experimental asymmetry, corrected for the measured beam polarization, is $A_{exp} = -15.1$ at $Q^2 = 0.477$ $(GeV/c)^2$ for the 1999 data. We also include the previously reported 1998 data [18], which gives $A_{exp} = -14.7$ ppm when extrapolated to the same Q^2 value but with approximately twice the statistical and systematic errors. In addition, three small corrections based on subsequent data analysis were made to the 1998 data: (i) the background correction was included; (ii) the measured beam polarization was reduced by 1.5%; and (iii) the Q^2 value was determined to be 0.474 $(GeV/c)^2$ instead of 0.479 $(GeV/c)^2$. An increase of 1% in Q^2 is expected to increase the magnitude of the asymmetry by 1.5%. The errors for the full data set are given in Table 1. Systematic errors in the beam polarimetry and in the measurement of the spectrometer angle were the most significant sources. The combined result is $A_{exp} - 15.05 \pm 0.98(stat) \pm 0.56(syst)$ ppm at the average kinematics $Q^2 = 0.477$ $(GeV/c)^2$ and $\theta = 12.3°$. This is the average asymmetry over the finite solid angle of the spectrometers; we estimate the value at the center of acceptance is smaller by 0.7%.

By using Eq. (1) and the theoretical value for A_A [21,22], we obtain $(G_E^0 + \beta G_M^0)/(G_M^{p\gamma}/\mu_p) = 1.527 \pm 0.048 \pm 0.027 \pm 0.011$. Here the first error is statistical, the second systematic, and the last error is due to the uncertainty from A_A. For our kinematics $\beta = 0.392$. The sensitivity to η_p is negligible. To determine the contribution due to strange form factors, we use Eq. 2 and data for the electromagnetic form factors. The values we use [27–34] are summarized in Table 2. Thus we have $G_E^s + \beta G_M^s = 0.025 \pm 0.020 \pm 0.014$, where the first error is the errors in G^0 combined in quadrature and the second due to the electromagnetic form factors. This value is consistent

with the hypothesis that the strange form factors are negligible.

We note that there are data for G_M^n [35] that are less precise but at variance with those of Ref. [29]. Our result for $G_E^s + \beta G_M^s$ would increase by 0.020 if the data from Ref. [35] were used. New data for both G_M^n and G_E^n are in the early stages of analysis and will be important both for validating our choices and also for interpreting future data on strange form factors.

In Fig. 4, we plot the above value for $G_E^s + \beta G_M^s$ as a band with the errors added in quadrature. The dots represent the predictions from those models that apply at our value of Q^2. Our result restricts significantly the possible "parameter space" for strangeness to be an important degree of freedom in nucleon form factors. However, our data are compatible with several models that predict large strange form factors, including two with $G_E^s \approx -0.39\,G_M^s$ [8,9], and one where the prediction happens to cross zero near our Q^2 value [5].

Our collaboration has two new experiments approved at JLab for a kinematic point at $Q^2 \sim 0.1$ $(GeV/c)^2$. One, using a hydrogen target, will measure

Table 2
Electromagnetic form factors normalized to G_M^p/μ_p. The last column is the error in A_{th} from the quoted error in the corresponding form factor

Form factor	Value	Ref.	$\delta A_{th}/A_{th}$
$G_E^p/(G_M^p/\mu_p)$	0.99 ± 0.02	[27,28]	3%
$G_E^n/(G_M^p/\mu_p)$	0.16 ± 0.03	[30–34]	4%
$(G_M^n/\mu_n)/(G_M^p/\mu_p)$	1.05 ± 0.02	[29]	2%
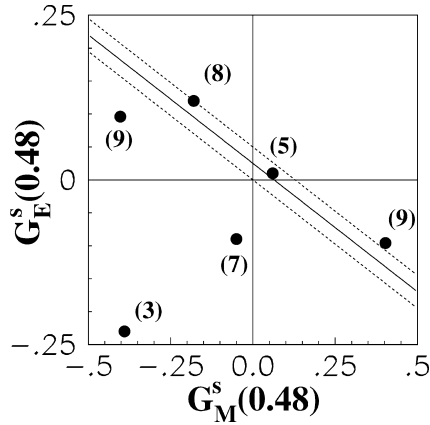
Fig. 4. Plot of G_E^s versus G_M^s at $Q^2 = 0.477$ $(GeV/c)^2$. The band is the allowed region derived from our results. The width of the band is computed by adding the errors in quadrature. The points are various estimates from models that make predictions at our value of Q^2. The numbers in the brackets are the reference of the models. Ref. [9] is plotted twice due to an ambiguity in the predicted sign.

the same combination of strange form factors at a low Q^2 [36] and the other, using a ^{4}He target, will be sensitive to G_E^s but not G_M^s [37]. Thus these experiments might detect the presence of strange form factors that cannot be excluded by the present result.

References

[1] P. Geiger, N. Isgur, Phys. Rev. D 55 (1997) 299.
[2] R.L. Jaffe, Phys. Lett. B 229 (1989) 275.
[3] H.-W. Hammer, U.-G. Meissner, D. Drechsel, Phys. Lett. B 367 (1996) 323.
[4] M.J. Musolf, M. Burkhardt, Z. Phys. C 61 (1994) 433.
[5] H. Weigel et al., Phys. Lett. B 353 (1995) 20.
[6] N.W. Park, J. Schecter, H. Weigel, Phys. Rev. D 43 (1991) 869.
[7] N.W. Park, H. Weigel, Nucl. Phys. A 541 (1992) 453.
[8] S.J. Dong, K.F. Liu, A.G. Williams, Phys. Rev. D 58 (1998) 074504.
[9] H.-W. Hammer, M.J. Ramsey-Musolf, Phys. Rev. C 60 (1999) 045205.
[10] S.-T. Hong, B.-Y. Park, D.-P. Min, Phys. Lett. B 414 (1997) 229.
[11] H. Ito, Phys. Rev. C 52 (1995) R1750.
[12] W. Koepf, E.M. Henley, J.S. Pollock, Phys. Lett. B 288 (1992) 11.
[13] U.-G. Meissner, V. Mull, J. Speth, J.W. Van Orden, Phys. Lett. B 408 (1997) 381.
[14] B.-Q. Ma, Phys. Lett. B 408 (1997) 387.
[15] D.B. Kaplan, A. Manohar, Nucl. Phys. B 310 (1988) 527.
[16] R.D. McKeown, Phys. Lett. B 219 (1989) 140.
[17] B. Mueller et al., Phys. Rev. Lett. 78 (1997) 3824.
[18] K. Aniol et al., Phys. Rev. Lett. 82 (1999) 1096.
[19] D.T. Spayde et al., Phys. Rev. Lett. 84 (2000) 1106.
[20] M.J. Musolf et al., Phys. Rep. 239 (1994) 1, and references therein.
[21] M.J. Musolf, B.R. Holstein, Phys. Lett. B 242 (1990) 461.
[22] S.-L. Zhu et al., Phys. Rev. D 62 (2000) 033008.
[23] R. Hasty et al., Science 290 (2000) 2117.
[24] Particle Data Group, C. Caso et al., Eur. Phys. J. C 3 (1998) 1. The electroweak radiative corrections are essentially the same as for atoms. In addition, the peaking approximation is used to correct for the radiative tail.
[25] W.E. Kahl, Ph.D. Thesis Syracuse University, 2000; G.W. Miller, Ph.D. Thesis, Princeton University, 2000; See also: K.S. Kumar, P.A. Souder, Prog. Part. Nucl. Phys. 45 (2000) S333.
[26] R.A. Mair et al., Phys. Lett. A 212 (1996) 231.
[27] R.C. Walker et al., Phys. Rev. D 49 (1994) 5671.
[28] M.K. Jones et al., Phys. Rev. Lett. 84 (2000) 1398.
[29] H. Anklin et al., Phys. Lett. B 428 (1998) 248.
[30] I. Passchier et al., Phys. Rev. Lett. 82 (1999) 4988.
[31] C. Herberg et al., Eur. Phys. J. A 5 (1999) 131.
[32] M. Ostrick et al., Phys. Rev. Lett. 83 (1999) 276.
[33] J. Becker et al., Eur. Phys. J. A 6 (1999) 329.
[34] D. Rohe et al., Phys. Rev. Lett. 83 (1999) 4257.
[35] E.E.W. Bruins et al., Phys. Rev. Lett. 75 (1995) 21. We have corrected these data down by 25% of these and those of Ref. [29], based on a private communication from B. Schoch.
[36] JLab experiment E99-115, K. Kumar and D. Lhuillier, spokespersons.
[37] JLab experiment E00-114, D. Armstrong and R. Michaels, spokespersons.

HAPPEX Collaboration, A. Acha et al., Phys. Rev. Lett. 98 (2007) 032301.

Precision Measurements of the Nucleon Strange Form Factors at $Q^2 \sim 0.1$ GeV^2

A. Acha,[1] K. A. Aniol,[2] D. S. Armstrong,[3] J. Arrington,[4] T. Averett,[3] S. L. Bailey,[3] J. Barber,[5] A. Beck,[6] H. Benaoum,[7]
J. Benesch,[8] P. Y. Bertin,[9] P. Bosted,[8] F. Butaru,[10] E. Burtin,[11] G. D. Cates,[12] Y.-C. Chao,[8] J.-P. Chen,[8] E. Chudakov,[8]
E. Cisbani,[13] B. Craver,[12] F. Cusanno,[13] R. De Leo,[14] P. Decowski,[15] A. Deur,[8] R. J. Feuerbach,[8] J. M. Finn,[3] S. Frullani,[13]
S. A. Fuchs,[3] K. Fuoti,[5] R. Gilman,[16,8] L. E. Glesener,[3] K. Grimm,[3] J. M. Grames,[8] J. O. Hansen,[8] J. Hansknecht,[8]
D. W. Higinbotham,[8] R. Holmes,[7] T. Holmstrom,[3] H. Ibrahim,[17] C. W. de Jager,[8] X. Jiang,[16] J. Katich,[3] L. J. Kaufman,[5]
A. Kelleher,[3] P. M. King,[18] A. Kolarkar,[19] S. Kowalski,[6] E. Kuchina,[16] K. S. Kumar,[5] L. Lagamba,[14] P. LaViolette,[5]
J. LeRose,[8] R. A. Lindgren,[12] D. Lhuillier,[11] N. Liyanage,[12] D. J. Margaziotis,[2] P. Markowitz,[1] D. G. Meekins,[8]
Z.-E. Meziani,[10] R. Michaels,[8] B. Moffit,[3] S. Nanda,[8] V. Nelyubin,[12,20] K. Otis,[5] K. D. Paschke,[5] S. K. Phillips,[3]
M. Poelker,[8] R. Pomatsalyuk,[21] M. Potokar,[22] Y. Prok,[12] A. Puckett,[6] Y. Qian,[23] Y. Qiang,[6] B. Reitz,[8] J. Roche,[8] A. Saha,[8]
B. Sawatzky,[10] J. Singh,[12] K. Slifer,[10] S. Sirca,[6] R. Snyder,[12] P. Solvignon,[10] P. A. Souder,[7] M. L. Stutzman,[8] R. Subedi,[24]
R. Suleiman,[6] V. Sulkosky,[3] W. A. Tobias,[12] P. E. Ulmer,[17] G. M. Urciuoli,[13] K. Wang,[12] A. Whitbeck,[8] R. Wilson,[25]
B. Wojtsekhowski,[8] H. Yao,[10] Y. Ye,[26] X. Zhan,[6] X. Zheng,[6,4] S. Zhou,[27] and V. Ziskin[6]

(HAPPEX Collaboration)

[1]*Florida International University, Miami, Florida 33199, USA*
[2]*California State University, Los Angeles, Los Angeles, California 90032, USA*
[3]*College of William and Mary, Williamsburg, Virginia 23187, USA*
[4]*Argonne National Laboratory, Argonne, Illinois 60439, USA*
[5]*University of Massachusetts Amherst, Amherst, Massachusetts 01003, USA*
[6]*Massachusetts Institute of Technology, Cambridge, Massachusetts 02139, USA*
[7]*Syracuse University, Syracuse, New York 13244, USA*
[8]*Thomas Jefferson National Accelerator Facility, Newport News, Virginia 23606, USA*
[9]*Université Blaise Pascal/CNRS-IN2P3, F-63177 Aubière, France*
[10]*Temple University, Philadelphia, Pennsylvania 19122, USA*
[11]*CEA Saclay, DAPNIA/SPhN, F-91191 Gif-sur-Yvette, France*
[12]*University of Virginia, Charlottesville, Virginia 22904, USA*
[13]*Istituto Nazionale di Fisica Nucleare, Sezione Sanità, 00161 Roma, Italy*
[14]*Istituto Nazionale di Fisica Nucleare, Sezione di Bari and University of Bari, I-70126 Bari, Italy*
[15]*Smith College, Northampton, Massachusetts 01063, USA*
[16]*Rutgers, The State University of New Jersey, Piscataway, New Jersey 08855, USA*
[17]*Old Dominion University, Norfolk, Virginia 23529, USA*
[18]*University of Illinois, Urbana, Illinois 61801, USA*
[19]*University of Kentucky, Lexington, Kentucky 40506, USA*
[20]*St. Petersburg Nuclear Physics Institute of Russian Academy of Science, Gatchina, 188350, Russia*
[21]*Kharkov Institute of Physics and Technology, Kharkov 310108, Ukraine*
[22]*Jozef Stefan Institute, 1000 Ljubljana, Slovenia*
[23]*Duke University, TUNL, Durham, North Carolina 27706, USA*
[24]*Kent State University, Kent, Ohio 44242, USA*
[25]*Harvard University, Cambridge, Massachusetts 02138, USA*
[26]*University of Science and Technology of China, Heifei, Anhui 230026, China*
[27]*China Institute of Atomic Energy, Beijing 102413, China*
(Received 6 September 2006; published 18 January 2007)

We report new measurements of the parity-violating asymmetry A_{PV} in elastic scattering of 3 GeV electrons off hydrogen and ^{4}He targets with $\langle \theta_{lab} \rangle \approx 6.0^\circ$. The ^{4}He result is $A_{PV} = (+6.40 \pm 0.23(\text{stat}) \pm 0.12(\text{syst})) \times 10^{-6}$. The hydrogen result is $A_{PV} = (-1.58 \pm 0.12(\text{stat}) \pm 0.04(\text{syst})) \times 10^{-6}$. These results significantly improve constraints on the electric and magnetic strange form factors G_E^s and G_M^s. We extract $G_E^s = 0.002 \pm 0.014 \pm 0.007$ at $\langle Q^2 \rangle = 0.077$ GeV^2, and $G_E^s + 0.09 G_M^s = 0.007 \pm 0.011 \pm 0.006$ at $\langle Q^2 \rangle = 0.109$ GeV^2, providing new limits on the role of strange quarks in the nucleon charge and magnetization distributions.

Over the past several decades, high-energy lepton-nucleon scattering has revealed the rich structure of the nucleon over a wide range of length scales. In recent years, increasingly sensitive measurements of elastic electron-nucleon scattering, mediated by photon exchange and Z^0 exchange, have enabled the measurement of the electromagnetic and neutral weak form factors. These functions of the 4-momentum transfer Q^2 characterize nucleon charge and magnetization distributions.

In particular, the neutral weak form factor measurements provide a way to probe dynamics of the "sea" of virtual light (up, down, and strange) quark-antiquark pairs that surrounds each valence quark in the nucleon. Since the Z^0 boson couples to various quarks with different relative strengths compared to the photon, a combined analysis of proton and neutron electromagnetic form factor and proton neutral weak form factor measurements, along with the assumption of charge symmetry, allows the determination of the strange electric and magnetic form factors G_E^s and G_M^s [1,2].

The established experimental technique to measure the electron-nucleon weak neutral current amplitude is parity-violating electron scattering [3,4]. Longitudinally polarized electron scattering off unpolarized targets can access a parity-violating asymmetry $A_{PV} \equiv (\sigma_R - \sigma_L)/(\sigma_R + \sigma_L)$, where $\sigma_{R(L)}$ is the cross section for incident right-(left-)handed electrons. Arising from the interference of the weak and electromagnetic amplitudes, A_{PV} increases with Q^2 [5].

Four experimental programs have been designed to access the Q^2 range of 0.1 to 1 GeV^2, where the A_{PV} expectations range from one to tens of parts per million (ppm). The published measurements [6–12] are mutually consistent. An intriguing pattern in the low-Q^2 behavior seen in [9,10] has marginal statistical significance.

In this Letter, we significantly improve our two previous measurements [11,12] of A_{PV} in elastic electron scattering from ^{1}H and ^{4}He nuclei. Since A_{PV} for ^{1}H is sensitive to a linear combination of G_E^s and G_M^s while that for ^{4}He is sensitive only to G_E^s, a simultaneous analysis of both measurements results in the most precise determination to date of G_E^s and G_M^s at $Q^2 \sim 0.1$ GeV^2.

The measurements were carried out in Hall A at the Thomas Jefferson National Accelerator Facility (JLab). As described in detail in two previous publications [11,12], a 35 to 55 μA continuous-wave beam of $\sim$3 GeV longitudinally polarized electrons was incident on 20 cm long cryogenic targets. Elastically scattered electrons were focused into background-free regions by a symmetric pair of high-resolution spectrometer systems. The scattered flux was intercepted by identical detector segments in each arm (two for ^{1}H, one for ^{4}He), resulting in Cherenkov light collected by photomultiplier tubes (PMTs).

The helicity of the electron beam, generated by photoemission off a GaAs wafer, is determined by the handed-ness of the incident laser light's circular polarization. This was selected pseudorandomly at 15 Hz and toggled to the opposing helicity after 33.3 ms, with each of these equal periods of constant helicity referred to as a "window." PMT and beam monitor responses for two consecutive windows of opposite helicity were carefully designed and grouped as a "pair" for asymmetry analysis.

The beam monitors, target, detector components, electronics, and accelerator tune were optimized such that the fluctuation in the PMT response over a pair was dominated by counting statistics of the scattered flux for rates up to 100 MHz. This facilitated A_{PV} measurements with statistical uncertainty as small as 100 parts per billion (ppb) in a reasonable length of time. To keep spurious beam-induced asymmetries under control at this level, the laser optics leading to the photocathode were carefully designed and monitored. Indeed, averaged over the entire period of data collection with the hydrogen target, the achieved level of control surpassed all previous benchmarks, as summarized in Table I.

The data collection took place over 55 days (^{4}He) and 36 days (^{1}H). A half-wave ($\lambda/2$) plate was periodically inserted into the laser optical path which passively reversed the sign of the electron beam polarization. With roughly equal statistics in each state, many systematic effects were suppressed. There were 121 (^{4}He) and 41 (^{1}H) such reversals. The data set between two successive $\lambda/2$ reversals is referred to as a "slug."

Loose requirements were imposed on beam quality to remove periods of instability, leaving about 95% of the data sample for further analysis. No helicity-dependent cuts were applied. The final data sample consisted of 35.0×10^6 (^{4}He) and 26.4×10^6 (^{1}H) pairs. The right−left helicity asymmetry in the integrated detector response, normalized to the beam intensity, was computed for each pair to form the raw asymmetry A_{raw}. The dependence of A_{raw} on fluctuations in the five correlated beam parameter differences Δx_i is quantified as $A_{beam} = \sum c_i \Delta x_i$, where the coefficients c_i quantify the A_{raw} beam parameter sensitivity. The electroweak physics of the signal and backgrounds is contained in $A_{corr} = A_{raw} - A_{beam}$.

TABLE I. Average beam asymmetries under polarization reversal in intensity and energy and differences in horizontal and vertical position (Δx, Δy) and angle ($\Delta x'$, $\Delta y'$).

	Helium	Hydrogen
$A_{intensity}$	−0.377 ppm	0.406 ppm
A_{energy}	3 ppb	0.2 ppb
Δx	−0.2 nm	0.5 nm
$\Delta x'$	4.4 nrad	−0.2 nard
Δy	−26 nm	1.7 nm
$\Delta y'$	−4.4 nrad	0.2 nrad

TABLE II. Raw and corrected asymmetries (in ppm) and reduced slug χ^2 ($r\chi^2$), broken up by $\lambda/2$ reversals. The differences between A_{raw} and A_{corr} result from corrections for energy, position, and angle differences.

	$\lambda/2$ OUT		$\lambda/2$ IN		BOTH	
^{4}He	(DOF = 59)		(DOF = 60)		(DOF = 120)	
	Asym.	$r\chi^2$	Asym.	$r\chi^2$	Asym.	$r\chi^2$
A_{raw}	4.80 ± 0.27	0.75	-5.41 ± 0.27	1.12	5.10 ± 0.19	0.95
A_{corr}	5.12 ± 0.27	0.78	-5.38 ± 0.27	1.07	5.25 ± 0.19	0.92
^{1}H	(DOF = 20)		(DOF = 19)		(DOF = 40)	
A_{raw}	-1.40 ± 0.15	0.73	1.42 ± 0.15	1.04	-1.41 ± 0.11	0.86
A_{corr}	-1.41 ± 0.15	0.81	1.43 ± 0.15	1.02	-1.42 ± 0.11	0.89

The A_{corr} window-pair distributions for the two complete data samples were perfectly Gaussian over more than 4 orders of magnitude with rms widths of 1130 ppm (^{4}He) and 540 ppm (^{1}H); the dominant source of noise in the PMT response was counting statistics. To further test that the data behaved statistically, A_{corr} averages and statistical errors for typical 1 h runs, consisting of about 50 k pairs each, were studied. Each set of roughly 400 average A_{corr} values, normalized by the corresponding statistical errors, populated a Gaussian distribution of unit variance as expected.

Systematic effects in A_{beam} estimations were studied. When averaged over all detector segments, the coefficients c_i were much smaller than those for individual detector segments due to the symmetric geometry of the apparatus. Limits on systematic uncertainties in the c_i's in the range of 10% to 30% were set by inspecting residual correlations of A_{corr}'s of individual detector segments with helicity-correlated beam asymmetries.

Another important validation was to use two independent methods to calculate c_i. The first relied on linear regression of the observed response of the detector PMTs to intrinsic beam fluctuations. The other used calibration data in which the beam was modulated, by amounts large compared to intrinsic beam fluctuations, using steering magnets and an accelerating cavity. Differences in the two A_{beam} calculations were always much smaller than corresponding A_{corr} statistical errors.

Final A_{corr} results were calculated using the beam modulation technique and are summarized in Table II. Because of the excellent control of beam parameter differences Δx_i summarized in Table I, $A_{\text{corr}} - A_{\text{raw}}$ values are of the order of, or much smaller than, the corresponding statistical errors. Under $\lambda/2$ reversal, the absolute values of A_{corr} are consistent within statistical errors. The reduced χ^2 for A_{corr} "slug" averages is close to 1 in every case, indicating that any residual beam-related systematic effects were small and randomized over the time period of $\lambda/2$ reversals (typically 5 to 10 h). The final A_{corr} results are $A_{\text{corr}}^{\text{He}} = +5.25 \pm 0.19(\text{stat}) \pm 0.05(\text{syst})$ ppm and $A_{\text{corr}}^{\text{H}} = -1.42 \pm 0.11(\text{stat}) \pm 0.02(\text{syst})$ ppm.

The physics asymmetry A_{phys} is formed from A_{corr},

$$A_{\text{phys}} = \frac{K}{P_b} \frac{A_{\text{corr}} - P_b \sum_i A_i f_i}{1 - \sum_i f_i}, \quad (1)$$

with corrections for the beam polarization P_b, background fractions f_i with asymmetries A_i and finite kinematic acceptance K. These corrections are summarized in Table III. The first line lists the cumulative A_{beam} corrections discussed above, scaled by K/P_b.

A powerful feature of the apparatus is the spectrometers' ability to focus the elastically scattered electrons into a compact region. Indeed, much less than 1% of the flux intercepted by the detectors originated from inelastic scattering in the target cryogen. Figure 1 shows charged particle spectra obtained with dedicated low-intensity runs and measured by drift chambers in front of the detectors. The dominant background was quasielastic (QE) scattering from target windows, separately measured using an equivalent aluminum target and computed to be $1.8 \pm 0.2\%$ (^{4}He) and $0.76 \pm 0.25\%$ (^{1}H).

An electron must give up more than 19 MeV to break up the ^{4}He nucleus and undergo quasielastic scattering off nucleons. Figure 1 shows that the quasielastic threshold lies beyond the edge of the detector. A limit of $0.15 \pm 0.15\%$ on this background was placed by detailed studies of the low-intensity data. For ^{1}H, the π^0 threshold is

TABLE III. Corrections to A_{corr} and systematic errors.

| Correction (ppb)	Helium	Hydrogen
Beam asyms.	183 ± 59	-10 ± 17
Target window bkg.	113 ± 32	7 ± 19
Helium QE bkg.	12 ± 20	$\cdots$
Rescatter bkg.	20 ± 15	2 ± 4
Nonlinearity	0 ± 58	0 ± 15
Scale factor	**Helium**	**Hydrogen**
Acceptance factor K	1.000 ± 0.001	0.979 ± 0.002
Q^2 Scale	1.000 ± 0.009	1.000 ± 0.017
Polarization P_b	0.844 ± 0.008	0.871 ± 0.009
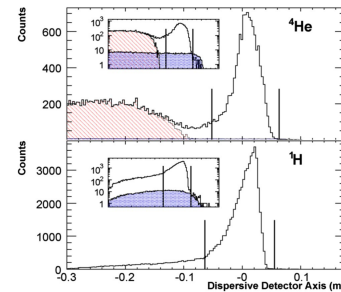
FIG. 1 (color online). Single-particle spectra obtained in dedicated low-current runs. The insets show the same spectra on a logarithmic scale. The vertical lines delineate the extent of the detectors. Inelastic scattering from ^{4}He is entirely contained in the hatched area. The shaded regions, visible only in the log plots, show the contribution from target windows.

beyond the extent of the plot; direct background from inelastic scattering is thus negligible.

Background from rescattering in the spectrometer apertures was studied by varying the spectrometer momentum in dedicated runs to measure inelastic spectra and to obtain the detector response as a function of scattered electron energy under running conditions. From these two distributions, the rescattering background was estimated to be $0.25 \pm 0.15\%$ (^{4}He) and $0.10 \pm 0.05\%$ (^{1}H).

For each source of background, a theoretical estimate for A_{PV} was used, with relative uncertainties taken to be 100% or more to account for kinematic variations and resonance contributions. The resulting corrections and the associated errors are shown in Table III. Upper limits on rescattering contributions from exposed iron in the spectrometer led to an additional uncertainty of 5 ppb.

Nonlinearity in the PMT response was limited to 1% in bench tests that mimicked running conditions. The relative nonlinearity between the PMT response and those of the beam intensity monitors was <2%. A nuclear recoil technique using a water-cell target [11] was used to determine the scattering angle θ_{lab}, thus keeping the scale error on $\langle Q^2 \rangle$ due to θ_{lab} to be <0.2%. The acceptance correction K accounted for the nonlinear dependence of the asymmetry with Q^2.

The beam polarization P_b was continuously monitored by a Compton polarimeter; results, averaged over the duration of each run, are listed in Table III. Redundant cross calibration of the recoil Compton electron spectrum restricted the relative systematic error to $\approx 1\%$. The results

were consistent, within systematic uncertainties, with those obtained from recoil Compton photon asymmetries, and with dedicated measurements using Møller scattering in the experimental hall and Mott scattering at low energy. Throughout the asymmetry and background analysis, blinding offsets were maintained on both results. After all corrections:

$$A_{\text{phys}}^{\text{He}} = +6.40 \pm 0.23(\text{stat}) \pm 0.12(\text{syst}) \text{ ppm},$$

$$A_{\text{phys}}^{\text{H}} = -1.58 \pm 0.12(\text{stat}) \pm 0.04(\text{syst}) \text{ ppm}.$$

The theoretical predictions $A_{\text{NS}}^{\text{He}}$ and A_{NS}^{H} with $G^s = 0$ were estimated using the formalism in [4] and described in our previous publications [11,12]. The electroweak radiative corrections, calculated using the $\overline{\text{MS}}$ renormalization scheme, introduced negligible uncertainties.

Assuming a pure isoscalar $0^+ \rightarrow 0^+$ transition, $A_{\text{NS}}^{\text{He}}$ is completely independent of nuclear structure and determined purely by electroweak parameters. D-state and isospin admixtures and meson exchange currents are negligible at the level of the experimental fractional accuracy of $\sim 3\%$ [13]. For our kinematics ($E_b = 2.75$ GeV, $\langle Q^2 \rangle = 0.077$ GeV^2) we obtain $A_{\text{NS}}^{\text{He}} = +6.37$ ppm.

Electromagnetic form factors from a phenomenological fit to the world data at low Q^2 [14] were used to calculate A_{NS}^{H}, with uncertainties governed by data near $Q^2 \sim 0.1$ GeV^2. The value used for $G_E^{\gamma n} = 0.037$, with a 10% relative uncertainty based on new data from the BLAST experiment [15]. For our kinematics ($E_b = 3.18$ GeV,
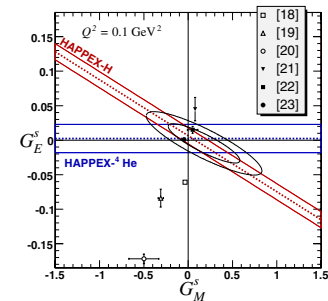

FIG. 2 (color online). 68% and 95% C.L. constraints in the $G_E^s - G_M^s$ plane from data from this apparatus ([11,12] and this Letter). Various theoretical predictions are plotted with published uncertainty estimates, when available. The $1-\sigma$ bands (a quadrature sum of statistical and systematic errors) and central values (dashed lines) from the new results alone are also shown.

$\langle Q^2 \rangle = 0.109$ GeV^2) we obtain $A_{\mathrm{NS}}^{\mathrm{H}} = -1.66 \pm 0.05$ ppm. This includes a contribution from the axial form factor G_A^Z, and associated radiative corrections [16], of -0.037 ± 0.018 ppm.

Comparing our results with the theoretical expectations, we extract $G_E^s = 0.002 \pm 0.014 \pm 0.007$ at $Q^2 = 0.077$ GeV^2 and $G_E^s + 0.09 G_M^s = 0.007 \pm 0.011 \pm 0.004 \pm 0.005$ (FF) at $Q^2 = 0.109$ GeV^2, where the uncertainties in the nucleon electromagnetic form factors govern the last error. Figure 2 displays the combined result for these and our previous measurements [11,12], taken with $\langle Q^2 \rangle$ between 0.077–0.109 GeV^2. The requisite small extrapolation to a common $Q^2 = 0.1$ GeV^2 was made assuming that $G_E^s \propto Q^2$ and that G_M^s is constant. The values $G_E^s = -0.005 \pm 0.019$ and $G_M^s = 0.18 \pm 0.27$ (correlation coefficient $= -0.87$) are obtained. The results are quite insensitive to variations in G_A^Z, as evidenced by the negligible change induced by an alternate fit similar to that in [17], where G_A^Z is constrained by other A_{PV} data.

Figure 2 also displays predictions from selected theoretical models [18–23]. Those that predict little strange quark dynamics in the vector form factors are favored [22,23]. A global fit to all low-Q^2 measurements of G_E^s and G_M^s, similar to that performed in [17], finds that other measurements [6,9,10] which had suggested nonzero strangeness effects are consistent, within quoted uncertainties, with our results at $Q^2 = 0.1$ GeV^2. Because of the improved statistical precision and lower G_A^Z sensitivity of our result, adding these other measurements in a global fit does not alter our conclusions.

In summary, we have reported the most precise constraints on the strange form factors at $Q^2 \sim 0.1$ GeV^2. The results, consistent within errors with other A_{PV} measurements, leave little room for observable nucleon strangeness dynamics at low Q^2. Theoretical uncertainties, especially regarding the assumption of charge symmetry [24], preclude significant improvement to the measurements reported here. While future experiments will pursue the search for nonzero strangeness at higher Q^2, it now becomes a challenge for various theoretical approaches to reconcile these results and enhance our understanding of nucleon structure.

[1] D. B. Kaplan and A. Manohar, Nucl. Phys. **B310**, 527 (1988).
[2] R. D. McKeown, Phys. Lett. B **219**, 140 (1989).
[3] C. Y. Prescott *et al.*, Phys. Lett. B **77**, 347 (1978).
[4] M. J. Musolf *et al.*, Phys. Rep. **239**, 1 (1994).
[5] Ya. B. Zel'dovich, J. Exp. Theor. Phys. **36**, 964 (1959).
[6] D. T. Spayde *et al.*, Phys. Lett. B **583**, 79 (2004).
[7] K. A. Aniol *et al.*, Phys. Lett. B **509**, 211 (2001); K. A. Aniol *et al.*, Phys. Rev. C **69**, 065501 (2004).
[8] F. E. Maas *et al.*, Phys. Rev. Lett. **93**, 022002 (2004).
[9] F. E. Maas *et al.*, Phys. Rev. Lett. **94**, 152001 (2005).
[10] D. S. Armstrong *et al.*, Phys. Rev. Lett. **95**, 092001 (2005).
[11] K. A. Aniol *et al.*, Phys. Rev. Lett. **96**, 022003 (2006).
[12] K. A. Aniol *et al.*, Phys. Lett. B **635**, 275 (2006).
[13] M. J. Musolf, R. Schiavilla, and T. W. Donnelly, Phys. Rev. C **50**, 2173 (1994); S. Ramavataram, E. Hadjimichael, and T. W. Donnelly, Phys. Rev. C **50**, 1175 (1994); M. J. Musolf and T. W. Donnelly, Phys. Lett. B **318**, 263 (1993).
[14] J. Friedrich and Th. Walcher, Eur. Phys. J. A **17**, 607 (2003).
[15] V. Ziskin, Ph.D. thesis, MIT, 2005.
[16] S.-L. Zhu *et al.*, Phys. Rev. D **62**, 033008 (2000).
[17] R. Young *et al.*, Phys. Rev. Lett. **97**, 102002 (2006).
[18] N. W. Park and H. Weigel, Nucl. Phys. **A541**, 453 (1992).
[19] H. W. Hammer, U. G. Meissner, and D. Drechsel, Phys. Lett. B **367**, 323 (1996).
[20] H. W. Hammer and M. J. Ramsey-Musolf, Phys. Rev. C **60**, 045204 (1999).
[21] A. Silva *et al.*, Phys. Rev. D **65**, 014016 (2001).
[22] R. Lewis *et al.*, Phys. Rev. D **67**, 013003 (2003).
[23] D. B. Leinweber *et al.*, Phys. Rev. Lett. **94**, 212001 (2005); **97**, 022001 (2006).
[24] B. Kubis and R. Lewis, Phys. Rev. C **74**, 015204 (2006).

S. Escoffier et al., Nuclear instruments and Methods in Physics Research A 551 (2005).

Accurate measurement of the electron beam polarization in JLab Hall A using Compton polarimetry

S. Escoffier[a,1], P.Y. Bertin[b], M. Brossard[b], E. Burtin[b], C. Cavata[a],
N. Colombel[a], C.W. de Jager[c], A. Delbart[a], D. Lhuillier[a,*], F. Marie[a],
J. Mitchell[c,2], D. Neyret[a], T. Pussieux[a]

[a]CEA Saclay, DSM/DAPNIA/SPhN bat 703, F-91191 Gif-sur-Yvette Cedex, France
[b]Université Blaise Pascal et CNRS/IN2P3 LPC, 6F-3177 Aubière Cedex, France
[c]Jefferson Lab, 12000 Jefferson Avenue, Newport News, VA 23606, USA

Abstract

A major advance in accurate electron beam polarization measurement has been achieved at Jlab Hall A with a Compton polarimeter based on a Fabry–Perot cavity photon beam amplifier. At an electron energy of 4.6 GeV and a beam current of 40 μA, a total relative uncertainty of 1.5% is typically achieved within 40 min of data taking. Under the same conditions monitoring of the polarization is accurate at a level of 1%. These unprecedented results make Compton polarimetry an essential tool for modern parity-violation experiments, which require very accurate electron beam polarization measurements.
© 2005 Elsevier B.V. All rights reserved.

*Corresponding author. Tel. 33 1 69 08 94 97,
fax: 33 1 69 08 75 84.
  E-mail address: dlhuillier@cea.fr (D. Lhuillier).
[1]Present address: CNRS/IN2P3/Centre de Physique des
Particules de Marseille, 163 avenue de Luminy, 13288 Marseille
Cedex 09, France.
[2]Present address: Renaissance Technologies Corp., Setauket,
NY 11733, USA.

1. Introduction

The Continuous Electron Beam Accelerator Facility (CEBAF) at the Jefferson Laboratory (JLab) is a new particle accelerator which makes extensive use of its highly polarized electron beam for the study of nucleons and nuclei. The polarization is measured at the injector with a 5 MeV

Mott polarimeter and in the Hall A beam line with a Møller polarimeter and a Compton polarimeter. Mott and Møller polarimeters require solid targets and operate respectively at low energy and at low intensity ($\approx 1\mu A$). Because of its thin ''photon target'', only Compton backscattering polarimetry provides an essential tool for accurate measurement and monitoring of the beam polarization under the same conditions as the running experiment. However, the mean Compton analyzing power (A_c) depends strongly on the beam energy — $A_c \approx 0.4\%/\text{GeV}$ — while the total cross-section is approximately constant at 0.6 barn. Therefore, the typical beam conditions provided by CEBAF, an energy of several GeV and a beam intensity up to 100 μA, require a high laser power to provide the required interaction luminosity. The design of the Compton polarimeter was challenging [1,2]. The photon density is amplified with a Fabry–Perot cavity of very high finesse which provides a power of 1700 W of IR light at the Compton interaction point. This performance, unequalled in a particle accelerator environment, results in a statistical accuracy for a polarization measurement below 1% within an hour at 4.6 GeV [3]. This number scales with the inverse of the beam energy.

In Section 2, we briefly summarize the experimental set-up of the Compton polarimeter. Section 3 describes its operational properties achieved during two polarized experiments, $N - \Delta$ [4,5] and GEp [6,7]. Next, we describe a new analysis method developed to restrain systematic uncertainties in the polarization measurement with a high confidence level. We explain in detail the sources of these systematic errors and present longitudinal electron polarization measurement results. Finally, we give for the first time at JLab a measurement of the polarization difference between the two helicity states of the electron beam.

2. Compton polarimeter at JLab

Compton scattering of polarized electrons off a circularly polarized photon beam shows an asymmetry of the counting rates $n^{+/-}$ for different orientations of the electron polarization [8]

$$A_{\exp} = \frac{n^+ - n^-}{n^+ + n^-} = P_e P_\gamma A_c \qquad (1)$$

where the asymmetry A_c is calculated from QED. Measurements of the experimental asymmetry $A_{\exp}$ and of the circular photon polarization P_γ give access to the mean longitudinal electron polarization P_e. The electron beam polarization is flipped at a 30 Hz rate to minimize systematic effects.

The Compton polarimeter is composed of a magnetic chicane of four identical dipoles connected in series and installed in the Hall A beam line. The Compton interaction takes place at the center of a symmetric Fabry–Perot cavity in which photons, originating from a 230 mW IR laser ($\lambda = 1064$ nm) interfere. The laser frequency is locked to one of the resonant frequencies of the cavity using the Pound-Drever feedback technique [9]. The maximum power inside the cavity reaches 1700 W, with a coupling to the fundamental mode of 92%. The detectors are installed between the third and the fourth dipoles of the chicane. The backscattered photons go through the gap of the third magnet in a calorimeter consisting of 25 PbWO$_4$ crystals ($2 \times 2 \times 23$ cm^3) and the scattered electrons are detected in 4 planes of 48 silicon strips (650 μm wide), segmented along the dispersive axis. The data acquisition can be triggered by either electrons, photons, or both (in coincidence). Typical running conditions at CEBAF during data taking in 2000 were an electron energy of $E = 4.6$ GeV and a beam current of $I_e = 40\mu A$. The Compton backscattered photons' energy range is from 0 to 340 MeV under these conditions.

3. Data taking

We describe here how the Compton polarimeter data-acquisition system works, and the strategy used to minimize false asymmetries.

3.1. Acquisition

The data acquisition is driven by the 30 Hz electron beam polarization flip. Two milliseconds

after each reversal, the trigger system is activated and events are taken from the photon and/or electron detectors, according to the trigger configuration determined by the user. The trigger system is inhibited a few ms before the next reversal.

Each detector has its own trigger logic. The photon calorimeter trigger system generates an event when the signal of one the photo-multiplier tubes exceeds a given threshold. This signal is then integrated over a period of 150 ns. The electron detector triggers when signals are detected in coincidence on a given number of the silicon strip planes, at the same dispersive position. A specific logic is used to take care of cases where both detectors fire in coincidence.

The data-acquisition system can read out photon and electron events at a rate greater than 100 kHz with a dead time of only a few percent. These data are read by either a custom-built buffer card for the electron detector signals, or 10 bits buffered ADCs for the photon calorimeter. Calibration signals from a LED can be used to monitor the gain variation of the photon detector.

All these raw data are read through VME block transfer by two Power PC CPU cards working alternatively at each electron polarization reversal. At the end of each polarization period, the CPU card that has read out the data, reads values from scaler cards which provide summary information of that period (counting rates, number of triggers, dead time, average value of electron and photon beams parameters, etc.). This CPU then transfers control of the VME crate to the other CPU, produces on-line calculations and sends a data block to a workstation where these data are stored. The goal of these on-line calculations is to reduce the huge amount of data coming from both detectors by producing computed values and histograms (in particular the energy spectra of the scattered photons). Only a small fraction of the raw data, controlled by prescaler factors, is kept for monitoring purposes. Thus, the data block stored at the end of each electron polarization state consists of the scalers' summary values, the result of the on-line calculations (computed values and histo-

gram), and pre-scaled photon, electron and coincidence raw data.

3.2. Photon polarization reversal

Helicity-correlated differences in the electron beam parameters (charge, position and angle) lead to false asymmetries b_i which add to the experimental asymmetry

$$A_{\mathrm{exp}} = P_{\mathrm{e}}P_{\gamma}A_{\mathrm{c}} + \sum_i b_i \qquad (2)$$

where i runs over the different sources of false asymmetries. The charge asymmetry is corrected to first order by normalizing the counting rates to the beam current. The remaining systematic effects from position and angle are independent of the photon beam polarization state. Hence, in changing the sign of the photon polarization the major part of this type of false asymmetries is canceled. This defines the procedure for data taking as a sequence of alternating right and left laser circular polarization, as illustrated in Fig. 1. Moreover, between two photon polarization states, the cavity is unlocked in order to measure the background. Thanks to a high quality vacuum in the beam pipe and the control of the beam envelope using quadrupoles upstream the magnetic chicane a signal over background ratio of 20 is routinely achieved.
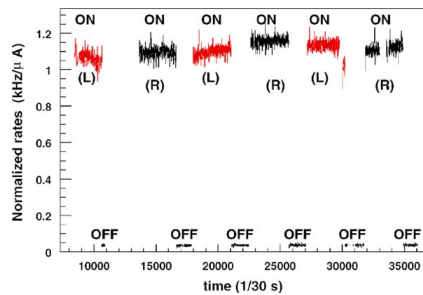

Fig. 1. Normalized counting rates versus time with alternate left (L) and right (R) circular polarization of the photon separated by laser OFF periods to monitor the background level.
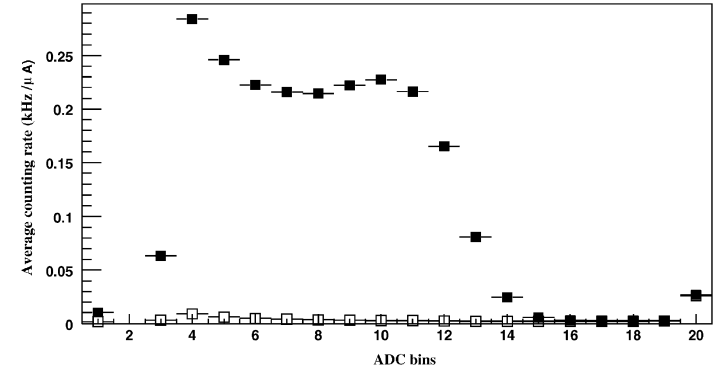
Fig. 2. Normalized counting rates versus ADC bins of the energy deposited in the photon calorimeter, for laser ON (solid squares) and laser OFF (empty squares) periods.

4. Experimental asymmetry

For a given circular photon polarization, right (R) or left (L), we can calculate the asymmetry of integrated event numbers for two consecutive windows of opposite electron helicity states, as

$$A_p^{\mathrm{R/L}} = \frac{n_{\mathrm{R/L}}^+ - n_{\mathrm{RR/L}}^-}{n_{\mathrm{R/L}}^+ + n_{\mathrm{R/L}}^-} \qquad (3)$$

where $n^{\pm}$ refers to the normalized numbers of photons with a deposited energy greater than a given threshold. These are defined as

$$n^{\pm} = \frac{\sum_{i>i_s} N_i^{\pm}}{I^{\pm}\Gamma^{\pm}} \qquad (4)$$

where $I\pm$ is the electron beam intensity, $\Gamma^{\pm}$ is the acquisition live time, $N_i^{\pm}$ is the number of detected events in the ith ADC bin and i_s is the threshold corresponding to the lower edge of the bin. The normalized counting rates $N\pm/I^{\pm}\Gamma^{\pm}$ are shown in Fig. 2 versus the energy in ADC bin units. The threshold i_s is a software threshold applied to the total charge deposited and not to the maximum amplitude reached by the signal. It can be varied off line in order to obtain the optimal value that
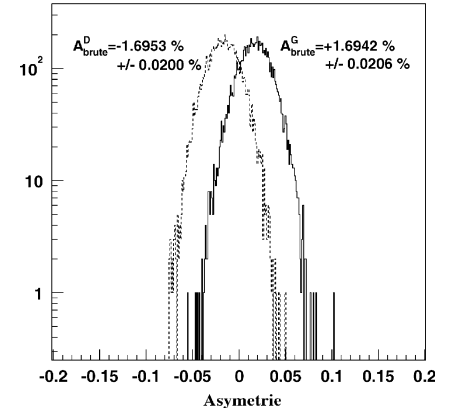

Fig. 3. Distribution of pulse-to-pulse asymmetries A_p for both right and left photon polarizations. The same size but opposite sign of the mean values is a check of systematic effects.

maximizes the statistical accuracy and minimizes the effect of false asymmetries. This operating point is found to be between the 6th and the 9th bin (see Section 6). For a typical 40 min run, a raw

asymmetry $A_{\mathrm{raw}}^{\mathrm{R/L}}$ is defined as the average of all pulse-to-pulse asymmetries $A_p^{\mathrm{R/L}}$. The distribution of these asymmetries is shown in Fig. 3, for both right and left photon polarizations. We can see that the pulse-to-pulse asymmetry distributions follow a Gaussian law. The raw asymmetry has to be corrected for background according to

$$A_{\exp}^{\mathrm{R/L}} = \left[1 + \frac{B^{\mathrm{R/L}}}{S}\right] A_{\mathrm{raw}}^{\mathrm{R/L}} - \frac{B^{\mathrm{R/L}}}{S} A_B \qquad (5)$$

where $(B/S)^{\mathrm{R/L}}$ is the background to signal ratio for each photon polarization and A_B is the background asymmetry. B/S is of the order of 0.06 with a threshold set to the 8th energy bin ($\approx 230\,\mathrm{MeV}$), and A_B is found to be compatible with zero at the 10^{-4} level.

Finally, the mean experimental asymmetry is computed as

$$<A_{\exp}> = \frac{\omega^{\mathrm{L}} A_{\mathrm{Exp}}^{\mathrm{L}} - \omega^{\mathrm{R}} A_{\mathrm{Exp}}^{\mathrm{R}}}{\omega^{\mathrm{L}} + \omega^{\mathrm{R}}} \qquad (6)$$

where $\omega^{\mathrm{R/L}}$ corresponds to the statistical weight of each experimental asymmetry.

The mean experimental asymmetries measured above the software threshold for $E = 4.6\,\mathrm{GeV}$ are around 6% and can be measured with a relative statistical accuracy of 0.65% in one hour at $I = 40\,\mu\mathrm{A}$.

5. Analysing power

The second part of this analysis concerns the determination of the analyzing power. In order to account for detection effects, we define the response function of the calorimeter $\mathcal{R}(\mathrm{ADC}, k)$ as the ADC spectrum for a set of photons with a given energy k. From this response function the probability to detect photons of energy k above a given ADC threshold ADC_s is

$$P(k) = \frac{\int_{\mathrm{ADC}_s}^{\infty} \mathcal{R}(\mathrm{ADC}, k)\,\mathrm{dADC}}{\int_0^{\infty} \mathcal{R}(\mathrm{ADC}, k)\,\mathrm{dADC}}. \qquad (7)$$

Using this probability one can then calculate the analyzing power of the polarimeter defined as the average of the Compton asymmetry weighted by

the Compton cross section

$$<A_s> = \frac{\int_0^{k_{\max}} P(k)\,\frac{\mathrm{d}\sigma_0}{\mathrm{d}k}\,A_{\mathrm{C}}(k)\,\mathrm{d}k}{\int_0^{k_{\max}} P(k)\,\frac{\mathrm{d}\sigma_0}{\mathrm{d}k}\,\mathrm{d}k}. \qquad (8)$$

5.1. Determination of the response function $\mathcal{R}(ADC, k)$

The calorimeter response function depends mostly on the intrinsic properties of the calorimeter. It is measured during dedicated runs where data are taken in photon–electron coincidence mode on an event-by-event basis.

Thanks to its very fine pitch the electron detector functions as an energy tagger of the incident photons. The distribution of the photon energy deposited in the central crystal for one selected strip of the electron detector is shown in Fig. 4. The tail at low energy is due to shower leakage to the sides of the central crystal (the Molière radius is 2.19 cm). For practical reasons it was found more accurate to model the response function of the central crystal rather than dealing with the inter-calibration of all the crystals of the 5x5 matrix [10]. The response function is described by an ad hoc asymmetrical function composed of two Gaussians and a 4th degree polynomial $P_4(x)$. Best fits were obtained with the following fit
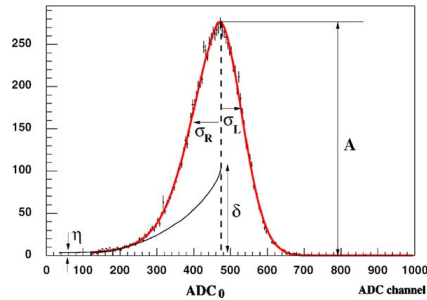

Fig. 4. Photon energy spectrum measured in coincidence with electrons hitting the 14th strip. Parameters of the fitting function are illustrated.

function

$$\mathcal{R}(\mathrm{ADC}, k) = A\,\mathrm{e}^{(\mathrm{ADC} - \mathrm{ADC}_0)^2 / 2\sigma_{\mathrm{R}}^2}, \qquad \mathrm{ADC} \geqslant \mathrm{ADC}_0$$

$$\mathcal{R}(\mathrm{ADC}, k) =$$

$$A\left[(1 - \delta)\,\mathrm{e}^{(\mathrm{ADC} - \mathrm{ADC}_0)^2 / 2\sigma_{\mathrm{L}}^2} + \eta + (\delta - \eta)\frac{\mathrm{ADC}^4}{\mathrm{ADC}_0^4}\right],$$

$$\mathrm{ADC} \leqslant \mathrm{ADC}_0 \qquad (9)$$

where A, ADC_0 and $\sigma_{\mathrm{R/L}}$ are Gaussian parameters, and η, δ denote proportional amplitudes $P_4(0)/A$ and $P_4(x_0)/A$, as described in Fig. 4. A is fixed by normalizing the integral of the response function to 1 in the denominator of Eq. (7). The remaining five parameters are functions of the scattered photon energy k, fitted to data from all electron detector strips which fired. The Gaussian widths $\sigma_{\mathrm{R/L}}$ are corrected for smearing due to the width of the electron strips ($\sigma_E \approx 5\,\mathrm{MeV}$).

The electron detector cannot be put closer than a few mm to the beam axis and thus restricts the range over which the response function can be determined. For instance, only photon energies between 150 and 340 MeV (Compton edge) could be explored with a 4.6 GeV beam. The determina-

tion of the calorimeter response function is well controlled inside this energy range but the extrapolation to lower energy induces larger systematic errors (see Section 6).

5.2. Calibration and analyzing power

The response function measured during a specific reference run has to be corrected for mean gain variations when used to analyze a later run. To this end a calibration coefficient λ is introduced which accounts for gain corrections

$$\mathcal{R}(\mathrm{ADC}, k) = \mathcal{R}\left(\frac{\mathrm{ADC}}{\lambda}, k\right) \qquad (10)$$

λ is fitted to the experimental spectrum of each run (Fig. 5) using the convolution of the unpolarized Compton cross-section $\mathrm{d}\sigma_0(k)/\mathrm{d}k$ with the response function

$$\frac{\mathrm{d}N(\mathrm{ADC})}{\mathrm{dADC}} = \int_0^{k_{\max}} \frac{\mathrm{d}\sigma_0(k)}{\mathrm{d}k} \mathcal{R}(\mathrm{ADC}, k)\,\mathrm{d}k. \qquad (11)$$

The probability of photon detection is deduced from Eq. (7), where the lower integration boundary ADC_s is replaced by ADC_s/λ. The analyzing
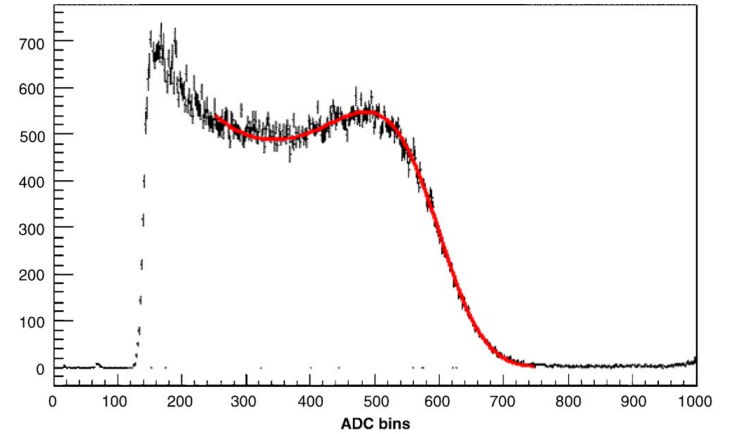

Fig. 5. Fit of the experimental photon spectrum using the smeared cross-section. The fit range is restricted to the validity energy range of the modelling.
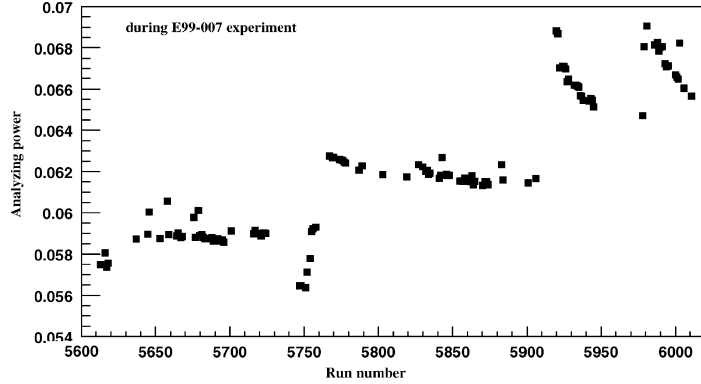
Fig. 6. Analysing power for each Compton run during the G_E^p experiment.

power is then calculated from Eq. (8) for each data run (with $i_s = 8$). An overview is given in Fig. 6 and shows relative variations of up to 10%. Most of the observed steps in the analyzing power originate from a retuning of the photon detection gain (PMT high voltage or gain of the amplifier). Reference runs are repeated every few hours to check the consistency of the extracted response function.

6. Systematic uncertainties

6.1. Experimental asymmetry

The largest source of systematic error in the experimental asymmetry is the false asymmetry related to the electron beam position, since the Compton luminosity is determined by the overlap of the electron and laser beams. If one assumes a Gaussian intensity profile for these two beams, the luminosity is also a Gaussian function of the distance between the two beam centroids. Since the optical axis of the cavity is fixed by the monolithic mechanic of the mirror holder, the position variation of the electron beam directly affects the Compton luminosity with a sensitivity equal to the derivative of this Gaussian function. In order to minimize this effect, two position-feedback sys-

tems were used, one at high frequency to reduce the jitter (down to 20 μm) and one at low frequency to lock the mean position at the point corresponding to the maximum of the Gaussian overlap curve, where the sensitivity to beam position goes to zero. Finally, averaging over several photon polarization reversals cancels out most of these false asymmetries provided that the statistical weights of right and left circularly photon polarization states are similar. In practice, these statistical weights $\omega^{R/L}$ are not exactly equal, and some residual effects must be taken into account. So, in agreement with Eqs. (2) and (6), we have:

$$\Delta A_{\exp_i}^{\rm syst} = {\rm res}(b_i) = \frac{\omega^{\rm L} b_i^{\rm L} - \omega^{\rm R} b_i^{\rm R}}{\omega^{\rm L} + \omega^{\rm R}}. \qquad (12)$$

Studies of the four beam parameters $(x, y, \theta_x, \theta_y)$ show that their correlations tend to reduce the total false asymmetry. As a safe and simpler estimate of the error we assume them to be uncorrelated. The final error quoted in Table 1 should be read as a typical run-to-run error. It corresponds to the width of the distribution of all res(b_i) which turns out to be centered at zero. For each individual run one can also choose to correct for res(b_i) and its error. When averaging the polarization over a sufficient number of runs N_r the two approaches are equivalent and the systematic error reduces as $1/\sqrt{N_r}$. The measured

background has a small rate and asymmetry, compared to the Compton process, resulting in a negligible systematic error. Similarly the beam current asymmetry is at the few 100 ppm level and does not affect significantly the Compton asymmetry. The correction for the acquisition dead time is checked by comparing the scaler asymmetry and the corrected ADC asymmetry without applying a software threshold.

6.2. Analyzing power

There are four main sources of uncertainties in the analyzing power. The first comes from the dependence of the response function on the parameterization used to describe it. To compute

Table 1
Run to run systematic uncertainties applied to Compton experimental asymmetry

Type	Error (%)
Background	0.05
Dead time	0.1
Beam intensity	—
Events cut	0.1
Position	0.3
Total on $<A_{\exp}>$	0.35

the systematic error we look at the variation of the analyzing power for a set of parameterizations with equivalent χ^2 and try to define an envelope (Fig. 7). For a threshold taken around ADC = 400 ($i_s = 8$, $E = 230\,{\rm MeV}$) the effect is less than 0.45%. Note that below the electron cut, located around channel 260 in Fig. 7, the systematic errors increase steeply. The second source of uncertainty arises from the momentum calibration of the electron detector which is used as an energy tagger in the determination of the response function (Section 5). This calibration error is due to the position resolution of the electron detector (200 μm). The impact of this effect on the analyzing power is shown in Fig. 8 as a function of the ADC threshold. For a threshold taken at ADC = 400 the effect is 0.6%. The third uncertainty is due to pile-up when two events are detected within the same acquisition gate (∼ 150 ns) and are recorded as a single event of higher energy. The Compton spectrum is then shifted to higher energies. This modifies not only the experimental asymmetry but also the analyzing power via the calibration coefficient λ. Monte-Carlo simulations [11] were performed for a measured pile-up rate of 0.9%. They show a relative effect of 0.45% for an ADC threshold $i_s = 8$. The fourth systematic uncertainty is due to the radiative corrections in real Compton scattering. The interfering process $e^-\gamma \rightarrow e^-\gamma\gamma$


Fig. 7. Relative effects on analyzing power due to modeling of response function parameters, versus ADC threshold.
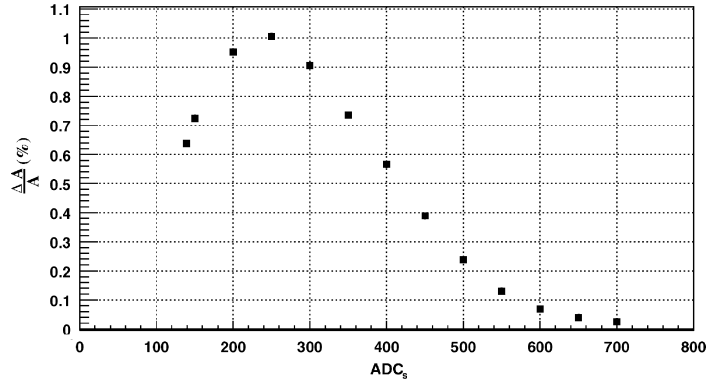
Fig. 8. Relative deviation of the analyzing power due to the calibration error of the electron detector.

Table 2
Relative systematic uncertainties applied to Compton analyzing power during and GEp experiments [6,7]

	Syst. error (%)
Response function	0.45
Energy calibration	0.6
Pile up	0.45
Radiative corrections	0.26
Total on $<A_s>$	0.95

causes a deviation of the analyzing power by about 0.26% [12] at an electron beam energy of 4.6 GeV. We decided not to correct for this effect and include it in the error budget. Systematic uncertainties on the analyzing power are summarized in Table 2.

6.3. Photon polarization

The circular photon polarization is measured at the exit of the Fabry-Perot cavity using an analysis device composed of a quarter-wave plate, a Wollaston prism and two integrating spheres. This device allows a complete polarization measurement through the four Stokes parameters by rotating the quarter-wave plate. In production mode the quarter-wave plate angle is fixed and the spheres only monitor the time variations of the degree of circular polarization (DOCP). The polarization at the center of the cavity where the Compton interaction takes places is deduced from the Stokes parameters, knowing the optical transport matrix of the exit line. This matrix is determined before the installation of the cavity using a dedicated setup where polarization measurements are performed for various orientations of the elliptic polarization of the light. With this method a precision of 0.4% is reached including both the modelisation of the transport and the measurement errors. After the cavity is installed, additional effects coming from mirror transmission, birefringence and optical alignment of photon beam must be taken into account. Since in production mode only the DOCP is measured, we use the observed variations and the transport matrix to determine the envelope of possible variations of the polarization inside the cavity. This results in a 0.4% systematic error. All uncertainties are summarized in Table 3 The mean value of the DOCP for both laser polarization states is

$$P_\gamma^L = +99.9\% \pm 0.6\%$$
$$P_\gamma^R = +99.3\% \pm 0.6\%. \quad (13)$$

The photon polarization used for the electron polarization measurement is the average value between the two polarization states :

$$P_\gamma = \frac{\omega^L P_\gamma^L - \omega^R P_\gamma^R}{\omega^L + \omega^R} \quad (14)$$

where we took to first order $\omega^L = \omega^R$.

7. Results and discussions

7.1. General results

A review of the uncertainties is given in Table 4. The last column shows the accuracy of the monitoring of the electron beam polarization

Table 3
Relative systematic uncertainties applied to each photon beam polarization states

Time fluctuations	0.4 %
Polarization transport	0.4 %
Mirrors transmission	0.14 %
Birefringence	0.05 %
Alignment	0.1 %
Total on $P_\gamma^{L/R}$	0.60 %

for which all normalization errors cancel. A summary graph of all polarization measurements performed during the N–Δ experiment is shown in Fig. 9 (300 measurements in 60 days). The jumps in the beam polarization are directly correlated with operations at the polarized electron source when the laser spot is displaced to illuminate a different spot on the photocathode in order to increase the beam current. These significant variations in the beam polarization demonstrate that the Compton polarimeter is an ideal and a mandatory tool to provide a meaningful polarization measurement over long data-taking periods.

Table 4
Review of uncertainties for an absolute (2nd column) and relative (3rd column) electron beam polarization measurement

|	Absolute Measurement %	Monitoring %
Experimental asymmetry	0.50	0.50
Analyzing power	0.95	0.45
Photon polarization	0.60	-
Total systematic	1.23	0.67
Statistical error	0.80	0.80
Total	1.47	1.04
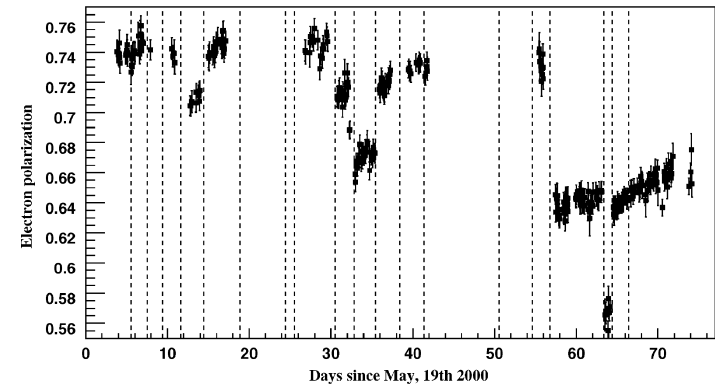
Fig. 9. Electron polarization measurements during N–Δ experiment. Vertical dash lines show laser spot moves on AsGa crystal at the polarized electron source

7.2. Determination of ΔP_e

Most of the polarized physics experiments in Hall A are only sensitive to the mean longitudinal electron polarization defined as

$$P_e = \frac{|P_e^+| + |P_e^-|}{2} \qquad (15)$$

where P_e^+ and P_e^- denote the electron polarization in each electron spin configuration (parallel or anti-parallel). However, some experiments, such as the N-Δ experiment, are sensitive to

$$\Delta P_e = \frac{|P_e^+| - |P_e^-|}{2} \qquad (16)$$

One way to measure this quantity is to use the photon polarization reversal, sacrificing the cancellation of helicity-correlated effects. Experimental asymmetries are thus computed from counting rates between two opposite signs of the photon polarization, for each electron helicity [11]. How-ever, the photon polarization is reversed every three minutes only, resulting in a false asymmetry of the same size as the Compton asymmetry itself. If one makes the assumption that these false asymmetries are independent of the backscattered photon's energy, variation of the Compton asymmetry with respect to energy allows one to isolate ΔP_e. An example is shown in Fig. 10 where the sum of both experimental asymmetries A_{exp}^+ and A_{exp}^- is fitted with a function such as

$$f(E) = \Delta P_e \cdot P_\gamma \cdot A_C(E) + cst. \qquad (17)$$

For a set of left/right photon reversals over several days, we assess ΔP_e for the first time at JLab and find it statistically compatible with zero at a level of 0.3%.

8. Conclusion

We have continuously measured the CEBAF electron beam polarization over two periods of 30 days at an electron energy of 4.6 GeV and an average current of 40 μA. The use of a highly segmented electron detector in coincidence with the photon detector was a key element to reduce the systematic errors. By using 40 min runs a total relative systematic error of 1.2% was achieved. Thanks to our high-gain optical cavity and a double beam position feed-back, a statistical accuracy of 1% could be reached within 25 min. In the relative variations of the beam polarization from one run to another the correlated errors cancel out and the systematic error is reduced to 0.7%. Because most of the recent experiments in Hall A take advantage of the highly polarized and intense electron beam available at JLab, the Compton polarimeter has been routinely operated over the last three years to monitor the beam polarization. Its performance is crucial for the upcoming parity experiments [13–15] which aim for a very accurate measurements (≤2%) in an energy range of 0.85 to 3.00 GeV. Such a precision remains challenging and require detectors and laser upgrades which are under study. At higher energy (6 GeV), sub-percent measurements are feasible with only minor upgrades of the present apparatus.

References

[1] G. Bardin, et al., Conceptual design report of a Compton polarimeter for CEBAF Hall A, CEA/DAPNIA/SPhN Note 96-14, 1996.
[2] J.P. Jorda, et al., Nucl. Instr. and Meth. A 412 (1998) 1–18.
[3] N. Falletto, et al., Nucl. Instr. and Meth. A 459 (2001) 412–425.
[4] A. Sarty, J.J. Kelly, R.W. Lourie, S. Frulliani, Investiga-tion of the $N\Delta$ transition via polarization observables in Hall A, JLab Hall A experiment E91-011, 1991
[5] R. Roche, Measurement of polarization observables in the electro-excitation of the proton to its first excited state, Ph.D. Thesis, Florida State University, 2003
[6] C.F. Perdrisat, M. Jones, V. Punjabi, E.J. Brash, Measurement of to $Q2 = 5.6$ GeV2 by the recoil polariza-tion method, JLab Hall A experiment E99-007, 1999.
[7] O. Gayou, et al., Phys. Rev. Lett. 88 (2002) 092301.
[8] C.Y. Prescott, Spin-dependent Compton scattering for use in analysing electron beam polarizations, SLAC Notes TN-73-1, 1973.
[9] R.W.P. Drever, et al., Appl. Phys. B 31 (1983) 97.
[10] M. Baylac, et al., Phys. Lett. B 539 (2002) 8–12.
[11] S. Escoffier Doctorate Thesis, University of Paris 7, Denis Diderot, 2001, see http://hallaweb.jlab.org/compton/Documentation/Papers/index.php.
[12] A. Denner, S. Dittmaier, Nucl. Phys. B 540 (1999) 58.
[13] D. Armstrong, R. Michaels, Parity violation from ^{4}He at low Q^2: a clean measurement of ρ_s, JLab Hall A experi-ment E00-114, 2000.
[14] K. Kumar, D. Lhuillier, Constraining the nucleon strangeness radius in parity-violating electron scattering, JLab Hall A experiment E99-115, 1999.
[15] R. Michaels, P. Souder, G. Urciuoli, Neutron skin of 208Pb through parity-violating electron scattering, JLab Hall A experiment E-00-003, 2000.
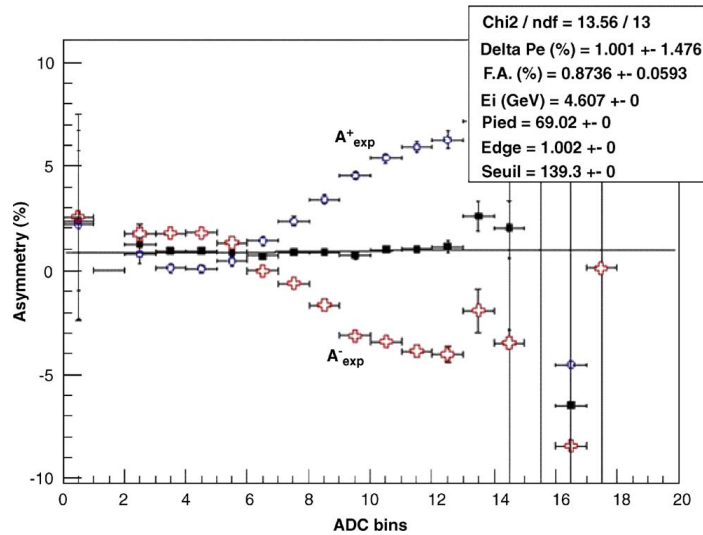

Fig. 10. Experimental asymmetries in regard with photon energy, for a positive(+) and negative(−) electron helicity state, and for the average of both (filled circles).

COMPASS Collaboration, M. Alekseev, Eur. Phys. J. C52 (2007) 255-265.

Double spin asymmetry in exclusive ρ^0 muoproduction at COMPASS

Abstract

The longitudinal double spin asymmetry A_1^ρ for exclusive leptoproduction of ρ^0 mesons, $\mu + N \rightarrow \mu + N + \rho$, is studied using the COMPASS 2002 and 2003 data. The measured reaction is incoherent exclusive ρ^0 production on polarised deuterons. The Q^2 and x dependence of A_1^ρ is presented in a wide kinematical range $3 \cdot 10^{-3} < Q^2 < 7$ (GeV/c)^2 and $5 \cdot 10^{-5} < x < 0.05$. The presented results are the first measurements of A_1^ρ at small Q^2 ($Q^2 < 0.1$ (GeV/c)^2) and small x ($x < 3 \cdot 10^{-3}$). The asymmetry is in general compatible with zero in the whole kinematical range.

The COMPASS Collaboration

M. Alekseev[29], V.Yu. Alexakhin[8], Yu. Alexandrov[18], G.D. Alexeev[8], A. Amoroso[29], A. Arbuzov[8], B. Badełek[30], F. Balestra[29], J. Ball[25], G. Baum[1], J. Barth[4], Y. Bedfer[25], C. Bernet[25], R. Bertini[29], M. Bettinelli[19], R. Birsa[28], J. Bisplinghoff[3], P. Bordalo[15,a], F. Bradamante[28], A. Bravar[16], A. Bressan[28], G. Brona[30], E. Burtin[25], M.P. Bussa[29], A. Chapiro[27], M. Chiosso[29], A. Cicuttin[27], M. Colantoni[29,b], S. Costa[29], M.L. Crespo[27], N. d'Hose[25], S. Dalla Torre[28], S. Das[7], S.S. Dasgupta[6], R. De Masi[20], N. Dedek[19], O.Yu. Denisov[29,c], L. Dhara[7], V. Diaz[27], A.M. Dinkelbach[20], S.V. Donskov[24], V.A. Dorofeev[24], N. Doshita[21], V. Duic[28], W. Dünnweber[19], P.D. Eversheim[3], W. Eyrich[9], M. Fabro[28], M. Faessler[19], V. Falaleev[11], A. Ferrero[29], L. Ferrero[29], M. Finger[22], M. Finger jr.[8], H. Fischer[10], C. Franco[15], J. Franz[10], J.M. Friedrich[20], V. Frolov[29,c], R. Garfagnini[29], F. Gautheron[1], O.P. Gavrichtchouk[8], R. Gazda[30], S. Gerassimov[18,20], R. Geyer[19], M. Giorgi[28], B. Gobbo[28], S. Goertz[2,4], A.M. Gorin[24], S. Grabmüller[20], O.A. Grajek[30], A. Grasso[29], B. Grube[20], R. Gushterski[8], A. Guskov[8], F. Haas[20], J. Hannappel[4], D. von Harrach[16], T. Hasegawa[17], J. Heckmann[2], S. Hedicke[10], F.H. Heinsius[10], R. Hermann[16], C. Heß[2], F. Hinterberger[3], M. von Hodenberg[10], N. Horikawa[21,d], S. Horikawa[21], C. Ilgner[19], A.I. Ioukaev[8], S. Ishimoto[21], O. Ivanov[8], Yu. Ivanshin[8], T. Iwata[21,32], R. Jahn[3], A. Janata[8], P. Jasinski[16], R. Joosten[3], N.I. Jouravlev[8], E. Kabuß[16], D. Kang[10], B. Ketzer[20], G.V. Khaustov[24], Yu.A. Khokhlov[24], Yu. Kisselev[1,2], F. Klein[4], K. Klimaszewski[30], S. Koblitz[16], J.H. Koivuniemi[13], V.N. Kolosov[24], E.V. Komissarov[8], K. Kondo[21], K. Königsmann[10], I. Konorov[18,20], V.F. Konstantinov[24], A.S. Korentchenko[8], A. Korzenev[16,c], A.M. Kotzinian[8,29], N.A. Koutchinski[8], O. Kouznetsov[8,25], N.P. Kravchuk[8], A. Kral[23], Z.V. Kroumchtein[8], R. Kuhn[20], F. Kunne[25], K. Kurek[30], M.E. Ladygin[24], M. Lamanna[11,28], J.M. Le Goff[25], A.A. Lednev[24], A. Lehmann[9], J. Lichtenstadt[26], T. Liska[23], I. Ludwig[10], A. Maggiora[29], M. Maggiora[29], A. Magnon[25], G.K. Mallot[11], A. Mann[20], C. Marchand[25], J. Marroncle[25], A. Martin[28], J. Marzec[31], F. Massmann[3], T. Matsuda[17], A.N. Maximov[8], W. Meyer[2], A. Mielech[28,30], Yu.V. Mikhailov[24], M.A. Moinester[26], A. Mutter[10,16], O. Nähle[3], A. Nagaytsev[8], T. Nagel[20], J. Nassalski[30], S. Neliba[23], F. Nerling[10], S. Neubert[20], D.P. Neyret[25], V.I. Nikolaenko[24], K. Nikolaev[8], A.G. Olshevsky[8], M. Ostrick[4], A. Padee[31], P. Pagano[28], S. Panebianco[25], R. Panknin[4], D. Panzieri[29,b], S. Paul[20], B. Pawlukiewicz-Kaminska[30], D.V. Peshekhonov[8], V.D. Peshekhonov[8], G. Piragino[29], S. Platchkov[25], J. Pochodzalla[16], J. Polak[14], V.A. Polyakov[24], J. Pretz[4], S. Procureur[25], C. Quintans[15], J.-F. Rajotte[19], V. Rapatsky[8], S. Ramos[15,a], G. Reicherz[2], A. Richter[9], F. Robinet[25], E. Rocco[28,29], E. Rondio[30], A.M. Rozhdestvensky[8], D.I. Ryabchikov[24], V.D. Samoylenko[24], A. Sandacz[30], H. Santos[15], M.G. Sapozhnikov[8], S. Sarkar[7], I.A. Savin[8], P. Schiavon[28], C. Schill[10], L. Schmitt[20], P. Schönmeier[9], W. Schröder[9], O.Yu. Shevchenko[8], H.-W. Siebert[12,16], L. Silva[15], L. Sinha[7], A.N. Sissakian[8], M. Slunecka[8], G.I. Smirnov[8], S. Sosio[29], F. Sozzi[28], V.P. Sugonyaev[24], A. Srnka[5], F. Stinzing[9], M. Stolarski[30,10], M. Sulc[14], R. Sulej[31], N. Takabayashi[21], V.V. Tchalishev[8], S. Tessaro[28], F. Tessarotto[28], A. Teufel[9], L.G. Tkatchev[8], G. Venugopal[3], M. Virius[23], N.V. Vlassov[8], A. Vossen[10], R. Webb[9], E. Weise[3], Q. Weitzel[20], R. Windmolders[4], S. Wirth[9], W. Wiślicki[30], K. Zaremba[31], M. Zavertyaev[18], E. Zemlyanichkina[8], J. Zhao[16], R. Ziegler[3], and A. Zvyagin[19]

[1] Universität Bielefeld, Fakultät für Physik, 33501 Bielefeld, Germany[e]
[2] Universität Bochum, Institut für Experimentalphysik, 44780 Bochum, Germany[e]
[3] Universität Bonn, Helmholtz-Institut für Strahlen- und Kernphysik, 53115 Bonn, Germany[e]
[4] Universität Bonn, Physikalisches Institut, 53115 Bonn, Germany[e]
[5] Institute of Scientific Instruments, AS CR, 61264 Brno, Czech Republic[f]
[6] Burdwan University, Burdwan 713104, India[h]
[7] Matrivani Institute of Experimental Research & Education, Calcutta-700 030, India[i]
[8] Joint Institute for Nuclear Research, 141980 Dubna, Moscow region, Russia
[9] Universität Erlangen–Nürnberg, Physikalisches Institut, 91054 Erlangen, Germany[e]
[10] Universität Freiburg, Physikalisches Institut, 79104 Freiburg, Germany[e]
[11] CERN, 1211 Geneva 23, Switzerland
[12] Universität Heidelberg, Physikalisches Institut, 69120 Heidelberg, Germany[e]
[13] Helsinki University of Technology, Low Temperature Laboratory, 02015 HUT, Finland and University of Helsinki, Helsinki Institute of Physics, 00014 Helsinki, Finland
[14] Technical University in Liberec, 46117 Liberec, Czech Republic[f]
[15] LIP, 1000-149 Lisbon, Portugal[g]
[16] Universität Mainz, Institut für Kernphysik, 55099 Mainz, Germany[e]
[17] University of Miyazaki, Miyazaki 889-2192, Japan[j]
[18] Lebedev Physical Institute, 119991 Moscow, Russia
[19] Ludwig-Maximilians-Universität München, Department für Physik, 80799 Munich, Germany[e]
[20] Technische Universität München, Physik Department, 85748 Garching, Germany[e]
[21] Nagoya University, 464 Nagoya, Japan[j]
[22] Charles University, Faculty of Mathematics and Physics, 18000 Prague, Czech Republic[f]
[23] Czech Technical University in Prague, 16636 Prague, Czech Republic[f]
[24] State Research Center of the Russian Federation, Institute for High Energy Physics, 142281 Protvino, Russia
[25] CEA DAPNIA/SPhN Saclay, 91191 Gif-sur-Yvette, France
[26] Tel Aviv University, School of Physics and Astronomy, 69978 Tel Aviv, Israel[k]
[27] ICTP–INFN MLab Laboratory, 34014 Trieste, Italy
[28] INFN Trieste and University of Trieste, Department of Physics, 34127 Trieste, Italy
[29] INFN Turin and University of Turin, Physics Department, 10125 Turin, Italy
[30] Sołtan Institute for Nuclear Studies and Warsaw University, 00-681 Warsaw, Poland[l]
[31] Warsaw University of Technology, Institute of Radioelectronics, 00-665 Warsaw, Poland[m]
[32] Yamagata University, Yamagata, 992-8510 Japan[j]

[a] Also at IST, Universidade Técnica de Lisboa, Lisbon, Portugal
[b] Also at University of East Piedmont, 15100 Alessandria, Italy
[c] On leave of absence from JINR Dubna
[d] Also at Chubu University, Kasugai, Aichi, 487-8501 Japan

1   Introduction

In this paper we present results on the longitudinal double spin asymmetry A_1^ρ for exclusive incoherent ρ^0 production in the scattering of high energy muons on nucleons. The experiment was carried out at CERN by the COMPASS collaboration using the 160 GeV muon beam and the large ^{6}LiD polarised target.

The studied reaction is

$$\mu + N \rightarrow \mu' + \rho^0 + N', \tag{1}$$

where N is a quasi-free nucleon from the polarised deuterons. The reaction (1) can be described in terms of the virtual photoproduction process

$$\gamma^* + N \rightarrow \rho^0 + N'. \tag{2}$$

The reaction (2) can be regarded as a fluctuation of the virtual photon into a quark-antiquark pair (in partonic language), or an off-shell vector meson (in Vector Meson Dominance model), which then scatters off the target nucleon resulting in the production of an on-shell vector meson. At high energies this is predominantly a diffractive process and plays an important role in the investigation of Pomeron exchange and its interpretation in terms of multiple gluon exchange.

Most of the presently available information on the spin structure of reaction (2) stems from the ρ^0 spin density matrix elements, which are obtained from the analysis of angular distributions of ρ^0 production and decay [1]. Experimental results on ρ^0 spin density matrix elements come from various experiments [2–6] including the preliminary results from COMPASS [7].

The emerging picture of the spin structure of the considered process is the following. At low photon virtuality Q^2 the cross section by transverse virtual photons σ_T dominates, while the relative contribution of the cross section by longitudinal photons σ_L rapidly increases with Q^2. At Q^2 of about 2 $(\text{GeV}/c)^2$ both components become comparable and at a larger Q^2 the contribution of σ_L becomes dominant and continues to grow, although at lower rate than at low Q^2. Approximately, the so called s-channel helicity conservation (SCHC) is valid, i.e. the helicity of the vector meson is the same as the helicity of the parent virtual photon. The data indicate that the process can be described approximately by the exchange in the t-channel of an object with natural parity P. Small deviations from SCHC are observed, also at the highest energies, whose origin is still to be understood. An interesting suggestion was made in Ref. [8] that at high energies the magnitudes of various helicity amplitudes for the reaction (2) may shed a light on the spin-orbital momentum structure of the vector meson.

A complementary information can be obtained from measurements of the double spin cross section asymmetry, when the information on both the beam and target polarisation is used. The asymmetry is defined as

$$A_1^\rho = \frac{\sigma_{1/2} - \sigma_{3/2}}{\sigma_{1/2} + \sigma_{3/2}}, \tag{3}$$

where $\sigma_{1/2(3/2)}$ stands for the cross sections of the reaction (2) and the subscripts denote the total virtual photon–nucleon angular momentum component along the virtual photon direction. In the following we will also use the asymmetry A_{LL} which is defined for reaction (1) as the asymmetry of muon–nucleon cross sections for antiparallel and parallel beam and target longitudinal spin orientations.

In the Regge approach [9] the longitudinal double spin asymmetry A_1^ρ can arise due to the interference of amplitudes for exchange in the t-channel of Reggeons with natural parity (Pomeron, ρ, ω, f, A_2) with amplitudes for Reggeons with unnatural parity (π, A_1). No significant asymmetry is expected when only a non-perturbative Pomeron is exchanged because it has small spin-dependent couplings as found from hadron-nucleon data for cross sections and polarisations.

Similarly, in the approach of Fraas [10], assuming approximate validity of SCHC, the spin asymmetry A_1^ρ arises from the interference between parts of the helicity amplitudes for transverse photons corresponding to the natural and unnatural parity exchanges in the t channel. While a measurable asymmetry can arise even from a small contribution of the unnatural parity exchange, the latter may remain unmeasurable in the cross sections. A significant unnatural-parity contribution may indicate an exchange of certain Reggeons like π, A_1 or in partonic terms an exchange of $q\bar{q}$ pairs.

In the same reference a theoretical prediction for A_1^ρ was presented, which is based on the description of forward exclusive ρ^0 leptoproduction and inclusive inelastic lepton-nucleon scattering by the off-diagonal Generalised Vector Meson Dominance (GVMD) model, applied to the case of polarised lepton–nucleon scattering. At the values of Bjorken variable $x < 0.2$, with additional assumptions [11], A_1^ρ can be related to the A_1 asymmetry for inclusive inelastic lepton scattering at the same x as

$$A_1^\rho = \frac{2A_1}{1 + (A_1)^2}. \tag{4}$$

This prediction is consistent with the HERMES results for both the proton and deuteron targets, although with rather large errors.

In perturbative QCD, there exists a general proof of factorisation [12] for exclusive vector meson production by longitudinal photons. It allows a decomposition of the full amplitude for reaction (2) into three components: a hard scattering amplitude for the exchange of quarks or gluons, a distribution amplitude for the meson and the non-perturbative description of the target nucleon in terms of the generalised parton distributions (GPDs), which are related to the internal structure of the nucleon. No similar proof of factorisation exists for transverse virtual photons, and as a consequence the interpretation of A_1^ρ in perturbative QCD is not possible at leading twist. However, a model including higher twist effects proposed by Martin et al. [13] describes the behaviour of both σ_L as well as of σ_T reasonably well. An extension of this model by Ryskin [14] for the spin dependent cross sections allows to relate A_1^ρ to the spin dependent GPDs of gluons and quarks in the nucleon. The applicability of this model is limited to the range $Q^2 \geq 4$ (GeV/c)^2. More recently another pQCD-inspired model involving GPDs has been proposed by Goloskokov and Kroll [15,16]. The non-leading twist asymmetry A_{LL} results from the interference between the dominant GPD H_g and the helicity-dependent GPD $\tilde{H}_g$. The asymmetry is estimated to be of the order $k_T^2 \tilde{H}_g/(Q^2 H_g)$, where k_T is the transverse momentum of the quark and the antiquark.

Up to now little experimental information has been available on the double spin asymmetries for exclusive leptoproduction of vector mesons. The first observation of a non-zero asymmetry A_1^ρ in polarised electron–proton deep-inelastic scattering was reported by the HERMES experiment [11]. In the deep inelastic region $(0.8 < Q^2 < 3$ (GeV/c)$^2)$ the measured asymmetry is equal to 0.23 ± 0.14 (stat) ± 0.02 (syst) [17], with little dependence on the kinematical variables. In contrast, for the 'quasi-real photoproduction' data, with $\langle Q^2 \rangle = 0.13$ (GeV/c)^2, the asymmetry for the proton target is consistent with

zero. On the other hand the measured asymmetry A_1^ρ for the polarised deuteron target and the asymmetry A_1^ϕ for exclusive production of ϕ meson either on polarised protons or deuterons are consistent with zero both in the deep inelastic and in the quasi-real photoproduction regions [17].

The HERMES result indicating a non-zero A_1^ρ for the proton target differs from the unpublished result of similar measurements by the SMC experiment [18] at comparable values of Q^2 but at about three times higher values of the photon-nucleon centre of mass energy W, i.e. at smaller x. The SMC measurements of A_{LL} in several bins of Q^2 are consistent with zero for both proton and deuteron targets.

2   The experimental set-up

The experiment [19] was performed with the high intensity positive muon beam from the CERN M2 beam line. The μ^+ beam intensity is $2 \cdot 10^8$ per spill of 4.8 s with a cycle time of 16.8 s. The average beam energy is 160 GeV and the momentum spread is $\sigma_p/p = 0.05$. The momentum of each beam muon is measured upstream of the experimental area in a beam momentum station consisting of several planes of scintillator strips or scintillating fibres with a dipole magnet in between. The precision of the momentum determination is typically $\Delta p/p \leq 0.003$. The μ^+ beam is naturally polarised by the weak decays of the parent hadrons. The polarisation of the muon varies with its energy and the average polarisation is -0.76.

The beam traverses the two cells of the polarised target, each 60 cm long, 3 cm in diameter and separated by 10 cm, which are placed one after the other. The target cells are filled with ^{6}LiD which is used as polarised deuteron target material and is longitudinally polarised by dynamic nuclear polarisation (DNP). The two cells are polarised in opposite directions so that data from both spin directions are recorded at the same time. The typical values of polarisation are about 0.50. A mixture of liquid ^{3}He and ^{4}He, used to refrigerate the target, and a small amount of heavier nuclei are also present in the target. The spin directions in the two target cells are reversed every 8 hours by rotating the direction of the magnetic field in the target. In this way fluxes and acceptances cancel in the calculation of spin asymmetries, provided that the ratio of acceptances of the two cells remains unchanged after the reversal.

The COMPASS spectrometer is designed to reconstruct the scattered muons and the produced hadrons in wide momentum and angular ranges. It is divided in two stages with two dipole magnets, SM1 and SM2. The first magnet, SM1, accepts charged particles of momenta larger than 0.4 GeV/c, and the second one, SM2, those larger than 4 GeV/c. The angular acceptance of the spectrometer is limited by the aperture of the polarised target magnet. For the upstream end of the target it is ± 70 mrad.

To match the expected particle flux at various locations in the spectrometer, COMPASS uses various tracking detectors. Small-angle tracking is provided by stations of scintillating fibres, silicon detectors, micromesh gaseous chambers and gas electron multiplier chambers. Large-angle tracking devices are multiwire proportional chambers, drift chambers and straw detectors. Muons are identified in large-area mini drift tubes and drift tubes placed downstream of hadron absorbers. Hadrons are detected by two large iron-scintillator sampling calorimeters installed in front of the absorbers and shielded to avoid electromagnetic contamination. The identification of charged particles is possible with a RICH detector, although in this paper we have not utilised the information from the RICH.

The data recording system is activated by various triggers indicating the presence of

a scattered muon and/or an energy deposited by hadrons in the calorimeters. In addition to the inclusive trigger, in which the scattered muon is identified by coincidence signals in the trigger hodoscopes, several semi-inclusive triggers were used. They select events fulfilling the requirement to detect the scattered muon together with the energy deposited in the hadron calorimeters exceeding a given threshold. In 2003 the acceptance was further extended towards high Q^2 values by the addition of a standalone calorimetric trigger in which no condition is set for the scattered muon. The COMPASS trigger system allows us to cover a wide range of Q^2, from quasi-real photoproduction to deep inelastic interactions.

A more detailed description of the COMPASS apparatus can be found in Ref. [19]

3 Event sample

For the present analysis the whole data sample taken in 2002 and 2003 with the longitudinally polarised target is used. For an event to be accepted for further analysis it is required to originate in the target, have a reconstructed beam track, a scattered muon track, and only two additional tracks of oppositely charged hadrons associated to the primary vertex. The fluxes of beam muons passing through each target cell are equalised using appropriate cuts on the position and angle of the beam tracks.

The charged pion mass hypothesis is assigned to each hadron track and the invariant mass of two pions, $m_{\pi\pi}$, calculated. A cut on the invariant mass of two pions, $0.5 < m_{\pi\pi} < 1$ GeV$/c^2$, is applied to select the ρ^0. As slow recoil target particles are not detected, in order to select exclusive events we use the cut on the missing energy, $-2.5 < E_{miss} < 2.5$ GeV, and on the transverse momentum of ρ^0 with respect to the direction of virtual photon, $p_t^2 < 0.5$ (GeV$/c)^2$. Here $E_{miss} = (M_X^2 - M_p^2)/2M_p$, where M_X is the missing mass of the unobserved recoiling system and M_p is the proton mass. Coherent interactions on the target nuclei are removed by a cut $p_t^2 > 0.15$ (GeV$/c)^2$. To avoid large corrections for acceptance and misidentification of events, additional cuts $\nu > 30$ GeV and $E_{\mu'} > 20$ GeV are applied.

The distributions of $m_{\pi\pi}$, E_{miss} and p_t^2 are shown in Fig. 1. Each plot is obtained applying all cuts except those corresponding to the displayed variable. On the left top panel of Fig. 1 a clear peak of the ρ^0 resonance, centred at 770 MeV$/c^2$, is visible on the top of the small contribution of background of the non-resonant $\pi^+\pi^-$ pairs. Also the skewing of the resonance peak towards smaller values of $m_{\pi\pi}$, due to an interference with the non-resonant background, is noticeable. A small bump below 0.4 GeV$/c^2$ is due to assignment of the charged pion mass to the kaons from decays of ϕ mesons. The mass cuts eliminate the non-resonant background outside of the ρ^0 peak, as well as the contribution of ϕ mesons.

On the right top panel of the figure the peak at $E_{miss} \approx 0$ is the signal of exclusive ρ^0 production. The width of the peak, $\sigma \approx 1.1$ GeV, is due to the spectrometer resolution. Non-exclusive events, where in addition to the recoil nucleon other undetected hadrons are produced, appear at $E_{miss} > 0$. Due to the finite resolution, however, they are not resolved from the exclusive peak. This background consists of two components: the double-diffractive events where additionally to ρ^0 an excited nucleon state is produced in the nucleon vertex of reaction (2), and events with semi-inclusive ρ^0 production, in which other hadrons are produced but escape detection.

The p_t^2 distribution shown on the bottom panel of the figure indicates a contribution from coherent production on target nuclei at small p_t^2 values. A three-exponential fit to this distribution was performed, which indicates also a contribution of non-exclusive background increasing with p_t^2. Therefore to select the sample of exclusive incoherent ρ^0
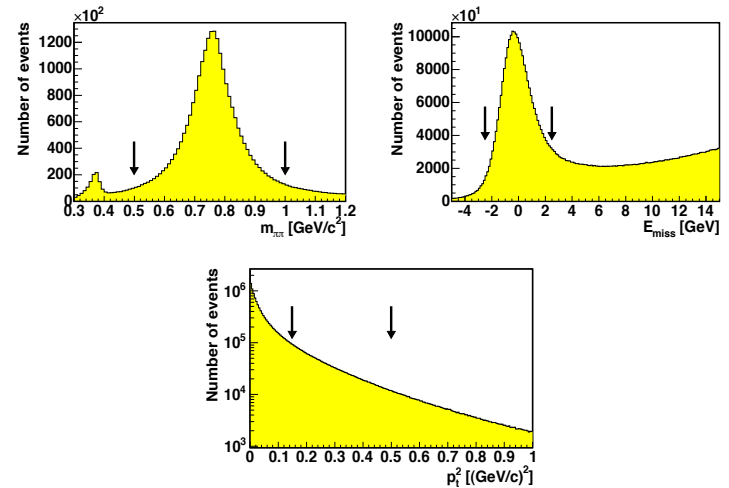

Figure 1: Distributions of $m_{\pi\pi}$ (top left), E_{miss} (top right) and p_t^2 (bottom) for the exclusive sample. The arrows show cuts imposed on each variable to define the final sample.

production, the aforementioned p_t^2 cuts, indicated by arrows, were applied.

After all selections the final sample consists of about 2.44 million events. The distributions of Q^2, x and W are shown in Fig. 2. The data cover a wide range in Q^2 and x which extends towards the small values by almost two orders of magnitude compared to the similar studies reported in Ref. [17]. The sharp edge of the W distribution at the low W values is a consequence of the cut applied on ν. For this sample $\langle W \rangle$ is equal to 10.2 GeV and $\langle p_t^2 \rangle = 0.27$(GeV$/c)^2$.

4 Extraction of asymmetry A_1^ρ

The cross section asymmetry $A_{LL} = (\sigma_{\uparrow\downarrow} - \sigma_{\uparrow\uparrow})/(\sigma_{\uparrow\downarrow} + \sigma_{\uparrow\uparrow})$ for reaction (1) , for antiparallel ($\uparrow\downarrow$) and parallel ($\uparrow\uparrow$) spins of the incoming muon and the target nucleon, is related to the virtual-photon nucleon asymmetry A_1^ρ by

$$A_{LL} = D\left(A_1^\rho + \eta A_2^\rho\right), \qquad (5)$$

where the factors D and η depend on the event kinematics and A_2^ρ is related to the interference cross section for exclusive production by longitudinal and transverse virtual photons. As the presented results extend into the range of very small Q^2, the exact formulae for the depolarisation factor D and kinematical factor η [20] are used without neglecting terms proportional to the lepton mass squared m^2. The depolarisation factor is given by

$$D(y, Q^2) = \frac{y\left[(1 + \gamma^2 y/2)(2 - y) - 2y^2 m^2/Q^2\right]}{y^2(1 - 2m^2/Q^2)(1 + \gamma^2) + 2(1 + R)(1 - y - \gamma^2 y^2/4)}, \qquad (6)$$
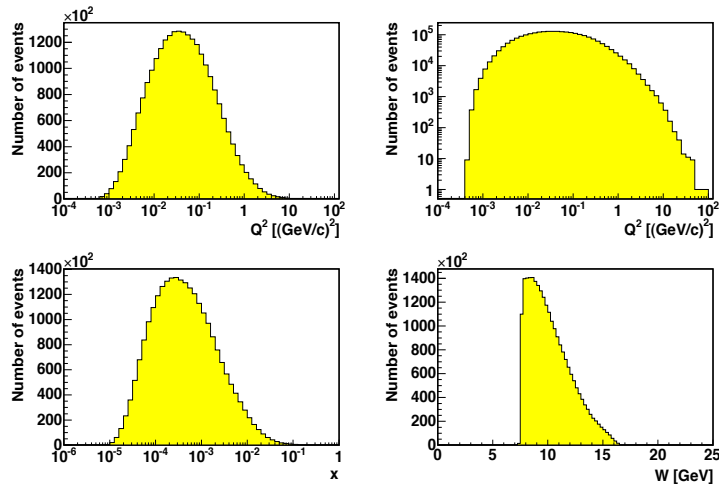
Figure 2: Distributions of the kinematical variables for the final sample: Q^2 with linear and logarithmic vertical axis scale (top left and right panels respectively), x (bottom left), and the energy W (bottom right).

where $R = \sigma_L/\sigma_T$, $\sigma_{L(T)}$ is the cross section for reaction (2) initiated by longitudinally (transversely) polarised virtual photons, the fraction of the muon energy lost $y = \nu/E_\mu$ and $\gamma^2 = Q^2/\nu^2$. The kinematical factor $\eta(y, Q^2)$ is the same as for the inclusive asymmetry.

The asymmetry A_2^ρ obeys the positivity limit $A_2^\rho < \sqrt{R}$, analogous to the one for the inclusive case. For $Q^2 \leq 0.1$ $(\text{GeV}/c)^2$ the ratio R for the reaction (2) is small, cf. Fig. 3, and the positivity limit constrains A_2^ρ to small values. Although for larger Q^2 the ratio R for the process (2) increases with Q^2, because of small values of η the product $\eta\sqrt{R}$ is small in the whole Q^2 range of our sample. Therefore the second term in Eq. 5 can be neglected, so that

$$A_1^\rho \simeq \frac{1}{D} A_{LL}, \qquad (7)$$

and the effect of this approximation is included in the systematic uncertainty of A_1^ρ.

The number of events N_i collected from a given target cell in a given time interval is related to the spin-independent cross section $\bar{\sigma}$ for reaction (2) and to the asymmetry A_1^ρ by

$$N_i = a_i \phi_i n_i \bar{\sigma}(1 + P_B P_T f D A_1^\rho), \qquad (8)$$

where P_B and P_T are the beam and target polarisations, ϕ_i is the incoming muon flux, a_i the acceptance for the target cell, n_i corresponding number of target nucleons, and f the target dilution factor. The asymmetry is extracted from the data sets taken before and after a reversal of the target spin directions. The four relations of Eq. 8, corresponding to the two cells (u and d) and the two spin orientations (1 and 2) lead to a second-
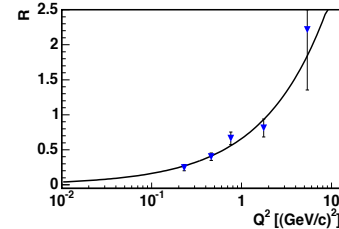
Figure 3: The ratio $R = \sigma_L/\sigma_T$ as a function of Q^2 measured in the E665 experiment. The curve is a fit to the data described in the text.

order equation in A_1^ρ for the ratio $(N_{u,1}N_{d,2}/N_{d,1}N_{u,2})$. Here fluxes cancel out as well as acceptances, if the ratio of acceptances for the two cells is the same before and after the reversal [21]. In order to minimise the statistical error all quantities used in the asymmetry calculation are evaluated event by event with the weight factor $w = P_B f D$. The polarisation of the beam muon, P_B, is obtained from a simulation of the beam line and parameterised as a function of the beam momentum. The target polarisation is not included in the event weight w because it may vary in time and generate false asymmetries. An average P_T is used for each target cell and each spin orientation.

The ratio R, which enters the formula for D and strongly depends on Q^2 for reaction (2), was calculated on an event-by-event basis using the parameterisation

$$R(Q^2) = a_0(Q^2)^{a_1}, \qquad (9)$$

with $a_0 = 0.66 \pm 0.05$, and $a_1 = 0.61 \pm 0.09$. The parameterisation was obtained by the Fermilab E665 experiment from a fit to their R measurements for exclusive ρ^0 muopro-duction on protons [3]. These are shown in Fig. 3 together with the fitted Q^2-dependence. The preliminary COMPASS results on R for the incoherent exclusive ρ^0 production on the nucleon [7], which cover a broader kinematic region in Q^2, agree reasonably well with this parameterisation. The uncertainty of a_0 and a_1 is included in the systematic error of A_1^ρ.

The dilution factor f gives the fraction of events of reaction (2) originating from nucleons in polarised deuterons inside the target material. It is calculated event-by-event using the formula

$$f = C_1 \cdot f_0 = C_1 \cdot \frac{n_\text{D}}{n_\text{D} + \Sigma_A n_\text{A}(\tilde{\sigma}_\text{A}/\tilde{\sigma}_\text{D})}. \qquad (10)$$

Here n_D and n_A denote numbers of nucleons in deuteron and nucleus of atomic mass A in the target, and $\tilde{\sigma}_\text{D}$ and $\tilde{\sigma}_\text{A}$ are the cross sections per nucleon for reaction (2) occurring on the deuteron and on the nucleus of atomic mass A, respectively. The sum runs over all nuclei present in the COMPASS target. The factor C_1 takes into account that there are two polarised deuterons in the ^{6}LiD molecule, as the ^{6}Li nucleus is in a first approximation composed of a deuteron and an α particle.

The measurements of the $\tilde{\sigma}_\text{A}/\tilde{\sigma}_\text{D}$ for incoherent exclusive ρ^0 production come from the NMC [2], E665 [22] and early experiments on ρ^0 photoproduction [23]. They were
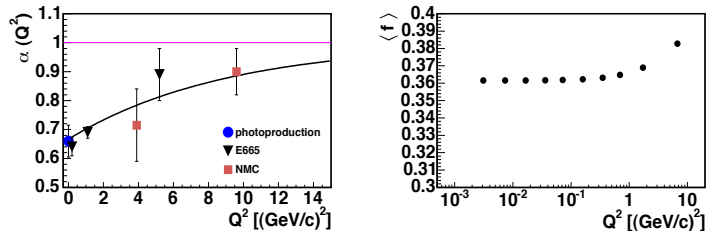
Figure 4: (Left) Parameter α of Eq. 11 as a function of Q^2 (from Ref. [24]). The experimental points and the fitted curve are shown. See text for details. (Right) The dilution factor f as a function of Q^2.

fitted in Ref. [24] with the formula:

$$\tilde{\sigma}_A = \sigma_p \cdot A^{\alpha(Q^2)-1}, \qquad \text{with} \ \ \alpha(Q^2) - 1 = -\frac{1}{3}\exp\{-Q^2/Q_0^2\}, \qquad (11)$$

where σ_p is the cross section for reaction (2) on the free proton. The value of the fitted parameter Q_0^2 is equal to 9 ± 3 $(\text{GeV}/c)^2$. The measured values of the parameter α and the fitted curve $\alpha(Q^2)$ are shown on the left panel of Fig. 4 taken from Ref. [24]. On the right panel of the figure the average value of f is plotted for the various Q^2 bins used in the present analysis. The values of f are equal to about 0.36 in most of the Q^2 range, rising to about 0.38 at the highest Q^2.

The radiative corrections (RC) have been neglected in the present analysis, in particular in the calculation of f, because they are expected to be small for reaction (1). They were evaluated [25] to be of the order of 6% for the NMC exclusive ρ^0 production analysis. The small values of RC are mainly due to the requirement of event exclusivity via cuts on E_{miss} and p_t^2, which largely suppress the dominant external photon radiation. The internal (infrared and virtual) RC were estimated in Ref. [25] to be of the order of 2%.

5   Systematic errors

The main systematic uncertainty of A_1^ρ comes from an estimate of possible false asymmetries. In order to improve the accuracy of this estimate, in addition to the standard sample of incoherent events, a second sample was selected by changing the p_t^2 cuts to

$$0 < p_t^2 < 0.5 \ (\text{GeV}/c)^2, \qquad (12)$$

and keeping all the remaining selections and cuts the same as for the 'incoherent sample'. In the following it will be referred to as the 'extended p_t^2 sample'. Such an extension of the p_t^2 range allows one to obtain a sample which is about five times larger than the incoherent sample. However, in addition to incoherent events such a sample contains a large fraction of events originating from coherent ρ^0 production. Therefore, for the estimate of the dilution factor f a different nuclear dependence of the exclusive cross section was used, applicable for the sum of coherent and incoherent cross sections [2]. The physics asymmetries A_1^ρ for both samples are consistent within statistical errors.

Possible, false experimental asymmetries were searched for by modifying the selection of data sets used for the asymmetry calculation. The grouping of the data into configurations with opposite target-polarisation was varied from large samples, covering at most two weeks of data taking, into about 100 small samples, taken in time intervals of the order of 16 hours. A statistical test was performed on the distributions of asymmetries obtained from these small samples. In each of the Q^2 and x bins the dispersion of the values of A_1^ρ around their mean agrees with the statistical error. Time-dependent effects which would lead to a broadening of these distributions were thus not observed. Allowing the dispersion of A_1^ρ to vary within its two standard deviations we obtain for each bin an upper bound for the systematic error arising from time-dependent effects

$$\sigma_{\text{falseA,tdep}} < 0.56 \ \sigma_{\text{stat}}. \qquad (13)$$

Here σ_{stat} is the statistical error on A_1^ρ for the extended p_t^2 sample. The uncertainty on the estimates of possible false asymmetries due to the time-dependent effects is the dominant contribution to the total systematic error in most of the kinematical region.

Asymmetries for configurations where spin effects cancel out were calculated to check the cancellation of effects due to fluxes and acceptances. They were found compatible with zero within the statistical errors. Asymmetries obtained with different settings of the microwave (MW) frequency, used for DNP, were compared in order to test possible effects related to the orientation of the target magnetic field. The results for the extended p_t^2 sample tend to show that there is a small difference between asymmetries for the two MW configurations. However, because the numbers of events of the data samples taken with each MW setting are approximately balanced, the effect of this difference on A_1^ρ is negligible for the total sample.

The systematic error on A_1^ρ also contains an overall scale uncertainty of 6.5% due to uncertainties on P_B and P_T. The uncertainty of the parameterisation of $R(Q^2)$ affects the depolarisation factor D. The uncertainty of the dilution factor f is mostly due to uncertainty of the parameter $\alpha(Q^2)$ which takes into account nuclear effects in the incoherent ρ^0 production. The neglect of the A_2^ρ term mainly affects the highest bins of Q^2 and x.

Another source of systematic errors is due to the contribution of the non-exclusive background to our sample. This background originates from two sources. First one is due to the production of ρ^0 accompanied by the dissociation of the target nucleon, the second one is the production of ρ^0 in inclusive scattering. In order to evaluate the amount of background in the sample of exclusive events it is necessary to determine the E_{miss} dependence for the non-exclusive background in the region under the exclusive peak (cf. Fig. 1). For this purpose complete Monte Carlo simulations of the experiment were used, with events generated by either the PYTHIA 6.2 or LEPTO 6.5.1 generators. Events generated with LEPTO come only from deep inelastic scattering and cover the range of $Q^2 > 0.5$ $(\text{GeV}/c)^2$. Those generated with PYTHIA cover the whole kinematical range of the experiment and include exclusive production of vector mesons and processes with diffractive excitation of the target nucleon or the vector meson, in addition to inelastic production.

The generated MC events were reconstructed and selected for the analysis using the same procedure as for the data. In each bin of Q^2 the E_{miss} distribution for the MC was normalised to the corresponding one for the data in the range of large $E_{miss} > 7.5$ GeV. Then the normalised MC distribution was used to estimate the number of background events under the exclusive peak in the data. The fraction of background events in the sample of incoherent exclusive ρ^0 production was estimated to be about 0.12 ± 0.06 in most

9

10

of the kinematical range, except in the largest Q^2 region, where it is about 0.24 ± 0.12. The large uncertainties of these fractions reflect the differences between estimates from LEPTO and PYTHIA in the region where they overlap. In the case of PYTHIA the uncertainties on the cross sections for diffractive photo- and electroproduction of vector mesons also contribute. For events generated with PYTHIA the E_{miss} distributions for various physics processes could be studied separately. It was found that events of ρ^0 production with an excitation of the target nucleon into N^* resonances of small mass, $M < 2$ GeV/c^2, cannot be resolved from the exclusive peak and therefore were not included in the estimates of number of background events.

An estimate of the asymmetry A_1^ρ for the background was obtained using a non-exclusive sample, which was selected with the standard cuts used in this analysis, except the cut on E_{miss} which was modified to $E_{miss} > 2.5$ GeV. In different high-E_{miss} bins A_1^ρ for this sample was found compatible with zero.

Because no indication of a non-zero A_1^ρ for the background was found, and also due to a large uncertainty of the estimated amount of background in the exclusive sample, no background corrections were made. Instead, the effect of background was treated as a source of systematic error. Its contribution to the total systematic error was not significant in most of the kinematical range, except for the highest Q^2 and x.

The total systematic error on A_1^ρ was obtained as a quadratic sum of the errors from all discussed sources. Its values for each Q^2 and x bin are given in Tables 1 and 2. The total systematic error amounts to about 40% of the statistical error for most of the kinematical range. Both errors become comparable in the highest bin of Q^2.

6 Results

The COMPASS results on A_1^ρ are shown as a function of Q^2 and x in Fig. 5 and listed in Tables 1 and 2. The statistical errors are represented by vertical bars and the total systematic errors by shaded bands.
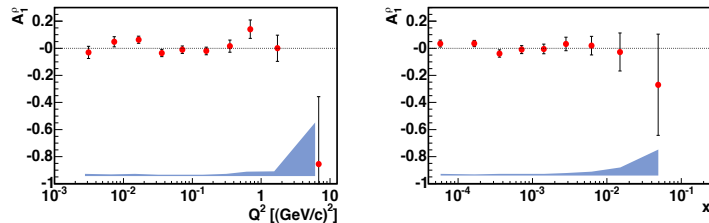
Figure 5: A_1^ρ as a function of Q^2 (left) and x (right) from the present analysis. Error bars correspond to statistical errors, while bands at the bottom represent the systematical errors.

The wide range in Q^2 covers four orders of magnitude from $3 \cdot 10^{-3}$ to 7 (GeV/c)^2. The domain in x which is strongly correlated with Q^2, varies from $5 \cdot 10^{-5}$ to about 0.05 (see Tables for more details). For the whole kinematical range the A_1^ρ asymmetry measured by COMPASS is consistent with zero. As discussed in the introduction, this indicates that the role of unnatural parity exchanges, like π- or A_1-Reggeon exchange, is

Table 1: Asymmetry A_1^ρ as a function of Q^2. Both the statistical errors (first) and the total systematic errors (second) are listed.

Q^2 range	$\langle Q^2 \rangle$ [(GeV/c)^2]	$\langle x \rangle$	$\langle \nu \rangle$ [GeV]	A_1^ρ
$0.0004 - 0.005$	0.0031	$4.0 \cdot 10^{-5}$	42.8	$-0.030 \pm 0.045 \pm 0.014$
$0.005 - 0.010$	0.0074	$8.4 \cdot 10^{-5}$	49.9	$0.048 \pm 0.038 \pm 0.013$
$0.010 - 0.025$	0.017	$1.8 \cdot 10^{-4}$	55.6	$0.063 \pm 0.026 \pm 0.014$
$0.025 - 0.050$	0.036	$3.7 \cdot 10^{-4}$	59.9	$-0.035 \pm 0.027 \pm 0.009$
$0.05 - 0.10$	0.072	$7.1 \cdot 10^{-4}$	62.0	$-0.010 \pm 0.028 \pm 0.008$
$0.10 - 0.25$	0.16	0.0016	62.3	$-0.019 \pm 0.029 \pm 0.009$
$0.25 - 0.50$	0.35	0.0036	60.3	$0.016 \pm 0.045 \pm 0.014$
$0.5 - 1$	0.69	0.0074	58.6	$0.141 \pm 0.069 \pm 0.030$
$1 - 4$	1.7	0.018	59.7	$0.000 \pm 0.098 \pm 0.035$
$4 - 50$	6.8	0.075	55.9	$-0.85 \pm 0.50 \pm 0.39$

small in that kinematical domain, which is to be expected if diffraction is the dominant process for reaction (2).

In Fig. 6 the COMPASS results are compared to the HERMES results on A_1^ρ obtained on a deuteron target [17]. Note that the lowest Q^2 and x HERMES points, referred to as 'quasi-photoproduction', come from measurements where the kinematics of the small-angle scattered electron was not measured but estimated from a MC simulation. This is in contrast to COMPASS, where scattered muon kinematics is measured even at the smallest Q^2.
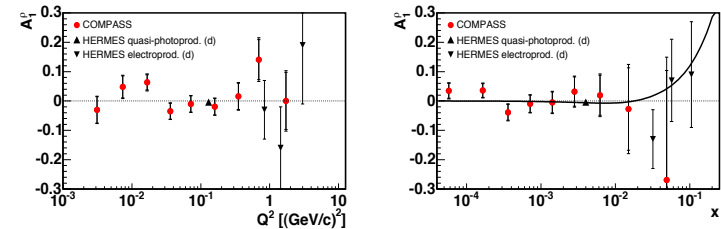

Figure 6: A_1^ρ as a function of Q^2 (left) and x (right) from the present analysis (circles) compared to HERMES results on the deuteron target (triangles). For the COMPASS results inner bars represent statistical errors, while the outer bars correspond to the total error. For the HERMES results vertical bars represent the quadratic sum of statistical and systematic errors. The curve represents the prediction explained in the text.

The results from both experiments are consistent within errors. The kinematical range covered by the present analysis extends further towards small values of x and Q^2 by almost two orders of magnitude. In each of the two experiments A_1^ρ is measured at different average W, which is equal to about 10 GeV for COMPASS and 5 GeV for

Table 2: Asymmetry A_1^ρ as a function of x. Both the statistical errors (first) and the total systematic errors (second) are listed.

x range	$\langle x \rangle$	$\langle Q^2 \rangle$ [(GeV/c)^2]	$\langle \nu \rangle$ [GeV]	A_1^ρ
$8 \cdot 10^{-6} - 1 \cdot 10^{-4}$	$5.8 \cdot 10^{-5}$	0.0058	51.7	$0.035 \pm 0.026 \pm 0.011$
$1 \cdot 10^{-4} - 2.5 \cdot 10^{-4}$	$1.7 \cdot 10^{-4}$	0.019	59.7	$0.036 \pm 0.024 \pm 0.010$
$2.5 \cdot 10^{-4} - 5 \cdot 10^{-4}$	$3.6 \cdot 10^{-4}$	0.041	61.3	$-0.039 \pm 0.027 \pm 0.012$
$5 \cdot 10^{-4} - 0.001$	$7.1 \cdot 10^{-4}$	0.082	60.8	$-0.010 \pm 0.030 \pm 0.010$
$0.001 - 0.002$	0.0014	0.16	58.6	$-0.005 \pm 0.036 \pm 0.013$
$0.002 - 0.004$	0.0028	0.29	54.8	$0.032 \pm 0.050 \pm 0.019$
$0.004 - 0.01$	0.0062	0.59	50.7	$0.019 \pm 0.069 \pm 0.026$
$0.01 - 0.025$	0.015	1.3	47.5	$-0.03 \pm 0.14 \pm 0.06$
$0.025 - 0.8$	0.049	3.9	43.8	$-0.27 \pm 0.38 \pm 0.19$

HERMES. Thus, no significant W dependence is observed for A_1^ρ on an isoscalar nucleon target.

The x dependence of the measured A_1^ρ is compared in Fig. 6 to the prediction given by Eq. 4, which relates A_1^ρ to the asymmetry A_1 for the inclusive inelastic lepton-nucleon scattering. To produce the curve the inclusive asymmetry A_1 was parameterised as $A_1(x) = (x^\alpha - \gamma^\alpha) \cdot (1 - e^{-\beta x})$, where $\alpha = 1.158 \pm 0.024$, $\beta = 125.1 \pm 115.7$ and $\gamma = 0.0180 \pm 0.0038$. The values of the parameters have been obtained from a fit of $A_1(x)$ to the world data from polarised deuteron targets [26–31] including COMPASS measurements at very low Q^2 and x [32]. Within the present accuracy the results on A_1^ρ are consistent with this prediction.

In the highest Q^2 bin, $\langle Q^2 \rangle = 6.8$ (GeV/c)^2, in the kinematical domain of applicability of pQCD-inspired models which relate the asymmetry to the spin-dependent GPDs for gluons and quarks (cf. Introduction), one can observe a hint of a possible nonzero asymmetry, although with a large error. It should be noted that in Ref. [18] a negative value of A_{LL} different from zero by about 2 standard deviations was reported at $\langle Q^2 \rangle = 7.7$ (GeV/c)^2. At COMPASS, including the data taken with the longitudinally polarised deuteron target in 2004 and 2006 will result in an increase of statistics by a factor of about three compared to the present paper, and thus may help to clarify the issue.

For the whole Q^2 range future COMPASS data, to be taken with the polarised proton target, would be very valuable for checking if the role of the flavour-blind exchanges is indeed dominant, as expected for the Pomeron-mediated process.

7   Summary

The longitudinal double spin asymmetry A_1^ρ for the diffractive muoproduction of ρ^0 meson, $\mu + N \rightarrow \mu + N + \rho$, has been measured by scattering longitudinally polarised muons off longitudinally polarised deuterons from the ^{6}LiD target and selecting incoherent exclusive ρ^0 production. The presented results for the COMPASS 2002 and 2003 data cover a range of energy W from about 7 to 15 GeV.

The Q^2 and x dependence of A_1^ρ is presented in a wide kinematical range $3 \cdot 10^{-3} \le Q^2 \le 7$ (GeV/c)^2 and $5 \cdot 10^{-5} \le x \le 0.05$. These results extend the range in Q^2 and x by

two orders of magnitude down with respect to the existing data from HERMES.

The asymmetry A_1^ρ is compatible with zero in the whole x and Q^2 range. This may indicate that the role of unnatural parity exchanges like π- or A_1-Reggeon exchange is small in that kinematical domain.

The x dependence of measured A_1^ρ is consistent with the prediction of Ref. [11] which relates A_1^ρ to the asymmetry A_1 for the inclusive inelastic lepton–nucleon scattering.

8   Acknowledgements

References

[1] K. Schilling and G. Wolf, Nucl. Phys. **B61** (1973) 381.

[2] NMC Collab., M. Arneodo et al., Nucl. Phys. **B429** (1994) 503.

[3] E665 Collab., M.R. Adams et al., Z. Phys. **C74** (1997) 237.

[4] ZEUS Collab., J. Breitweg et al., Eur. Phys. J. **C12** (2000) 393.

[5] H1 Collab., C. Adloff et al., Eur. Phys. J. **C13** (2000) 371;
H1 Collab., C. Adloff et al., Phys. Lett. **B 539** (2002) 25.

[6] HERMES Collab., K. Ackerstaff et al., Eur. Phys. J. **C18** (2000) 303.

[7] A. Sandacz (on behalf of the COMPASS Collaboration), Nucl. Phys. **B 146** (Proc. Suppl.) (2005) 581.

[8] I.P. Ivanov, N.N. Nikolaev, JETP Lett. **C29** (1999) 294;
I.P. Ivanov, *Diffractive production of vector mesons in Deep Inelastic Scattering within k_t-factorization approach*, hep-ph/0303053.

[9] S.I. Manaenkov, *Regge description of spin-spin asymmetry in photon diffractive dissociation*, Preprint DESY 99-016 (see also hep-ph/9903405).

[10] H. Fraas, Nucl. Phys. **B113** (1976) 532.

[11] HERMES Collab., A. Airapetian et al., Phys. Lett. **B513** (2001) 301.

[12] J.C. Collins, L. Frankfurt and M. Strikman, Phys. Rev. **D56** (1997) 2982.

[13] A.D. Martin, M.G. Ryskin and T. Teubner, Phys. Rev. **D55** (1997) 4329.

[14] M.G. Ryskin, Phys. Atom. Nucl. **62** (1999) 315; Yad. Fiz. **62** (1999) 350.

[15] S.V. Goloskokov and P. Kroll, Eur. Phys. J. **C42** (2005) 281.

[16] S.V. Goloskokov and P. Kroll, hep-ph/0611290.

[17] HERMES Collab., A. Airapetian et al., Eur. Phys. J. **C29** (2003) 171.

[18] A. Tripet, Nucl. Phys. **B79** (Proc. Suppl.) (1999) 529.

[19] COMPASS Collab., P. Abbon et al., Nucl. Instrum. Meth. **A577** (2007) 455.

[20] J. Kiryluk, Ph.D. thesis, Warsaw University, 2000.

[21] SMC Collab., D. Adams et al., Phys. Rev. **56** (1997) 5330.

[22] E665 Collab., M.R. Adams et al., Phys. Rev. Lett. **74** (1995) 1525.

[23] T. Bauer et al., Rev. Mod. Phys. **50** (1978) 261, Erratum: *ibid.*, **51** (1979) 407.

[24] A. Tripet, Ph.D. thesis, Universität Bielefeld, 2002.

[25] K. Kurek, *QED radiative corrections in exclusive ρ^0 leptoproduction*, preprint DESY-96-209, June 1996 (see also hep-ph/9606240).

[26] SMC Collab., B. Adeva et al., Phys. Rev. **D58** (1998) 112001.

[27] E143 Collab., K. Abe et al., Phys. Rev. **D58** (1998) 112003.

[28] E155 Collab., P.L. Anthony *et al.*, Phys. Lett. **B463** (1999) 339.

[29] SMC Collab., B. Adeva *et al.*, Phys. Rev. **D60** (1999) 072004; Erratum: *ibid.*, **D62** (2000) 079902.

[30] HERMES Collab., A. Airapetian *et al.*, Phys. Rev. **D75** (2007) 012007.

[31] COMPASS Collab., V.Yu. Alexakhin *et al.*, Phys. Lett. **B647** (2007) 8.

[32] COMPASS Collab., V.Yu. Alexakhin *et al.*, Phys. Lett. **B647** (2007) 330.

COMPASS Note-2009-10, E. Burtin et al., "Exclusive ρ^0 production using tranversely polarized ^{6}LiD (2004) and NH$_3$ (2007) targets".

Exclusive ρ^0 production using transversely polarized ^{6}LiD (2004) and NH$_3$ (2007) targets

E. Burtin, N. d'Hose, H. Fischer, G. Jegou, A. Sandacz, H. Wollny

June 9, 2009

COMPASS Note 2009-XXX

Abstract

This note describes the selection of exclusive incoherent production of ρ^0 mesons for the transversely polarized ^{6}LiD target (2004 data) and NH$_3$ target (2007 data).

Results for the extracted raw asymmetry $A_{\mathrm{UT}}^{\sin(\phi-\phi_S)}$ for the COMPASS 2007 data are presented. They have been cross checked in independent analyses realized at Freiburg and Saclay. A similar work was done for the COMPASS 2002-2004 data (COMPASS note 2007-9 [1]).

The final goal of this work will be to correct the raw asymmetry for the remaining non-exclusive background and to separate the longitudinal and transverse observables using a good knowledge of the acceptance. In parallel the spin density matrix element r_{00}^{04} and the t-dependence of the cross section will be determined. This work is still in progress for the 2004 and 2007 data and will be presented in a further analysis meeting.

1

Contents

Part I

Introduction

1   Theoretical Motivation

The ultimate goal of this analysis is to determine the Transverse Target Spin Asymmetry $A_{UT}^{\sin(\phi-\phi_s)}$ for *exclusive incoherent* ρ^0 production in the scattering of high energy muons on nucleons. The experiment is carried out at CERN by the COMPASS collaboration using the 160 GeV muon beam and the transversely polarised ^{6}LiD target (for 2004 data) and transversely polarised NH$_3$ target (for 2007 data).

The studied reaction is

$$\mu + N \rightarrow \mu' + \rho^0 + N' \tag{1}$$

where N is a quasi-free nucleon from the polarised material (proton or neutron for ^{6}LiD and only proton for NH$_3$). The reaction (1) can be described in terms of the virtual photoproduction process

$$\gamma^* + N \rightarrow \rho^0 + N' \tag{2}$$

Exclusive vector meson production has played an important role in studying strong interaction and gained a renewed interest, as it can give access to Generalized Parton Distributions (GPDs) and thus to a wealth of information on the nucleon structure. Moreover it was pointed out that vector meson production on a transversely polarised target is sensitive to the nucleon helicity-flip GPD E [2, 3]. This GPD offers unique views on the orbital angular momentum carried by partons in the proton [4] and on the correlation between polarisation and spatial distribution of partons [5].

In the limit of large Q^2 at fixed x_B and small momentum transfer t, the $\gamma^* p$ amplitude factorizes into the convolution of a hard-scattering subprocess with GPDs in the nucleon and the light-cone distribution amplitude of the produced mesons. The factorization theorem [6, 7] shows that the leading transitions in the large Q^2 limit have both the virtual photon and the produced meson *longitudinally* polarised, all other transitions being suppressed by at least one power of $1/Q$.

The longitudinally polarised vector meson channels $\rho^{0,\pm}, \omega, \phi, ...$ are sensitive only to the GPDs H and E while the pseudo-scalar channels $\pi^{0,\pm}, \eta, ...$ are sensitive only to $\tilde{H}$ and $\tilde{E}$. Quark and gluon GPDs contribute both for the meson production as the GPDs for gluons enter at the same order in α_s as those for quarks. Decomposition on flavor quark and gluon contributions can be illustrated

as follows:

$$H_{\rho^0} = \frac{1}{\sqrt{2}}\left(\frac{2}{3}H^u + \frac{1}{3}H^d + \frac{3}{8}H^g\right) \quad H_\omega = \frac{1}{\sqrt{2}}\left(\frac{2}{3}H^u - \frac{1}{3}H^d + \frac{1}{8}H^g\right) \quad H_\phi = -\frac{1}{3}H^s - \frac{1}{8}H^g \tag{3}$$

The relative production of these three meson $\rho{:}\omega{:}\phi$ will give ratios as 9:1:2 in the region where the gluon GPDs dominate over those for quarks. Evidence for substantial gluon contribution for values of x_B around 0.1 has been given in Ref. [8]. These properties make the hard meson production reactions complementary to the DVCS process as it provides an additional tool or filter to disentangle the different GPDs.

2 Cross section and Asymmetry

The references [9, 10] provide a very detailed framework to our study which is summarized here. The cross section of the reaction (1) on transversely polarised nucleon is a function of the following kinematic variables x_B, Q^2, t, ϕ and ϕ_S. ϕ is the azimuthal angle between the lepton plane and the hadron plane and ϕ_S is the azimuthal angle of the target spin vector S_T w.r.t. the virtual photon direction (see Fig. 1). Note, that the target transverse polarisation w.r.t. the lepton beam direction will be denoted by P_T.

The spin dependent photoabsorption cross sections and interference terms can be expressed in terms of the amplitudes $\mathcal{A}_m^i$ for the subprocess of the reaction (2) with the target nucleon helicity i and the photon helicity m:

$$\sigma_{mn}^{ij}(x_B, Q^2, t) \propto \Sigma_{spins}(\mathcal{A}_m^i)^* \mathcal{A}_n^j \tag{4}$$

For the sake of legibility we note the target spin states by $\pm$ instead of $\pm\frac{1}{2}$ and the photon spin states $+, 0, -$. We can use also the common notation $\sigma_T = \frac{1}{2}(\sigma_{++}^{++} + \sigma_{++}^{--})$ and $\sigma_L = \sigma_{00}^{++}$ for the transverse and longitudinal virtual photon cross sections.

Below the lepton-proton differential cross section is given for a transversely polarised target with respect to the lepton beam. The dependence on x_B, Q^2, ϕ, and ϕ_S is shown explicitly, whereas t-dependence is implied. The other used variables are: the fraction y of the energy of the initial lepton taken by the virtual photon, the virtual photon polarisation parameter $\epsilon = \frac{1-y-\frac{1}{4}y^2\gamma^2}{1-y+\frac{1}{2}y^2+\frac{1}{4}y^2\gamma^2}$, and the polar angle θ_γ of the virtual photon relatively to the incident lepton direction, for which $\sin\theta_\gamma = \gamma\sqrt{\frac{1-y-\frac{1}{4}y^2\gamma^2}{1+\gamma^2}}$ with $\gamma = 2\,x_B\,M_p/Q$:
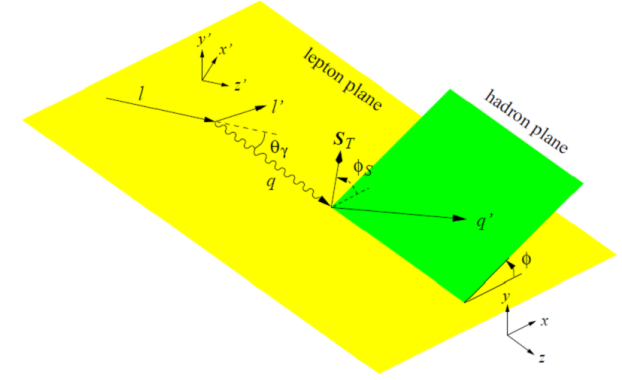
Figure 1: Definition of the angles ϕ between the hadron production plane and the lepton scattering plane and of the angle ϕ_S between the lepton scattering plane and the target spin vector. S_T is the transverse component of the target spin vector w.r.t. the virtual photon direction.

$$\left[\frac{\cos\theta_\gamma}{1-\sin^2\theta_\gamma\sin^2\phi_S}\right]^{-1}\left[\frac{\alpha_{em}}{8\pi^3}\frac{y^2}{1-\epsilon}\frac{1-x_B}{x_B}\frac{1}{Q^2}\right]^{-1}\frac{d\sigma}{dx_B\,dQ^2\,d\phi\,d\phi_S} = \tag{5}$$

$$\frac{1}{2}(\sigma_{++}^{++} + \sigma_{++}^{--}) + \epsilon\,\sigma_{00}^{++} - \epsilon\cos(2\phi)\,\mathrm{Re}\sigma_{+-}^{++} - \sqrt{\epsilon(1+\epsilon)}\,\cos\phi\,\mathrm{Re}(\sigma_{+0}^{++} + \sigma_{+0}^{--})$$

$$-\frac{P_T}{\sqrt{1-\sin^2\theta_\gamma\sin^2\phi_S}}\left[\sin\phi_S\,\cos\theta_\gamma\,\sqrt{\epsilon(1+\epsilon)}\,\mathrm{Im}\sigma_{+0}^{+-}\right.$$

$$+\sin(\phi-\phi_s)\,(\cos\theta_\gamma\,\mathrm{Im}(\sigma_{++}^{+-} + \epsilon\,\sigma_{00}^{+-}) + \frac{1}{2}\sin\theta_\gamma\,\sqrt{\epsilon(1+\epsilon)}\,\mathrm{Im}(\sigma_{+0}^{++} - \sigma_{+0}^{--}))$$

$$+\sin(\phi+\phi_s)\,(\cos\theta_\gamma\,\frac{\epsilon}{2}\,\mathrm{Im}\sigma_{+-}^{+-} + \frac{1}{2}\sin\theta_\gamma\,\sqrt{\epsilon(1+\epsilon)}\,\mathrm{Im}(\sigma_{+0}^{++} - \sigma_{+0}^{--}))$$

$$+\sin(2\phi-\phi_s)\,(\cos\theta_\gamma\,\sqrt{\epsilon(1+\epsilon)}\,\mathrm{Im}\sigma_{+0}^{-+} + \frac{1}{2}\sin\theta_\gamma\,\epsilon\,\mathrm{Im}\sigma_{+-}^{++})$$

$$+\sin(2\phi+\phi_s)\,\frac{1}{2}\sin\theta_\gamma\,\epsilon\,\mathrm{Im}\sigma_{+-}^{++}$$

$$\left.+\sin(3\phi-\phi_s)\,\cos\theta_\gamma\,\frac{\epsilon}{2}\,\mathrm{Im}\sigma_{+-}^{-+}\right]$$

$$+ \text{ terms dependent on the lepton polarisation } P_\ell.$$

The Transverse Target Spin Asymmetry w.r.t. the virtual photon direction is defined as:

$$A_{UT}(\phi, \phi_S) = \frac{1}{S_T} \cdot \frac{d\sigma(\phi, \phi_S) - d\sigma(\phi, \phi_S + \pi)}{d\sigma(\phi, \phi_S) + d\sigma(\phi, \phi_S + \pi)} \tag{6}$$

According to the previous formula the modulation in $\sin(\phi - \phi_s)$ will give:

$$A_{UT}^{\sin(\phi-\phi_s)}(\phi, \phi_S) \quad \propto \quad \frac{(\cos\theta_\gamma \ \mathrm{Im}(\sigma_{++}^{+-} + \epsilon \ \sigma_{00}^{+-}) + \frac{1}{2}\sin\theta_\gamma \ \sqrt{\epsilon(1+\epsilon)} \ \mathrm{Im}(\sigma_{+0}^{++} - \sigma_{+0}^{--}))}{\frac{1}{2}(\sigma_{++}^{++} + \sigma_{++}^{+}) + \epsilon \ \sigma_{00}^{++}} \ ,$$

which in deep inelastic kinematics becomes

$$\propto \quad \frac{\mathrm{Im}(\sigma_{++}^{+-} + \epsilon \ \sigma_{00}^{+-})}{\frac{1}{2}(\sigma_{++}^{++} + \sigma_{++}^{--}) + \epsilon \ \sigma_{00}^{++}} \ . \tag{7}$$

The only leading-twist observables are the longitudinal cross section σ_{00}^{++} and the interference term σ_{00}^{+-}. Transverse-longitudinal interference terms σ_{+0}^{ij} are at least suppressed by $1/Q$ while cross sections σ_{++}^{ij} and interference terms σ_{+-}^{ij} with transverse photon polarisation are suppressed by $1/Q^2$. The leading-twist contributions can be written as:

$$\frac{1}{\Gamma'}\frac{d\sigma_{00}^{++}}{dt} = (1 - \xi^2)|\mathcal{H}_M|^2 - (\xi^2 + \frac{t}{4M_p^2})|\mathcal{E}_M|^2 - 2\xi^2 \mathrm{Re}(\mathcal{E}_M^* \mathcal{H}_M), \tag{8}$$

$$\frac{1}{\Gamma'}\frac{d\sigma_{00}^{+-}}{dt} = -\sqrt{1-\xi^2}\frac{\sqrt{t_0 - t}}{M_p}\mathrm{Im}(\mathcal{E}_M^* \mathcal{H}_M) \ , \tag{9}$$

where $\Gamma' = \alpha_{em}/Q^6 \times x_B^2/(1 - x_B)$, the skewedness variable is $\xi = x_B/(2 - x_B)$ and the minimal four-momentum transfer is $t_0 = -4\xi^2 M_p^2/(1 - \xi^2)$. The quantities $\mathcal{H}_M$ and $\mathcal{E}_M$ are weighted sums of integrals over the GPD $H^{q,g}$ and $E^{q,g}$ respectively. The weights depend on the contributions of quarks of various flavours and of gluons to the production of meson M.

3 Angular Distribution of the ρ^0 decay and SDME

For electroproduction of vector mesons one experimentally finds that the ratio σ_L/σ_T is not very large for Q^2 of a few GeV^2 which means that the predicted power suppression of transverse photon amplitudes is numerically not yet very effective in these kinematics. One finds also that transitions with the same helicity for photon and meson are clearly dominant over those changing the helicity. This is commonly referred as approximate s-channel helicity conservation. So the measurement of the decay angular distribution of the vector meson, $\rho \to \pi^+\pi^-$, will help towards isolating the twist-two (longitudinal) observables. If only the dependence on the

polar decay angle θ is considered, one can separate the longitudinal and transverse ρ polarisation:

$$\frac{d\sigma_{mn}^{ij}(\gamma^* p \to \rho \ p)}{d(\cos\theta)} = \frac{3\cos^2\theta}{2}\sigma_{mn}^{ij}(\gamma^* p \to \rho_L p) + \frac{3\sin^2\theta}{4}\sigma_{mn}^{ij}(\gamma^* p \to \rho_T p) \tag{10}$$

σ_{++}^{++}, σ_{++}^{--} and σ_{00}^{++} are related to the spin density matrix element r_{00}^{04}. Note that the interference terms between longitudinal and transverse ρ^0 are cancelled as the cross section is integrated over the azimuthal decay angle φ.

4 t-dependence of the cross section

QCD factorisation relies on the fact that for $Q^2 \to \infty$ the meson is predominantly produced by small-size hadronic components of virtual photon, whose coupling to the target is weak and can be computed perturbatively. The approach to the small size regime with increasing Q^2 can be verified experimentally in a model-independent way and constitutes a crucial test of the reaction mechanism. The t-slope of the differential cross section measures the transverse area of the interaction region, reflecting the size of the target and the size of the hadronic components of the virtual photon which contribute to the produced meson. As Q^2 increases, small size meson configurations become more important, and one expects the t-slope to decrease and approach a constant value. This behaviour is observed at HERA where the exponential t-slope of ρ^0 and ϕ production changes from a slope of 10 GeV^2 at Q^2=0 to a slope of 5 GeV^2 at Q^2 around 10 GeV^2. This latter value is close to the one of J/ψ production, which is practically Q^2-independent because the J/ψ is produced by small configurations even at $Q^2 = 0$. These observations attest to the approach to the small size regime in vector meson production at high Q^2 and validate QCD factorisation. The limiting value of the t-slope for $Q^2 \to \infty$ reflects the size of the target only and can be associated with the t-dependence of the GPDs.

5   Different steps in the analysis

The goal of this note is to present the extraction of $A_{UT}^{\sin(\phi-\phi_S)}$. Selection of exclusive incoherent production is described. In the near future corrections for acceptance and background and separation of longitudinal and transverse virtual photon contributions will be given. At the same time the determination of SDME r_{00}^{04} and the study of the t-dependence of the cross section will be performed.

For the moment only cross check for the raw asymmetry $A_{UT}^{\sin(\phi-\phi_S)}$ on the NH$_3$ (2007) has been performed thanks to Guillaume and Heiner (REQUEST FOR

RELEASE). While the next steps have been mostly realized by Guillaume for the 2004 data, they remain to be done for the 2007 data.

Part II

Event Selection and Asymmetry Calculation

6   Event Selection

The initial data sample for this analysis is based on COMPASS data, taken during the years 2004 and 2007 with the transverse target spin configuration. As this data sample is the same as for the analysis of Collins and Sivers asymmetries for unidentified hadrons, more detailed information on the basic event selection and the data quality can be found in the COMPASS notes 2006-12 [13] and 2008-10 [14].

In the following, the additional selection of exclusive ρ^0 events is described in detail, illustrated for both 2004 and 2007 data.

6.1   Beam and Scattered Muon

Only events with a best primary vertex are selected for the analysis. In addition, in order to ensure that the same beam flux passes through each target cell, the cut on the radial position of the vertex was applied. The maximal allowed radial distance of the vertex was 1.3 cm for 2004 data and 1.9 cm for 2007 data. The values were chosen taking into account the actual target position. Another requirement on the incident beam particle is the good fit quality of its track, which is ensured by a reduced $\chi^2_{\rm red}$ smaller than 10 for a reconstructed beam track.

Since selected events have to originate in one of the target cells, the spatial coordinates of the primary vertex are checked. After applying a cut on the radial distance of the primary vertex from the beam axis, the z coordinate has to be within the range of one of the target cells. The spatial distributions of the primary vertex are shown in Fig. 2 and Fig. 3.

The scattered μ' is selected with a PHAST routine. This "tagged" μ' candidate has to fulfill the same criteria regarding $\chi^2_{\rm red}$ as the beam muon and in addition, the calculated penetration length of the μ' track, expressed in units of the radiation length, has to exceed a minimal value, i.e. $X/X_0 > 30$. Aside from the PHAST routine a additional recovering procedure is used, which is based on hit information from the Muon Wall detectors. In the case when one of the outgoing particles from the primary vertex causes more than 4 hits in MA01 or more then 6 hits in MA02,
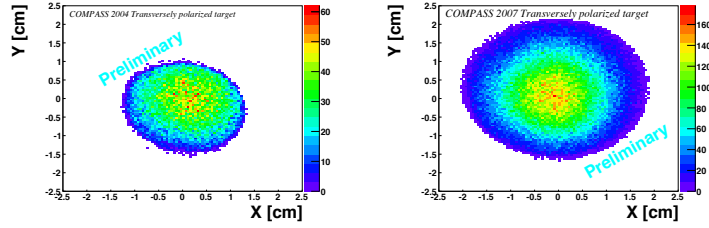
Figure 2: The spatial distributions of the primary vertex in the plane perpendicular to the beam axis for the 2004 sample (left) and 2007 sample (right).
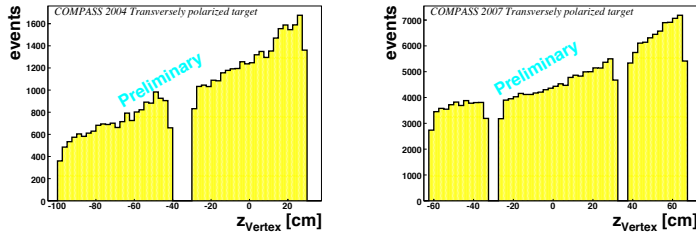
Figure 3: The spatial distributions of the primary vertex in z-direction for the 2004 sample (left) and 2007 sample (right).

it is considered as a scattered muon. If the particle additionally fulfills the same requirements on $\chi^2_{\rm red}$ and X/X_0 as the "tagged" μ', the particle is marked as a "recovered" muon. Finally, only events containing one and only one scattered muon (either a "tagged" or a "recovered" one) enter the further analysis. Moreover, the whole event is rejected if the μ' track crosses the yoke of SM2.

6.2 Inclusive Scattering Variables

Inclusive scattering variables are calculated using the incident and outgoing muon tracks. To obtain a final data sample, consisting of events in the deep inelastic scattering regime, the negative four-momentum squared of the virtual photon is restricted to $Q^2 > 1.0$ $({\rm GeV}/c)^2$, while the region of hadron resonances is excluded by applying a cut on the invariant mass of the final state $W > 5.0$ GeV. Another cut is applied on the variable y, $0.1 < y < 0.9$, in order to remove events with large radiative corrections (large y) or poorly reconstructed kinematics (low y).

6.3 Hadrons

For the selection of exclusive events, three outgoing (final state) particles from the primary vertex are required: the scattered muon and two hadrons of opposite charge. Similar to the requirements on the μ tracks the tracks of the hadron candidates have to satisfy the condition $\chi^2_{\rm red} < 10$. Moreover, hadrons tracks have to start before z=350 cm and to stop before z=3300 cm. On the other hand, hadron tracks should not pass more than 10 radiation lengths. Finally, the event is rejected if one of hadron tracks crosses the yoke of SM2 (CrossYokeSM2 function) or if the positive hadron can be a muon (CanBeMuon function).

6.4 Exclusive ρ^0 Sample

The invariant mass distribution of the two selected hadrons is depicted in Fig. 4 and shows clearly a peak at the expected value of about $M_\rho = 775.5$ MeV/c^2. The RICH identification was not used in the present analysis and to calculate energies of both hadrons the charged pion mass was assumed. In the following we require an invariant mass of

$$-0.3~{\rm GeV}/c^2 < ({\rm M}_\rho - {\rm M}_{\pi\pi}) < 0.3~{\rm GeV}/c^2~.$$

With this cut the non-resonant background is reduced, and ϕ mesons ($\phi \to K^+K^-$) seen as a reflection at low invariant masses are removed from the sample.
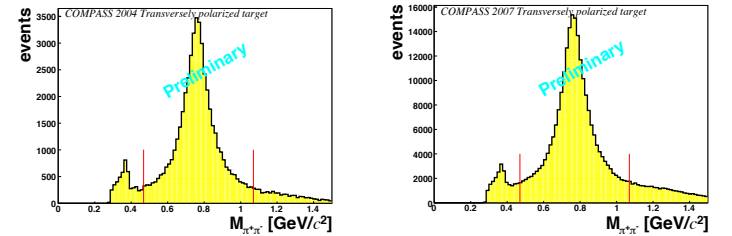
Figure 4: Invariant mass spectrum $M_{\pi^+\pi^-}$ with all restrictions except a requirement on the mass range applied for the 2004 sample (left) and 2007 sample (right).

As already mentioned, the final sample should be enhanced with exclusive ρ^0 mesons. To minimize the non-exclusive background, the missing energy

$$E_{\rm miss} = \frac{M_{\rm X}^2 - M_{\rm P}^2}{2 \cdot M_{\rm P}} = \frac{(p + q - \rho)^2 - M_{\rm P}^2}{2 \cdot M_{\rm P}} \tag{11}$$

is limited in the range -2.5 GeV $< E_{\text{miss}} < 2.5$ GeV. Here M_{P} is the proton mass and M_{X} is the mass of the undetected recoiling system. The latter is calculated from the four-momentum vectors p, q and ρ of the proton, the photon and the ρ^0 meson. The four-momentum vector of the meson is reconstructed via its decay particles. Fig. 5 shows the distribution of the missing energy E_{miss} before applying the cut.
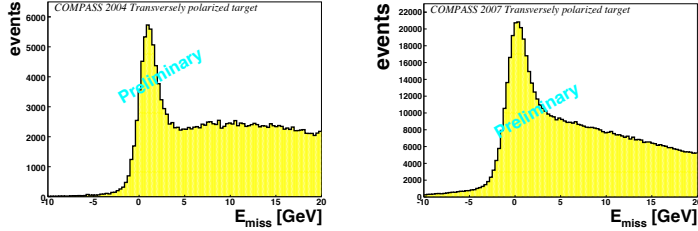

Figure 5: Distribution of the missing energy E_{miss} before applying the cut for the 2004 sample (left) and 2007 sample (right).

To reduce the non-exclusive background and allow its simpler parametrisation as a function of E_{miss} we use a cut on E_ρ. Fig. 6 shows the correlation between the reconstructed ρ energy E_ρ and E_{miss}. Due to kinematic constraints, if $y \geq 0.1$, $E_\rho \geq 16$ GeV at $p_{\text{T}}^2=0$. If p_{T}^2 varies up to 0.5 $(\text{GeV}/c)^2$ the ρ energy stays really above 15.5 GeV. For safety all events with $E_\rho \geq 15$ GeV are selected.
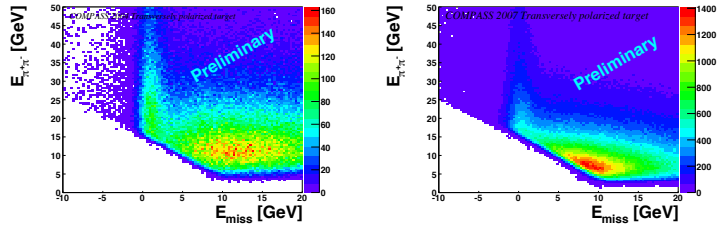
Figure 6: Correlation between E_{miss} and E_ρ (equal to the sum of energies of the two pions) with all selections except the cut on E_ρ. Both the 2004 data (left) and 2007 data (right) are shown.

In Fig. 7 p_{T}^2 distributions are shown for 2007 data (4 upper plots) and for 2004 data (4 lower plots). In the following we will use varibale p_{T}^2 rather than t' for

an experimental reason. The variable t' is poorly determined and systematically biased towards larger values of $|t'|$ for the non-exclusive events, which are a non-negligible part of our sample. The discussion of this bias and the advantage of using the variable p_{T}^2 was presented in Ref. [11]. We should also mention that for the real exclusive events in COMPASS kinematics p_{T}^2 is a good approximation for $|t'|$.

In order to reject coherent events from Lithium, He^4, He^3 and Deuterium nuclei (2004 data) or from Nitrogen, He^4 and He^3 nucleus (2007 data), a lower limit for the transverse component p_{T}^2 of the ρ^0 meson momentum vector with respect to the virtual photon direction is applied. The upper limit for this variable was chosen to further minimize non-exclusive background. Therefore, the kinematically permitted range for the 2004 data is

$$0.1 \ (\text{GeV}/c)^2 \ < p_{\text{T}}^2 < 0.5 \ (\text{GeV}/c)^2$$

and the kinematically permitted range for the 2007 data is

$$0.05 \ (\text{GeV}/c)^2 \ < p_{\text{T}}^2 < 0.5 \ (\text{GeV}/c)^2$$

An evaluation of the remaining coherent contribution and of the non-exclusive background after the p_{T}^2 cuts was estimated using a fit of sum of 3 exponentials. A fitted curve as well as each individual exponentials are displayed in Fig. 7. The values of the p_{T}^2-slopes B are 52.5, 7.7, 2.3 (for 2007) and 40.9, 7.7, 2.2 (for 2004), and in the simple interpretation we identify them with coherent, incoherent and non-exclusive contributions respectively.

Using above fits one can estimate that after the cuts it remains less 5% of coherent contribution in the final sample for 2007 data and 2% for 2004 data.

However, it is expected that at small p_{T}^2 the distributions for incoherent/coherent events deviate from simple exponential dependences, and the largest differences occur for the nuclei with the lowest atomic mass A (in particular for the deuteron). Quantitative evaluations of this effect for ρ^0 productin on the deuteron target were obtained using Glauber Model approach and two different mechanisms of meson leptoproduction: VMD model and the color dipol model. The results for various cuts on p_{T}^2 were shown in Ref. [12]. According to this estimates the residual contribution of coherent events from the deuteron target with the lower p_{T}^2 cut $= 0.1 \ (\text{GeV}/c)^2$ is about 8%. Therefore our conservative estimate of the residual coherent background in the final sample is 5% for 2007 data and 8% for the 2004 data.

The non-exclusive background 35% (24 %) for the 2007 (2004) sample is important and will be rejected at a further step.

6.5   summary of all the cuts applied

topology	Primary Vertex reconstructed with
	1 incident muon μ
	1 outgoing muon μ'
	2 charged tracks with opposite charge h^+, h^-
vertex in the target	in PHAST routine z cut and
	$\sqrt{(x-x_0)^2 + (y-y_0)^2} < 1.3$ cm (for 2004)
	$\sqrt{(x-x_0)^2 + (y-y_0)^2} < 1.9$ cm (for 2007)
beam energy	$E_\mu < 200$ GeV
muon identification	$X/X_0(\mu') > 30$
hadron identification	$X/X_0(h^+) < 10$ and $X/X_0(h^-) < 10$
quality of the tracks	$\chi^2_{\mathrm{red}} < 10$ for μ, μ', h^+, h^-
	$z_{first}(h^+) < 350$ cm
	$z_{first}(h^-) < 350$ cm
	$350 < z_{last}(h^+) < 3300$ cm
	$350 < z_{last}(h^-) < 3300$ cm
	h^+, h^- and μ' do not cross SM2 yoke (Phast routine)
	h^+ cannot be a muon (Phast routine)
quality of data	Pure ECAL1 trigger rejected for periods:
	W27-W28-W39-W40-W41-W42a
domain of analysis	$Q^2 > 1 (\mathrm{GeV}/c)^2$
	$W > 5$ GeV$/c$
	$0.1 < y < 0.9$
	$0.003 < x_B < 0.35$
production of meson ρ	$-0.3\ (\mathrm{GeV}/c)^2 < (\mathrm{M}_\rho - \mathrm{M}_{\pi\pi}) < 0.3\ (\mathrm{GeV}/c)^2$
exclusivity	-2.5 GeV $< E_{\mathrm{miss}} < 2.5$ GeV
background rejection	$E_{\pi^+\pi^-} \geq 15$ GeV
	$p_{\mathrm{T}}^2 < 0.5 (\mathrm{GeV}/c)^2$
without coherent rejection	$p_{\mathrm{T}}^2 > 0.01\ (\mathrm{GeV}/c)^2$
with coherent rejection	$p_{\mathrm{T}}^2 > 0.1\ (\mathrm{GeV}/c)^2$ (for 2004)
	$p_{\mathrm{T}}^2 > 0.05\ (\mathrm{GeV}/c)^2$ (for 2007)

6.6   Final Data Sample

The event yields of exclusive ρ mesons per year after the entire event selection is listed below:

Year	# Events	
	without coherent rejection	with coherent rejection
2004	153.735	47.586
2007	576.788	227.376

Rejection of coherent events was not done in the previous analysis for the 2002-2004 data presented in the COMPASS note 2007-9 [1].

The distributions of the most important kinematic variables for the full statistics of 2004 and 2007 can be found in Fig. 8, Fig. 9 and Fig. 10. The mean values for the kinematic variables Q^2, W, x and P_{T}^2 are given in the following table.

Year	$< Q^2 >$	$< W >$	$< x >$	$< P_{\mathrm{T}}^2 >$
2004	1.99	8.73	0.031	0.23
2007	2.17	8.11	0.040	0.18
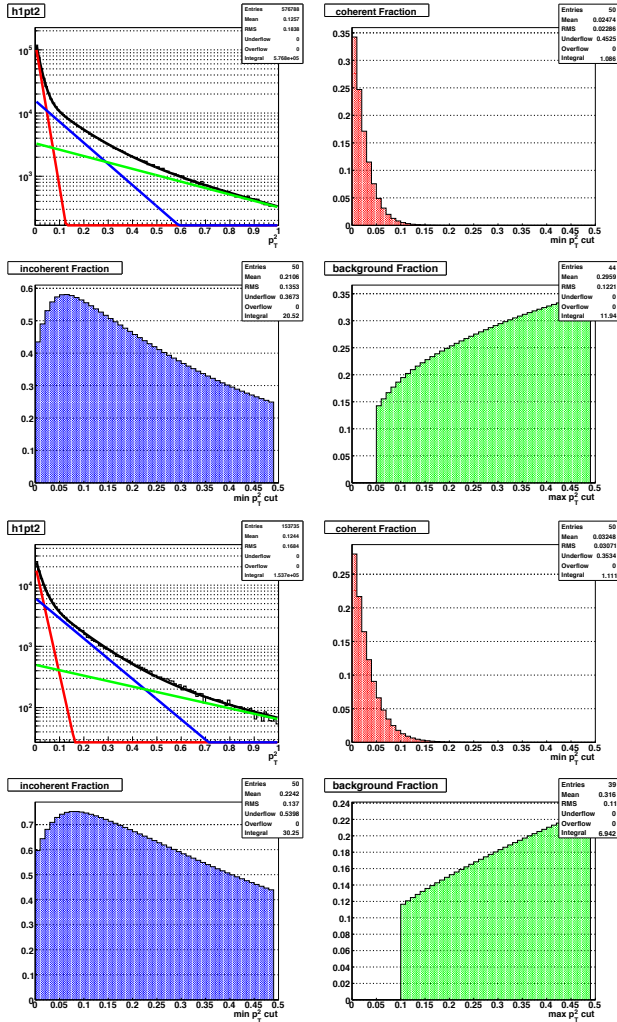
Figure 7: Distribution of p_{T}^2 before applying the cut is shown for 2007 (4 upper plots) and 2004 (4 bottom plots) data. For more details see the text.
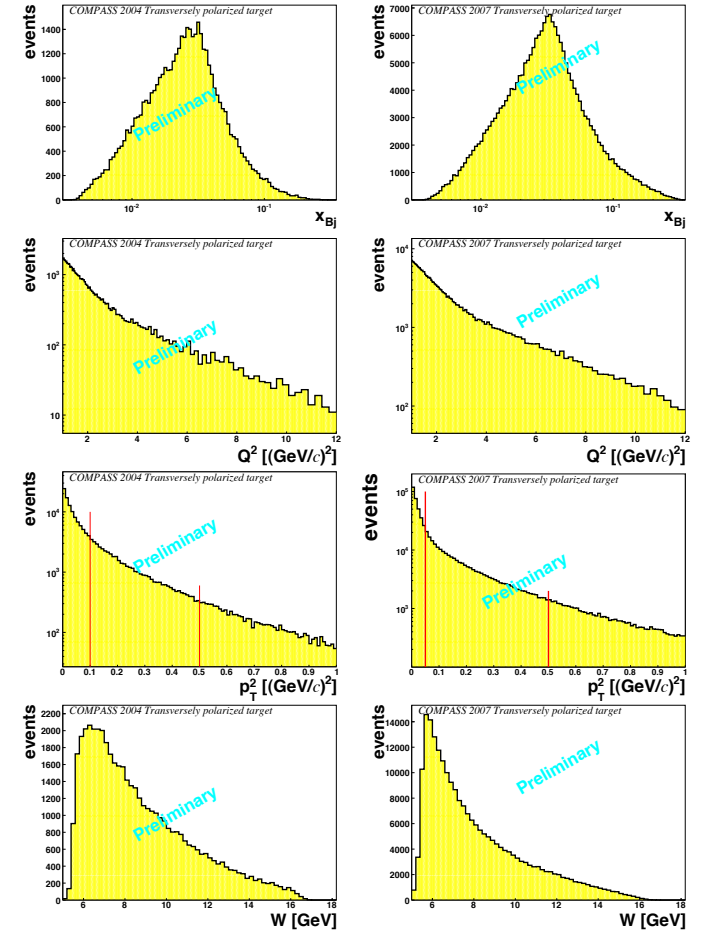
Figure 8: The distributions of x_{bj}, Q^2, p_{T}^2 and W for the full 2004 (left) and 2007 (right) data samples.
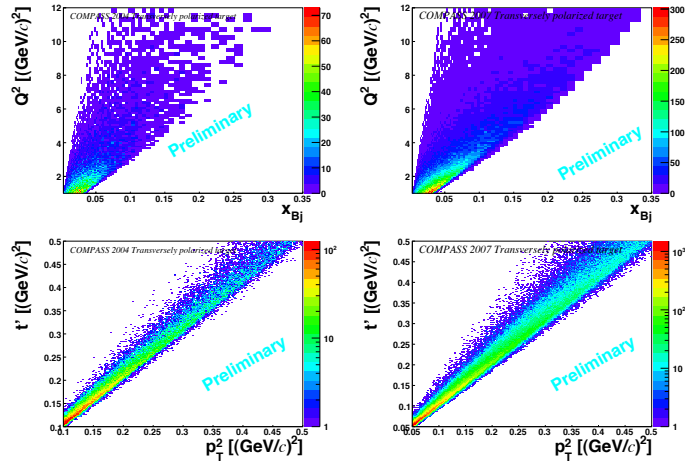
Figure 9: Correlations between Q^2 and x_{bj} and between t' and p_{T}^2.
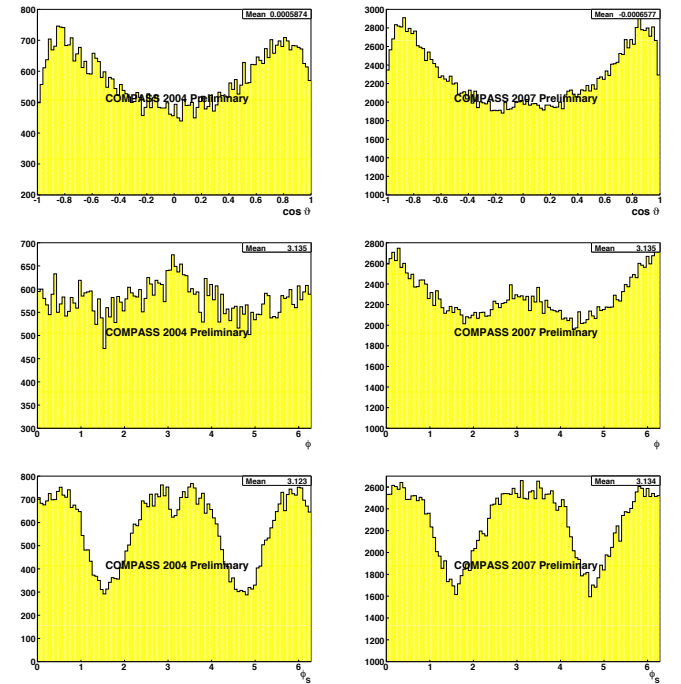
Figure 10: Distributions of the kinematic variables for the full 2004 (left) and 2007 (right) data sample. In particular the angular variables θ polar angle of the ρ decay, ϕ angle between the hadron plane and the lepton scattering plane and ϕ_S angle between lepton scattering plane and the target spin vector (see Fig. 1).

7 Asymmetry Calculation

7.1 Calculation of the raw asymmetries

In this section the calculation of the raw asymmetries is presented shortly. The method used for the calculation of the raw asymmetries as well as the extraction of the physical asymmetry is the same as for the analysis of the Collins and Sivers asymmetries.

The numbers of events as a function of the angle $\eta = \phi - \phi_S$ between the ρ^0-production plane and the target spin vector (cf. Fig. 1) is given by

$$N(\eta) = Fn\sigma\mathrm{u}(\eta)(1 + \epsilon sin(\eta)) \,, \tag{12}$$

where F is the muon flux, n the number of target particles, σ the spin averaged cross-section and $\mathrm{u}(\eta)$ the product of angular acceptance and efficiency of the apparatus. In the analysis of the data it has to be taken into account that $\mathrm{u}(\eta)$ is largely unknown and it is different for the different target cells.

To minimize acceptance effects, the double ratio method was chosen. Therefore the double ratio (DR) is calculated for 10 equidistant angular bins in η:

$$F(\eta) = \frac{N^\uparrow_{\mathrm{up}}(\eta) \cdot N^\uparrow_{\mathrm{down}}(\eta)}{N^\downarrow_{\mathrm{up}}(\eta) \cdot N^\downarrow_{\mathrm{down}}(\eta)} = \frac{(1 + \epsilon \cdot sin(\eta))^2}{(1 - \epsilon \cdot sin(\eta))^2} \,, \tag{13}$$

or

$$F(\eta) = \frac{(N^\uparrow_{up}(\eta) + N^\uparrow_{down}(\eta)) \cdot N^\uparrow_{center}(\eta)}{(N^\downarrow_{up}(\eta) + N^\downarrow_{down}(\eta)) \cdot N^\downarrow_{center}(\eta)} = \frac{(1 + \epsilon \cdot sin(\eta))^2}{(1 - \epsilon \cdot sin(\eta))^2} \,, \tag{14}$$

where Eq. 13 refers to the DR calculation for the two cells configurations (i.e. 2004 data) and Eq. 14 refers to the DR calculation for the three cells configurations (i.e. 2007 data). In Eq. 13 and 14, $\uparrow(\downarrow)$ signifies up/down target polarisation, $up/down/center$ denotes the target cells. These relations are obtained with a reasonable assumption that the ratio of acceptances $a^\pm_{u,d}(\eta)$ for each cell is the same before and after the polarisation reversal:

$$\frac{a^-_u(\eta)}{a^+_d(\eta)} = \frac{a^+_u(\eta)}{a^-_d(\eta)} \,. \tag{15}$$

For the three cells configuration, the upstream and downstream cells are considered as one cell. In this case the assumption is:

$$\frac{a^-_u(\eta) + a^-_d(\eta)}{a^+_c(\eta)} = \frac{a^+_u(\eta) + a^+_d(\eta)}{a^-_c(\eta)} \,. \tag{16}$$

The DR is plotted versus the angle $\eta = \phi - \phi_S$. From this evolution, the amplitude ϵ is determined from a fit of the DR with the adequate function 13 or 14, which provides the raw asymmetries ϵ.

7.2 Transverse Target Single Spin Asymmetry

The Transverse Target Single Spin Asymmetry A_{UT} is extracted from the raw asymmetry via the expression

$$\mathrm{A}^{\sin(\phi-\phi_\mathrm{s})}_{\mathrm{UT}} = \frac{\epsilon}{f \cdot \langle P_T \rangle} \,, \tag{17}$$

where $f \sim 0.14$ is the mean value of the dilution factor evaluated in PHAST on an event-by-event basis and $\langle P_T \rangle$ is the mean target polarisation value, calculated as the average over polarisation values for one kinematic bin.

Part III

Data Analysis

8 Data Quality for the 2007 data: NH₃ target

The data quality criteria have been defined by the transversity group in the recent COMPASS notes 2008-10 [14] and 2009-XX [15].

So we use the 6 following periods W25, W26 with the production 1, W27 with the production 3, W28, W30, W31 with the production 2, W39, W40, W41, W42, W43 with the production 1 and we form the combinations:
- W25-W26; W27-W28; W30-W31
- W39-W40; W41-W42a; W42b-W43

9 Comparison of independent analyses performed in Freiburg and Saclay for the 6 periods

The results of the raw Transverse Target Spin asymmetries $\epsilon = f \cdot \langle P_T \rangle \cdot A_{UT}^{\sin(\phi-\phi_s)}$ have been compared using the two independent analyses, label as Freiburg and Saclay in the following. Even if the two analyses apply identical cuts, there are some differences, like the numerical procedure to evaluate some physics quantities.

An almost satisfactory agreement is obtained for the two independent analyses over the 6 periods. Fig. 11 and Fig. 12 show $\epsilon = f \cdot \langle P_T \rangle \cdot A_{UT}^{\sin(\phi-\phi_s)}$ as a function of Q^2, x and p_T^2 .

The quality of the agreement is determined by the distribution of differences of the measured asymmetries from Freiburg and Saclay analyses, plotted for all the 6 periods of data taking and the 3 main kinematic variables p_T^2 (in 4 bins), Q_2 (in 4 bins) and x_B (in 3 bins). Fig. 13 shows this difference for the corresponding 66 entries. From this comparison, the distribution is really close to a gaussian, the reduced χ^2 is 1.04 and the difference between the results for the asymmetries is of the order of 3.7% of the statistical error. This difference can be explained as the fit of the double ratio is done as a function of $\eta = \phi - \phi_S$ using the central value of the bin for η in the Freiburg analysis and using the mean value of η in the bin for the Saclay analysis.

The consistency over the periods seems also rather correct.

10 Comparison of the evolution of the TTSA as a function of Q^2, x_B and p_T^2

The results for the Transverse Target Spin asymmetries $A_{UT}^{\sin(\phi-\phi_s)}$ are presented for the two analyses as a function of the 3 main kinematic variables Q^2, x_B and P_T^2 in the following Fig. 14.

There is a rather good agreement between the 2 analyses which indicates also the good evaluation of f and $\langle P_T \rangle$.

The measured Transverse Target Spin asymmetries is consistent with a zero value within the statistical errors.

11 Comparison of consecutive and global determination of the TTSA

The results of two methods of the asymmetry calculation, the first considering the mean value over all the whole experiment and the second considering the mean value of all asymmetries for a consecutive couples of periods, were compared. The results are rather close (see Fig. 15) and indicate that the systematic errors are smaller than the statistical errors.

12 Approximate estimate of the effects of the non-excusive background

There exists a systematic error due to the non-exclusive background. This background to signal ratio is always smaller than 1/2 (see Part II). The value of the corresponding asymmetry is expected to be close to zero. So the background dilutes the asymmetry and to take into account this contribution, the asymmetry and its statistical error should be enlarged by a factor sqrt(1+B/S)=1.2. This correction is not taken into account in the Figures.

13   Final results for $A_{UT}^{\sin(\phi-\phi_s)}$ for incoherent production

Figs. 16 and 17 present $A_{UT}^{\sin(\phi-\phi_s)}$ as a function of Q^2, x_B or p_T^2 for the NH$_3$ (proton) and ^{6}LiD (deuteron) targets respectively (with coherent rejection).

14   Comparison to HERMES and theory

Figs. 18 present the asymmetry $A_{UT}^{\sin(\phi-\phi_s)}$ obtained by the HERMES collaboration [16] for the proton case. A further analysis for longitudinal and transverse separation has also been performed.

Theoretical predictions have been done by Goloskokov and Kroll for $A_{UT}^{\sin(\phi-\phi_s)}$. The value is predicted around -0.02 for ρ production and around -0.1 for ω production [17, 18, 19] on the proton.
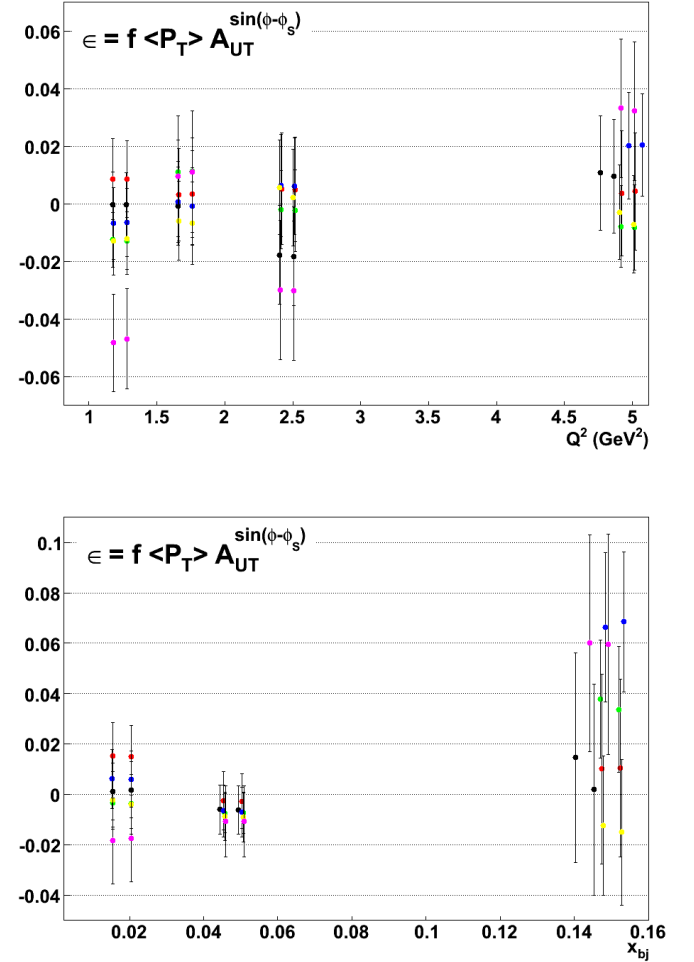
Figure 11: Comparison of the two different analyses for the 6 periods presented as a function of Q^2 (upper plot) and x (lower plot). The results of the Freiburg analysis are slightly shifted on the right for convenience for each value of Q^2 or x.
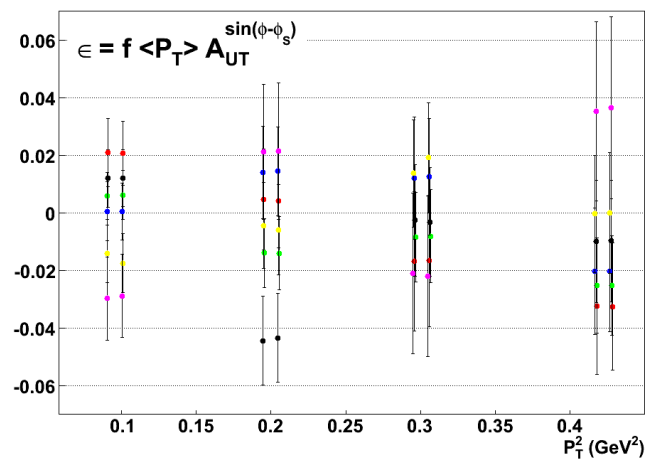
Figure 12: Comparison of the two different analyses for the 6 periods presented as a function of p_{T}^2. The results of the Freiburg analysis are slightly shifted on the right for convenience for each value of p_{T}^2.
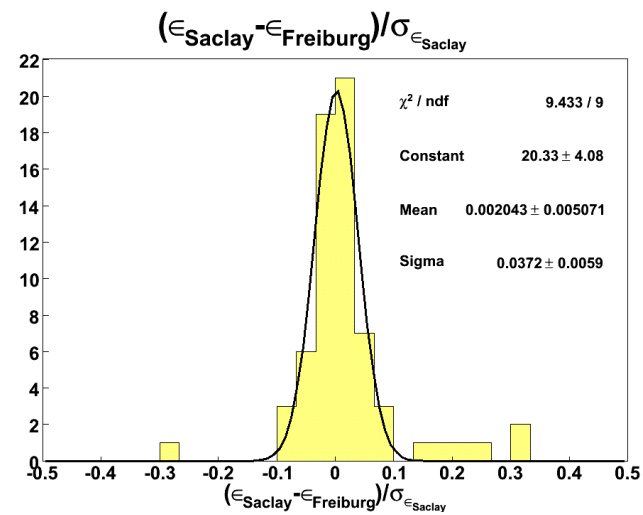
Figure 13: Distribution of the differences of the asymmetries for the 2 analyses divided by the statistical errors.
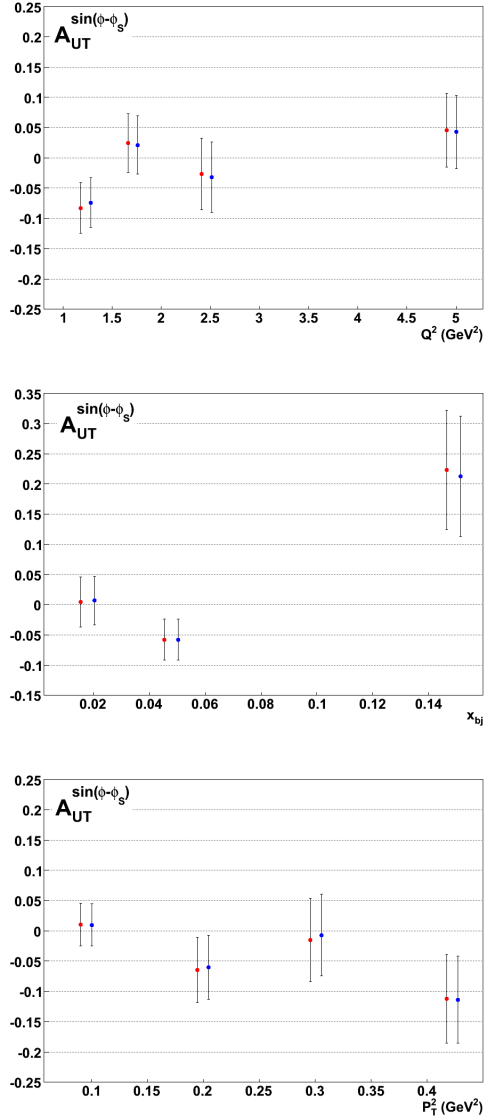
Figure 14: Results for $A_{UT}^{\sin(\phi-\phi_s)}$ vs Q^2, x_B and p_T^2 for the 2 analyses (Saclay in red, Freiburg in blue). Freiburg points are slightly shifted in abscissa on the right for better visibility.
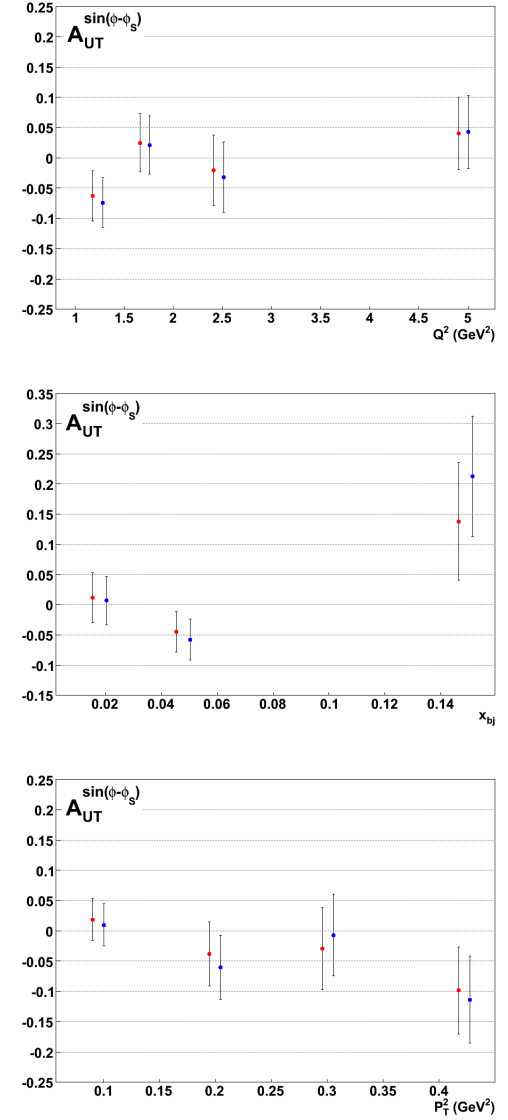
Figure 15: Results for $A_{UT}^{\sin(\phi-\phi_s)}$ vs Q^2, x_B and p_T^2 for the 2 determinations of the asymmetry (consecutive method in red, global method in blue). Points for the global method are slightly shifted in abscissa on the right for better visibility.
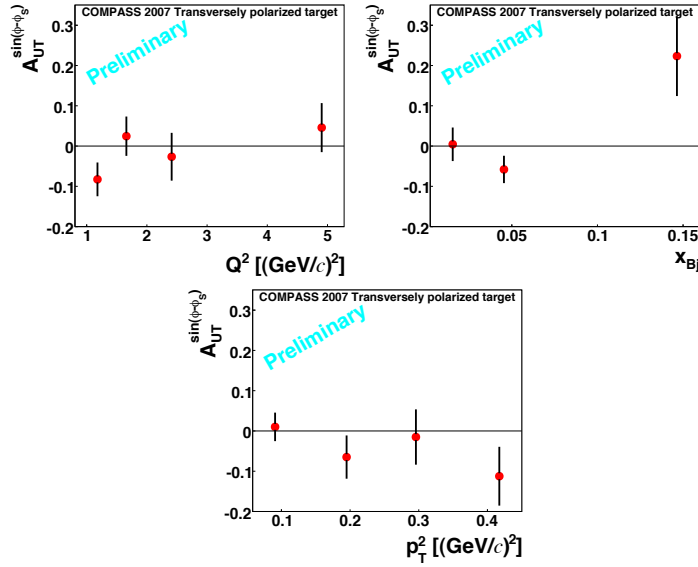
Figure 16: Results for $A_{UT}^{\sin(\phi-\phi_s)}$ vs Q^2, x_B, p_T^2 the 2007 data using the NH$_3$ target (with coherent rejection).
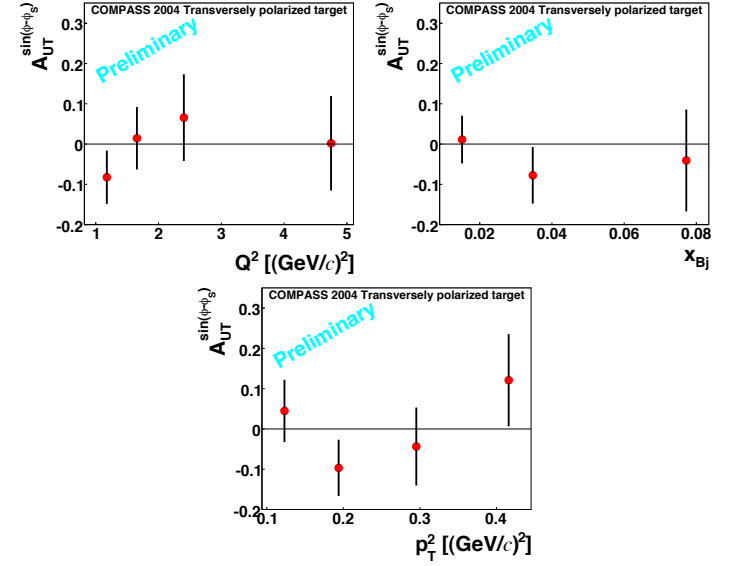
Figure 17: Results for $A_{UT}^{\sin(\phi-\phi_s)}$ vs Q^2, x_B, p_T^2 the 2004 data using the ^{6}LiD target (with coherent rejection).
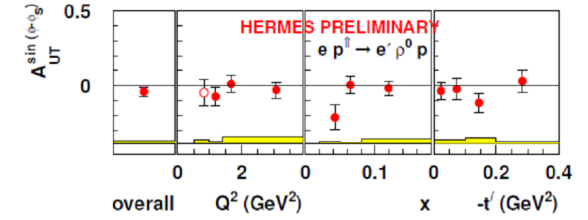
Figure 18: $A_{UT}^{\sin(\phi-\phi_s)}$ obtained by the HERMES collaboration [16]. For these data the longitudinal and transverse separation has been also performed (not shown here).

References

[1] J. Bisplinghoff, F. Bradamante, A. Bressan, E. Burtin, N. d'Hose, W. Eyrich, H. Fischer, F. Hinterberger, G. Jegou, R. Joosten, J. Kiefer, A. Kotzinian, A. Martin, F. Massmann, T. Negrini, M. Nehmé, B. Parsamyan, A. Richter, A. Sandacz, G. Sbrizzai, P. Schiavon, C. Schill, F. Sozzi, G. Venugopal, A. Vossen, *Extraction of Transverse Target Single Spin Asymmetry for Exclusive ρ^0 Production from COMPASS 2002-2004*, COMPASS note 2007-9.

[2] K. Goeke, M.V. Polyakov, M. Vanderhaeghen, Prog. Part. in Nucl. Phys. 47 (2001) 401, hep-ph/0106012.

[3] F. Ellinghaus, W.-D. Nowak, A.V. Vinnikov, and Z. Ye, Eur. Phys. J. C **46** (2006) 729, hep-ph/0506264.

[4] X. Ji, Phys. Rev. Lett. **78** (1997) 610, hep-ph/9603249.

[5] M. Burkardt, Int. J. Mod. Phys. A **18** (2003) 173, hep-ph/0207047.

[6] J.C. Collins, L. Frankfurt and M. Strikman, Phys. Rev. D **56**, 2982 (1997).

[7] M. Diehl, T. Gousset, B. Pire, Phys. Rev. D **59** (1999) 034023, hep-ph/9808479;
J.C. Collins, M. Diehl, Phys. Rev. D **61** (2000) 114015, hep-ph/9907498.

[8] M. Diehl and A.V. Vinnikov, hep-ph/0412162.

[9] M. Diehl and S. Sapeta, Eur. Phys. J. C **41** (2005) 515, hep-ph/0503023.

[10] M. Diehl, JHEP 0709:064 (2007), hep-ph/0704.1565.

[11] NMC Collab., P. Amaudruz *et al*, Z.Phys, C **41** (1999) 239.

[12] A. Sandacz, *Separation of coherent and incoherent exclusive processes*, presentation at the COMPASS Analysis meeting, August 2, 2007.

[13] COMPASS note 2006-12, Collins and Sivers asymmetries on hadrons identified as pions and kaons from COMPASS 2003/2004 transverse run, The transversity group

[14] COMPASS note 2008-10, Collins and Sivers asymmetries from 2007 proton transverse run, The transversity group.

[15] COMPASS note 2009-XX, Single-Hadron and Two-Hadron Asymmetries from the 2007 transversely polarized proton data, The transversity group.

[16] HERMES Collab., A.Rostomyan *et al*, hep-ex/07072486 and DIF08, AIP conf. proc. 1105 (2009).

[17] S.V. Goloskokov, P. Kroll, Eur. Phys. J. C **42** (2005) 281, hep-ph/0501242.

[18] S.V. Goloskokov, P. Kroll, Eur. Phys. J. C **53** (2008) 367, hep-ph/0708.3569.

[19] S.V. Goloskokov, P. Kroll, Eur. Phys. J. C **59** (2009) 809, hep-ph/0809.4126.

COMPASS-Note-2009-4, J.Bernhard et al., "The first observation of exclusive single-photon muoproduction at COMPASS in 2008 DVCS test run".

The first observation of exclusive single-photon muoproduction at COMPASS in 2008 DVCS test run

J. Bernhard[1], E. Burtin[2], N. d'Hose[2], G. Jegou[2], V. Kolosov[3], O. Kouznetsov[4] and A. Magnon[2]

Contents

Abstract

A measurement of high energy exclusive single-photon production using the COMPASS hadron setup and a 160 GeV muon beam was performed during a short test run in 2008. Photons are reconstructed with the two electromagnetic calorimeters ECAL1 and ECAL2. Recoil protons are detected using the newly constructed Recoil Proton Detector which surrounds the 40 cm long liquid hydrogen target. A statistics of about 100 exclusive single-photon events has been obtained. This measurement is a first (successful) step aimed at establishing the feasibility of measurements of Deeply Virtual Compton Scattering at COMPASS.

[1]University of Mainz
[2]CEA-Saclay, IRFU/SPhN
[3]Protvino, IHEP
[4]Dubna, JINR & University of Mainz

1 Introduction

The study of Generalised Parton Distribution functions (GPD) using the Deeply Virtual Compton Scattering (DVCS) process is one of the topics proposed for the COMPASS future plans. The physics motivations are briefly described in a Letter of Intent (LoI) [1] submitted to the CERN/SPSC end of January 2009 describing the projected measurements.

In the LoI projected errors based on simulations are given for DVCDS which depend on many parameters from which some are still poorly known. A good knowledge of the overall Figure of Merit (FoM) of the experiment is required to quantify the final beam time request for the proposal. However, simulations are based upon rather ideal descriptions for certain equipments, also the sources and yields of background are still poorly known and should be quantified.

As shown in Fig. 1 the two main processes which contribute to the production of an exclusive photon along with a slow recoiling proton are the DVCS and Bethe-Heitler (BH) processes, where the latter can be exactly calculated in QED. Depending on the relative yields, the separation of these two processes requires accurate flux determination, a precise knowledge of the acceptance and control of overall detection efficiencies.
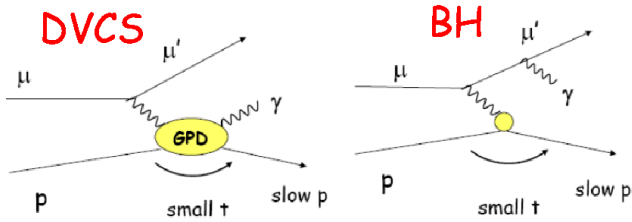
Figure 1: The two main processes of exclusive photon production: DVCS and the known (QED) Bethe-Heitler.

Additinally there are background processes as exclusive π^0 production which can simulate DVCS. The setup presently used for the meson spectroscopy measurements with hadron beam happens to be an excellent "prototype" to perform validation measurements for DVCS.

2 Exclusive γ detection with the COMPASS hadron setup

A first measurement of exclusive γ production on a Liquid Hydrogen (LH) target, with detection of the slow recoiling proton in the Recoil Proton Detector (RPD) has been performed during a short (< 2 days) test run in 2008, using 160 GeV μ^+ and μ^-) beams.

The measurements performed use the present hadron setup which comprises a 40 cm long LH target surrounded by a recoil proton detector, all the standard COMPASS tracking detectors, the ECAL1 and ECAL2 electromagnetic calorimeters for photon detection and appropriate triggers.

DVCS and BH have indistinguishable 3-body final states, namely one single photon produced: $\mu + p \rightarrow \mu' + \gamma + p$. Kinematic variables and possible constraints to select

this final state are described in Appendix A.1. An accurate measurement of the incoming muon momentum p_μ is important to guarantee good exclusivity. For that purpose, it was planned to re-install the Beam Momentum Station (BMS) which is removed for hadron beam data taking to minimise the amount of material in the beam. Unfortunately the early shutdown of the North Area, consequence of the LHC incident, did not permit to re-install the BMS. Therefore there is no measurement of the incoming muon momentum, the distribution of which is determined by the M2 beam acceptance and has a relative spread $\sigma p_\mu / p_\mu \sim 4\%$. Fig. 2 shows the principle of exclusive photon and recoiling proton detection using the COMPASS apparatus.
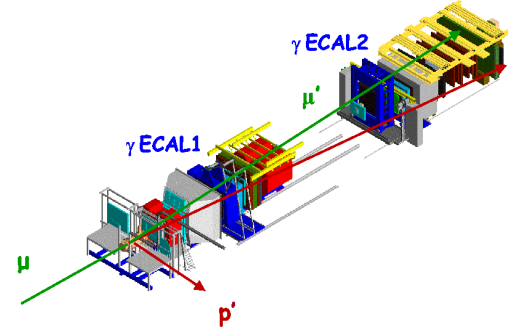

Figure 2: Exclusive photon production with recoil proton detection

The full spectrometer including RPD, ECAL1 and ECAL2 has been commissioned and calibrated prior to the 2008 hadron run. The main modification to the setup was the implementation of new triggers which were commissionned before data taking with muon beam.

The RPD providing identification and momentum determination of the recoiling particle requires a dedicated and refined calibration. This involves timing calibration and also application of suitable corrections to the energy loss of the emitted low-energy proton; which uses the precise vertex determination from tracking. This calibration has been (and will be) performed with a hadron beam for which recoiling protons from elastic scattering are more abundant compared to with a muon beam. An illustration is given in Fig. 3 which shows the difference in the missing momentum component p_{perp} obtained from vertex reconstruction and RPD, as a function of p_{perp}.

The status of the COMPASS electromagnetic calorimetry with ECAL1 and ECAL2 detectors was described in details in note [2] where the relevant information about the calibrations, the noisy channel suppression and the cluster reconstruction can be found. The performances of ECAL1 and ECAL2 are discussed in this analysis.

Data were taken with μ^- and μ^+ beams at intensities of $5.9 \times 10^7 \mu^-$/spill and $1.54 \times 10^8 \mu^+$/spill, respectively, with a SPS spill of 9.6 s/33.6 s (width/period). The definition of the different trigger settings used and the list of runs recorded are given in Appendix A.2. Note that the RPD is in coincidence in most of the trigger components.

RPD : Energy loss correction
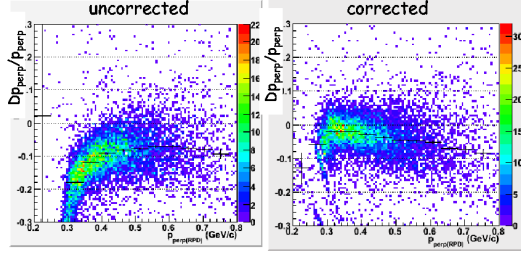
Figure 3: Difference between the missing momentum component p_{perp} obtained from vertex reconstruction and from the RPD measurement, properly back-propagated to the vertex before (left) and after (right) suitable corrections for energy loss.

3   Data analysis

3.1   Preselection of $\mu p \to \mu' p \gamma$ events

Preselection of exclusive single-photon events has been performed as follows:

– there are only *two* charged tracks ($\mu\mu'$) at the primary vertex,

– there is only *one* photon with energy ≥ 5 GeV in ECAL1 and *no* photon with energy ≥ 10 GeV in ECAL2, or

– there is only *one* photon with energy ≥ 10 GeV in ECAL2 and *no* photon with energy ≥ 5 GeV in ECAL1[1]

– there is only *one* proton candidate in the RPD and it has a momentum < 1 GeV/c.
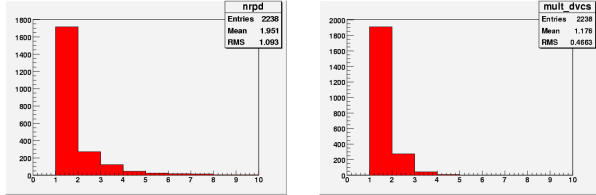
Figure 4: Left: multiplicities in the Recoil Proton Detector for proton candidates. Right: multiplicities in the ECALs for single-photon candidates.

Fig. 4 (left) shows the multiplicity in the RPD for proton candidates with momentum < 1 GeV/c. Events with one proton track represent $\sim 75\%$ of the recorded events. Fig. 4 (right) shows the multiplicity in the ECALs for the single-photon candidates, $E_\gamma > 5$ GeV in ECAL1 and $E_\gamma > 10$ GeV in ECAL2. Events with one high energy photon represent $\sim 85\%$ of the recorded statistics. Finally 1329 events remain from this first preselection.

---

[1] The thresholds of 5 (10) GeV correspond to the lowest energy expected for DVCS and BH photons given the angular coverage of ECAL1 (ECAL2).

4
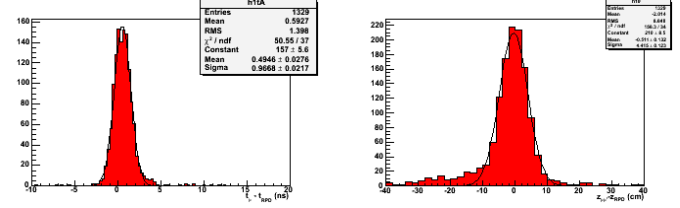
Figure 5: Timing (left) and Z position (right) differences between the reconstructed $\mu\mu'\gamma$ vertex and the single proton position detected in RPD.
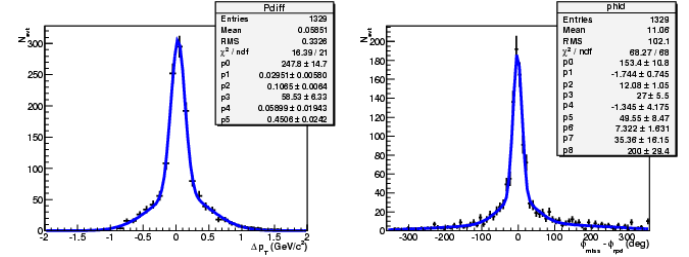

Figure 6: The difference $\Delta p_T = |p_{Tmissing}| - |p_{Trpd}|$ (left) and the difference $\Delta\phi = (\phi_{miss} - \phi_{rpd})$ (right).
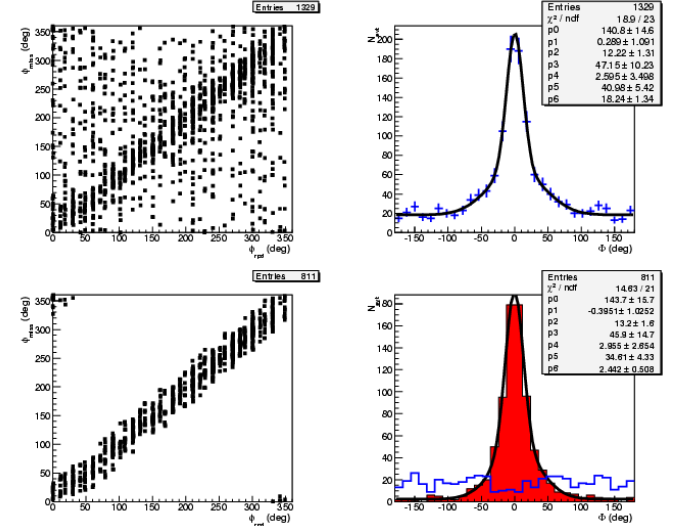

Figure 7: Left: the correlation between ϕ_{miss} and ϕ_{rpd}. Right: the Φ angle between the $\mu\mu'$ plane and the produced γp plane. All events (top), cut on correlated events (bottom).

5

The correlation between the muon vertex and the RPD information is shown in Fig. 5. The left plot shows the difference between the incoming muon time and the RPD time both properly extrapolated to the vertex. The random noise level in the 30 ns window is less than 2%, a gaussian fit gives $\sigma_t \simeq 1$ ns. The right plot shows $\Delta Z = (Z_{Vertex} - Z_{rpd})$, the difference between the longitudinal position of the vertex reconstructed using the incoming and the scattered muons and the position reconstructed using the RPD. It shows a peak with a 4.5 cm width and a tail in the left part of the distribution. There is no cut applied on this distribution since most of the events in the tail will be discarded by the exclusivity cuts later in the analysis.

In the transverse plane the $\mu'\gamma$ system provides the missing momentum $p_{Tmissing}$, sign of the possible presence of a recoil proton. On the other hand, having a selected event with one track in the RPD allows us to calculate the transverse momentum p_{Trpd} of the proton candidate. Fig. 6 (left) shows the difference $\Delta p_T = |p_{Tmissing}| - |p_{Trpd}|$. From a fit of this distribution a cut for further backgound suppression was determined as: $|\Delta p_T| < 0.2$ GeV. Fig. 6 (right) shows the difference between two angles: the missing momentum azimuthal angle ϕ_{miss} calculated in the transverse plane from $\mu'\gamma$ system and the azimuthal angle ϕ_{rpd} of the proton candidate. These highly visible correlations confirm at this very first step of analysis an indication of exclusive high energy photon production with a 3-body final state being the essential part of preselected events.

Assuming that the selected event is a pure 3-body final state $\mu p \rightarrow \mu'\gamma p$ (p being a recoil proton) one can reconstruct the Φ angle between the $\mu\mu'$ plane (lepton plane) and the plane spanned by the outgoing γ and the recoiling proton (hadron plane). The Φ angle distribution is expected to have a peak at $\Phi = 0$ for Bethe-Heitler events. Using the correlation between the azimuthal angles ϕ_{miss} and ϕ_{rpd}, one can significantly suppress the background as illustrated in Fig. 7. The upper two plots of Fig. 7 show for the preselected events the ϕ_{miss} vs ϕ_{rpd} correlation and the Φ distribution fitted by two Gaussian plus a constant term. The Φ distribution is well centered and shows the behaviour expected for Bethe-Heitler events. The constant term - parameter p6 - reflects the background contribution. The two plots in the bottom of Fig. 7 show the background suppression selecting the well correlated events in the interval $\pm 3 \times \sigma$ ($\Delta\phi = 36$ deg), ($\sigma \sim 12$ deg taken from the first Gaussian function - parameter p2 - Fig. 6). In the right plot the rejected background events are shown (blue). The constant term from the fit goes down from 18 to 2.4 - parameter p6 - and the peak of the distribution decreases from 200 to 180. These facts indicate that the distribution of background is flat over the angular range from -180 deg to $+180$ deg.

Using the assumption of a 3-body final state one can also exploit the polar angle $\theta_{\gamma^*\gamma}$ between the virtual photon γ^* and the detected real photon γ. Fig. 8 (left) shows the difference between the $\theta_{\gamma^*\gamma}$'s calculated using the $\mu\mu'\gamma$ or the $\mu\mu'p$ (p being the recoil proton) vertex informations as defined in Appendix A.1. A correlation appears, as above, in this polar angle variable. The coloured (red) curve shows the correlation for events which do not fulfill the applied exclusivity cuts in the Δp_T, $\Delta\phi$ and E_{miss} variables. Fig. 8 (right) shows the value of E_{miss} for preselected events. Note the tail extending towards large values of E_{miss}.
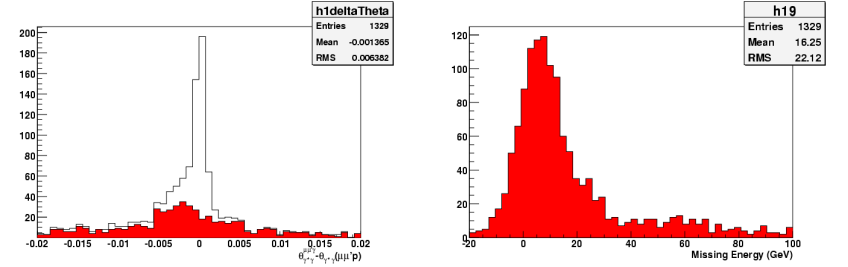
Figure 8: Left: $\Delta\theta_{\gamma^*\gamma}$ for all events (white) and for events out of the exclusivity cuts (red). Right: E_{miss} distribution.

3.2 Additional clusters in ECAL1 and ECAL2

Fig. 9 shows the XY coordinates of the high energy photons in ECAL1 and ECAL2 for the single-photon events preselected as described above.
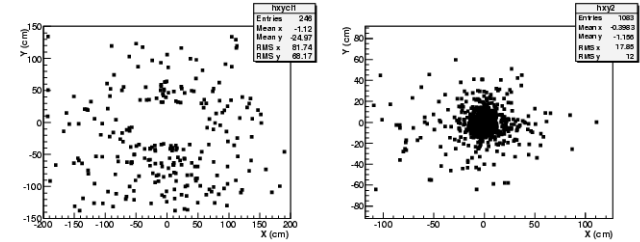

Figure 9: Left: position of single-photon events in ECAL1. Right: position of single-photon candidate events in ECAL2.

Fig. 10 (Fig. 11) shows for each preselected event having $E_\gamma > 5$ GeV in ECAL1 ($E_\gamma > 10$ GeV in ECAL2) the pattern of the additional photons in ECAL1 and ECAL2 seen below the thresholds of 5 GeV and 10 GeV, respectively. The plots show the cluster multiplicities (top), the energy distribution for the reconstructed clusters, i.e. photons (middle) and the XY coordinate of these clusters (bottom).

A large fraction of the high energy photon preselected events have additional clusters in ECAL1 and ECAL2. When comparing to the similar distribution obtained for random trigger events and shown in Fig. 12 one concludes that these additional photons belong to the selected events. Understanding the origin and/or eliminating these additional photons will be a crucial issue for the final selection of exlusive single-photon events.
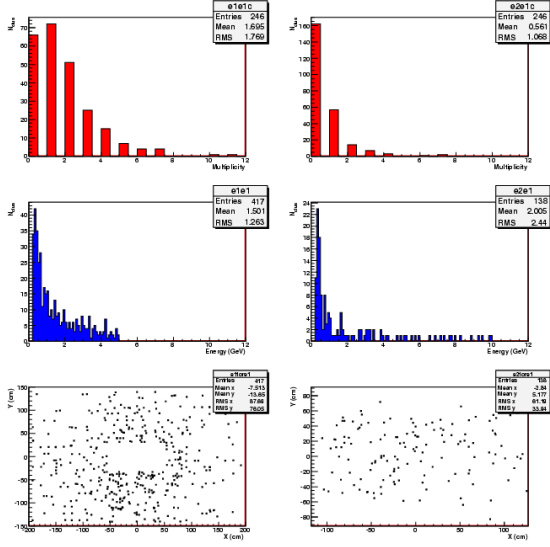
Figure 10: Additional clusters multiplicities (top), corresponding γ energies (middle) and XY positions (bottom), ECAL1 (left) and ECAL2 (right) for events with one photon of $E_\gamma > 5$ GeV in ECAL1.
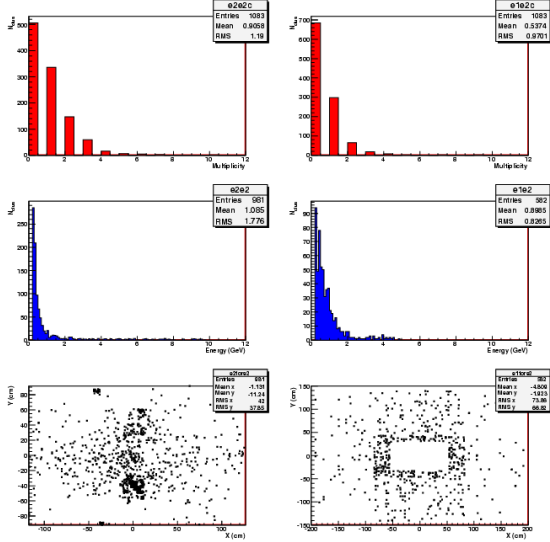

Figure 11: Same as above for events with one photon of $E_\gamma > 10$ GeV in ECAL2. ECAL2 (left) and ECAL1 (right).

Fig. 12 shows the cluster multiplicity (top), the cluster energies (middle) and the XY coordinate of these clusters (bottom) for random trigger events after application of the noisy channels suppression procedure. A probability for the noisy channels suppression of 5×10^{-4} for ECAL1 and of 10^{-4} for ECAL2 was chosen. As can be seen for most events, there exists no electromagnetic cluster in the calorimeters. In the ECAL2 it is clearly visible that the parasitic clusters are due to pile-up.
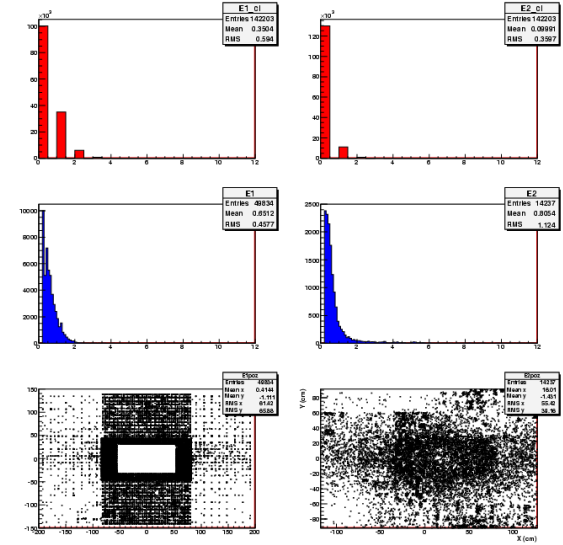
Figure 12: The clusters multiplicities (top), their energies (middle) and XY positions (bottom) for random trigger events after noisy channels suppression. ECAL1 (left) and ECAL2 (right).

3.3 Lowering ECALs thresholds in $\mu p \to \mu' p \gamma$ preselection

The choice of the optimum threshold to eliminate events having additional photon(s) is a critical issue. Fig. 13 shows the variation of the Signal/Backgound (Signal and Background being the correlated and uncorrelated components as shown in the ϕ_{miss} vs ϕ_{rpd} distribution of Fig. 7).

An optimum is seen for a set of threshold around 1(2) GeV for ECAL1(ECAL2). Note that this setting was already proposed as a good compromise to get a good separation between γ and π^0 events [3] and also to provide a good noise rejection in the ECALs [2].
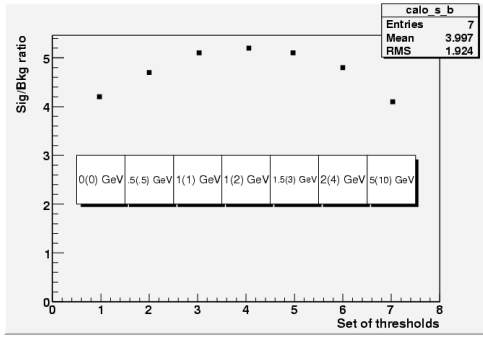
Figure 13: Signal/Background ratio for different sets of low energy threshold applied to ECAL1 and ECAL2

For further analysis the events having additional low energy photon(s) above 1 GeV and above 2 GeV for ECAL1 and ECAL2 respectively are rejected (new selection). Fig. 14 shows for the 990 events of this new selection the differences in timing and Z-position, Fig. 15 shows the differences Δp_T and $\Delta \phi$ and Fig 16 shows the correlation between the ϕ_{miss} and ϕ_{rpd} azimuthal angles and the Φ angle distribution.
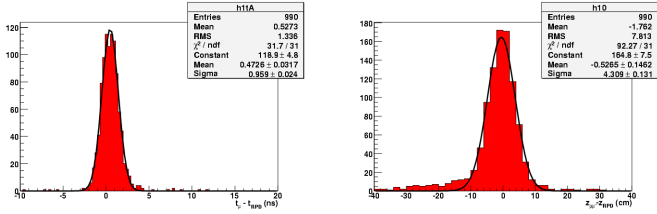
Figure 14: New selection: timing (left) and Z position (right) differences between the reconstructed $\mu\mu'\gamma$ vertex and the single proton position detected in RPD.
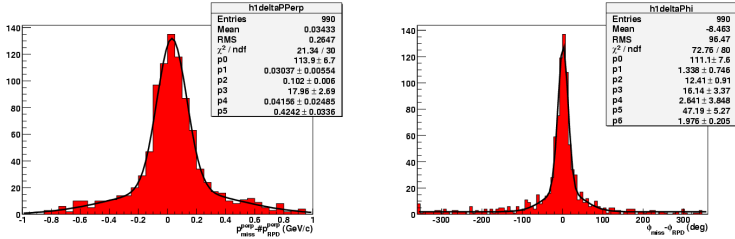

Figure 15: New selection: the difference $\Delta p_T = |p_{Tmissing}| - |p_{Trpd}|$ (left) and the difference $\Delta \phi = (\phi_{miss} - \phi_{rpd})$ (right).
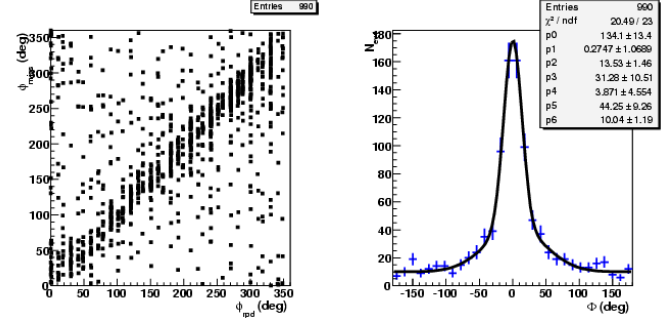

Figure 16: New selection: the correlation between ϕ_{miss} and ϕ_{rpd} (left), the Φ angle between the $\mu\mu'$ plane and the produced γp plane for all events (right).

Fig. 17 (left) shows the correlation in the $\theta_{\gamma^*\gamma}$ polar angle variable, as previously shown in Fig. 8. Fig. 17 (right) shows the value of E_{miss} for the new selection. Note that the large tail in the E_{miss} distribution has been reduced compared to its size seen in the first preselection (see Fig. 8 (right)).
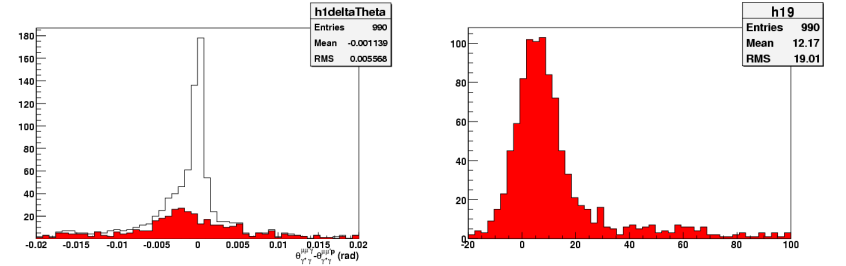

Figure 17: New selection. Left: $\Delta\theta_{\gamma^*\gamma}$ for all events (white) and for events out of the exclusivity cuts (red). Right: E_{miss} distribution.

3.4 Final selection of the $\mu p \rightarrow \mu' p \gamma$ events

In order to compare with simulations, one has to guarantee as much as possible that exclusive $\mu p \rightarrow \mu' p \gamma$ events are selected and a cut $E_{miss} < 30$ Gev will be applied. Starting from the above sample of 990 evts obtained with the optimum 1 GeV (2 GeV) threshold in ECAL1 (ECAL2) for additional photon rejections the following successive cuts have been applied:
- cut $\Delta P_T < 0.2$ GeV/c (see Fig. 18),
- cut $\Delta P_T < 0.2$ GeV/c + cut $E_{miss} < 30$ GeV (see Fig. 19),
- cut $\Delta P_T < 0.2$ GeV/c + cut $E_{miss} < 30$ GeV + cut $|\phi_{miss} - \phi_{rpd}| < 36$ deg (see Fig. 20),
- finally, cuts 1+2+3 plus selecting only $Q^2 > 1$ (GeV/c)^2 events and applying $r < 1.6$ cm to eliminate contributions from the LH target walls (see Fig. 21).
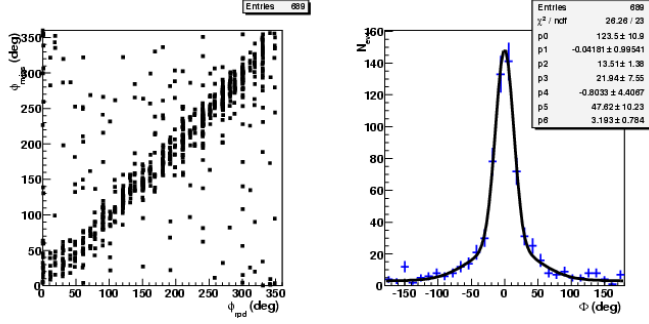
Figure 18: New selection plus cut $\Delta P_T < 0.2$ GeV/c.
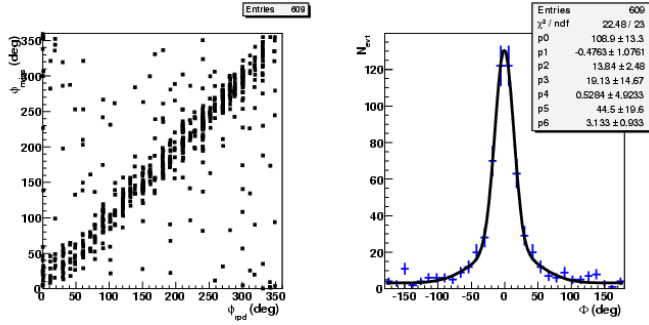
Figure 19: New selection plus cuts $\Delta P_T < 0.2$ GeV/c & $E_{miss} < 30$ GeV.
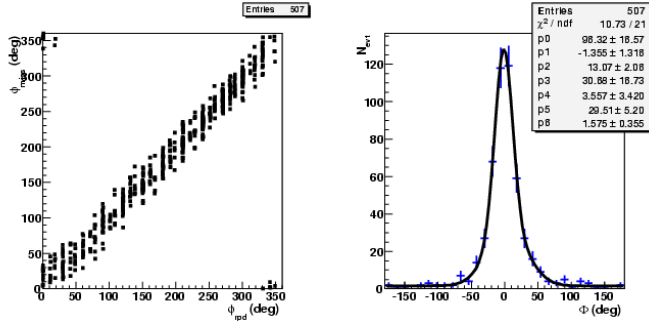
Figure 20: New selection plus $\Delta P_T < 0.2$ GeV/c & $E_{miss} < 30$ GeV & $|\phi_{miss} - \phi_{rpd}| < 36$ deg.
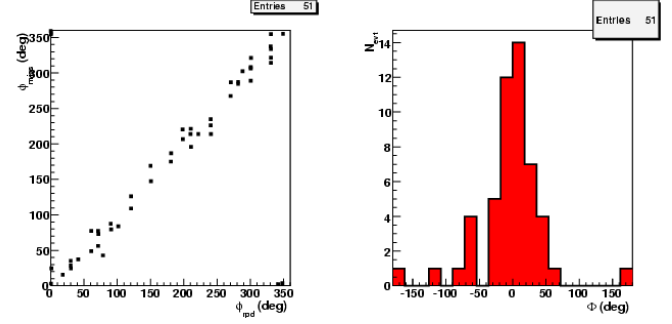

Figure 21: New selection plus cuts 1&2&3 plus selection of $Q^2 > 1$ (GeV/c)^2 events.

Fig. 22 shows the variation of the number of selected events as a function of the low energy (anti)-threshold cut applied on ECAL1 and ECAL2 keeping the relation threshold on ECAL2 = 2× threshold on ECAL1.
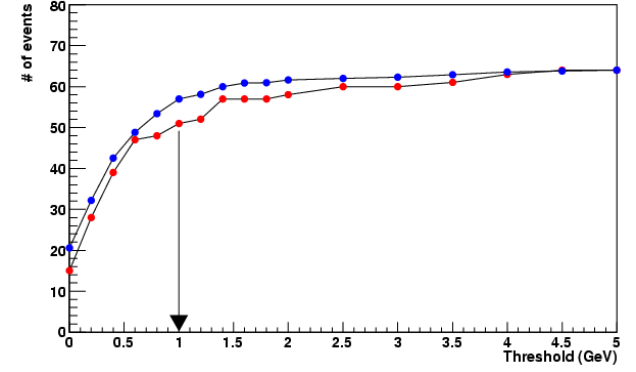

Figure 22: Number of events vs the (low energy) thresholds applied on ECAL1 and ECAL2 (thr._ECAL2 = 2× thr._ECAL1), blue: no Q^2 cut (division factor of 10), red: $Q^2 > 1$ (GeV/c)^2.

Since the data were obtained using different incident muon fluxes and different trigger mixes, having (or not) prescaling factors, a proper normalisation is required. This is developed in section 4.

3.5 Possible π^0 background

By definition, a $\mu p \to \mu' \gamma p$ exclusive event should have *one* and *only one* photon, i.e. zero additional photon. It is therefore important to understand the source of the additionnal clusters (photons) seen in ECAL1 and ECAL2 which belong to the preselected high energy photon events.

Possible sources are:
- pile-up which certainly contributes but does not dominate, as shown in the random trigger events sample,
- photons parasitically produced but *not* at the primary vertex,
- photons from the decay of a particle produced at the vertex (like $\mu p \to \mu' \pi^0 p$) which, if not well identified, will mock up DVCS events.

In this subsection the last source of background, namely the one from π^0, will be considered. The analysis was done by studying the invariant mass $M_{\gamma\gamma}$ distribution of the high energy photon with the additional photons (see section 3.2) in the event. It should be stressed that ALL such combinations were taken into account, hence the number of entries on the $M_{\gamma\gamma}$ plot corresponds to the number of additional photons in the event.
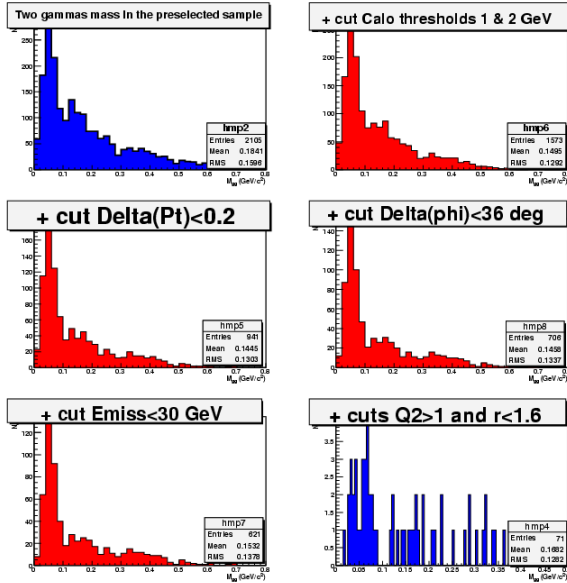

Figure 23: The invariant mass $M_{\gamma\gamma}$ distributions of the high energy photon with the additional photons in the event. The plots demonstrate the impact of the different exclusive photon selection cuts applied step by step. Here and in all further $M_{\gamma\gamma}$ distributions with all cuts the X scale of the plot has been shortened to enhance the π^0 mass region.

Six plots on Fig. 23 show the impact of analysis cuts on the $M_{\gamma\gamma}$ distribution. On the first blue plot there is a bump in the expected π^0 mass region. On the second blue plot after applying all cuts there remain several π^0 candidates.

As $M_{\gamma\gamma}$ mass resolution in ECAL1 and ECAL2 are different the next figures present the contribution from ECAL1 and ECAL2 separately.
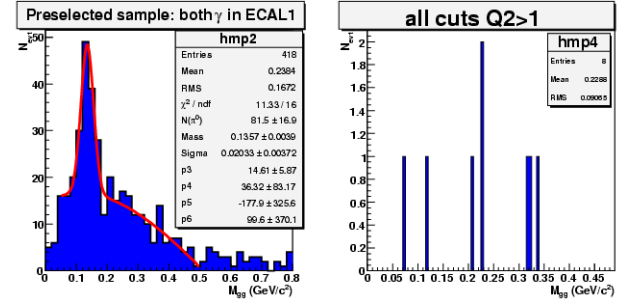
Figure 24: Invariant mass of two γ detected only in ECAL1. From the distribution on the left plot a possible π^0 contamination in the exclusive photon candidates can be estimated.
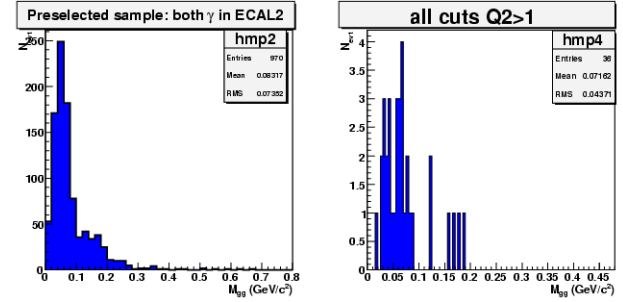

Figure 25: The same plots as previous for ECAL2.
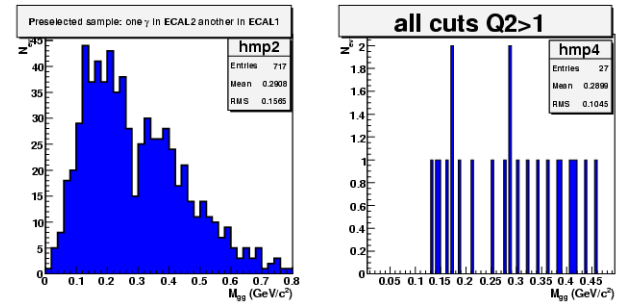
Figure 26: The same plots as previous but one photon detected in ECAL1 and another one in ECAL2

Fig. 24 shows the $M_{\gamma\gamma}$ distribution before and after all cuts if both photons are detected in ECAL1. A clear π^0 peak is seen on the left plot with a mass resolution σ equals to 20 MeV. From the right plot we can conclude that there is only one π^0 candidate in the $\pm 3\sigma$ interval.

Fig. 25 shows the $M_{\gamma\gamma}$ distribution before and after all cuts if both photons are detected in ECAL2. The π^0 peak on the left plot is hardly seen due to a huge background. Since we haven't results from the fit we count the entries in the 0.1-0.2 MeV interval as the π^0 candidates. There are 6 entries from 4 events.

Fig. 26 shows the $M_{\gamma\gamma}$ distribution before and after all cuts if one photon is detected in ECAL1 and another in ECAL2. As on the previous plot the π^0 peak on the left plot is not clearly seen. Using the procedure applied to ECAL2 photons we count 7 entries from 7 events.

At this step of analysis we consider 12 events with possible 14 π^0 candidates, the number of π^0 candidates being larger than the number of events.

For further clarification the multiplicities of the additional clusters in the final sample of 51 exclusive photon events are shown in Table 1 and Table 2. The numbers in () correspond to $M_{\gamma\gamma}$ in the mass interval compatible with the π^0 mass. It is seen that a) in the case when "exclusive photon" is detected in ECAL1 the multiplicity of additional clusters is equal to one in both calorimeters, b) in the case when "exclusive photon" is detected in ECAL2 the multiplicity of additional clusters is equal to one in ECAL1 but is equal to one *and two* in ECAL2.

Multiplicity	Clusters in ECAL1	Clusters in ECAL2
0	3	4
1	4 **(1)**	3 **(2)**
2	0	0

Table 1: Multiplicity of additional clusters (γ) for the 7 events with a high energy γ in ECAL1. Numbers in () correspond to π^0 candidates.

Multiplicity	Clusters in ECAL1	Clusters in ECAL2
0	32	18
1	12 **(5)**	17 **(0)**
2	0	9 **(6)**

Table 2: Multiplicity of additional clusters (γ) for the 44 events with a high energy γ in ECAL2. Numbers in () correspond to π^0 candidates.

The ECAL2 appears particularly noisy for events for which the high energy photon is precisely detected in ECAL2, as illustrated in Fig. 11. From Table 1 and Table 2 we notice that only in this particular case the multiplicity of additional clusters is elevated. For further analysis we kept only events with not more than one additional cluster in each calorimeter. All π^0 candidates with both photons detected in ECAL2 are eliminated using this criteria.

Finally we consider 8 π^0 candidates (8 events) in our - 51 events - exclusive photon sample. It should be noted that the main contribution to the π^0 sample is from configurations with one photon detected in ECAL1 and another in ECAL2 (7 π^0 candidates out of 8)

Due to very limited statistics this estimation was based only on mass value criteria, thefore we consider this number as an upper limit. This possible π^0 contamination of about $16 \pm 6\%$ is not in contradiction with the expectation that the π^0/Bethe-Heitler production ratio should be similar to the DVCS/Bethe-Heitler production ratio (about 10%).

It should be mentioned another possible source of π^0 contamination. Both gammas from very energetic π^0 ($E_{\pi^0} > 90$ - 100 GeV) can hit the same cells of ECAL2 and being reconstructed as a single cluster. This problem of "double photon clusters" was studied in Primakoff analysis [4]. It was proposed to use RMS of cluster and R4 ratio to separate single and "double photon clusters". In our analysis we used only RMS criteria.[2] Roughly if RMS > 3.4 cm this cluster is a π^0 candidate. The RMS of cluster was calculated using the X and Y coordinates of cells and the relative energy deposition in each cell as a weight. Fig. 27 shows the RMS distribution for our 21 gammas with energy $E_\gamma > 100$ GeV. On this statistics we don't see any "double photon cluster" and hence we do not have π^0 contribution from this source in our final sample.
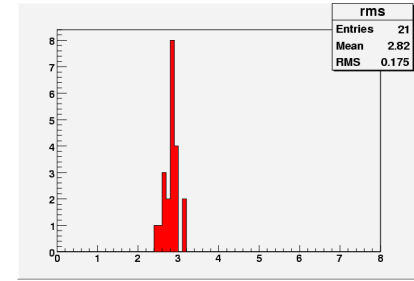

Figure 27: RMS distribution of ECAL2 clusters with energy $E_\gamma > 100$ GeV

4   Sharing between triggers, corrected event rates and FoM

The main triggers used in this analysis have either the RPD or the Middle Trigger (MT) or both in coincidence. Because of severe time constraints in the preparation of the beam test, only the upper half of the Middle Trigger was operationnal. Since it is the preferred trigger there was no prescaling factor applied (see Table 1, Appendix A.2). The RPD trigger was also used with the veto applied. For μ^+ running, a prescaling factor P = 6 was applied to the RPD trigger to cope for the higher intensity and trigger rate. This factor has to be unfolded in the analysis of the data.

The position of the scattered muon in the transverse plane at the position of the H4 hodoscopes (Z = 40 m) is illustrated in Fig. 28. It shows that for this data taking period only the top part of the Middle Trigger was activated (black dots). The red (blue) dots are events for μ^- (μ^+) beam for which the RPD trigger has fired. They are homogeneously spread and illustrate the optimal coverage required for the future trigger system.

---

[2] R4 is the ratio of energy of the *four* most energetic cells to the energy of the cluster. As cut on R4 was tuned using the difference of R4 distributions in pion and muon data (Primakoff data) assuming that the amount of "double photon clusters" in muon data is negligible we cannot to use R4 criteria in our analysis.
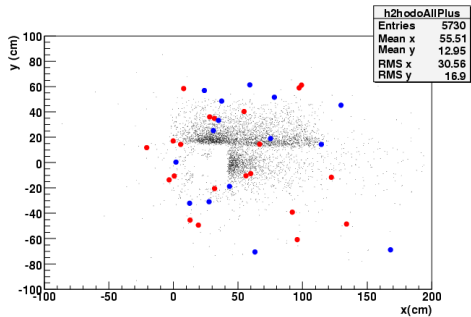
Figure 28: Impact point distribution for triggers events at Z = 40 m.

In principle, the spread for μ^+ running should favor the active area of the MT because of the prescaling factor applied on RPD although statistics is too scarce to really observe it.

Trigger	μ^-	μ^+	μ^+corr	Total
RPD only	21	16	96	117
MT only	0	0	0	0
RPD&MT	3	11	11	14
N_{Total}	24	27	107	131 ± 25
Flux $\times 10^{11}$	0.73		2.55	3.3
evts $/10^{11}\mu$	33		42	40

Table 3: Sharing between the different triggers

The sharing between the different triggers is described in Table 3 below for μ^+ and μ^-. It shows a relative enhancement of the RPD&MT trigger for μ^+ which is a consequence of the prescaling (P) of the RPD trigger mentioned above. The third column (μ^+corr) contains the number of events corrected for this factor. The estimate of the total number of events and statistical error has to incorporate this correction. For the final event selection (shown in Fig. 21) we have measured $N_{Total} = 131 \pm 25$ corresponding to an integrated flux of 3.3×10^{11} muons.

$$N_{Total} = 35 + P \times 16 = 131 \quad \text{and} \quad \Delta N tot = \sqrt{35 + P^2 \times 16} = 25$$

This figure can now be used to evaluate the efficiency of detection of exclusive photon production using the present COMPASS set-up. For this task, two "fast" Monte-Carlo simulation programs have been developed [5] for which the expected number of events (mostly from the Bethe-Heitler process) has been presently cross-checked at a level of 10%.

A way to tag tho observed process is to look at the distribution of the angle Φ between the leptonic and hadronic planes as discussed in section 3.1. The Bethe-Heitler events (expected to dominate our events) show a peak at $\Phi \sim 0$. The observed distribution, after applying the proposed cuts, already shown in Fig. 21 (right), is now displayed in Fig. 29 with the prediction from the Monte-Carlo simulation.
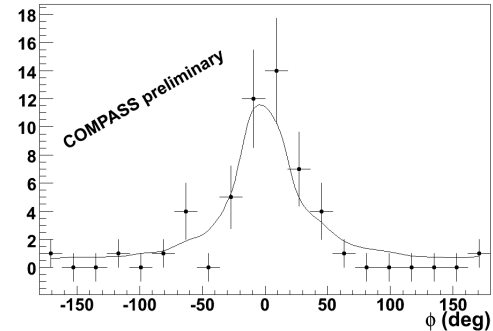

Figure 29: The distribution in the azimuthal angle Φ ($\mu\mu'$ vs γp planes) for the measured exclusive $\mu p \rightarrow \mu' p \gamma$ ($Q^2 > 1$ (GeV/c)^2) events (black dots) and a comparison with simulation [5].

The shape of the observed distribution is compatible with the Bethe-Heitler process. The overall detection efficiency can be deduced from the relative normalisation of the two distributions. The result is $\epsilon = 0.32 \pm 0.13$. The final global efficiency incorporates additional factors such as availability of the SPS, data taking efficiency and also realistic detection and trigger efficiencies and livetimes when running at nominal beam intensity (not the case for the present data). The estimate of these factors provided in the LoI would lead to an additional factor $\epsilon_{Add} \sim 0.8^4 = 0.41$ which then leads to what we defined in the LoI as the "global Figure of Merit" FoM $= 0.13 \pm 0.05$. The value presently used in the LoI [1] of $= 0.1$ is in very good agreement with this first direct estimate. In order to obtain definite conclusions on the important issue of target length and running time for future running, further measurements and simulations are still needed.

5   Conclusions

An exclusive single-photon production signal has been observed for the first time using the COMPASS hadron setup and a 160 GeV muon beam. The observed ϕ distribution is clearly typical of a dominant Bethe-Heitler contribution. A first direct evaluation of the *global efficiency* (or global FoM used in the LoI [1]) has been performed (FoM_measured$= 0.13 \pm 0.05$) which is in agreement with the value (FoM_estimated$= 0.1$) used in the LoI.

With the present limited statistics (about 100 events), the yield for events originated from pure DVCS process or DVCS-BH interference (about 1/10 of the total observed yield), has the same order of magnitude that the yield of exclusive π^0 originated from the selected high energy photon plus a low-energetic extra photon.

The main goal for 2009 run is a first evaluation of the relevant contributions DVCS and DVCS-BH interference and a better understanding of backgrounds.

References

[1] COMPASS Medium and Long Term Plans, The COMPASS Collaboration, CERN-SPSC-2009-003, SPSC-I-238, January 21, 2009.

[2] Present performances of COMPASS electromagnetic calorimetry from data analysis. V. Kolosov, O. Kouznetsov, A. Magnon, F. Nerling, COMPASS note 2008-5, June 16, 2008.

[3] Tests in 2008 to prepare the GPD experiments with the muon beam. Nicole d'Hose, COMPASS collaboration meeting, January 17-18, 2008.

[4] Primakoff scattering analysis. A.Guskov, COMPASS analysys meating, March 27-28, 2008.

[5] Monte Carlo simulations of Bethe-Heitler and DVCS using COMPASS apparatus. Etienne Burtin and Andrzej Sandacz.

A Appendix

A.1 Kinematical constraints for Exclusive Single Photon production

The studied reaction is the one single photon production on the nucleon

$$\mu + p \to \mu' + \gamma + p$$

The kimematic variables in the lab are:

k, k, θ_μ	four-momentum, momentum and angle of the incident muon μ
k', k', $\theta_{\mu'}$	four-momentum, momentum and angle of the outgoing muon μ'
$q = k - k'$, q, ν	four-momentum, momentum and energy of the virtual photon $\gamma*$
q', q'	four-momentum and momentum of the outgoing real photon γ
p, m	four-momentum of the incident proton and its mass
p', p', E'_p	four-momenentum, momentum and energy of the recoiling proton

without BMS k = $\pm$ 6 GeV (one σ)

$P_{miss} = k - k' - q'$

$E_{miss} = E_\mu - E_{\mu'} - E_\gamma$

Q^2 is the negative four-momentum squared of the virtual photon

$Q^2 = 4kk'\sin^2((\theta_{\mu'} - \theta_\mu)/2)$

the error on Q^2 due to the bad knowledge of k is 4%

$t = (p - p')^2 = (q - q')^2$ is the four-momentum transfer

t is a very useful variable to link photon and proton kinematics

t can be determined by the recoil proton detection: $t = (p - p')^2 = 2m(m - E_{p'})$

$\sigma_t/|t| = (4m^2 - t)/(2m^2 - t) \times \sigma_{p'}/p' \sim 2\sigma_{p'}/p'$

ν can be estimated using t and photon energy: $\nu = q' - t/(2m)$

and then we can estimate $x = Q^2/(2m\nu)$

$t = (q - q')^2 = -Q^2 - 2q'(\nu - q\cos\theta_{\gamma*\gamma})$

and then $\cos\theta_{\gamma*\gamma} = \nu/q(1 + m/\nu \times (t + Q^2)/(t + 2m\nu))$

$$\cos\theta_{\gamma*\gamma} = \frac{1}{\sqrt{1 + 4m^2x^2/Q^2}} \left(1 + \frac{2m^2x}{Q^2}\frac{t + Q^2}{t + Q^2/x}\right) \tag{1}$$

The following kinematical constraints can be applied:

– Correlation in transverse momentum relatively to the incident muon direction:
plot $P_{miss}^\perp$ - $P_{RPD}^\perp$

– Correlation in azimuthal angle relatively to the incident muon direction:
plot $\phi_{P_{miss}}$ - ϕ_{RPD}

– Correlation in polar angle
the detection of photon and muons allows to build $\cos\theta_{\gamma*\gamma}^{\text{via photon}} = (\vec{k} - \vec{k'}) \cdot \vec{q'}/(qq')$
the detection of proton and muons allows to build $\cos\theta_{\gamma*\gamma}^{\text{via proton}}$ according the formula 1: plot $\cos\theta_{\gamma*\gamma}^{\text{via photon}}$ - $\cos\theta_{\gamma*\gamma}^{\text{via proton}}$

A.2 Trigger settings and list of runs recorded

Trigger	Definition						
Trigger_1	RPD&veto:6	MT:1	MT&RPD:1	CT:20	BT:8000	RPD:200	rand:400
Trigger_2	RPD&FH&veto:1	MT:60	MT&RPD:1		MT&BT:80000	RPD&FH:400	rand:1000
Trigger_3	RPD&veto:600	MT:60	MT&RPD:1		BT:80000		rand:1000
Trigger_4	RPD&veto:4	MT:1	MT&RPD:1	CT:80	BT:8000	RPD:200	rand:400
Trigger_5	RPD&veto:3	MT:3	MT&RPD:1	CT:80	BT:4000	RPD:100	rand:400
Trigger_6	RPD&veto:3	MT:10	MT&RPD:1	CT:40	BT:4000	RPD:100	rand:400
Trigger_10	RPD&veto:1	MT:1	MT&RPD:1	CT:40	BT:4000	RPD:100	rand:400
Trigger_11	RPD&veto:1	MT:1	MT&RPD:1	CT:40	BT:10000	RPD:100	rand:400
Trigger_12	RPD&FH&veto:1	MT:1	MT&RPD:1	CT:40	BT:10000	RPD&FH:100	rand:400
Trigger_MM1	RPD&veto:6	MT:1	MT&RPD:1	CT:20 VI:1000 Halo:200 BT:8000 RPD:200 rand:40			

Table 1: Trigger settings used for μ^- and μ^+ data taking

Run	spills	Tag	$n_\mu/spill$	Trigger	comment
71421	75	Good/OK	$5.9 \times 10^7 \mu^-$	Trigger_11	RPD threshold 60 60 500
71424	201	Good/OK	-	Trigger_11	-
71425	33	Good/OK	-	Trigger_12	-
71427	156	Good/OK	-	Trigger_11	-
71429	96	Good/OK	-	Trigger_10	-
71430	127	Prob/Prob	-	Trigger_10	Pb on MW1
71434	201	Good/OK	-	Trigger_10	-
71435	28	Prob/Prob	-	Trigger_10	Pb on SciFi-D 151
71436	201	Good/OK	-	Trigger_10	-
71437	201	Prob/Prob	-	Trigger_10	-
Total spills = 1319 (μ^-)					

Table 2: Runs and corresponding trigger settings taken with μ^- beam

Run	spills	Tag	$n_\mu/spill$	Trigger	comment
71445	16	Good/OK	$1.54 \times 10^8 \mu^+$	Trigger_6	RPD threshold 60 60 500
71446	19	Good/OK	-	Trigger_5	-
71447	159	Good/OK	-	Trigger_4	-
71448	34	Good/OK	-	Trigger_1	-
71449	188	Good/OK	-	Trigger_1	-
71450	32	Good/OK	-	Trigger_1	-
71453	201	Good/OK	-	Trigger_1	
71454	201	Good/OK	-	Trigger_1	
71455	201	Good/OK	-	Trigger_1	
71456	201	Good/OK	-	Trigger_1	
71457	24	Good/OK	-	Trigger_1	
71463	202	Prob/Prob	-	Trigger_MM1	MM02X(Y) $\rightarrow$ nominal position
71466	201	Good/OK	-	Trigger_1	
Total spills = 1679 (μ^+)					

Table 3: Runs and corresponding trigger settings taken with μ^+ beam

COMPASS-Note-2009-11, J.Bernhard et al., "A new analysis of the 2008 DVCS test run data using the precise timing information for photons detected in the electromagnetic calorimeters ECAL1/ECAL2".

COMPASS Note 2009-11
(Addendum to Note 2009-4)
October 7, 2009

A new analysis of the 2008 DVCS test run data using the precise timing information for photons detected in the electromagnetic calorimeters ECAL1/ECAL2.

J. Bernhard[1], E. Burtin[2], N. d'Hose[2], G. Jegou[2], V. Kolosov[3], O. Kouznetsov[4] and A. Magnon[2]

Abstract

The data obtained during the short DVCS test run in 2008 on high energy exclusive photon production using the COMPASS hadron setup and a 160 GeV muon beam have been reprocessed incorporating the photon timing information using the SADCs readout in both ECAL1 and ECAL2. The resulting improvement of the cleanliness of the exclusive photon sample is discussed.

[1]University of Mainz
[2]CEA-Saclay, IRFU/SPhN
[3]Protvino, IHEP
[4]Dubna, JINR

Contents

1 New analysis versus the previous one

The 2008 DVCS test data have been recently reproduced providing an improved cluster reconstruction (mainly in ECAL2) and also having available the ECALs cluster time with respect to the trigger time. The new analysis uses the newly reproduced data. Both the old [1] and the new analysis involve common steps:

Preselection of exclusive single-photon events.
- there are only *two* charged tracks ($\mu\mu'$) at the primary vertex,
- there is only *one* proton candidate in the Recoil Proton Detector (RPD) and it has a momentum < 1 GeV/c.
- there is only *one* photon with energy ≥ 5 GeV in ECAL1 and *no* photon with energy ≥ 10 GeV in ECAL2, or
- there is only *one* photon with energy ≥ 10 GeV in ECAL2 and *no* photon with energy ≥ 5 GeV in ECAL1.[1]

It should be noted that the preselected events may have additional low-energy photons. In the old analysis, the suppression of additional photons was done by an appropriate choice of ECALs thresholds.
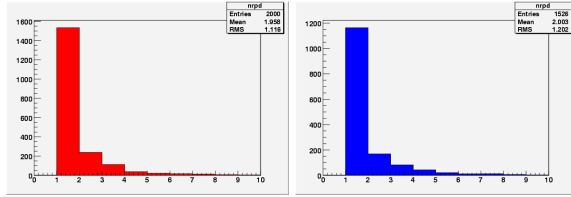

Figure 1: The multiplicities in the Recoil Proton Detector for proton candidates. *Left*: old production *Right*: new production.
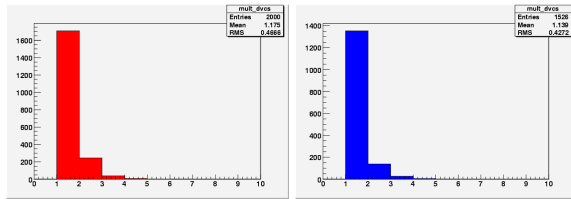

Figure 2: The multiplicities in the ECALs for high energy photon candidates. *Left*: old production *Right*: new production.

One step before this preselection of exclusive single-photon events the RPD and ECALs multiplicities were checked. Fig. 1 shows the multiplicities in the RPD for proton candidates with momentum < 1 GeV/c for old and new productions. Fig. 2 shows the multiplicities in the ECALs for high energy photon candidates, E > 5 GeV in ECAL1

---

[1] The thresholds of 5 (10) GeV correspond to the lowest energy expected for DVCS and BH photons given the angular coverage of ECAL1 (ECAL2).

and E > 10 GeV in ECAL2. As can be seen, the distributions in the new production are very similar to those of the old one.

We preselect events with one RPD proton and one single high energy photon candidate. The conclusion from the old analysis [1] that the events with one proton track represent $\sim 75\%$ of the initial sample is confirmed in the new production. The fraction of events with one high energy photon is now $\sim 90\%$ of the initial sample, compared to $\sim 85\%$ previously.

Choice of optimum threshold of 1 GeV and 2 GeV for ECAL1 and ECAL2, respectively, to eliminate events having additional photons.

This painful problem seems to be resolved in the new production. The reduction of additional photons comes essentially from two sources: a) general improvement of the ECAL software and calibration, b) imposing a cut on the ECALs timing information.

In the old data production, only the energy and the spatial coordinate of each cluster were available. In the new production, the cluster time defined as the moment when the front SADC signal amplitude reaches half of its maximum value is also available.

Fig. 3 shows the timing resolution for clusters reconstructed in ECAL1 and ECAL2 for the 2008 DVCS run. The timing resolution is $\sigma_t \sim 1.7(1.6)$ ns for all gammas and $\sigma_t \sim 1.5(1.4)$ ns for the (energetic) gammas having $E_\gamma \geq 5(10)$ GeV in ECAL1(2). The timing cuts to accept a cluster were evaluated to be $|t_{\text{cell}} - 0.05| < 5.35$ ns for ECAL1 and $|t_{\text{cell}} - 0.13| < 4.93$ ns for ECAL2. The cut is chosen to $\sim 3.5 \times (\sigma_t$ for energetic γ's) which was shown to maximize the number of selected events.
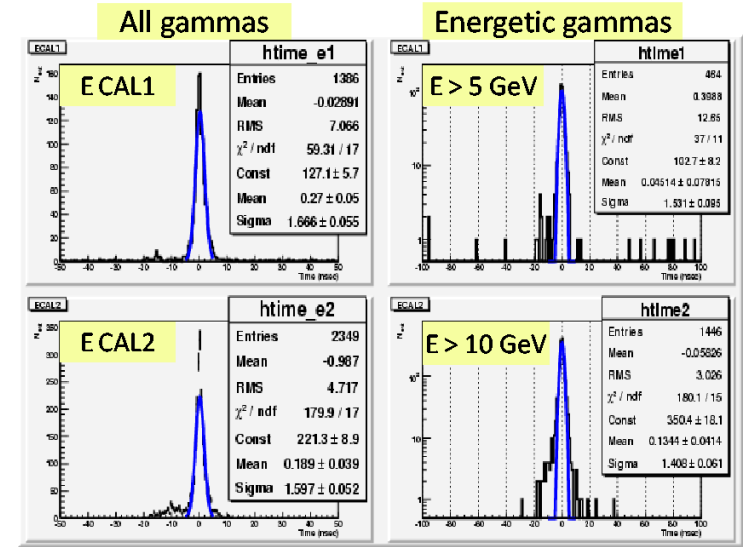

Figure 3: Timing resolution for ECAL1 (top) and ECAL2 (bottom) for all gammas (left) and only energetic gammas (right).

In the new production the average multiplicities and energy of the additional clusters (low energy γ's) have changed drastically. Table 1 and Table 2 present the improvements with respect to the old production seen in the new production without and with timing cut. As can be seen, in both calorimeters the average multiplicities decrease but the average energy of the remaining clusters increases, a consequence of the strong suppression of non correlated low energy background. Applying the timing cut opens the possibility to efficiently select exclusive single photon events without applying any thresholds for ECALS as it had to be done in the old analysis [1].

For the final selection an optimum set of cuts is chosen to guarantee that as many as possible exclusive $\mu p \to \mu' p \gamma$ events are selected.

- $\Delta P_T < 0.2$ GeV/c ($\Delta p_T = |p_{Tmissing}| - |p_{Trpd}|$, transverse missing momentum balance),
- $E_{miss} < 30$ GeV (the large value is due to the absence of the Beam Momentum Station),
- $|\phi_{miss} - \phi_{rpd}| < 36$ deg (difference between the azimuthal angle ϕ_{miss} of the missing momentum and the azimuthal angle ϕ_{rpd} of the proton candidate),
- $Q^2 > 1$ (GeV/c)^2 (a cut for physics),
- $r < 1.6$ cm (a cut to eliminate contributions from the LH2 target walls).

Table 1: Average multiplicities and energy of additional clusters in events with a single high energy ($E_\gamma > 5$ GeV) photon candidate in ECAL1.

$E_\gamma < 10$ GeV in ECAL2 and $E_\gamma < 5$ GeV in ECAL1					
	Old production (OP)		New production (NP)		NP with timing cut	
	Ecal1	Ecal2	Ecal1	Ecal2	Ecal1	Ecal2
Mean (multip)	1.70	0.56	1.46	0.24	1.31	0.23
RMS (multip)	1.77	1.07	1.73	0.72	1.65	0.72
Mean (E, GeV)	1.50	2.00	1.64	3.49	1.80	3.52
RMS (E, GeV)	1.26	2.44	1.35	2.51	1.38	2.57

Table 2: Average multiplicities and energy of additional clusters in events with a single high energy ($E_\gamma > 10$ GeV) photon candidate in ECAL2.

$E_\gamma < 10$ GeV in ECAL2 and $E_\gamma < 5$ GeV in ECAL1					
	Old production (OP)		New production (NP)		NP with timing cut	
	Ecal1	Ecal2	Ecal1	Ecal2	Ecal1	Ecal2
Mean (multip)	0.91	0.54	0.52	0.17	0.27	0.09
RMS (multip)	1.19	0.97	0.92	0.63	0.76	0.67
Mean (E, GeV)	1.08	0.90	1.70	1.15	2.35	1.42
RMS (E, GeV)	1.77	0.83	1.81	0.98	2.19	1.15

2 Impact of the timing information from the ECALS on the selection of exclusive single-photon events.

Fig. 4 shows, for the old production, the distribution of the Φ angle between the $\mu\mu'$ plane and the γp plane for the 51 selected events (left). Among the 51 events, 36 events have an additional photon, i.e. only 15 events can be named purely exclusive events (i.e. γ multiplicity equal to one) as shown in Fig. 4 (right). It should be noted that among the 36 events, 8 lead to an invariant mass for the two γ's compatible with the π^0 mass corresponding to an upper limit of of $16 \pm 6\%$ for a possible π^0 contamination in the selected events.

Fig. 5 shows the same distributions as before (Fig. 4) but using the new production, still without applying any timing cuts. A slight increase in the number of selected events ($51 \to 55$) and a significant increase ($15 \to 34$) in the number of selected events with photon multiplicity equal to 1 are seen. It was verified that the main exclusivity cuts $\Delta P_T < 0.2$ GeV/c and $|\phi_{miss} - \phi_{rpd}| < 36$ deg are equally well applicable for this new analysis .
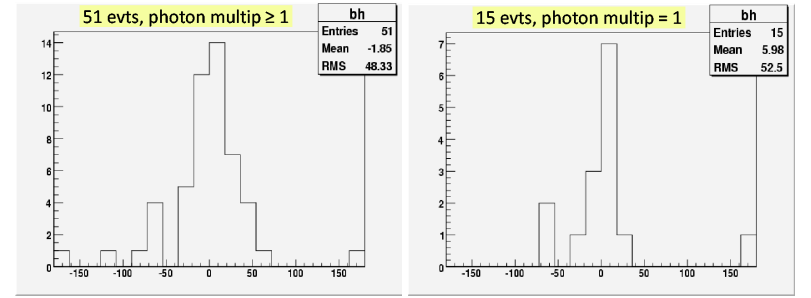

Figure 4: Old production. The Φ angle between the $\mu\mu'$ plane and the γp plane for the 51 selected events with photon multiplicity ≥ 1 (left). The same for the 15 events with photon multiplicity $= 1$ (right).
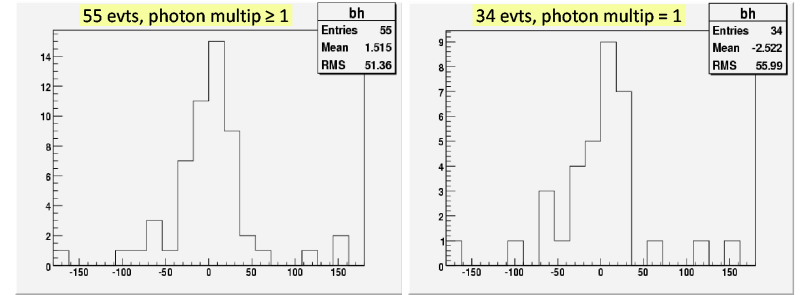

Figure 5: New production without timing cuts. The same as in Fig. 4, 55 selected events with photon multiplicity ≥ 1 (left) and 34 events with photon multiplicity $= 1$ (right).

Fig. 6 shows the impact of the timing cuts $|t_{cell} - 0.05| < 5.35$ ns for ECAL1 and $|t_{cell} - 0.13| < 4.93$ ns for ECAL2 on the selection of exclusive single-photon events. Comparing now Fig. 6 (new production and timing cuts) with Fig. 4 (old production) and left (mult. ≥ 1) and right (mult. $= 1$) for both figures we note the slight increase of the final number of selected events ($51 \rightarrow 55$) and the significant increase of the number of events with no additional clusters ($15 \rightarrow 52$). Among the 51 events of the old production a contamination by π^0 candidates of up to 16% could not be excluded and the only way to avoid this contamination is to select (mult. $= 1$) which leaves only $\sim 1/3$ of the selected events. Now, among the 55 events, there are only 3 events with additional clusters and those 3 events have only one additional cluster. The mass combination of the additional cluster with the high energy photon is compatible with the π^0 mass. This leads to an upper limit for the π^0 contamination of about 5%. Note that these 3 events can be simply removed asking purely exclusive single-photon events (Fig. 6 right). The contamination from π^0 mesons for this selected single photon sample (52 events) is now coming only from the cases where one of the photons from the π^0 decay is converted and not detected in ECALs.
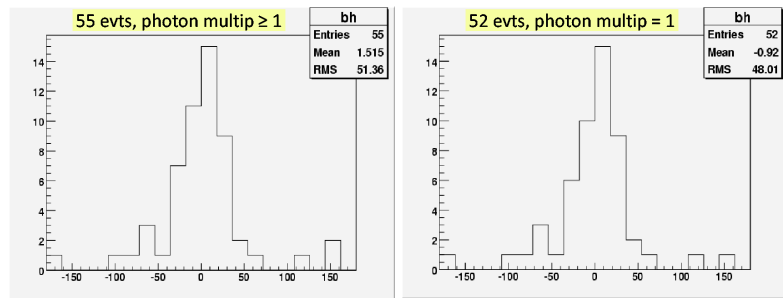

Figure 6: New production. The same as in Fig. 5 but applying the timing cut, 55 selected events with photon multiplicity ≥ 1 (left) and 52 events with photon multiplicity $= 1$ (right) .

3   Conclusions

Using the time information for clusters along with general improvements of the ECALs software the multiplicity of low energy additional photons is considerably reduced. Our old result - 51 events with up to (16 ± 6)% of π^0 contamination due to the low energy additional photons - is superseded by the new result - 52 events without such kind of background. In the final exclusive single-photon sample of 52 events the reason for a π^0 contamination can only be is that one of the two photons is not detected in the ECALs, or has an energy even lower than the hardware threshold. The larger statistics expected in exclusive π^0 events from the 2009 DVCS test run may help to determine quantitatively this type of background.

References

[1] J.Bernhard et al. The first observation of exclusive single-photon muoproduction at COMPASS in 2008 DVCS test run. COMPASS Note 2009-4.

Bibliography

[1] R.G. Sachs, Phys. Rev. 126 (1962) 2256.

[2] M.N. Rosenbluth, Phys. Rev. 79, 615 (1950)

[3] J. Friedrich and T. Walcher, Eur. Phys. J. A17(2003)607.
J..J. Kelly, Phys. Rev. C70(2004)068202.

[4] A.I. Akhiezer and M.P. Rekalo, Sov. J. Part. Nucl. 3, 277 (1974).

[5] O. Gayou et al, Phys. Rev. Lett. 88(2002)092301.

[6] F. Halzen and A.D. Martin, "Quarks and Leptons", Willey (1984).

[7] R. Jaffe and A. Manohar, Nucl. Phys. B 337 (1990) 509.

[8] N. Isgur, "Spin structure of the nucleon: a quark modeler's view", Ettore Majorana International School of Nucleon Structure, Erice, Italy (1995).

[9] A. Manohar, "An introduction to spin dependant deep inelastic scattering", Lake Louise Winter Institute, (1992) and UCSD/PTH 92-10.

[10] M. Burkardt, A. Miller, W.-D. Nowak, Rept. Prog. Phys. 73:016201 (2010).

[11] D. Müller et al., Forstch. Phys. 42 (1994) 101.

[12] J. C. Collins et al., Phys. Rev. D59 (1999) 074009.

[13] J.C. Collins and M. Diehl, Phys. Rev. D61 (2000)114015

[14] X. Ji, Phys. Rev. D 55 (1997) 7114
X. Ji, Phys. Rev. Lett. 78 (1997) 610.

[15] A. V. Radyushkin, Phys. Lett. B 385 (1996) 333; Phys Rev. D 55 (1997).

[16] M. Diehl, Phys. Rept. 388, 41 (2003).

[17] K. Goeke, M. V. Polyakov and M. Vanderhaeghen, Prog. Part. Nucl. Phys. 47 (2001)401.

[18] A.V. Belitsky, D. Müller, A. Kirchner, Nucl. Phys. B 629 (2002) 323.

[19] A.V. Belitsky, A.V. Radyushkin, Phys. Rept. 418 (2005)1.

[20] M. Burkardt, Phys. Rev. D62(2000)071503.
     M. Burkardt, Int. J. Mod. Phys. A18(2003)173.

[21] M. Diehl, Eur. Phys. J. C25(2002) 223.

[22] L. Mossé, Thèse de doctorat, Université Paris-Sud XI (2002).

[23] M. Vanderhaeghen, P.A.M. Guichon, M. Guidal, Phys. Rev. D 60 (1999) 094017.

[24] LHPC, P. Hagler et al., Phys. Rev. Lett. 93 (2004) 112001.
     LHPC, P. Hagler et al., Phys. Rev. D77 (2008) 094502.
     QCDSF-UKQCD, D. Brommel et al., PoS LAT2007 (2007) 158.

[25] D. Kaplan and A. V. Manohar, Nucl. Phys. B310, 527 (1988).

[26] M.J. Musolf et al., Phys. Rep. 239 (1994) 1.

[27] J. Jardillier, Thèse de doctorat, Université Blaise Pascal, Clermont-Ferrand (1999).

[28] Hall A Collaboration, J. Alcorn et al., Nucl. Instr. Meth. A522 (2004) 294.

[29] HAPPEX Collaboration, K.A. Aniol, et al., Phys. Lett. B 509 (2001) 211.

[30] HAPPEX Collaboration, A. Acha et al., Phys. Rev. Lett. 98 (2007) 032301.

[31] D. Lhuillier, Mémoire d'habilitation, CEA/DSM/DAPNIA-07-142 (2007).

[32] F.E. Maas, Phys. Rev. Lett. 94:152001,2005

[33] D. T. Spayde et al. (SAMPLE), Phys. Lett. B 583, 79 (2004).

[34] S. Baunack et al., (PVA4), Phys. Rev. Lett. 102, 151803 (2009).

[35] D. S. Armstrong et al., (G0), Phys. Rev. Lett. 95, 092001 (2004).

[36] J.P. Jorda et al., Nucl. Instrum. Meth. A412:1-18, 1998.
     N. Falletto et al., Nucl. Instrum. Meth. A459:412-425, 2001.

[37] S. Escoffier et al., Nucl. Instrum. Meth. A551:563-574,2005.

[38] COMPASS Collaboration, P. Abbon et al., Nucl.Instrum.Meth.A577:455-518,(2007).

[39] T. Sjostrand et al., PYTHIA 6.2 Physics and Manual, arXiv:hep-ph/0108264.

[40] COMPASS Collaboration, M. Alekseev et al., Phys. Lett. B 676 (2009) 31–38
     COMPASS Collaboration, by H. Fisher, DIS 2010, Firenze Italy (2010).

[41] COMPASS Collaboration, E.S. Ageev et al., Phys. Lett. B 633 (2006) 25–32
COMPASS Collaboration, by M. Stolarski, DIS 2008, London U.K. (2008).

[42] G. Jegou, Thèse de doctorat, Université Paris Sud, Orsay (2009).

[43] By COMPASS Collaboration, E. Burtin for the collaboration. Baryons 2004 proceedings, Nucl.Phys.A755:630-633,2005.

[44] H1 Collaboration, C. Adloff et al, Phys Lett. B 539 (2002) 25.
ZEUS Collaboration, S. chekanov et al, Nucl. Phys. B 718 (2005) 3.
NMC Collaboration, M. Arneodo et al., Nucl. Phys. B 429 (1994) 503.
Fermilab E665 Collaboration, M.R. Adams et al., Zeit. Phys.C 74 (1997) 237.
CLAS Collaboration, S. Morrow et al., Eur. Phys. J. A 39 (2009) 5.

[45] HERMES Collaboration, A. Airapetian et al., Eur. Phys. J. C 62 (2009) 659.

[46] M. Diehl, A.V. Vinnikov, Phys.Lett.B609:286-290,2005.

[47] K. Schilling and G. Wolf, Nucl. Phys. B 61 (1973) 381.

[48] COMPASS Note-2004-9. E. Burtin et al, "Angular distributions and $R = \sigma_L/\sigma_T$ for exclusive ρ^0 production".

[49] M.G. Ryskin, Z. Phys. C57 (1993) 89.
M. Arneodo et al., Comput. Phys. Commun. 100 (1997) 195; hep-ph/9610286.

[50] A. Sandacz, private communication.

[51] COMPASS Collaboration, M. Alekseev, Eur. Phys. J. C52 (2007) 255-265.

[52] H. Fraas, Nucl. Phys. B113 (1976) 532.

[53] HERMES Collaboration, A. Airapetian et al., Eur. Phys. J. C 29 (2003) 171.

[54] S.I. Manaenkov, Regge description of spin-spin asymmetry in photon diffractive dissociation, Preprint DESY 99-016 (see also hep-ph/9903405).

[55] COMPASS Collaboration, V.Yu. Alexakhin et al., Phys. Lett. B647 (2007) 330.

[56] S. V. Goloskokov and P. Kroll, Eur. Phys. J. C 42 (2005) 281.

[57] COMPASS Note-2007-9, J. Bisplinghoff et al., "Extraction of transverse target single spin assymetry for exclusive ρ^0 production from COMPASS 2002-2004"
COMPASS Note-2009-10, E. Burtin et al., "Exclusive ρ^0 production using tranversely polarized ^{6}LiD (2004) and NH$_3$ (2007) targets".

[58] M. Diehl and S. Sapeta, Eur. Phys. J. C41 (2005) 515.

[59] M. Diehl, JHEP 0709 :064 (2007).

[60] S. V. Goloskokov and P. Kroll, Eur. Phys. J. C53 (2008) 367.
S. V. Goloskokov and P. Kroll, Eur. Phys. J. C59 (2009) 809.

[61] COMPASS II proposal, CERN-SPSC-2010-014 ; SPSC-P-340.
http://wwwcompass.cern.ch/compass/proposal/compass-II_proposal/compass-II_proposal.pdf

[62] Conceptual Design Report (CDR) for The Science and Experimental Equipment for The 12 GeV Upgrade of CEBAF (Prepared for the DOE Science Review, April 6–8, 2005), Editors J. Arrington et al., Jefferson Lab (2005), http://www.jlab.org/div_dept/physics_division/GeV/doe_review/CDR_ for_Science_Review.pdf.

[63] A. Sandacz, http://wwwcompass.cern.ch/compass/gpd/index.html, April 27,2009.

[64] By H1 Collaboration (F.D. Aaron et al.) Phys.Lett.B681:391-399,2009.

[65] K. Kumericki et al., arXiv:0904.0458 [hep-ph].

[66] HERMES Collaboration, A. Airapetian et al., JHEP 06 (2008) 066.

[67] JLab CLAS Collaboration, F.X. Girod et al., Phys. Rev. Lett. 100 (2008) 162002; R. de Masi et al., Phys. Rev. C 77(2008) 042201; S. Morrow et al., Eur. Phys. Jour. A39 (2009) 5.

[68] JLab Hall A Collaboration, C. Munoz Camacho et al., Phys.Rev.Lett.97:262002 (2006); M. Mazouz et al. Phys.Rev.Lett.99:242501 (2007).

[69] F. Senée, mémoire d'ingénieur, CNAM, Paris (2008).

[70] COMPASS-Note-2009-4, J.Bernhard et al., "The first observation of exclusive single-photon muoproduction at COMPASS in 2008 DVCS test run".
COMPASS-Note-2009-11, J.Bernhard et al., "A new analysis of the 2008 DVCS test run data using the precise timing information for photons detected in the electromagnetic calorimeters ECAL1/ECAL2".

[71] G. Audit et al., in Nucl. Instrum. Meth. A301:473-481,1991.

[72] COMPASS-Note-2010-xx , E. Burtin et al., in preparation.